UNIVERSIDAD DE CIENCIAS Y ARTES DE CHIAPAS

INSTITUTO DE INVESTIGACIÓN E INNOVACIÓN EN ENERGÍAS RENOVABLES

T E S I S

EFECTOS DE LA INCERTIDUMBRE EN LA ESTIMACIÓN DE LAS PROPIEDADES TERMOFÍSICAS DE LOS NANOFLUIDOS SOBRE LA TRANSFERENCIA DE CALOR Y GENERACIÓN DE ENTROPÍA

QUE PARA OBTENER EL GRADO DE DOCTOR

EN MATERIALES Y SISTEMAS ENERGÉTICOS RENOVABLES

PRESENTA

RODOLFO ESTRADA CRUZ

DIRECTOR

DR. GUILLERMO ROGELIO IBÁÑEZ DUHARTE

Tuxtla Gutiérrez, Chiapas, México.   Noviembre de 2024.

UNIVERSIDAD DE CIENCIAS Y ARTES DE CHIAPAS
AUTÓNOMA

POR LA CULTURA DE MI RAZA

Tuxtla Gutiérrez, Chiapas a 28 de octubre de 2024
Oficio No. SA/DIP/0750/2024
Asunto: Autorización de Impresión de Tesis

C. Rodolfo Estrada Cruz
CVU: 1077585
Candidato al Grado de Doctor en Materiales y Sistemas Energéticos Renovables
Instituto de Investigación e Innovación en Energías Renovables
UNICACH
P r e s e n t e

Con fundamento en la **opinión favorable** emitida por escrito por la Comisión Revisora que analizó el trabajo terminal presentado por usted, denominado **Efectos de la incertidumbre en la estimación de las propiedades termofísicas de los nanofluidos sobre la transferencia de calor y generación de entropía** cuyo Director de tesis es el Dr. Guillermo Rogelio Ibáñez Duharte (CVU 215574) quien avala el cumplimiento de los criterios metodológicos y de contenido; esta Dirección a mi cargo **autoriza** la impresión del documento en cita, para la defensa oral del mismo, en el examen que habrá de sustentar para obtener el **Grado de Doctor en Materiales y Sistemas Energéticos Renovables.**

Es imprescindible observar las características normativas que debe guardar el documento impreso, así como realizar la entrega en esta Dirección de un ejemplar empastado.

Atentamente
"Por la Cultura de mi Raza"

Dra. Carolina Orantes García
Directora

DIRECCIÓN DE
INVESTIGACIÓN Y POSGRADO

C.c.p. Dr. José Francisco Pola Albores, Director del Instituto de Investigación e Innovación en Energías Renovables UNICACH. Para su conocimiento.
Dra. Laura Elena Verea Valladares, Coordinadora de Posgrado, Instituto de Investigación e Innovación en Energías Renovables, UNICACH. Para su conocimiento.
Archivo/minutario.

RJAG/COG/hvb/igp/gtr

2024 Año de Felipe Carrillo Puerto
BENEMÉRITO DEL PROLETARIADO,
REVOLUCIONARIO Y DEFENSOR DEL MAYAB.

Dirección de
Investigación
y Posgrado

Secretaría Académica
Dirección de Investigación y Posgrado
Libramiento Norte Poniente No. 1150
Colonia Lajas Maciel C.P. 29039
Tuxtla Gutiérrez, Chiapas, México
Tel:(961)6170440 EXT.4360
investigacionyposgrado@unicach.mx

T H E S I S

EFFECTS OF UNCERTAINTY IN THE ESTIMATION OF THE THERMOPHYSICAL PROPERTIES OF NANOFLUIDS ON HEAT TRANSFER AND ENTROPY GENERATION

BY

RODOLFO ESTRADA CRUZ

THESIS ADVISOR

DR. GUILLERMO ROGELIO IBÁÑEZ DUHARTE

Tuxtla Gutiérrez, Chiapas, México.

November 2024.

CONTENTS

LIST OF FIGURES

LIST OF TABLES

ACKNOWLEDGEMENTS

I thank God for allowing me to complete this research work, for presenting me with the circumstances and opportunities that enabled me to study, and for providing me with the health and strength I always needed.

To my thesis advisor, Dr. Guillermo Ibañez Duharte, for his invaluable teachings which were crucial for the development of this work and significant in my professional formation, for his excellent thesis direction, and for offering me his valuable friendship.

I extend my gratitude to my tutorial committee, Dra. Aracely López Grijalva, Dr. Joel Pantoja Enriquez, Dr. Orlando Lastres Danguillecourt and Dr. Juan Andrés Reyes Nava, for all the observations and contributions made, which enriched this research.

My special thanks and appreciation to Dra. Daisy Escobar Castillejos, who encouraged and supported me unconditionally to undertake this challenge, for her valuable advice, and for the friendship she offered.

I am grateful to the CONAHCYT for the support and resources provided, which facilitated the development of this doctoral training process.

For the love of my life Cynthia, for supporting and encouraging me to undertake this project, for your patience, for being my strength, and for your unwavering love all these years... ♥

ABSTRACT

In this work, two case studies related to the flow of MHD nanofluids over microchannels with porous media are analyzed. The main objective was to find optimal operating conditions with minimum useful energy losses and enhanced heat transfer for these flows. In the first case study, a unitary nanofluid flow is modeled considering effects of different nanoparticle shapes and the effects of uncertainty in thermophysical properties on the optimal operating conditions. Al_2O_3+H_2O, Cu+H_2O and TiO_2+H_2O nanofluids are analyzed. Momentum and energy equations are solved analytically. The results revealed that optimum values of Biot number and hydrodynamic slip with minimum global entropy and maximum heat transport were achieved for symmetric slip conditions and asymmetric heat transfer. The platelet shape of nanoparticles was the most effective to achieve the optimum conditions with the lowest minimum value of global entropy, while the blade shape was the most effective to reach the optimum conditions with the highest maximum value of heat transport. The results also indicated that the greatest variations of optimum operating conditions occurred when the experimental correlations of viscosity and thermal conductivity were used compared to theoretical correlations. This is because the estimated values of viscosity and conductivity using the different theoretical correlations differ very little from each other.

In the second case study, a nonlinear MHD Darcy-Forchheimer flow of hybrid nanofluids in an inclined microchannel is analyzed considering different nanoparticle mixing ratios, internal heat source, nonlinear radiation and various nanoparticle shapes. For this purpose, the coupled momentum and energy equations were solved using the Runge-Kutta-Fehlberg (RKF-45) method with shooting technique. Al_2O_3+Cu+H_2O, TiO_2+Cu+H_2O and Al_2O_3+TiO_2+H2O hybrid nanofluids were examined. New nanoparticle mixing ratios for Al_2O_3+Cu+H_2O hybrid nanofluids with minimum global entropy not yet reported in previous works were achieved. The maximum heat transfer on the hot plate was found at Grashof number Gr=0.6 with a maximum Nusselt increase of 8.2% when the radiation parameter Rd was increased from 1 to 1.1. For TiO_2+Cu+H_2O, a minimum global entropy was achieved by appropriately selecting the nanoparticle mixing ratio of $\phi_{TiO2}/\phi_{Cu} = (0.07/0.03)$. Furthermore, the Al_2O_3+TiO_2+H2O hybrid nanofluid provided the highest heat transfer values on the hot bottom plate with a maximum Nusselt higher by 0.5% compared to the other two nanofluids explored and the smallest friction coefficient was found for TiO_2+Cu+H_2O using spherical shape.

SUMMARY

This thesis is comprised of five chapters in which two case studies referring to the modeling and optimization of thermal systems based on nanofluids are addressed. In **Chapter I**, a general introduction to the context of nanofluids is given, the problem to be investigated, the justification of the work and the established objectives are presented.

The **Chapter II** presents the theoretical bases for modeling an MHD flow and its analysis by the entropy generation minimization method. The assumptions of linear irreversible thermodynamics, the momentum and energy balance equations, as well as their simplification through the magnetohydrodynamic approximation are presented. Furthermore, the main thermophysical properties of nanofluids and the different correlations used are described.

In **Chapter III**, the first case study is presented, where a conventional MHD nanofluid flow is analyzed in a horizontal microchannel formed by two parallel permeable plates, considering the combined effects of hydrodynamic slip, porous medium, transverse magnetic field, suction/injection, linear thermal radiation and convective boundary conditions. Furthermore, an analysis of the effects of uncertainty is carried out by using different correlations of thermophysical properties on the optimal values found for heat transfer and entropy generation. Finally, the main results and contributions are presented.

In **Chapter IV** the second case study is developed, here the flow of an MHD hybrid nanofluid in an inclined microchannel is modeled and solved, considering nonlinear thermal radiation, the Darcy-Forchheimer model, transverse magnetic field, suction/injection, the effect of internal heat generation and convective boundary conditions. The effects of using different shapes of nanoparticle and different types of nanoparticle (Al_2O_3, Cu and TiO_2) are analyzed. The results are discussed and the main contributions are presented.

Finally, in **Chapter V**, final comments are presented and future lines of research are suggested.

CHAPTER I

METHODOLOGICAL FRAMEWORK

1.1 INTRODUCTION

Currently, there are various needs regarding the optimal use of energy and improvement of thermal efficiency. As indicated in [1], a wide range of microscale products will soon be available, miniaturizing sensors, actuators, motors, heat exchangers, heat pumps, valves, fuel cells, instruments, medical devices, robots, etc.

In a specific case, the development of miniscale heat exchangers has led researchers to discover new alternatives to enhance heat transfer in devices. The implementation of nanofluids as new working fluids in heat exchangers is attributed to Stephen Choi, who published a work in the early 1990s proposing the use of fluids integrated with small metal particles to increase heat transfer [2]. Choi's work describes how the need arose to use nanofluids as the best alternative towards improving miniscale heat exchangers. Initially, when conventional fluids were used, the use of minichannels (channels less than 10 mm wide) was implemented, which reduced costs in experiments, but the heat transfer rate still needed improvement. First, the channel diameter was reduced, and then the normally used working fluids were replaced. Choi points out that while miniscale heat exchangers are small and effective, microscale heat exchangers have greater advantages by further reducing size and increasing efficiency. Nitrogen was used in liquid form in microchannels (channel dimensions less than 1 mm), but it was found that the pressure drop limit significantly increased as the passage diameter decreased, meaning that a heat exchanger with liquid nitrogen would be excellent, but high pumping power and an expensive cryogenic system would be needed to cool the liquid nitrogen [1]. Because of this, Choi focused on developing a new concept that would reduce pumping power and eliminate the need for a cryogenic system. Therefore, his study focused on improving the thermal conductivity of the working fluid instead of reducing the channel diameter.

Since 1873, the idea of using metallic particles to enhance the thermal conductivity of fluids had already been proposed by Maxwell. Choi built on this idea to develop metallic nanoparticles and incorporate them into the working fluid of micro heat exchangers, thereby introducing the concept of "nanofluid" as a new term for working fluids with added metallic nanoparticles to improve heat transfer [1].

A nanofluid can be considered as a working fluid consisting of two elements: the base fluid and the nanoparticle. Examples of base fluids include water, oil, and glycols. Nanoparticles at the nanoscale are added to this fluid, such as metals, oxides, or graphenes, for example, aluminum oxide (Al_2O_3), titanium oxide (TiO_2), copper (Cu), gold (Au), silver (Ag), among others. For a fluid to be classified as a nanofluid, the nanoparticles must be within the size range of 1 to 100 nanometers; otherwise, it is not considered a nanofluid [2, 3].

Today, the use of nanofluids in micro heat exchangers has led to significant advances in energy optimization, achieving high heat transfer rates and considerable energy savings. Numerous studies have positively pointed towards the development of nanofluids as working fluids replacing conventional fluids such as water and oil.

According to Choi [1], for many high heat load applications, microchannel heat exchangers using nanofluids would represent a significant advancement in cooling technology, offering desirable heat transfer area and high thermal conductivity.

Research on nanofluids in microchannel heat exchangers has increased over the past decades since their definition in the 1990s. These investigations have focused on experimenting with different types of nanoparticles and base fluids, considering nanoparticle volume fraction, the effects of magnetic fields on the fluid, porous media, and nanoparticle shape. Nanofluids are currently used in automotive, electronics, industrial, and energy sectors, among others, underscoring the importance of further research to enhance their thermal performance [2-4].

Various researchers have defined a "unitary" or "conventional" nanofluid as a nanofluid that contains a single type of nanoparticle, and the term "hybrid nanofluid" as a nanofluid that combines two or more nanoparticles in one or more base fluid mixtures. Recently, the nanofluid that contains three different types of nanoparticle has been called "ternary nanofluid". To determine the ideal nanofluid, researchers work on experimental mixtures and theoretical models, making variations in its composition [3].

Theoretical work on nanofluids has allowed the prediction of the operation of these technologies. Mathematical models and fluid dynamics equations are used to simulate their behavior, this allows obtaining optimized values and configurations, saving costs of laboratory experiments. Therefore, the development of prediction models and the study of related factors is of utmost importance.

This thesis consists of five chapters, addressing two case studies related to the modeling and optimization of thermal systems using nanofluids. Chapter I provides a general introduction to the context of nanofluids, defines the research problem, justifies the study, and outlines the established objectives. Chapter II illustrates the basic principles of thermal system modeling, defining transport equations and outlining the most commonly used models for predicting thermophysical properties of nanofluids, which are fundamental for understanding the topic.

Chapter III focuses on the first case study, modeling and solving the flow of a unitary magnetohydrodynamic nanofluid in a horizontal microchannel. It considers linear thermal radiation and the effect of a porous medium, presenting key results and contributions.

In Chapter IV the second case study is developed, here the flow of a magnetohydrodynamic hybrid nanofluid in an inclined microchannel is modeled and solved, considering nonlinear thermal radiation, the Darcy-Forchheimer model and the effect of internal heat generation. The results are discussed and the main contributions are presented.

Finally, in Chapter V, final comments are presented and future lines of research are suggested.

1.2 PROBLEM STATEMENT

Despite recent advances in nanofluid-related research, there are still needs in the development of models for nanofluid-based thermal systems. In the theoretical study of nanofluids, various correlations between thermophysical properties and volume fraction are used to estimate thermophysical properties, such as thermal conductivity, density, viscosity, electrical conductivity, etc., and although new mathematical models have been developed, improving the precision of property calculations by Compare them with experimental studies, discrepancies have also been found in their results.

Current studies have been found not to consider the potential impact of using different correlations on the optimization of the physical and geometric parameters of systems with nanofluids, through entropy minimization and heat transfer maximization in thermal systems. Moreover, there are few studies on unitary and hybrid nanofluids in microchannels considering porous media, the effect of a magnetic field, thermal radiation, and nanoparticle shape effects, optimizing flow through entropy minimization methods. Most studies found do not consider all combined effects and the various irreversibilities that a thermal system may present.

1.3 JUSTIFICATION

Studies are needed regarding the effects of using different correlations to estimate the thermophysical properties of nanofluids, as it is necessary to analyze possible variations in the found optimal results.

There are few studies on hybrid nanofluids where optimal operating conditions with minimal entropy generation have been identified. No reports have been found detailing optimal volume fraction ratios of nanoparticles with minimal entropy generation for hybrid nanofluids.

1.4 GENERAL OBJECTIVE

To optimize the flow of unitary and hybrid nanofluids and evaluate the effect of different correlations on estimating the thermophysical properties of nanofluids on the optimal conditions of heat transfer and entropy generation in MHD thermal systems, considering various nanoparticle shapes and combined physical effects.

1.5 SPECIFIC OBJECTIVES

- To model a flow of unitary nanofluid in a horizontal microchannel with a porous medium, transverse magnetic field, and internal heat transfer with linear radiation.

- To solve the momentum and energy equations analytically and determine optimal design parameters using the entropy minimization method.

- To analyze the effect of using different correlations for estimating thermal conductivity and dynamic viscosity on the optimal values. Consider effects of nanoparticle shape and the use of different types of nanoparticle materials.

- To model a flow of hybrid nanofluid in an inclined microchannel with a porous medium, transverse magnetic field, internal heat generation, and internal heat transfer with non-linear radiation.

- To solve the momentum and energy equations numerically and determine optimal design conditions using the entropy minimization method.

- To analyze the effect of using different shapes and types of nanoparticle on the optimized configurations.

1.6 REFERENCES

[1] Choi SUS. Nanofluid technology: current status and future research (No. ANL/ET/CP-97466). *Argonne National Lab. (ANL)*. 1998. https://www.osti.gov/biblio/11048

[2] Okonkwo EC, Wole-Osho I, Almanassra IW, Abdullatif YM, Al-Ansari T. An updated review of nanofluids in various heat transfer devices. *Journal of Thermal Analysis and Calorimetry*. 2020; 1-56. https://doi.org/10.1007/s10973-020-09760-2

[3] Babu JR, Kumar KK, Rao SS. State-of-art review on hybrid nanofluids. *Renewable and Sustainable Energy Reviews*. 2017; 77: 551-565. https://doi.org/10.1016/j.rser.2017.04.040

[4] Mahian O, Mahmud S, Zeinali Heris S. Effect of uncertainties in physical properties on entropy generation between two rotating cylinders with nanofluids. *Journal of Heat Transfer*. 2012; 134(10). https://doi.org/10.1115/1.4006662

CHAPTER II

THEORETICAL FRAMEWORK

2.1 INTRODUCTION

Classical thermodynamics focuses on studying systems in a state of equilibrium, but in a strict sense, natural systems are not balanced phenomena. These natural systems are considered non-ideal, so they have disturbances that affect the equilibrium state. If an idealized process is considered as a reversible process, a reversible process is a phenomenon that manages to return to its initial state after having applied a perturbation [1]. Reversible processes do not leave any trace of energy loss or evidence of disturbance, so they do not really exist in nature and are idealized, therefore, non-reversible or irreversible processes are the real processes that occur in nature.

From here stems the need to study these phenomena from both thermodynamic and mathematical perspectives. These processes involve losses of useful energy or irreversibilities caused by various physical factors such as friction, free expansion of materials, mixing of two fluids, heat transfer, electrical resistance, etc. The thermodynamics of irreversible processes is the discipline capable of studying these processes, examining how a system reaches equilibrium from a macroscopic viewpoint and treating them using concepts and methods analogous to classical thermodynamics of equilibrium processes [2]. The thermodynamics of irreversible processes studies systems based on the second law of thermodynamics, where the entropy variable is defined. Entropy is associated with the change in a value between two equilibrium states in a system, and there will be criteria to determine if a process between these states can occur and under what conditions. Some researchers, lacking a clear conception of the phenomenological concept of entropy S, have turned to molecular models of matter to interpret S as a measure of molecular disorder, often without first defining the concept of order. García [2] also states that entropy is commonly associated with the irreversibility or directionality in time of real processes or irreversible processes.

This chapter presents the fundamental concepts underlying the modeling of nanofluids in microchannels under the influence of an electromagnetic field. The second law of thermodynamics is employed to determine the losses of useful energy in nanofluid-based heat exchangers. The significance lies in the fact that nanofluids exhibit variations in their most important properties, and different combinations of these variables lead to different outcomes in heat transfer. Therefore, to identify the optimal nanofluid for maximum heat transfer and minimal losses of useful energy (minimum entropy production), variations in the physical and geometric parameters of the system are necessary until configurations are achieved that result in minimal entropy and maximal heat transfer points.

In the study of a nanofluid flow over a heat exchanger microchannel, velocity and temperature values can be used to define entropy. The entropy production equation arises from the Gibbs equation, which relates the entropy flow to the thermal flow; therefore, considering the dynamic and thermal behavior of the nanofluid, a measure of entropy production can be defined.

Conductive fluids subjected to an electromagnetic field are termed magnetohydrodynamic (MHD) fluids. These fluids exhibit behavior distinct from common fluids because induced forces are generated by the magnetic field. This effect is beneficial for controlling fluid movement, particularly its velocity. However, to model the behavior of these magnetohydrodynamic fluids, the equations of fluid mechanics and electromagnetism need to be combined to formulate magnetohydrodynamic equations. These equations are capable of describing electromagnetic interactions such as the emergence of forces and the exchange of energy between the fluid and the magnetic field.

2.2 THERMODYNAMICS OF IRREVERSIBLE PROCESSES

Linear irreversible thermodynamics (LIT) is a phenomenological theory for describing irreversible processes occurring in a wide variety of systems [1]. LIT builds upon the foundations of continuum mechanics theory, linking entropy generation to various irreversible processes within the system. Entropy is an extensive quantity, meaning it depends on the sum of its parts. Therefore, specific entropy or entropy density S per unit mass is used to determine the global entropy $< \dot{S} >$.

This theory relates state variables as thermodynamic and kinematic quantities, expressed as functions of space and time. Because entropy cannot be directly measured, constitutive equations for mass, momentum, and energy are used to describe the dynamic-thermal behavior and represent the various irreversibilities associated with the system. In LIT, if intensive variables such as temperature, pressure, density, etc., are constant, the system can be considered in equilibrium, and physical laws can be easily applied in this state. Therefore, LIT can treat irreversible systems as transient processes in equilibrium; when equilibrium is disturbed, the parameters become functions of position and time. Ibañez [1] states that when the disturbance is removed, the system undergoes an irreversible decay process and passes through different non-equilibrium states until it reaches equilibrium.

2.3 MAGNETOHYDRODYNAMICS

Magnetohydrodynamics (MHD) is responsible for studying the movement of electrically conductive fluids in the presence of magnetic fields. The magnetic field induces an electric current in the fluid and this electric current induces effects on the field itself. In addition, these currents give rise to mechanical forces that modify the movement of the fluid. The MHD treats the fluid from a macroscopic point of view, considering it as a continuum that can be described in terms of local properties [3].

A fluid affected by an electromagnetic field does not behave in the same way as a normal fluid, the classical hydrodynamic equations are not sufficient to explain its behavior, therefore, the electromagnetism equations are used to complement the analysis of this type of fluids.

There are numerous fluids that can be used in magnetohydrodynamics, but electrolytes and liquid metals are the primary fluids that have been studied. Some main applications of MHD in nanofluids include the control and propulsion of the conductive fluid or the possibility of being directly actuated by a magnetic field.

Through Maxwell's equations (Eqs. 2.1-2.4), the equations of fluid mechanics can be related to treat MHD fluids. These equations are considered as the basic relationships that account for the electric field intensity $\mathbf{E}$, the electric current density $\mathbf{j}$, the magnetic induction $\mathbf{B}$ and the charge density ρ_e.

$$\nabla \cdot \mathbf{E} = \frac{\rho z}{\varepsilon} \tag{2.1}$$

$$\nabla \cdot \mathbf{B} = 0 \tag{2.2}$$

$$\nabla \times \mathbf{E} = -\frac{\partial \mathbf{B}}{\partial t} \tag{2.3}$$

$$\nabla \times \mathbf{B} = \mu \left(\mathbf{j} + \varepsilon \frac{\partial \mathbf{E}}{\partial t} \right) \tag{2.4}$$

Where ε and μ are scalars known as the electric permittivity and magnetic permeability of the medium, respectively. The characteristics of the electromagnetic field in different material media depend on the structure of such media and their thermodynamic state. In the case of liquid metals, ε and μ can be considered constants, or an approximation of $\mu = \mu_0$ can be made, where μ_0 is the magnetic permeability in vacuum, [1, 3].

2.4 BALANCE EQUATIONS FOR AN MHD FLUID

The equations for an MHD fluid consider the combination of the conservation equations of mass, momentum, and energy with the equations of electromagnetism, simplified through magnetohydrodynamic approximations.

2.4.1 Conservation of mass

The mass conservation equation, or continuity equation, states that the mass of a fluid volume does not vary over time. Therefore, the total mass is conserved and can only change if matter flows through the volume element. The continuity equation in its differential form is defined as

$$\frac{\partial \rho}{\partial t} = -\nabla \cdot \rho \mathbf{v} \qquad (2.5)$$

where ρ is the mass density and $\mathbf{v}$ is the fluid velocity vector. Equation (2.5) is not affected by electromagnetic interaction and therefore does not contain any elements related to Maxwell's equations. For an incompressible fluid $\partial \rho / \partial t \approx 0,$ and extracting ρ from the divergence, the continuity equation becomes

$$\nabla \cdot \mathbf{v} = 0 \qquad (2.6)$$

In terms of the specific volume $V = 1/\rho$, the mass conservation equation is defined as

$$\rho \frac{\partial V}{\partial t} = \nabla \cdot \mathbf{v} \qquad (2.7)$$

2.4.2 Momentum balance

According to Newton's second law, the variation in the momentum of a fluid volume over time is defined by the momentum conservation equation. The linear momentum conservation equation considers the total forces exerted on the fluid. Here, the mass times acceleration is equivalent to the sum of surface and body forces acting on the control volume. The differential form of the momentum balance equation can be defined as follows [3]

$$\rho \frac{D\mathbf{v}}{Dt} = -\nabla \cdot \tau' + \mathbf{f} \qquad (2.8)$$

Where $\frac{D\mathbf{v}}{Dt}$ is the material derivative that accounts for the temporal and spatial change in the fluid's motion $\frac{D}{Dt} = \frac{\partial}{\partial t} + \mathbf{v} \cdot \nabla$, the stress tensor or surface forces is τ' and $\mathbf{f}$ is the body force density.

If the effect of the magnetic field is considered a body force, it would be equivalent to the Lorentz force applied to the fluid. According to Ibañez [1], the electromagnetic field equations can be simplified and added to the linear momentum equation. Through the magnetohydrodynamic approximation, significant simplifications can be made. The Lorentz force effect can be defined as the cross product of the current density and the magnetic induction $\mathbf{f} = \mathbf{j} \times \mathbf{B}$. Substituting into equation (2.8)

$$\rho \frac{D\mathbf{v}}{Dt} = -\nabla \cdot \tau' + \mathbf{j} \times \mathbf{B} \tag{2.9}$$

Equation (2.9) is the momentum balance equation for a conducting fluid moving in the presence of an electromagnetic field.

The term $-\nabla \cdot \tau'$ represents the net surface forces, thus in terms of the pressure gradient and the divergence of the viscous stress tensor τ.

$$-\nabla \cdot \tau' = -\nabla p + \nabla \cdot \tau \tag{2.10}$$

Considering the gravitational force g applied to the control volume ρg and equation (2.10), equation (2.9) becomes

$$\rho \frac{D\mathbf{v}}{Dt} = -\nabla p + \nabla \cdot \tau + \rho g + \mathbf{j} \times \mathbf{B} \tag{2.11}$$

Where p denotes the pressure and y τ is the viscous stress tensor.

2.4.3 Energy balance

The energy balance equation is the formulation of the first law of thermodynamics, which states that the internal energy per unit volume is equivalent to the various variations in heat flux induced by different mechanical, electrical, or magnetic interactions. According to Ibañez [1] and Cuevas [3], the energy balance equation can be defined considering the Joule effect due to the magnetic field as

$$\rho \frac{De}{Dt} = -\nabla \cdot \mathbf{J}_q + \tau':\nabla\mathbf{v} + \mathbf{j} \cdot (\mathbf{E} + \mathbf{v} \times \mathbf{B}) \tag{2.12}$$

Where $\frac{De}{Dt}$ is the material derivative of the internal energy of the fluid per unit mass, $\mathbf{J}_q$ is the heat flux vector, τ' is the stress tensor, and $\mathbf{j} \cdot (\mathbf{E} + \mathbf{v} \times \mathbf{B})$ represents the work done by the electromagnetic forces on the fluid. This term describes the rate at which electromagnetic energy is converted into thermal or mechanical energy in the fluid and is known as the Joule effect.

The total work due to the stresses in the fluid can be decomposed into viscous stresses and the pressure in the fluid.

$$\tau' \colon \nabla \mathbf{v} = -p \nabla \cdot \mathbf{v} - \tau \colon \nabla \mathbf{v} \tag{2.13}$$

Using equation (2.7), we have

$$\rho \frac{De}{Dt} = -\nabla \cdot \mathbf{J}_q - \rho p \frac{dv}{dt} - \tau \colon \nabla \mathbf{v} + \mathbf{j} \cdot (\mathbf{E} + \mathbf{v} \times \mathbf{B}) \tag{2.14}$$

In an incompressible fluid, the term related to the work done by pressure forces is considered null, since $\nabla \cdot \mathbf{v} = 0$.

$$\rho \frac{De}{Dt} = -\nabla \cdot \mathbf{J}_q - \tau \colon \nabla \mathbf{v} + \mathbf{j} \cdot (\mathbf{E} + \mathbf{v} \times \mathbf{B}) \tag{2.15}$$

2.4.4 Entropy balance

From the perspective of the second law of thermodynamics, which states that the spontaneous change of an irreversible process in an isolated system always proceeds in the direction of increasing entropy, entropy can be defined as a measure of the number of microstates for the same macrostate in equilibrium of a system. It can be said that a system always evolves to its most probable configuration, which is the one with the most microstates and therefore the most entropy.

According to Ibáñez [1], the entropy balance equation is defined as

$$\rho \frac{Ds}{Dt} = -\nabla \cdot \mathbf{J}_s + S \tag{2.16}$$

Where $\frac{Ds}{Dt}$ is the material derivative of entropy per unit mass, ρ is the mass density, $\mathbb{J}_s$ is the entropy flux and S is the rate of internal entropy production.

Considering a single-component fluid system out of equilibrium, the entropy per unit mass s, is a function of internal energy e and density ρ, which are the necessary parameters to completely define the state of the system.

According to Ibáñez [1], the local equilibrium hypothesis implies the local validity of the Gibbs relation, where the differentials in it must be taken as functions of coordinates and time, that is, it will be a relation between total derivatives.

$$T\frac{Ds}{Dt} = \frac{De}{Dt} - \frac{p}{\rho^2}\frac{\partial \rho}{\partial t}$$

(2.17)

Where T is the absolute temperature and p is the pressure. Therefore, considering the formulated principles, the Gibbs equation (2.17) allows us to deduce how the system's entropy changes with respect to time, given the equations that describe the temporal evolution of the internal energy e and density ρ.

From equations (2.12) and (2.17), an explicit form for entropy flux and production can be obtained. Considering an incompressible fluid with no density variation over time $\frac{\partial \rho}{\partial t} = 0$, the term $\frac{p}{\rho^2}\frac{\partial \rho}{\partial t}$ in the Gibbs equation (2.17) can be neglected. Multiplying the equation by ρ/T, we get

$$\rho\frac{Ds}{Dt} = \frac{\rho}{T}\frac{De}{Dt}$$

(2.18)

Equating Eq. (2.16) with Eq. (2.18)

$$-\nabla \cdot \mathbf{J}_s + S = \frac{\rho}{T}\frac{De}{Dt}$$

(2.19)

Substituting the energy equation (2.12) into Eq. (2.19)

$$-\nabla \cdot \mathbf{J}_s + S = -\frac{1}{T}(\nabla \cdot \mathbf{J}_q) + \frac{1}{T}\tau':\nabla\mathbf{v} + \frac{1}{T}\mathbf{j}\cdot(\mathbf{E} + \mathbf{v}\times\mathbf{B})$$

(2.20)

Applying the vector rule $\nabla \cdot (f\mathbf{A}) - \nabla f \cdot \mathbf{A} = f(\nabla \cdot \mathbf{A})$ to the first term on the right-hand side of Eq. (2.20), considering a scalar $f = 1/T$ and a vector $\mathbf{A} = \mathbf{J}_q$.

$$\frac{1}{T}(\nabla \cdot \mathbf{J}_q) = \nabla \cdot \left(\frac{1}{T}\mathbf{J}_q\right) - \nabla\left(\frac{1}{T}\right)\cdot\mathbf{J}_q$$

(2.21)

Applying the rule $\nabla\left(\frac{f}{g}\right) = \frac{g\nabla f - f\nabla g}{g^2}$ to the term $\nabla\left(\frac{1}{T}\right)$ on the right-hand side of Eq. (2.21), where $f = 1$ and $g = T$, both are scalars.

14

$$\nabla\left(\frac{1}{T}\right) = \frac{T\nabla(1) - (1)\nabla(T)}{T^2} = -\frac{1}{T^2}\nabla T \qquad (2.22)$$

Therefore, Eq. (2.21) becomes

$$\frac{1}{T}\left(\nabla \cdot \mathbf{J}_q\right) = \nabla \cdot \left(\frac{1}{T}\mathbf{J}_q\right) + \frac{1}{T^2}\nabla T \cdot \mathbf{J}_q \qquad (2.23)$$

Substituting Eq. (2.23) into Eq. (2.20)

$$-\nabla \cdot \mathbf{J}_s + \dot{S} = -\nabla \cdot \left(\frac{1}{T}\mathbf{J}_q\right) - \frac{1}{T^2}\nabla T \cdot \mathbf{J}_q + \frac{1}{T}\tau':\nabla\mathbf{v} + \frac{1}{T}\mathbf{j} \cdot (\mathbf{E} + \mathbf{v} \times \mathbf{B}) \qquad (2.24)$$

Comparing terms in Eq. (2.24), the entropy flux $\mathbf{J}_s$ is

$$\mathbf{J}_s = \frac{\mathbf{J}_q}{T} \qquad (2.25)$$

Substituting Eq. (2.13) and Eq. (2.19) into Eq. (2.24), for an incompressible flow the entropy per unit mass is

$$\rho\frac{Ds}{Dt} = -\nabla \cdot \frac{\mathbf{J}_q}{T} - \frac{1}{T^2}\nabla T \cdot \mathbf{J}_q - \frac{1}{T}\tau:\nabla\mathbf{v} + \frac{1}{T}\mathbf{j} \cdot (\mathbf{E} + \mathbf{v} \times \mathbf{B}) \qquad (2.26)$$

Comparing terms in Eq. (2.24), the entropy production S is equivalent to

$$S = -\frac{1}{T^2}\mathbf{J}_q \cdot \nabla T - \frac{1}{T}\tau:\nabla\mathbf{v} + \frac{1}{T}\mathbf{j} \cdot (\mathbf{E} + \mathbf{v} \times \mathbf{B}) \qquad (2.27)$$

In Eq. (2.25) it is observed that the entropy flux depends on the heat flux $\mathbf{J}_q$, and in the entropy production equation (Eq. 2.27), $\dot{S}$ depends on different contributions that produce irreversibilities, where the first term is related to losses due to heat conduction, the second term is associated with friction in a viscous flow, and the third term is due to irreversibilities caused by electrical conduction. Here, the heat flux is related to the temperature gradient, viscous phenomena are attributed to velocity gradients, and the movement of charged particles is driven by electromagnetic fields.

2.5 PROPERTIES OF NANOFLUIDS

As defined in Chapter I, a nanofluid is the combination of nanometer-sized nanoparticles (1 – 100 nm) in a base fluid to improve thermal performance. This special type of fluid has a higher thermal conductivity than traditional working fluids and is used in devices where a high heat transfer coefficient is needed. Nanoparticles can be metals (e.g. copper, nickel, aluminum, gold, silver, etc.), oxides (e.g. alumina, titania, copper oxide, silica, iron oxide, etc.) and other elements (e.g. example, carbon nanotubes, graphene, silicon carbide, calcium carbonate, titanium nanotubes, etc.), the base fluids can include, for example: glycols, water, motor oil, etc., [4].

Research into nanofluids has grown over the last two decades, because it has been proven that the use of these as a replacement for traditional refrigerants such as water and oils improves heat transfer by convection, compared to these fluids.

This technology promises considerable advances in improving the heat transfer rate in engineering devices. Recent discoveries indicate that nanofluids are an excellent alternative to microrefrigeration systems, solar collectors and heat exchangers; therefore, their study in channels and microchannels is of great importance for the advancement and development of this branch of engineering.

The theoretical study of nanofluids contemplates the use of various models to calculate thermophysical properties. The main properties studied are dynamic viscosity and thermal conductivity, density, heat capacity and electrical conductivity. The existence and use of various prediction models produce uncertainties associated with the determination of thermophysical properties, therefore, when calculating the velocity, temperature, heat transfer and entropy in nanofluids, it is possible to find variations when using different models.

Most models for calculating thermophysical properties are based on the volume fraction of the nanoparticle, therefore, the variations that occur are mainly due to modifying this parameter. For unitary nanofluids, where the use of a single type of nanoparticle is contemplated, the volume fraction is defined as ϕ. On the other hand, when using hybrid nanofluids, ϕ is denoted with the subscripts 1 and 2, to represent the two types of nanoparticles, for example ϕ_1 and ϕ_2.

Recently, it has been determined that some properties change with increasing temperature, and experimental correlations have been developed considering this factor, but this effect will not be studied in this research.

2.5.1 Thermal conductivity

The thermal conductivity is measured in W/m·K, it has been experimentally demonstrated that nanofluids have a higher thermal conductivity than common base fluids, this is because the addition of nanoparticles increases this parameter. This is due to Brownian motion, which is a mechanism that controls the behavior of particles in suspension [4]. Nanolayers are also produced around the particles, which are structures that are created in the interaction of liquid molecules with a solid. The nanolayers act as a thermal bridge between the nanoparticles and the base liquid, therefore, the structured arrangement of the nanolayer allows to reduce the thermal resistance of the nanoparticle, therefore the heat transfer from the nanoparticle to the fluid becomes more efficient, increasing the overall thermal conductivity.

The main factors affecting thermal conductivity in nanofluids are mainly the nanoparticle volume fraction, particle size, shape and temperature of the nanofluid [4]. It has been experimentally proven that an increase in the percentage of the volume fraction of nanoparticles produces a proportional increase in the thermal conductivity. This means that, as the amount of nanoparticles increases, the thermal conductivity of the nanofluid also increases linearly.

Experiments have been performed to determine the effects of different nanoparticle shapes on thermal conductivity, such as in Xie et al. [5] and Timofeeva et al. [6], where it has been found that experimentally cylindrical shapes show better performance than spherical shapes, however theoretical models indicate that the blade shape results in greater thermal conductivity, surpassing the cylindrical and spherical shapes, hence the importance of studying the uncertainties in the different models.

A higher temperature increases the thermal conductivity of the nanofluid, which is why it is very common to apply nanofluids to heat exchangers. Also, one of the first factors that was studied was the size of the particle. Many authors suggest that the size of the particle influences in thermal conductivity, such that, the smaller the particle size, the thermal conductivity increases [4, 5, 6]. This is attributed to the increase in Brownian motion, which appears when the particles are reduced to nanometric sizes, therefore, there is greater energy exchange, hence the importance of using nanoparticles.

The mathematical models to calculate thermal conductivity are varied; there are various models reported in the literature, which vary in range of application and effects considered. The most used model is Maxwell's equation (Eq. 2.28) [7-10] for thermal conductivity. For spherical nanoparticles this model is defined as

$$\frac{k_{nf}}{k_f} = \frac{k_s + 2k_f + 2\phi(k_s + k_f)}{k_s + 2k_f - \phi(k_s - k_f)} \tag{2.28}$$

where ϕ is the volume fraction of the nanoparticle, with ($\phi \ll 1$), k_{nf}, k_f and k_s are the thermal conductivity of the nanofluid, the base fluid and the solid nanoparticle, respectively. For spherical nanoparticles, this equation considers the volume fraction, the thermal conductivity of the nanoparticles and the base fluid to predict the thermal conductivity of the nanofluid. This relationship was determined experimentally. It is noted that this model does not consider the size of the nanoparticle.

Other relationships have been derived from Maxwell's model (Eq. 2.28), which consider factors such as temperature, shape or the effect of the liquid nanolayer.

Farooq et al. and Hussain et al. in Saqib et al. [9], theoretically adjusted the Maxwell model for hybrid nanofluids.

$$\frac{k_{hnf}}{k_f} = \frac{\left(\frac{\phi_1 k_{s1} + \phi_2 k_{s2}}{\phi}\right) + 2k_f + 2(\phi_1 k_{s1} + \phi_2 k_{s2}) - 2\phi k_f}{\left(\frac{\phi_1 k_{s1} + \phi_2 k_{s2}}{\phi}\right) + 2k_f - (\phi_1 k_{s1} + \phi_2 k_{s2}) + \phi k_f} \qquad (2.29)$$

Where k_{hnf} is the thermal conductivity of the hybrid nanofluid, ϕ_1 and k_{s1} are the volume fraction and thermal conductivity of nanoparticle 1, respectively; ϕ_2 and k_{s2} are the volume fraction and thermal conductivity of nanoparticle 2, respectively and ϕ is the total volume fraction, $\phi = \phi_1 + \phi_2$.

The Hamilton-Crosser model [7-10], (Eq. 2.30), considers the effects of different types of nanoparticle shapes. When using this model, it is considered that the shapes are of the same type throughout the nanofluid, so that two or more nanoparticle shapes cannot be simulated simultaneously, this model is defined as

$$\frac{k_{nf}}{k_f} = \frac{k_s + (s-1)k_f + (s-1)\phi(k_s + k_f)}{k_s + (s-1)k_f - \phi(k_s - k_f)} \qquad (2.30)$$

where s is the shape factor and is calculated using the relationship $s = 3/\psi$. The variable ψ is the coefficient of sphericity, and takes different values depending on the shape of the nanoparticle (see Table 2.1).

Table 2.1 *Values of ψ for different nanoparticle shapes.*

	Sphere	Blade	Brick	Platelet	Cylinder
ψ	1	0.36	0.81	0.52	0.62

Benkhedda et al. [11], presents the Hamilton-Crosser model for hybrid nanofluids (Eq. 2.31). Where two different types of nanoparticles ($\phi_1 k_{s1}$ and $\phi_2 k_{s2}$) are considered in a base fluid (k_f) with the possibility of choosing only one type of nanoparticle shape (s). This model does not consider the size of the nanoparticle, only the volume fraction (ϕ).

$$\frac{k_{hnf}}{k_f} = \frac{(s-1)k_f + \left(\frac{\phi_1 k_{s1} + \phi_2 k_{s2}}{\phi}\right) + (s-1)\phi\left(\left(\frac{\phi_1 k_{s1} + \phi_2 k_{s2}}{\phi}\right) + k_f\right)}{(s-1)k_f + \left(\frac{\phi_1 k_{s1} + \phi_2 k_{s2}}{\phi}\right) - \phi\left(\left(\frac{\phi_1 k_{s1} + \phi_2 k_{s2}}{\phi}\right) - k_f\right)} \qquad (2.31)$$

Bruggeman [7-10] defines the thermal conductivity for spherical particles in the following way

$$\frac{k_{nf}}{k_f} = \frac{1}{4}\left[(3\phi - 1)\frac{k_s}{k_f} + (2 - 3\phi)\right] + \frac{k_f}{4}\sqrt{\Delta} \qquad (2.32)$$

where

$$\Delta = \left[(3\phi - 1)^2 (\frac{k_s}{k_f})^2 + (2 - 3\phi)^2 + 2(2 + 9\phi - 9\phi^2)\frac{k_s}{k_f}\right] \qquad (2.33)$$

The Yu-Choi thermal conductivity model [12] considers the effect of the liquid nanolayer, this model is based on the Maxwell model and is limited to spherical particles.

$$\frac{k_{nf}}{k_f} = \frac{k_s + 2k_f - 2\phi(k_f - k_s)(1 - \xi)^3}{k_s + 2k_f + \phi(k_f - k_s)(1 - \xi)^3} \qquad (2.34)$$

Where ξ is the ratio between the thickness of the liquid nanolayer and the radius of the oxide nanoparticle, commonly $\xi = 0.1$.

There are various theoretical and experimental models for thermal conductivity, which will be presented in the topic effects of uncertainty, in chapter III.

2.5.2 Dynamic viscosity

Viscosity is defined as the internal resistance of a fluid to flow and is related to the movement of a fluid's molecules. If the internal collision of the particles is higher, there is greater friction and greater viscosity, on the other hand, a small collision results in lower viscosity [4]. Dynamic viscosity is denoted by μ or η, and the unit is kg/m/s which is equal to Pa/s. The viscosity of a nanofluid is affected by temperature, particle size and concentration of nanoparticles, mainly [4].

In the case of the effect of temperature on viscosity, some experiments suggest that increasing temperature decreases the viscosity of the nanofluid [4]. Studies of the effect of temperature on the viscosity of Al_2O_3+water and CuO+water nanofluids report that the viscosity decreases with an increase in temperature from 20° to 50° [13, 14].

There are certain discrepancies about the effect of nanoparticle size on viscosity, since there are few studies available on this aspect. Nguyen et al. [15] studied the nanoparticle size effect of Al_2O_3 + water and observed that the particle size effects are more significant for high nanoparticle volume fraction values, and for low nanoparticle volume concentrations (below 4%) changes in viscosity are not significant.

The viscosity of nanofluids has a strong dependence on the shape of nanoparticles [6]. Some authors report that elongated particles such as platelets and cylinders produce a higher viscosity in the same volume fraction and spherical particles provide a lower viscosity [4]. Unlike the size of the nanoparticle, most of the research available in the literature in relation to the effect of volume fraction on viscosity determines that the viscosity of nanofluids increases with increasing volume fraction.

The models to calculate the viscosity of nanofluids are mostly presented based on the nanoparticle volume fraction; one of the oldest models is that of Einstein (Eq. 2.35), [7, 8]. This model is based on kinetic molecular theory, however, this equation is not currently used as much. This model is applicable for volume fractions below 1% and spherical nanoparticles

$$\frac{\eta_{nf}}{\eta_f} = 1 + 2.5\phi \tag{2.35}$$

where η_{nf} is the dynamic viscosity of the nanofluid and η_f is the dynamic viscosity of the base fluid.

One of the most used models today is the Brinkman model [7-10], this model can be used for $0 \leq \phi \leq 0.4\%$, with spherical nanoparticles.

$$\frac{\eta_{nf}}{\eta_f} = \frac{1}{(1-\phi)^{2.5}} \tag{2.36}$$

Farooq et al. and Hussain et al. in Saqib et al. [9] presented the Brinkman model for hybrid nanofluids as follows

$$\frac{\eta_{hnf}}{\eta_f} = \frac{1}{(1 - (\phi_1 + \phi_2))^{2.5}} \tag{2.37}$$

where η_{hnf} is the dynamic viscosity of the hybrid nanofluid and ϕ_1 and ϕ_2 are the volume fraction of nanoparticles 1 and 2.

The Einstein-Batchelor viscosity model (Eq. 2.38) considers the effect of the nanoparticle shape [7-10]; the empirical shape coefficients a and b are calculated experimentally. The values determined for a and b, are shown in Table 2.2.

$$\frac{\eta_{nf}}{\eta_f} = (1 + a\phi + b\phi^2) \tag{2.38}$$

Table 2.2 *Values of a and b for different nanoparticle shapes.*

	Sphere	Blade	Brick	Platelet	Cylinder
a	2.55	14.6	1.9	37.1	13.5
b	6.2	123.3	471.4	612.6	904.4

For hybrid nanofluids, the Einstein-Batchelor model considering the effect of nanoparticle shapes is expressed in Eq. (2.39).

$$\frac{\eta_{hnf}}{\eta_f} = (1 + a(\phi_1 + \phi_2) + b(\phi_1 + \phi_2)^2) \tag{2.39}$$

where the values of a and b are shown in Table 2.2.

Wang et al. [8, 9] developed a model from experimental correlations for a water-based Al_2O_3 nanofluid, for spherical nanoparticles, which has been used in certain studies.

$$\frac{\eta_{nf}}{\eta_f} = 1 + 7.3\phi + 123\phi^2 \tag{2.40}$$

There are other experimental relations for viscosity which consider different effects, but they will be presented in section 3.4.

2.5.3 Density

Density is the amount of mass in a unit volume, it is denoted by ρ and the unit is kg/m^3. The density depends mainly on the material of the nanoparticle. The other geometric parameters, such as nanoparticle size and shape, do not affect the density significantly [16]. Solids have a higher density compared to liquids, therefore, the density of nanofluids increases with the addition of nanoparticles [4].

The experiments show that the density increases with increasing nanoparticle volume fraction ϕ, and in all cases, the nanofluid obtains a higher density than the base liquid. With a higher density of the nanoparticles, the density of the mixture obviously increases, the increasing trend is almost linear. Like viscosity, density decreases with increasing fluid temperature.

There is no diversity of models for this property, this is a direct consequence of the fact that the density of the particles is the same as that of a solid of the same material. Pak et al. [17] used the equation developed for micrometer-sized particles applying it to nanometer nanoparticle sizes to calculate the density, the equation is expressed as

$$\frac{\rho_{nf}}{\rho_f} = (1 - \phi) + \phi \frac{\rho_s}{\rho_f} \tag{2.41}$$

Where ρ_{nf} and ρ_f are the density of the nanofluid and the base fluid respectively. Eq. (2.41) is the Pak & Cho model, which is the most used expression for determining the density in nanofluids.

For a hybrid nanofluid, the Pak & Cho model becomes

$$\frac{\rho_{hnf}}{\rho_f} = \left((1 - \phi)\rho_f + \phi_1 \rho_{s1} + \phi_2 \rho_{s2} \right) / \rho_f \tag{2.42}$$

where ρ_{hnf} is the density of the hybrid nanofluid, ρ_{s1} is the density of nanoparticle 1 and ρ_{s2} is the density of nanoparticle 2.

2.5.4 Specific heat capacity

The specific heat capacity or specific heat is the amount of heat necessary to be supplied to an object to produce a unit change in its temperature [4]. It is denoted by C_p and the unit is J/kg · K. Pak et al. [17], Fakoor et al. [18] and Strandberg et al. [19] have shown that the specific heat of nanofluids decreases with an increase in nanoparticle volume fraction.

Although, generally, this heat capacity decreases with the addition of particles, some authors have also observed the opposite trend; this will depend on the size, shape, material and temperature of the nanoparticle.

In the case of the size of the nanoparticle, there are contradictory results on the effects on the specific heat, however, most researchers have agreed that the specific heat increases with increasing diameter of the nanoparticles [4]. Because this property depends mainly on the material of the nanoparticle, for Al_2O_3 + water, it has been shown that the specific heat decreases with an increase in temperature, however, above 50°C, the decrease in specific heat is irrelevant [20]. For CuO nanoparticles, Saeedinia et al. [21] showed that the specific heat also decreases with an increase in temperature.

The most common model for calculating heat capacity was presented by Pak et al. [17] based on the idea of the formula of mixing liquid particles. The Pak & Cho model expression for heat capacity is showed in Eq. (2.43).

$$\frac{(\rho C_p)_{nf}}{(\rho C_p)_f} = (1 - \phi) + \phi \frac{(\rho C_p)_s}{(\rho C_p)_f} \tag{2.43}$$

Where $(C_p)_{nf}$ is the heat capacity of the nanofluid, $(C_p)_f$ is the heat capacity of the base fluid and $(C_p)_s$ is the heat capacity of the nanoparticle.

According to [9], the heat capacity model for a hybrid nanofluid is

$$\frac{(\rho C_p)_{hnf}}{(\rho C_p)_f} = \left((1 - \phi)(\rho C_p)_f + \phi_1 (\rho C_p)_{s1} + \phi_2 (\rho C_p)_{s2} \right) / (\rho C_p)_f \tag{2.44}$$

where $(C_p)_{hnf}$ is the heat capacity of the hybrid nanofluid, $(C_p)_{s1}$ is the heat capacity of nanoparticle 1 and $(C_p)_{s2}$ is the heat capacity of nanoparticle 2.

2.5.5 Thermal expansion coefficient

The coefficient of thermal expansion measures the change in length, area, or volume of a material in response to a change in temperature. It is called β and is measured in inverse temperature units, its unit is the inverse kelvin $1/K$ or K^{-1}.

Nayak et al. [22] indicates that the thermal expansion coefficient of a nanofluid is much higher than water, because the addition of nanoparticles increases this parameter. This occurs because some metals or oxides have a higher thermal expansion value than fluids.

It has been experimentally proven that increasing the volume fraction of nanoparticles ϕ results in a decrease in the coefficient of thermal expansion [23]. On the other hand, according to Nayak et al., increasing temperature also increases this coefficient.

Similar to heat capacity, Saqib et al. [9] and López et al. [24], define the thermal expansion coefficient of a nanofluid as

$$\frac{(\rho\beta)_{nf}}{(\rho\beta)_f} = (1 - \phi) + \phi\frac{(\rho\beta)_s}{(\rho\beta)_f} \tag{2.45}$$

where β_{nf} is the thermal expansion coefficient of the nanofluid, β_s is the thermal expansion coefficient of the nanoparticle and β_f is the thermal expansion coefficient of the base fluid.

Farooq et al., Hussain et al. and Devi and Devi in Saqib et al. [9], adapted Eq. (2.45) for a hybrid nanofluid

$$\frac{(\rho\beta)_{hnf}}{(\rho\beta)_f} = \left((1 - \phi)(\rho\beta)_f + \phi_1(\rho\beta)_{s1} + \phi_2(\rho\beta)_{s2}\right)/(\rho\beta)_f \tag{2.46}$$

where β_{hnf} is the thermal expansion coefficient of the hybrid nanofluid, β_{s1} is the thermal expansion coefficient of nanoparticle 1 and β_{s2} is the thermal expansion coefficient of nanoparticle 2.

2.5.6 Electrical conductivity

Electrical conductivity is the measure of the ability of a material or substance to allow electric current to flow through it. It is denoted by σ and the unit is S/m (siemens per meter). There are few studies about the effects on the electrical conductivity of nanofluids. Minea et al. [25] performed measurements of the electrical conductivity of the Al_2O_3 + water nanofluid, with nanoparticles of 12 nm diameter, and found that electrical conductivity increases linearly with volume fraction and temperature.

There are not many models for electrical conductivity in the literature, the most used model has been the Maxwell expression (Eq. 2.47), however, recent studies have found some discrepancies compared to experimental results. Maxwell's model is

$$\frac{\sigma_{nf}}{\sigma_f} = 1 + 3\left(\frac{\sigma_s}{\sigma_f} - 1\right)\phi \Big/ \left(\left(\frac{\sigma_s}{\sigma_f} + 2\right) - \left(\frac{\sigma_s}{\sigma_f} - 1\right)\phi\right) \tag{2.47}$$

where σ_{nf} is the electrical conductivity of the nanofluid, σ_f is the electrical conductivity of the fluid and σ_s is the electrical conductivity of the nanoparticle. For spherical nanoparticles, this equation considers the volume fraction, the electrical conductivity of the nanoparticles and the base fluid to predict the electrical conductivity of the nanofluid. This relationship was determined experimentally. It is noted that this model does not consider the size of the nanoparticle

For a hybrid nanofluid, an alternative form of the Maxwell's model [9, 11] is adopted

$$\frac{\sigma_{hnf}}{\sigma_f} = 1 + \frac{3\phi\big(\phi_1\sigma_{s1} + \phi_2\sigma_{s2} - \phi\sigma_f\big)}{\big(\phi_1\sigma_{s1} + \phi_2\sigma_{s2} + 2\phi\sigma_f\big) - \phi\big(\phi_1\sigma_{s1} + \phi_2\sigma_{s2} - \phi\sigma_f\big)} \tag{2.48}$$

where σ_{hnf} is the electrical conductivity of the hybrid nanofluid, σ_{s1} is the thermal conductivity of nanoparticle 1 and σ_{s2} is the thermal conductivity of nanoparticle 2.

Ganguly et al. [26] conducted an experimental study to measure the electrical conductivity of the Al$_2$O$_3$ + water nanofluid, and determined an experimental model for the electrical conductivity of the nanofluid as a correlation that depends on the volume fraction and temperature. Furthermore, it was determined that the nanoparticle volume fraction has a greater influence on electrical conductivity than temperature. The expression is as follows

$$\frac{\sigma_{nf}}{\sigma_f} = 3679.049\phi + 1.085779T - 43.6384 \tag{2.49}$$

where T is the temperature of the nanofluid.

Ganguly et al. [26] expressed that this model can be compared with the results obtained with the classical Maxwell model for thermal conductivity, taking T equal to room temperature, for values where $\phi \ll 1$. Selimefendigil et al. [27] performed a comparison of the performance of three electrical conductivity models (Maxwell, Ganguly and Minea-Luciu) for heat transfer in an Al$_2$O$_3$ + water nanofluid, in a trapezoidal channel, finding significant variations in the results. Nabati et al. [28] experimentally measured the electrical conductivity of nanofluids with aluminum nanoparticles, magnesium oxide, copper oxide, titanium oxide and zinc oxide, and compared the results with the Maxwell model, determining that this model was not able to predict the electrical conductivity of the nanofluid under these conditions.

2.6 REFERENCES

[1] Ibáñez G. Optimización de procesos y dispositivos energeticos, basada en la producción de entropía. *Tesis de doctorado, Centro de Investigación en Energía, UNAM*. 2003. https://repositorio.unam.mx/

[2] García L. De la máquina de vapor al cero absoluto (calor y entropía). *Fondo de Cultura Económica, S.A. De C.V.* 1986.

[3] Cuevas S. Transferencia de calor en un flujo magnetohidrodinamico con condiciones a la frontera de tercer tipo. *Tesis de maestría, UNAM*. 1989. https://repositorio.unam.mx/

[4] Mahbubul IM. Preparation, characterization, properties, and application of nanofluid. *Elsevier-William Andrew*. 2019.

[5] Xie H, Wang J, Xi T, Liu Y, Ai F, Wu Q. Thermal conductivity enhancement of suspensions containing nanosized alumina particles. *Journal of applied physics. 2002*; 91(7): 4568-4572. https://doi.org/10.1063/1.1454184

[6] Timofeeva EV, Routbort JL, Singh D. Particle shape effects on thermophysical properties of alumina nanofluids. *Journal of applied physics*. 2009; 106(1): 014304. https://doi.org/10.1063/1.3155999

[7] Gupta M, Singh V, Kumar R, Said Z. A review on thermophysical properties of nanofluids and heat transfer applications. *Renewable and Sustainable Energy Reviews*. 2017; 74: 638-670. https://doi.org/10.1016/j.rser.2017.02.073

[8] Minea AA. A review on the thermophysical properties of water-based nanofluids and their hybrids. *The Annals of "Dunarea de Jos" University of Galati. Fascicle IX, Metallurgy and Materials Science.* 2016; 39: 35-47. https://www.gup.ugal.ro/ugaljournals/index.php/mms/article/view/1279

[9] Saqib M, Khan I, Shafie S. Recent advancement in thermophysical properties of nanofluids and hybrid nanofluids: an overview. *International Journal of Computacional Analysis.* 2019; 1: 16-25. https://doi.org/10.33959/cuijca.v3i2.27

[10] Mahian O, Kianifar A, Kleinstreuer C, Al-Nimr MA, Pop I, Sahin AZ, Wongwises S. A review of entropy generation in nanofluid flow. *International Journal of Heat and Mass Transfer*. 2013; 65: 514-532. https://doi.org/10.1016/j.ijheatmasstransfer.2013.06.010

[11] Benkhedda M, Boufendi T, Tayebi T. Convective heat transfer performance of hybrid nanofluid in a horizontal pipe considering nanoparticles shapes effect. *Journal of Thermal analysis and Calorimetry*. 2020; 140: 411-425. https://doi.org/10.1007/s10973-019-08836-y

[12] Yu W, Choi S. The role of interfacial layers in the enhanced thermal conductivity of nanofluids: A renovated Maxwell model. *Journal of Nanoparticle Research*. 2003; 5: 167–171. https://doi.org/10.1023/A:1024438603801

[13]   Chen H, Yang W, He Y, Ding Y, Zhang L, Tan C, Bavykin DV. Heat transfer and flow behaviour of aqueous suspensions of titanate nanotubes (nanofluids). *Powder technology*. 2008; 183(1): 63-72. https://doi.org/10.1016/j.powtec.2007.11.014

[14]   Anoop KB, Sundararajan T, Das SK. Effect of particle size on the convective heat transfer in nanofluid in the developing region. *International journal of heat and mass transfer*. 2009; 52(9-10): 2189-2195. https://doi.org/10.1016/j.ijheatmasstransfer.2007.11.063

[15]   Nguyen CT, Desgranges F, Roy G, Galanis N, Maré T, Boucher E, Mintsa HA. Temperature and particle-size dependent viscosity data for water-based nanofluids–hysteresis phenomenon. *International journal of heat and fluid flow*. 2007; 28(6): 1492-1506. https://doi.org/10.1016/j.ijheatfluidflow.2007.02.004

[16]   Timofeeva EV, Yu W, France DM, Singh D, Routbort JL. Nanofluids for heat transfer: an engineering approach. *Nanoscale research letters*. 2011; 6(1): 1-7. https://doi.org/10.1186/1556-276X-6-182

[17]   Pak BC, Cho YI. Hydrodynamic and heat transfer study of dispersed fluids with submicron metallic oxide particles. *Experimental Heat Transfer an International Journal*. 1998; 11(2): 151-170. https://doi.org/10.1080/08916159808946559

[18]   Fakoor M, Akhavan MA, Razi P. An experimental investigation on thermo-physical properties and overall performance of MWCNT/heat transfer oil nanofluid flow inside vertical helically coiled tubes. *Experimental Thermal and Fluid Science*. 2012; 40: 103-111. https://doi.org/10.1016/j.ijthermalsci.2012.10.014

[19]   Strandberg R, Das DK. Influence of temperature and properties variation on nanofluids in building heating. *Energy Conversion and Management*. 2010; 51(7): 1381-1390. https://doi.org/10.1016/j.enconman.2010.01.006

[20]   Harkirat. Preparation and characterization of nanofluids and some investigation in biological applications. *Thesis, Patiala: Thapar University*. 2010. http://dx.doi.org/10.13140/RG.2.1.3485.7442/1

[21]   Saeedinia M, Akhavan-Behabadi MA, Razi P. Thermal and rheological characteristics of CuO–Base oil nanofluid flow inside a circular tube. *International Communications in Heat and Mass Transfer*. 2012; 39(1): 152-159. https://doi.org/10.1016/j.icheatmasstransfer.2011.08.001

[22]   Nayak AK, Singh RK, Kulkarni PP. Measurement of volumetric thermal expansion coefficient of various nanofluids. *Technical Physics Letters*. 2010; 36: 696-698. https://doi.org/10.1134/S1063785010080055

[23]   Bianco V, Manca O, Nardini S, Vafai K. Heat transfer enhancement with nanofluids. Eds. 2015.

[24]   López A, Ibáñez G, Pantoja J, Moreira J, Lastres O. Entropy generation analysis of MHD nanofluid flow in a porous vertical microchannel with nonlinear thermal radiation, slip flow and convective-radiative boundary conditions. *International Journal of Heat and Mass Transfer*. 2017; 107: 982-994. https://doi.org/10.1016/j.ijheatmasstransfer.2016.10.126

[25]   Minea AA, Luciu RS. Investigations on electrical conductivity of stabilized water based Al_2O_3 nanofluids. *Microfluidics and nanofluidics*. 2012; 13(6): 977-985. https://doi.org/10.1007/s10404-012-1017-4

[26]   Ganguly F, Sikdar S, Basu S. Experimental investigation of the effective electrical conductivity of aluminum oxide nanofluids. *Power Technology.* 2009; 196: 326-330. https://doi.org/10.1016/j.powtec.2009.08.010

[27]   Selimefendigil F, Oztop HF. Modeling and optimization of MHD mixed convection in a lid-driven trapezoidal cavity Þlled with alumina-water nanoßuid: Effects of electrical conductivity models. *International Journal of Mechanical Sciences.* 2017; 136: 264-278. https://doi.org/10.1016/j.ijmecsci.2017.12.035

[28]   Nabati S, Jamali J, Keshavarz M. Electrical conductivity, viscosity, and density of different nanofluids: An experimental study. *Experimental Thermal and Fluid Science*. 2016; 74: 339-346.
http://dx.doi.org/10.1016/j.expthermflusci.2016.01.004

CHAPTER III

ANALYSIS OF HEAT TRANSFER AND OPTIMIZATION OF A UNITARY NANOFLUID FLOW BASED ON ENTROPY MINIMIZATION CONSIDERING DIFFERENT CORRELATIONS FOR THE ESTIMATION OF ITS THERMOPHYSICAL PROPERTIES

3.1 INTRODUCTION

The study of nanofluids considers various geometries and enclosures used in different case studies. Geometries such as channels are based on the magnitude of the width or hydraulic diameter and can be classified into three groups: conventional channels, minichannels, and microchannels. Particularly, the investigation of laminar stable forced convection fluid flow through parallel plates in microchannels has numerous important applications in engineering, ranging from the design of cooling systems for microelectronic devices to various electromechanical micro-scale systems such as MHD micro-pumps, micro-turbines, fuel cells, etc., where this type of geometry can be observed [1-12].

This chapter presents the development of the first case study where the various effects considered in the system are explained. The process of analytical resolution of homogeneous and non-homogeneous differential equations is described, using the method of undetermined coefficients and variation of parameters. Solutions to the momentum and energy equations are provided, model is validated by comparing the data with other models taken from the literature. The results obtained with different configurations of the physical parameters of the model are explained, identifying optimal values with a minimum generation of entropy. The effects of the use of thermophysical properties are analyzed, using 15 different combinations of correlations on the optimal parameters found in the study model. Furthermore, variations due to different shapes of nanoparticles and types of nanofluids are studied.

Due to the current need to enhance heat transfer in energy systems, the use of nanofluids as working fluids in thermal devices has gained prominence in recent years using different types of nanoparticles and base fluids [1-24]. Thus, many authors have used optimization methods that focus on finding the maximum heat transport and the minimum loss of useful energy. For this purpose, mathematical models that include the fundamental parameters and the physical effects of the system are used.

In recent literature, a wide range of effects, geometries, and nanofluid variations have been explored. These studies have focused on examining the influence of various physical parameters within the system, such as nanoparticle volume fraction, Hartmann number, Reynolds number, thermal radiation and porous medium. There are theoretical works that simulate the performance of nanofluids in various applications, such as microchannels [1-2,19-24], microcooling systems for CPUs [3], transmission fluids [4], heat exchangers [5], solar collectors [6, 7] and other applications [8-12].

For example, Ramezanpour et al. [1] conducted a pore-scale simulation for a microchannel using nanofluids. They considered effects of Brownian motion, drag, buoyancy and gravity. They demonstrated that the nanoparticle deposition ratio decreased from 0.98 to 0.4 as the nanoparticle diameter increased from 30 to 150 nm.

Additionally, an increase in temperature and a decrease in nanoparticle diameter increased the nanoparticle deposition. Soumya et al. [2] examined the flow of a tangent-hyperbolic nanoliquid in a vertical microchannel, taking into consideration various forces and conditions. Nonlinear partial differential equations were transformed into ordinary ones through similarity transformations. The RKF45 method with the shooting technique was employed for the numerical solution of system. The influences of thermophoresis, Brownian motion, and chemical reactions were study. The results indicated that an increase in the thermal Grashof number led to an augmentation in the channel's flow. Furthermore, an increase in thermal energy was recorded under specific parameter conditions.

Izadi et al. [3] conducted a modeling study to investigate the impingement cooling of a CPU within a porous metal cooler saturated with nanofluid under the influence of a magnetic field. They employed the Darcy-Brinkman-Forchheimer model to simulate nanofluid flow through the porous medium and introduced suitable similarity variables to analyze the heat transfer. Their findings suggested that a stronger magnetic field can enhance heat transfer performance in the CPU cooler. Qasemian et al. [4] investigated the effects of using nanofluids in an automatic transmission, a theoretical analysis of hydraulic and thermal effects was conducted. Khoshtarash et al. [5] investigated the convective heat transfer and flow characteristics of two-phase nanofluid flow in open-cell metal foams (OCMFs) using a pore-scale approach. Their study demonstrated that Brownian motion can significantly enhance heat transfer in OCMFs.

These studies support the notion that the presence of a porous medium has a significant impact on enhancing heat transfer when nanofluids are used. However, it is imperative to evaluate the performance of nanofluids and also consider the principles of the second law of thermodynamics and the effect of different correlations for the estimation of thermophysical properties on the results.

As indicated in references [13-18], semi-empirical (theoretical) and empirical (experimental) correlations to estimate the thermophysical properties of nanofluids provide enough information to predict their behavior, but there are considerable differences in the results depending on the used correlation. Therefore, in the optimization of nanofluid flows, it is possible that a correlation model alters the obtained results, thus the study of these correlations and their influences on optimum theoretical results is of great importance.

Studies about uncertainty in nanofluid properties have not been very extensive and some combinations of different correlations have been analyzed. For example, Ho et al. [13] studied the effects of the uncertainties in the dynamic viscosity and thermal conductivity of Al_2O_3/water nanofluid on the heat transfer for a vertical square enclosure. The mathematical model was solved numerically considering two different correlations to determine the viscosity and thermal conductivity of nanofluid.

The results clearly demonstrated that the uncertainty associated with the different expressions used had a great influence on the convective heat transfer characteristics of the studied geometry. Mansour et al. [14] investigated the effects of uncertainty in thermophysical properties on forced convection heat transfer with nanofluids. They considered two different correlations for viscosity and thermal conductivity. It was indicated that the real amount of experimental data about the properties of nanofluids, in particular thermal conductivity and dynamic viscosity, was limited. This induced significant discrepancies in the determination of these properties and caused considerable errors when the performance of nanofluids in various thermal applications was evaluated.

Arefmanesh et al. [15] investigated the effects of uncertainty in the dynamic viscosity of a water-based Al_2O_3 nanofluid on fluid flow and heat transfer in a square cavity. Here two different viscosity models were considered for uncertainty analysis. The results showed that there are significant differences in heat transfer results depending on the used viscosity correlation. It was also found that the average Nusselt number of the hot wall increased as the nanoparticle concentration increased.

Mahdy et al. [16] performed a numerical analysis of the flow and heat transfer of a viscous nanofluid on a nonlinear stretching sheet considering Cu, Ag, CuO, Al_2O_3 and TiO_2 nanoparticles in water as base fluid. In addition, they performed an analysis of the impacts of uncertainty on the flow and heat transfer characteristics using four different models of thermal conductivity and dynamic viscosity. The authors concluded that the velocity and temperature profiles were affected by the nanoparticle concentration, the nonlinear stretching parameter, the Eckert number and the Prandtl number. Minea [17] carried out a study about the effect of uncertainty in thermal conductivity on the heat transfer by forced convection with Al_2O_3/water nanofluid. She used three different models for thermal conductivity and determined that the heat transfer coefficient of nanofluid increased between 3.4% and 27.8% compared to pure water for a fixed Reynolds number.

Selvakumar et al. [18] performed a numerical analysis of flow and heat transfer around a hot circular cylinder with uniform stream of nanofluid. They used a water-based TiO_2 nanofluid and analyzed three cases. In the first and second cases two sets of semi-empirical models of thermal conductivity and viscosity were used while a set of empirical data of thermal conductivity and viscosity were studied in the third case. It was seen that the flow and heat transfer characteristics differ quantitatively and qualitatively for each case and it was obtained that the choice of effective property models had a significant effect on the flow and heat transport prediction. This indicated that it is very important to have effective and accurate correlations of viscosity and thermal conductivity. In the above studies [13-18], it can be noted that the effects of different thermophysical correlations on the entropy production were not investigated.

Analysis of entropy production and optimization of nanofluid flows based on second law analysis has been reported by some authors [19-25]. However, there are few works related to the impacts of uncertainty in the nanofluid thermophysical properties on entropy production and optimum operating conditions. For example, Mahian et al. [26] studied the effect of uncertainty in physical properties on entropy generation between two rotating cylinders for a constant laminar flow of Al_2O_3/ethylene glycol nanofluid. Six different models obtained from the combinations of three correlations for thermal conductivity (Bruggeman, Hamilton-Crosser, and Yu-Choi) and two correlations for dynamic viscosity (Brinkman and Maiga et al.) were investigated.

Ibáñez et al. [27] presented the optimization of MHD flow of Al_2O_3 nanofluid in a vertical microchannel filled with a porous medium considering nonlinear thermal radiation, slip flow and convective-radiative boundary conditions. They reached optimal operating conditions, which had not been reported in previous similar configurations. Also, they carried out an analysis of the effects of the uncertainty in the thermophysical properties of nanofluids on heat transfer and entropy generation using four correlations to determine the nanofluid properties, Brinkman and Wang for dynamic viscosity, and Hamilton–Crosser and Yu–Choi for thermal conductivity. The authors determined that similar trends were obtained with optimum operating conditions for the explored combinations of the four models. In addition, they stated that the change of dynamic viscosity correlation in the model had a significant influence on the results.

The above investigations were carried out for nanofluids considering spherical shape of nanoparticles and theoretical correlations of physical properties. However, some studies also considered different nanoparticle shapes as in Refs. [28-33]. It was found that the nanoparticle shape affected the results obtained for the velocity, temperature and heat transfer characteristics. Therefore, it is necessary to determine the role of nanoparticle shape in the performance of thermal systems with the presence of nanofluid flow.

For example, Aaiza et al. [28] carried out a study with Al_2O_3, Fe_2O_4, TiO_2, Cu and Ag nanoparticles in two base fluids, namely ethylene glycol $C_2H_6O_2$ and water H_2O. In this work, the unstable magnetohydrodynamic mixed flow of an incompressible nanofluid inside a vertical channel with a porous medium was considered. The explored nanoparticle shapes were platelet, cylindrical, blade and brick. The results showed that the parameters with the greatest influence on the temperature variations were the viscosity and the thermal conductivity. It was concluded that elongated particles such as cylindrical and platelet shapes have lower velocity due to their higher viscosity values compared to blade and brick shapes. Sheikholeslami et al. [29] conducted a study of the water-based Al_2O_3 nanofluid in a cylindrical tube with a porous medium considering a magnetic field and thermal radiation for different shapes of nanoparticles (spherical, bricks, cylinders and platelets).

They found that the platelet form had a higher Nusselt number. Also, the results illustrated that the convection improved with the decrease of the magnetic field but it was reduced with the decrease of the radiative heat transfer.

Benkhedda et al. [30] conducted a numerical study for two nanofluids, the conventional TiO_2/water nanofluid and the hybrid Ag-TiO_2/water nanofluid in an isothermally heated horizontal tube. Four different kinds of nanoparticle shapes were considered in this study: spherical, cylindrical, platelet and blade for different nanoparticle volume fractions. Their results indicated that the friction factor of the two nanofluids increased as the nanoparticle volume fraction increased while it decreased as the Reynolds number increased for all types of nanoparticle shapes. On the other hand, the Nusselt number increased with the concentration of nanoparticles and the Reynolds number. The highest heat transfer rate was obtained for the highest volume concentration of blade-shaped nanoparticles followed by platelet, cylindrical and spherical shapes, respectively.

Saleem et al. [31] investigated a nanofluid dissipative flow induced by a moving flat plate considering spherical, blade and platelet shapes. Their obtained results revealed that the nanofluid with platelet-shaped nanoparticles offered the greatest improvement in heat transfer compared to the nanofluid with spherical and blade-shaped nanoparticles. Ghadikolaei et al. [32] studied the effect of the induced magnetic field on the flow of a conventional Cu nanofluid and a TiO_2-Cu hybrid nanofluid in water as base fluid on a stretchable sheet. The results indicated that the use of the hybrid TiO_2-Cu nanofluid was more efficient compared to the conventional Cu nanofluid because the Nusselt number obtained was higher. In addition, it was found that the application of platelet-shaped nanoparticles had a higher heat transfer compared to cylindrical and blade shapes. Sindhu et al. [33] studied the effect of nanoparticle shape on heat transfer for a hybrid nanofluid. The results showed that the Nusselt number was higher for blade shape of nanoparticles compared to other shapes.

It is worth mentioning that in these previous works [28-33], although the effect of nanoparticle shapes was analyzed, a second law analysis was not carried out. However, there are several works where the calculation of entropy generation was performed and the effects of nanoparticle shapes were investigated [34-37].

Kumar et al. [34] examined the flow of a hybrid nanofluid (Al_2O_3–Cu/H_2O) over a rotating disk considering the effect of Hall current. The impacts of the relevant system parameters on velocity, temperature and entropy, and the effects of the shape of the Al_2O_3 and Cu nanoparticles on the surface drag force and heat transport were investigated. The result showed that the entropy decreases with the increase in the magnetic parameter and Brinkman number. Ellahi et al. [35] investigated the effect of nanoparticle shapes on the entropy generation of a Cu/water nanofluid in an inverted cone, considering the simultaneous effects of porous medium, magnetic field, thermal

radiation and power law index. The studied shapes of nanoparticles were cylindrical, platelet and blade. In this study, it was observed that the nanofluid velocity decreased and the temperature increased when the values of the nanoparticle concentration, magnetic field, radiation parameter and porosity parameters increased. Ellahi found that the largest temperature gradient was achieved for the platelet shape of nanoparticles and therefore the rate of entropy generation was higher for this nanoparticle shape.

Zeeshan et al. [36] examined the influences of the Cu nanoparticle shape on a rotating disk. They determined the irreversibility associated to heat flow and friction and obtained that maximum irreversibility was reached for the platelet shape followed by cylindrical and spherical shapes. Seyyedi et al. [37] studied the entropy generation of a Cu/water nanofluid in a semi-annular cavity considering spherical, cylindrical and platelet nanoparticle shapes. The momentum and energy equations were solved numerically using the finite element method and then the entropy generation was calculated. They considered the effects of Rayleigh number, nanoparticle volume fraction, nanoparticle shape and enclosure twist angle on the entropy generation calculation. The main results indicated that the entropy generation increases when the Rayleigh number, the nanoparticle concentration and the angle of the enclosure increase. Also, the entropy generation was higher for the platelet shape.

In summary, it is found that most of the studies related to the effects of both the uncertainty in the thermophysical properties of nanofluids and the shapes of nanoparticles have focused on conventional nanofluids (with a single nanoparticle) for different geometries and physical effects. However, these effects of uncertainty in the thermophysical properties of nanofluids and nanoparticle shapes on the design optimum conditions have not been considered. This is an important gap in the literature. Moreover, in the most of studies that appear in the consulted literature about this subject the mathematical models are solved numerically and analytical solutions are not available. The present contribution aims to fill this gap.

In particular, this study is an extension of the work of Ibáñez et al. [22] in order to include the presence of a porous medium and the impacts of both the different shapes of nanoparticles and the uncertainty in the nanofluid thermophysical properties on the system optimum operating conditions. To the best of the author knowledge, analytical results of the impacts of nanoparticle shapes and uncertainty in thermophysical properties on optimal design conditions, such as those obtained in the present work, have not yet been reported for a similar configuration. The goal is to achieve both the desired flow and the desired heat transfer with minimum losses of useful energy and maximum heat transport.

The current results might be suitable to contrast the results of other problems on this topic in which similar tendencies should also be present. Moreover, the preceding results are relevant for the optimum design of energy systems with applications in nanofluids or microfluids as MHD micropumps and heat exchangers for refrigeration of microelectronic equipments.

3.2 PROBLEM DESCRIPTION AND GOVERNING EQUATIONS
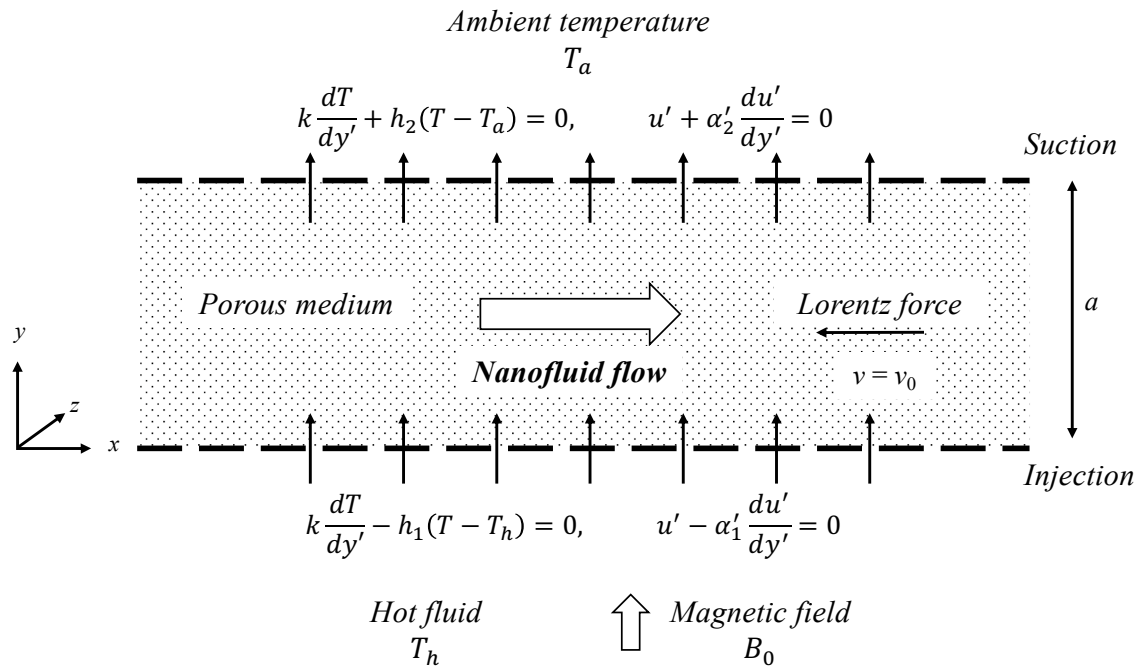
Fig. 3.1 *System geometry (Case I).*

A fully developed MHD flow of steady, incompressible and viscous unitary nanofluid through a horizontal microchannel of permeable parallel plates, with a porous medium and in presence of a constant transverse magnetic field B_0 (see Fig. 3.1). The plates are separated by a distance a. Hot nanofluid is injected into the bottom plate and suction occurs in the top plate. Sliding and convective heat transfer conditions at the nanofluid-plate interface are considered, and are used to solve the momentum and energy equations. Linear radiative flux, viscous and ohmic dissipation are considered. Here, the movement of nanofluid in presence of the transverse magnetic field induces an electric current that alters the dynamic and thermal behavior of nanofluid due to the presence of Lorentz force and Joule heating, respectively.

In our study, only the Darcy term is considered in the momentum equation because for the fluid flow through a porous medium at low velocities as in the current study (laminar flow), the pressure drop in the direction of flow is proportional to the velocity of the fluid and the mathematical expression used for its modeling is the Darcy's law.

3.2.1 Velocity field

The system is modeled based on the following assumptions

1. The flow is stationary, that is $\frac{\partial}{\partial t} = 0$.
2. The length of the plates in the z axis is much greater than the width of the channel, so that the effects on z are neglected.
3. The y component of the velocity is $v = v_0$, which represents the flow through the permeable plates, v_0 is constant.
4. There is a constant pressure gradient p with respect to the x axis.
5. The velocity field is two-dimensional so that the velocity $w = 0$ and $\frac{\partial}{\partial z}$ of any velocity component is zero.
6. The effect of gravity is neglected.
7. The fluid is incompressible $\frac{\partial \rho}{\partial t} = 0$.

From the continuity equation for an incompressible flow in Cartesian coordinates (Eq. 2.6), the divergence of the velocity field **v** is developed

$$\frac{\partial u}{\partial x} + \frac{\partial v}{\partial y} + \frac{\partial w}{\partial z} = 0 \tag{3.1}$$

Considering that $\frac{\partial w}{\partial z} = 0$, and that $v = v_0$ is constant, $\frac{\partial v_0}{\partial y} = 0$, the corresponding terms are eliminated, then

$$\frac{\partial u}{\partial x} = 0 \tag{3.2}$$

Which indicates that u is not a function of x and there is a fully developed flow; if u is not a function of time and z, then u depends only on y.

$$u = u(y) \tag{3.3}$$

From Eq. (2.11) for momentum, the material derivative for the moment at x is developed.

$$\rho \left(\frac{\partial u}{\partial t} + u \frac{\partial u}{\partial x} + v \frac{\partial u}{\partial y} + w \frac{\partial u}{\partial z} \right) = -\frac{\partial p}{\partial x} + \nabla \cdot \tau + \rho g + \mathbf{j} \times \mathbf{B} \qquad (3.4)$$

For an incompressible fluid, the divergence of the viscous stress tensor from the velocity component u is equivalent to

$$\nabla \cdot \tau = \eta \nabla^2 \mathbf{v} = \eta \left(\frac{\partial^2 u}{\partial x^2} + \frac{\partial^2 u}{\partial y^2} + \frac{\partial^2 u}{\partial z^2} \right) \qquad (3.5)$$

where η is the dynamic viscosity of the fluid. Substituting Eq. (3.5) into Eq. (3.4)

$$\rho \left(\frac{\partial u}{\partial t} + u \frac{\partial u}{\partial x} + v \frac{\partial u}{\partial y} + w \frac{\partial u}{\partial z} \right)$$
$$= -\frac{\partial p}{\partial x} + \eta \left(\frac{\partial^2 u}{\partial x^2} + \frac{\partial^2 u}{\partial y^2} + \frac{\partial^2 u}{\partial z^2} \right) + \rho g + \mathbf{j} \times \mathbf{B} \qquad (3.6)$$

In Eq. (3.6), terms containing the velocity w, the partial derivatives $\frac{\partial}{\partial z}$ and $\frac{\partial}{\partial t}$, are eliminated, because the flow movement in z is negligible and stationary in all its components. The effect of gravity is neglected $g = 0$ and from the continuity equation it is known that $\frac{\partial u}{\partial x} = 0$, Additionally $v = v_0$ is considered constant, therefore, Eq. (3.6) is reduced to

$$\rho \left(v_0 \frac{\partial u}{\partial y} \right) = -\frac{\partial p}{\partial x} + \eta \left(\frac{\partial^2 u}{\partial y^2} \right) + \mathbf{j} \times \mathbf{B} \qquad (3.7)$$

The momentum equation is based on Newton's second law, which states that the sums of forces are equal to mass times acceleration. In Eq. (3.7) the terms on the left side represent the mass times acceleration and the terms on the right side are the sum of forces acting on the fluid.

From the Darcy's equation, the term that represents the pressure gradient in a porous medium ∇p_m along the x axis is added

$$-\frac{\partial p_m}{\partial x} = -\frac{\eta}{K} u \qquad (3.8)$$

where K is the permeability coefficient of the porous medium.

Then Eq. (3.7) becomes

$$\rho \left(v_0 \frac{\partial u}{\partial y} \right) = -\frac{\partial p}{\partial x} + \eta \left(\frac{\partial^2 u}{\partial y^2} \right) + \mathbf{j} \times \mathbf{B} - \frac{\eta}{K} u \qquad (3.9)$$

The term $\mathbf{j} \times \mathbf{B}$ is expressed as the vector product of two vectors. The analytical expression is obtained with Ohm's law.

$$\mathbf{j} = \sigma (\mathbf{E} + \mathbf{v} \times \mathbf{B}) \qquad (3.10)$$

where σ is the electrical conductivity of the fluid. The electric field $\mathbf{E}$ is neglected because it is too small compared to $\mathbf{v} \times \mathbf{B}$, the velocity vector is considered a single component $\mathbf{v} = \mathbf{v}(u, 0, 0)$ and the magnetic field is applied transversely to the direction of the flow $\mathbf{B} = \mathbf{B}(0, B_0, 0)$, where B_0 is the magnetic field intensity, so the electric current density is obtained like this

$$\mathbf{j} = \sigma \begin{bmatrix} \hat{\imath} & \hat{\jmath} & \hat{k} \\ u & 0 & 0 \\ 0 & B_0 & 0 \end{bmatrix} = \sigma(0\,\hat{\imath} - 0\,\hat{\jmath} + uB_0\,\hat{k}) \qquad (3.11)$$

If the electric current is in a direction perpendicular to the movement of the flow and the direction of the magnetic field, its direction corresponds to the negative z axis, therefore, the expression for the Lorentz force is

$$\mathbf{j} \times \mathbf{B} = \begin{bmatrix} \hat{\imath} & \hat{\jmath} & \hat{k} \\ 0 & 0 & \sigma uB_0 \\ 0 & B_0 & 0 \end{bmatrix} = -\sigma uB_0^2\,\hat{\imath} - 0\,\hat{\jmath} + 0\,\hat{k}) \qquad (3.12)$$

The right-hand rule assumes a force in the opposite direction to the movement of the fluid caused by the Lorentz force.

$$\mathbf{j} \times \mathbf{B} = -\sigma B_0^2 u \qquad (3.13)$$

Therefore, substituting Eq. (3.13) into Eq. (3.9), the momentum balance equation for a viscous nanofluid with the effect of a transverse magnetic field through a porous medium is obtained

$$\rho_{nf} v_0 \frac{\partial u}{\partial y} = -\frac{\partial p}{\partial x} + \eta_{nf} \frac{\partial^2 u}{\partial y^2} - \sigma_{nf} B_0^2 u - \frac{\eta_{nf}}{K} u \qquad (3.14)$$

where u is the fluid velocity, v_0 is the uniform suction/injection velocity at the microchannel plates, η_{nf} is the dynamic viscosity, σ_{nf} is the electrical conductivity, K is the permeability coefficient of the porous medium and ρ_{nf} is the nanofluid density. The first term, from left to right, is the convective term related to fluid movement, the second term is the pressure gradient in x direction, the third term is related to the friction forces, the fourth term represents the effect of the magnetic field or Lorentz force and the last term is the Darcy term related to the permeability and friction of the porous medium which is valid for the laminar flow regime.

The Eq. (3.13) is transformed in terms of ordinary derivatives.

$$\rho_{nf} v_0 \frac{du'}{dy'} = -\frac{dp}{dx'} + \eta_{nf} \frac{d^2 u'}{dy'^2} - \sigma_{nf} B_0^2 u' - \frac{\eta_{nf}}{K} u' \tag{3.15}$$

Assuming that the surface roughness of each plate is different, the slip lengths have not a same value and therefore the boundary conditions are written as [22]

$$u' - \alpha_1' \frac{du'}{dy'} = 0, \ at \ y' = 0 \tag{3.16}$$

$$u' + \alpha_2' \frac{du'}{dy'} = 0, \ at \ y' = a \tag{3.17}$$

where α_1' y α_2' are the slip lengths of the bottom and top plates, respectively and a is the distance between plates.

Considering the relationships of density, viscosity and electrical conductivity of nanofluid and introducing the following dimensionless variables

$$u = \frac{\rho_f a u'}{\eta_f}, \qquad y = \frac{y'}{a}, \qquad \alpha_1 = \frac{\alpha_1'}{a}, \qquad \alpha_2 = \frac{\alpha_2'}{a},$$
$$Re = \frac{v_0 a \rho_f}{\eta_f}, \qquad P = \frac{a^3 \rho_f}{\eta_f^2}\left(-\frac{dp}{dx'}\right), \quad M = B_0 a \sqrt{\sigma_f / \eta_f}, \qquad Da = \frac{K}{a^2} \tag{3.18}$$

Equation (3.15) become

$$\frac{\rho_{nf}}{\rho_f} Re \frac{du}{dy} = P + \frac{\eta_{nf}}{\eta_f} \frac{d^2 u}{dy^2} - \frac{\sigma_{nf}}{\sigma_f} M^2 u - \frac{\eta_{nf}}{\eta_f} \frac{u}{Da} \tag{3.19}$$

and the boundary conditions Eqs. (3.16) and (3.17)

$$u - \alpha_1 \frac{du}{dy} = 0 \ \ at \ \ y = 0 \tag{3.20}$$

$$u + \alpha_2 \frac{du}{dy} = 0 \ \ at \ \ y = 1 \tag{3.21}$$

where u is the velocity of nanofluid and α_1 and α_2 are the slip parameters on the bottom and top plates, respectively.

3.2.2 Temperature field

Considering the constitutive relationship for heat flow or Fourier's law

$$\mathbf{J}_q = -k\nabla T \tag{3.22}$$

Where k is the thermal conductivity and T is the temperature of the fluid. Substitute Eq. (3.22) into the energy equation Eq. (2.15).

$$\rho \frac{De}{Dt} = k\nabla^2 T - \tau : \nabla \mathbf{v} + \mathbf{j} \cdot (\mathbf{E} + \mathbf{v} \times \mathbf{B}) \tag{3.23}$$

The internal energy of the fluid e, neglecting the kinetic and potential energy, is equal to the enthalpy [38], therefore, it can be expressed as $e = C_p T$. Where C_p is the heat capacity of the fluid. Substituting and solving the material derivative $\frac{De}{Dt}$ to Eq. (3.23).

$$\rho C_p \left(\frac{\partial T}{\partial t} + (\mathbf{v} \cdot \nabla)T \right) = k\nabla^2 T - \tau : \nabla \mathbf{v} + \mathbf{j} \cdot (\mathbf{E} + \mathbf{v} \times \mathbf{B}) \tag{3.24}$$

The term $\tau : \nabla \mathbf{v}$ representing the energy flux on the fluid surface can be transformed by substituting the stress τ with the Newton's law of viscosity

$$\tau : \nabla \mathbf{v} = -\eta \Phi \tag{3.25}$$

where Φ is the viscous dissipation function. Therefore, the energy equation for a viscous MHD flow with constant properties is expressed as

$$\rho C_p \left(\frac{\partial T}{\partial t} + (\mathbf{v} \cdot \nabla)T \right) = k\nabla^2 T + \eta \Phi + \mathbf{j} \cdot (\mathbf{E} + \mathbf{v} \times \mathbf{B}) \tag{3.26}$$

41

Expanding the terms, we have

$$\rho C_p \left(\frac{\partial T}{\partial t} + u\frac{\partial T}{\partial x} + v\frac{\partial T}{\partial y} + w\frac{\partial T}{\partial z} \right)$$
$$= k\left(\frac{\partial^2 T}{\partial x^2} + \frac{\partial^2 T}{\partial y^2} + \frac{\partial^2 T}{\partial z^2} \right) + \eta\Phi + \mathbf{j}\cdot(\mathbf{E}+\mathbf{v}\times\mathbf{B}) \tag{3.27}$$

The viscous dissipation function Φ is expressed as [38]

$$\Phi = 2\left[\left(\frac{\partial u}{\partial x}\right)^2 + \left(\frac{\partial v}{\partial y}\right)^2 + \left(\frac{\partial w}{\partial z}\right)^2 \right]$$
$$+ \left[\left(\frac{\partial u}{\partial y}+\frac{\partial v}{\partial x}\right)^2 + \left(\frac{\partial w}{\partial x}+\frac{\partial u}{\partial z}\right)^2 + \left(\frac{\partial w}{\partial y}+\frac{\partial v}{\partial z}\right)^2 \right] \tag{3.28}$$

Substituting Eq. (3.28) into Eq. (3.27), we have

$$\rho C_p \left(\frac{\partial T}{\partial t} + u\frac{\partial T}{\partial x} + v\frac{\partial T}{\partial y} + w\frac{\partial T}{\partial z} \right)$$
$$= k\left(\frac{\partial^2 T}{\partial x^2} + \frac{\partial^2 T}{\partial y^2} + \frac{\partial^2 T}{\partial z^2} \right) + 2\eta\left[\left(\frac{\partial u}{\partial x}\right)^2 + \left(\frac{\partial v}{\partial y}\right)^2 + \left(\frac{\partial w}{\partial z}\right)^2 \right]$$
$$+ \eta\left[\left(\frac{\partial u}{\partial y}+\frac{\partial v}{\partial x}\right)^2 + \left(\frac{\partial w}{\partial x}+\frac{\partial u}{\partial z}\right)^2 + \left(\frac{\partial w}{\partial y}+\frac{\partial v}{\partial z}\right)^2 \right]$$
$$+ \mathbf{j}\cdot(\mathbf{E}+\mathbf{v}\times\mathbf{B}) \tag{3.29}$$

Considering stationary operating conditions $\frac{\partial T}{\partial t}=0$ and the effects in the x and z direction are negligible due to the length of the plates, such that w, $\frac{\partial}{\partial z}$ and $\frac{\partial}{\partial x}$ are zero in all variables and the velocity $v=v_0$ is constant, the associated terms in Eq. (3.29) are eliminated, therefore, we have

$$\rho C_p \left(v_0\frac{\partial T}{\partial y} \right) = k\left(\frac{\partial^2 T}{\partial y^2} \right) + \eta\left(\frac{\partial u}{\partial y}\right)^2 + \mathbf{j}\cdot(\mathbf{E}+\mathbf{v}\times\mathbf{B}) \tag{3.30}$$

Eq. (3.30) expresses that the net energy transferred by convection by the fluid, out of the control volume, is equal to the net energy transferred towards this volume by heat conduction. In Eq. (3.30), the term related to the radiation heat flux is added considering it as an approximation of the Rosseland diffusion equation [20]

$$q_r = -\frac{4\sigma_*}{3k_*}\frac{\partial T^4}{\partial y} \tag{3.31}$$

where T^4 can be expanded by a Taylor series [39, 40]. Rearranging terms and expanding T^4 to T_∞, we have that $T^4 \cong 4T_\infty^3 T - 3T_\infty^4$, from this expansion we obtain

$$\frac{\partial q_r}{\partial y} = -\frac{16\sigma_* T_\infty^3}{3k_*}\frac{\partial^2 T}{\partial y^2} \tag{3.32}$$

where T_∞ is the bulk temperature, which is the average fluid temperature, σ is the Stefan-Boltzmann constant and k_* is the Rosseland mean absorption coefficient.

On the other hand, the term that represents the dissipation of energy due to the porous medium can be expressed as an increase in heat due to fluid friction. For a one-dimensional flow, this drag force is proportional to the square of the fluid velocity, this dissipation term can be expressed as

$$q_p = \frac{\eta}{K}u^2 \tag{3.33}$$

Therefore, taking into account the previous statements, the energy equation considering thermal radiation and the effect of a porous medium is

$$\rho C_p \left(v_0 \frac{\partial T}{\partial y}\right) = k\left(\frac{\partial^2 T}{\partial y^2}\right) + \eta \left(\frac{\partial u}{\partial y}\right)^2 + \mathbf{j}\cdot(\mathbf{E} + \mathbf{v}\times\mathbf{B}) - \frac{\partial q_r}{\partial y} + \frac{\eta}{K}u^2 \tag{3.34}$$

In the expression $\mathbf{j}\cdot(\mathbf{E} + \mathbf{v}\times\mathbf{B})$, the electric field $\mathbf{E}$ is neglected because it is too small compared to $\mathbf{v}\times\mathbf{B}$. The vector $\mathbf{j}$ is determined by Ohm's law $\mathbf{j} = \sigma(\mathbf{E} + \mathbf{v}\times\mathbf{B})$, where $\mathbf{E} \approx 0$.

The velocity vector is considered a single component $\mathbf{v} = \mathbf{v}(u,0,0)$ and the magnetic field is applied transversally to the flow direction $\mathbf{B} = \mathbf{B}(0, B_0, 0)$, therefore

$$\mathbf{E} + \mathbf{v}\times\mathbf{B} = 0 + \begin{vmatrix} \hat{\imath} & \hat{\jmath} & \hat{k} \\ u & 0 & 0 \\ 0 & B_0 & 0 \end{vmatrix} = 0\,\hat{\imath} - 0\,\hat{\jmath} + uB_0\,\hat{k} \tag{3.35}$$

From equations (3.11) and (3.35) we have that $\mathbf{j} = \sigma(0\,\hat{\imath} - 0\,\hat{\jmath} + uB_0\,\hat{k})$ and $\mathbf{E} + \mathbf{v} \times \mathbf{B} = 0\,\hat{\imath} - 0\,\hat{\jmath} + uB_0\,\hat{k}$, therefore, the result of the dot product is

$$\mathbf{j} \cdot (\mathbf{E} + \mathbf{v} \times \mathbf{B}) = \left(\sigma(0\,\hat{\imath} - 0\,\hat{\jmath} + uB_0\,\hat{k})\right) \cdot \left(0\,\hat{\imath} - 0\,\hat{\jmath} + uB_0\,\hat{k}\right) = \sigma(u^2 B_0^2) \qquad (3.36)$$

Substituting Eq. (3.36) into Eq. (3.34), the energy balance equation for a viscous nanofluid in the presence of a magnetic field and a porous medium reduces to

$$\left(\rho C_p\right)_{nf} v_0 \left(\frac{\partial T}{\partial y}\right) = k_{nf} \frac{\partial^2 T}{\partial y^2} + \eta_{nf} \left(\frac{\partial u}{\partial y}\right)^2 + \sigma_{nf} B_0^2 u^2 - \frac{\partial q_r}{\partial y} + \frac{\eta_{nf}}{K} u^2 \qquad (3.37)$$

Transforming into ordinary derivatives, the energy balance equation is developed from the differential heat transfer equation considering viscous dissipation and adding the magnetic field term and Darcy's equation. Therefore, for a viscous nanofluid in presence of a magnetic field and a porous medium, the energy equation becomes [20,27]

$$\left(\rho C_p\right)_{nf} v_0 \left(\frac{dT}{dy'}\right) = k_{nf} \frac{d^2 T}{dy^2} + \eta_{nf} \left(\frac{du'}{dy'}\right)^2 + \sigma_{nf} B_0^2 u'^2 - \frac{dq_r}{dy'} + \frac{\eta_{nf}}{K} u'^2 \qquad (3.38)$$

Where T is the temperature of the nanofluid, k_{nf} the thermal conductivity, $\left(\rho C_p\right)_{nf}$ the density and heat capacity of the nanofluid and σ_{nf} is the electrical conductivity of the nanofluid.

The first term of the energy balance equation is the convective term, the second term considers the heat flow by conduction, the third term is the viscous dissipation, the fourth term is the Joule dissipation described in terms of Ohm's law, the fifth term considers the heat flux due to thermal radiation and the sixth term represents the effects of the porous medium. The term q_r related to the radiation heat flux is [22, 39, 40]

$$q_r = -\frac{16\sigma^* T_b^3}{3k^*} \frac{dT}{dy'} \qquad (3.39)$$

where, T_b is the global temperature.

The third kind thermal boundary conditions that the Eq. (3.38) must satisfy are [22]

$$k_{nf} \frac{dT}{dy'} - h_1(T - T_h) = 0 \quad at \quad y' = 0 \tag{3.40}$$

$$k_{nf} \frac{dT}{dy'} + h_2(T - T_a) = 0 \quad at \quad y' = a \tag{3.41}$$

where h_1 and h_2 are the heat transfer coefficients on the bottom and top plates, respectively, T_h is the temperature of the hot nanofluid, T_a is the ambient temperature.

Considering the relationships of density, viscosity and electrical conductivity of nanofluid and introducing the following dimensionless variables

$$u = \frac{u'}{v_0}, \qquad y = \frac{y'}{a}, \qquad \theta = \frac{T - T_a}{T_h - T_a}, \qquad Re = \frac{v_0 a \rho_f}{\eta_f},$$

$$M = B_0 a \sqrt{\sigma_f / \eta_f}, \qquad Da = \frac{K}{a^2}, \qquad Ec = \frac{v_0^2}{(C_p)_f}(T_h - T_a), \qquad Pr = \frac{\eta_f (C_p)_f}{k_f}, \tag{3.42}$$

$$Rd = \frac{16\sigma^* T_b^3}{3k^* k_f}, \qquad Pe = RePr, \qquad Bi_1 = ah_1/k_f, \qquad Bi_2 = ah_2/k_f$$

Equations (3.38), (3.40), (3.41) become

$$Pe \frac{(\rho C_p)_{nf}}{(\rho C_p)_f} \frac{d\theta}{dy}$$

$$= \left(\frac{k_{nf}}{k_f} + Rd\right)\frac{d^2\theta}{dy^2} \tag{3.43}$$

$$+ Pr\, Ec\left[\frac{\eta_{nf}}{\eta_f}\left(\frac{du}{dy}\right)^2 + M^2 \frac{\sigma_{nf}}{\sigma_f} u^2 + \frac{\eta_{nf}}{\eta_f}\frac{u^2}{Da}\right]$$

$$\frac{k_{nf}}{k_f}\frac{d\theta}{dy} - Bi_1(\theta - 1) = 0 \quad at \quad y = 0 \tag{3.44}$$

$$\frac{k_{nf}}{k_f}\frac{d\theta}{dy} + Bi_2(\theta) = 0 \quad at \quad y = 1 \tag{3.45}$$

where θ is the dimensionless temperature of nanofluid and Bi_1 and Bi_2 are Biot numbers on the bottom and top plates, respectively.

3.2.3 Entropy generation

From Eq. (2.27), which is the internal generation rate of entropy S, the terms associated with irreversibilities are considered. Ohm's law Eq. (3.10) for the electromagnetic field, Fourier's law Eq. (3.22) for heat flow and Newton's law of viscosity Eq. (3.25) for irreversibility due to viscous dissipation, are considered.

Substituting Eq. (3.22), Eq. (3.25) and Eq. (3.36) into Eq. (2.27)

$$S = \frac{k}{T^2} \nabla T \cdot \nabla T + \frac{\eta}{T} \Phi + \frac{\sigma}{T} (u^2 B_0^2) \tag{3.46}$$

Considering that the effects in the x and z direction are negligible due to the length of the plates, such that $w, \frac{\partial}{\partial z}$ and $\frac{\partial}{\partial x}$ are zero, the viscous dissipation term is

$$\eta \Phi = \eta \left(\frac{\partial u}{\partial y}\right)^2 \tag{3.47}$$

Substituting Eq. (3.47) into Eq. (3.46) we get

$$S = \frac{k}{T^2} \nabla T \cdot \nabla T + \frac{\eta}{T} \left(\frac{\partial u}{\partial y}\right)^2 + \frac{\sigma}{T} (u^2 B_0^2) \tag{3.48}$$

because $\nabla T \cdot \nabla T = \left(\frac{\partial T}{\partial x}\right)^2 + \left(\frac{\partial T}{\partial y}\right)^2 + \left(\frac{\partial T}{\partial z}\right)^2$, the components $\frac{\partial}{\partial x}$ and $\frac{\partial}{\partial z}$ are neglected, then Eq. (3.48) becomes

$$S = \frac{k}{T^2} \left(\frac{\partial T}{\partial y}\right)^2 + \frac{\eta}{T} \left(\frac{\partial u}{\partial y}\right)^2 + \frac{\sigma}{T} (u^2 B_0^2) \tag{3.49}$$

The effect of irreversibility due to radiation heat transfer is taken from Eq. (3.38), where

$$q_r = -\frac{16 \sigma^* T_b^3}{3 k_*} \nabla T \tag{3.50}$$

Similar to Fourier's law, the Rosseland term Eq. (3.50) is incorporated, where the radiation irreversibility is

$$-\frac{1}{T^2} (q_r) \cdot \nabla T = -\frac{1}{T^2} \left(-\frac{16 \sigma^* T_b^3}{3 k_*}\right) \nabla T \cdot \nabla T = \frac{1}{T^2} \left(\frac{16 \sigma^* T_b^3}{3 k_*}\right) \left(\frac{\partial T}{\partial y}\right)^2 \tag{3.51}$$

And the irreversibility due to friction in the porous medium is added considering Eq. (3.33). Therefore, Eq. (3.49) remains

$$S = \frac{k}{T^2}\left(\frac{\partial T}{\partial y}\right)^2 + \frac{1}{T^2}\left(\frac{16\sigma^* T_b^3}{3k_*}\right)\left(\frac{\partial T}{\partial y}\right)^2 + \frac{\eta}{T}\left(\frac{\partial u}{\partial y}\right)^2 + \frac{\sigma}{T}(u^2 B_0^2) + \frac{1}{T}\frac{\eta}{K}u^2 \tag{3.52}$$

Where S is the local entropy. The exact solutions of the velocity and temperature fields are used to calculate the entropy production as a function of the fundamental parameters that characterize the system. This entropy generation function must consider all the irreversible sources present in the thermal system [22, 27, 41]. Therefore, transforming into ordinary derivatives and simplifying Ec. (3.52), the expression of the local entropy production for a nanofluid is

$$S' = \frac{1}{T^2}\left(k_{nf} + \frac{16\sigma^* T_b^3}{3k*}\right)\left(\frac{dT}{dy'}\right)^2 + \frac{1}{T}\left[\eta_{nf}\left(\left(\frac{du'}{dy'}\right)^2 + \frac{u'^2}{K}\right) + \sigma_{nf}B_0^2 u'^2\right] \tag{3.53}$$

Eq. (3.53) in dimensionless terms becomes

$$S = \frac{\left(\frac{d\theta}{dy}\right)^2}{[\theta+1]^2}\left(\frac{k_{nf}}{k_f} + Rd\right) + \frac{EcPr}{\theta+1}\left[\frac{\eta_{nf}}{\eta_f}\left(\left(\frac{du}{dy}\right)^2 + \frac{u^2}{Da}\right) + \left[\frac{\sigma_{nf}}{\sigma_f}M^2 u^2\right]\right] \tag{3.54}$$

where S is normalized by k_f/a^2. The first term on the right hand side of Eq. (3.54) corresponds to the irreversibilities associated with heat transfer by conduction and radiation, the second term is related to viscous dissipation in the nanofluid domain, and the third and fourth terms express the irreversibilities associated with shear stresses at the solid porous medium-nanofluid interface and Joule heating, respectively.

The calculation of the global entropy production rate $< \dot{S} >$ is done by integrating Eq. (3.54) with respect to y, taking into account the width of the microchannel $a = 1$, therefore

$$< \dot{S} > = \int_0^1 S\, dy \tag{3.55}$$

3.2.4 Heat transfer

The internal heat transfer by convection can be calculated through the Nusselt number Nu.

$$Nu = \frac{h \cdot a}{k_f} \tag{3.56}$$

where h is the heat transfer coefficient and a is the distance between plates. With Newton's cooling law and considering Eqs. (3.22) and (3.39).

$$h = \frac{q}{\Delta T} = \frac{\left(-k_{nf} - \frac{16\sigma^* T_b^3}{3k^*}\right)\left(\frac{dT}{dy'}\right)}{T - T_b} \tag{3.57}$$

Substituting Eq. (3.57) into (3.56), the Nusselt number becomes

$$Nu = -\frac{a\left(k_{nf} + \frac{16\sigma^* T_b^3}{3k^*}\right)}{k_f(T - T_b)}\left(\frac{dT}{dy'}\right) \tag{3.58}$$

For the hot plate at $y' = 0$, the expression is [22, 27]

$$Nu = -\frac{a\left(k_{nf} + \frac{16\sigma^* T_b^3}{3k^*}\right)}{k_f(T_{y'=0} - T_b)}\left(\frac{dT}{dy'}\right)_{y'=0} \tag{3.59}$$

Where $T_b = \frac{\int_0^1 u\theta\, dy}{\int_0^1 u\, dy}$ is the global temperature or the average temperature of the nanofluid in a cross section of microchannel and $T_{y'=0}$ is the plate temperature at $y' = 0$, respectively [27]. In dimensionless terms Ec. (3.59) becomes

$$Nu = -\frac{\left(\frac{k_{nf}}{k_f} + Rd\right)}{\theta_{y=0} - \frac{\int_0^1 u\theta\, dy}{\int_0^1 u\, dy}}\left(\frac{d\theta}{dy}\right)_{y=0} \tag{3.60}$$

To obtain Nu on the upper plate, the temperature and temperature gradient is evaluated at $y = 1$.

3.3 SOLUTION OF EQUATIONS

Analytical solutions are presented for the momentum equation and the energy equation. These solutions can be used in the future to calibrate similar physical models. The results are given based on the models of thermophysical properties, constant parameters and dimensionless numbers.

The expressions that describe the generation of entropy and the internal heat transfer by the Nusselt number are determined using the *Wolfram Mathematica* software, from the solutions obtained for velocity and temperature.

3.3.1 Analytical solution of moment equation

The momentum equation (3.19) is solved analytically using the method of undetermined coefficients. In this method, the general solution of the equation is determined as the sum of the solution of the corresponding homogeneous equation plus the particular solution of the non-homogeneous one. In our case, the particular solution of the non-homogeneous equation is proposed as a constant considering the form of the term that makes the equation non-homogeneous.

The general solution of Eq. (3.19) is given by

$$u = u_h + u_p \tag{3.61}$$

Where u_h is the homogeneous solution and u_p is the particular solution. Arranging terms of Eq. (3.19) we have

$$\frac{\eta_{nf}}{\eta_f}\frac{d^2u}{dy^2} - \frac{\rho_{nf}}{\rho_f}Re\frac{du}{dy} - \left(\frac{\sigma_{nf}}{\sigma_f}M^2 - \frac{\eta_{nf}}{\eta_f}\frac{1}{Da}\right)u = -P \tag{3.62}$$

To obtain the homogeneous part of Eq. (3.61), Eq. (3.62) is divided by $\frac{\eta_{nf}}{\eta_f}$ and simplifying

$$\frac{d^2u}{dy^2} - \left(\frac{\eta_f}{\eta_{nf}}\frac{\rho_{nf}}{\rho_f}Re\right)\frac{du}{dy} - \left(\frac{Da\sigma_{nf}\eta_f M^2 + \sigma_f\eta_{nf}}{\sigma_f\eta_{nf}Da}\right)u = -\frac{\eta_f}{\eta_{nf}}P \tag{3.63}$$

Defining constant terms

$$F_1 = \frac{\eta_f}{\eta_{nf}}\frac{\rho_{nf}}{\rho_f}Re \tag{3.64}$$

$$F_2 = \frac{Da\sigma_{nf}\eta_f M^2 + \sigma_f \eta_{nf}}{\sigma_f \eta_{nf} Da} \tag{3.65}$$

Substituting Eqs. (3.64) and (3.65) in Eq. (3.63), the homogeneous equation to be solved is

$$\frac{d^2 u}{dy^2} - F_1 \frac{du}{dy} - F_2 u = 0 \tag{3.66}$$

Considering a characteristic equation associated in the form $m^2 - F_1 m - F_2 = 0$, with the general formula it is solved for m

$$m_1 = \frac{F_1 + \sqrt{F_1{}^2 + 4F_2}}{2} = \frac{F_1}{2} + \frac{\sqrt{F_1{}^2 + 4F_2}}{2} \tag{3.67}$$

$$m_2 = \frac{F_1 - \sqrt{F_1{}^2 + 4F_2}}{2} = \frac{F_1}{2} - \frac{\sqrt{F_1{}^2 + 4F_2}}{2} \tag{3.68}$$

Therefore, the homogeneous solution remains

$$u_h = C_1 e^{m_1 y} + C_2 e^{m_2 y} \tag{3.69}$$

Simplifying terms we have

$$\begin{aligned} u_h &= C_1 e^{\frac{F_1}{2}y} e^{\frac{\sqrt{F_1{}^2 + 4F_2}}{2}y} + C_2 e^{\frac{F_1}{2}y} e^{\frac{-\sqrt{F_1{}^2 + 4F_2}}{2}y} \\ &= e^{\frac{F_1}{2}y} \left(C_1 e^{\frac{\sqrt{F_1{}^2 + 4F_2}}{2}y} + C_2 e^{\frac{-\sqrt{F_1{}^2 + 4F_2}}{2}y} \right) \end{aligned} \tag{3.70}$$

$$u_h = e^{\frac{F_1}{2}y} \left(C_1 \sinh\left(\frac{\sqrt{F_1{}^2 + 4F_2}}{2} y \right) + C_2 \cosh\left(\frac{\sqrt{F_1{}^2 + 4F_2}}{2} y \right) \right) \tag{3.71}$$

To find the particular solution, it is considered that u_p is constant, so $u_p = Cte$, $u'_p = 0$ y $u''_p = 0$. Taking into account the previous assumptions and substituting Eqs. (3.64) and (3.65) in Eq. (3.63) we have that

$$(0) - F_1(0) - F_2(Cte) = -\frac{\eta_f}{\eta_{nf}} P \tag{3.72}$$

Solving, we have that $Cte = \frac{\eta_f}{\eta_{nf}} \frac{P}{F_2}$, then

$$u_p = Cte = \frac{\eta_f}{\eta_{nf}} \frac{P}{F_2} \tag{3.73}$$

Substituting Eqs. (3.71) and (3.73) in Eq. (3.61), remains

$$u = e^{\frac{F_1}{2}y}\left(C_1 \sinh\left(\frac{\sqrt{F_1^2 + 4F_2}}{2}y\right) + C_2 \cosh\left(\frac{\sqrt{F_1^2 + 4F_2}}{2}y\right)\right) + \frac{\eta_f}{\eta_{nf}} \frac{P}{F_2} \tag{3.74}$$

Considering the simplifications

$$F_3 = \frac{\eta_f}{\eta_{nf}} \frac{P}{F_2} \tag{3.75}$$

$$A = \frac{\sqrt{F_1^2 + 4F_2}}{2} \tag{3.76}$$

Equation (3.74) remains

$$u = e^{\frac{F_1}{2}y}(C_1 \sinh(Ay) + C_2 \cosh(Ay)) + F_3 \tag{3.77}$$

Solve Eq. (3.77) taking into account the boundary conditions Eqs. (3.20) and (3.21). Substituting $y = 0$ and $y = 1$, in Eq. (3.77)

$$u_{y=0} = C_2 + F_3 \tag{3.78}$$

$$u_{y=1} = e^{\frac{F_1}{2}}(C_1 \sinh(A) + C_2 \cosh(A)) + F_3 \tag{3.79}$$

Deriving Eq. (3.77), for $y = 0$ and $y = 1$ we have

$$\frac{du}{dy}_{y=0} = C_1 A + \frac{F_1 C_2}{2} \tag{3.80}$$

$$\frac{du}{dy}_{y=1} = e^{\frac{F_1}{2}}(C_1 A \cosh(A) + C_2 A \sinh(A)) \\ + \frac{F_1}{2} e^{\frac{F_1}{2}}(C_1 \sinh(A) + C_2 \cosh(A)) \tag{3.81}$$

Substituting Eqs. (3.78) and (3.80) in Eq. (3.20)

$$C_2 + F_3 - \alpha_1 \left(C_1 A + \frac{F_1 C_2}{2} \right) = 0 \tag{3.82}$$

Substituting Eqs. (3.79) and (3.81) in Eq. (3.21)

$$e^{\frac{F_1}{2}}(C_1 \sinh(A) + C_2 \cosh(A)) + F_3 \\ + \alpha_2 \left(e^{\frac{F_1}{2}}(C_1 A \cosh(A) + C_2 A \sinh(A)) \right. \\ \left. + \frac{F_1}{2} e^{\frac{F_1}{2}}(C_1 \sinh(A) + C_2 \cosh(A)) \right) = 0 \tag{3.83}$$

With Eqs. (3.82) and (3.83), a system of linear equations is obtained that is solved analytically by the substitution method to find the constant terms C_1 y C_2, the development of the solution is not shown here because it is too extensive.

Once the system of equations has been solved, the solution to the moment differential equation is obtained

$$u = e^{\frac{F_1 y}{2}}(C_1 Sinh(Ay) + C_2 Cosh(Ay)) + F_3 \tag{3.84}$$

where

$$C_1 = \frac{F_3}{A\alpha_1} \left[1 - \frac{(A\alpha_1 + F_4)(2 - \alpha_1 F_1)}{(2 - \alpha_1 F_1)F_4 + 2A\alpha_1 F_5} \right] \tag{3.85}$$

$$C_2 = \frac{-2F_3(A\alpha_1 + F_4)}{(2 - \alpha_1 F_1)F_4 + 2A\alpha_1 F_5} \tag{3.86}$$

$$A = \sqrt{\frac{F_1^2}{4} + F_2} \tag{3.87}$$

$$F_1 = \frac{\eta_f \rho_{nf} Re}{\eta_{nf} \rho_f} \qquad F_2 = \frac{\sigma_{nf} \eta_f M^2}{\sigma_f \eta_{nf}} + \frac{1}{Da} \qquad F_3 = \frac{\eta_f P}{\eta_{nf} F_2} \tag{3.88}$$

$$F_4 = e^{\frac{F_1}{2}} \left[Sinh(A) \left(1 + \alpha_2 \frac{F_1}{2} \right) + A\alpha_2 Cosh(A) \right] \tag{3.89}$$

$$F_5 = e^{\frac{F_1}{2}} \left[Cosh(A) \left(1 + \alpha_2 \frac{F_1}{2} \right) + A\alpha_2 Sinh(A) \right] \tag{3.90}$$

3.3.2 Analytical solution of energy equation

The energy equation (3.43) is solved analytically using the method of variation of constants. In this method, the arbitrary constants that appear in the solution of the homogeneous system are replaced by functions of the independent variable. These functions must be chosen in such a way that the inhomogeneous system is satisfied.

From Eq. (3.43) terms are regrouped and ordered

$$\frac{d^2\theta}{dy^2} - \frac{Pe}{\left(\frac{k_{nf}}{k_f} + Rd\right)} \frac{(\rho C_p)_{nf}}{(\rho C_p)_f} \left(\frac{d\theta}{dy}\right)$$
$$= -\frac{Pr\,Ec}{\left(\frac{k_{nf}}{k_f} + Rd\right)} \left[\frac{\eta_{nf}}{\eta_f} \left(\frac{du}{dy}\right)^2 + M^2 \frac{\sigma_{nf}}{\sigma_f} u^2 + \frac{\eta_{nf}}{\eta_f} \frac{u^2}{Da} \right] \tag{3.91}$$

Using the method of variation of parameters, the homogeneous part is

$$\frac{d^2\theta}{dy^2} - \frac{Pe}{\left(\frac{k_{nf}}{k_f} + Rd\right)} \frac{(\rho C_p)_{nf}}{(\rho C_p)_f} \left(\frac{d\theta}{dy}\right) = 0 \tag{3.92}$$

Considering constant terms

$$F_6 = \frac{Pe}{\left(\frac{k_{nf}}{k_f} + Rd\right)} \frac{(\rho C_p)_{nf}}{(\rho C_p)_f} = \frac{\frac{k_f}{k_{nf}} RePr \frac{(\rho C_p)_{nf}}{(\rho C_p)_f}}{1 + Rd \frac{k_f}{k_{nf}}} \tag{3.93}$$

The Eq. (3.92) remains

$$\frac{d^2\theta}{dy^2} - F_6 \left(\frac{d\theta}{dy}\right) = 0 \tag{3.94}$$

The characteristic equation associated is $m^2 - F_6 m = 0$, so solving for m

$$m_1 = 0 \tag{3.95}$$

$$m_2 = F_6 \tag{3.96}$$

The homogeneous solution is of the form

$$\theta_h = E(e^{m_1 y}) + F(e^{m_2 y}) \tag{3.97}$$

where E and F, are constants. Substituting Eqs. (3.95) and (3.96) into Eq. (3.97), the homogeneous solution becomes

$$\theta_h = E + F(e^{F_6 y}) \tag{3.98}$$

The proposed particular solution is of the form

$$\theta_p = U_1(y) + U_2(y)e^{F_6 y} \tag{3.99}$$

where $U_1(y)$ and $U_2(y)$ are functions of y. Calculating the Wronskian (w), considering $y_1 = 1$, $y_2 = e^{F_6 y}$, $y_1' = 0$ and $y_2' = F_6 e^{F_6 y}$.

$$w = \begin{bmatrix} y_1 & y_2 \\ y_1' & y_2' \end{bmatrix} = \begin{bmatrix} 1 & e^{F_6 y} \\ 0 & F_6 e^{F_6 y} \end{bmatrix} = (1)F_6 e^{F_6 y} - (0)e^{F_6 y} \tag{3.100}$$

$$w = F_6 e^{F_6 y} \tag{3.101}$$

The non-homogeneous part of Eq. (3.91) is

$$f(y) = -\frac{Pr\,Ec}{\left(\frac{k_{nf}}{k_f} + Rd\right)} \left[\frac{\eta_{nf}}{\eta_f}\left(\frac{du}{dy}\right)^2 + M^2 \frac{\sigma_{nf}}{\sigma_f} u^2 + \frac{\eta_{nf}}{\eta_f}\frac{u^2}{Da}\right] \tag{3.102}$$

54

Then by formula, it is considered that

$$U_1(y) = -\int \frac{y_2 f(y)}{w} dy \tag{3.103}$$

$$U_2(y) = \int \frac{y_1 f(y)}{w} dy \tag{3.104}$$

Substituting the values y_1, y_2 and Eqs. (3.101) and (3.102) into Eqs. (3.103) and (3.104), simplifying terms we have

$$U_1(y) = \frac{(\rho C_p)_f}{(\rho C_p)_{nf}} \frac{Ec}{Re} \int \left[\frac{\eta_{nf}}{\eta_f} \left(\frac{du}{dy}\right)^2 + (M^2 \frac{\sigma_{nf}}{\sigma_f} + \frac{\eta_{nf}}{\eta_f} \frac{1}{Da}) u^2 \right] dy \tag{3.105}$$

$$U_2(y) = -\frac{(\rho C_p)_f}{(\rho C_p)_{nf}} \frac{Ec}{Re} \int \left[\left(\frac{\eta_{nf}}{\eta_f} \left(\frac{du}{dy}\right)^2 \right. \right.$$
$$\left. \left. + \left(M^2 \frac{\sigma_{nf}}{\sigma_f} + \frac{\eta_{nf}}{\eta_f} \frac{1}{Da}\right) u^2 \right) e^{-F_6 y} \right] dy \tag{3.106}$$

Therefore, the general solution to the differential equation (3.91) is

$$\theta(y) = \theta_h + \theta_p \tag{3.107}$$

Substituting Eqs. (3.98) and (3.99) into Eq. (3.107), we get

$$\theta(y) = (E + F(e^{F_6 y})) + (U_1(y) + U_2(y)e^{F_6 y})$$
$$= (U_1(y) + E) + (U_2(y) + F)e^{F_6 y} \tag{3.108}$$

Therefore, the general solution for the energy equation is

$$\theta(y) = C_3 + C_4 e^{F_6 y} \tag{3.109}$$

where

$$F_6 = \frac{\frac{k_f}{k_{nf}} RePr \frac{(\rho C_p)_{nf}}{(\rho C_p)_f}}{1 + Rd \frac{k_f}{k_{nf}}} \tag{3.110}$$

$$C_3 = \frac{Ec}{ReA_4} \int \left[\frac{\eta_{nf}}{\eta_f} \left(\frac{du}{dy} \right)^2 + \left(M^2 A_3 + \frac{\eta_{nf}}{\eta_f} \frac{1}{Da} \right) u^2 \right] dy + E \tag{3.111}$$

$$C_4 = \frac{-Ec}{ReA_4} \int \left[\left(\frac{\eta_{nf}}{\eta_f} \left(\frac{du}{dy} \right)^2 + \left(M^2 \frac{\sigma_{nf}}{\sigma_f} + \frac{\eta_{nf}}{\eta_f} \frac{1}{Da} \right) u^2 \right) e^{-F_6 y} \right] dy + F \tag{3.112}$$

$$
\begin{aligned}
\frac{\eta_{nf}}{\eta_f} &\left(\frac{du}{dy} \right)^2 + \left(M^2 \frac{\sigma_{nf}}{\sigma_f} + \frac{\eta_{nf}}{\eta_f} \frac{1}{Da} \right) u^2 \\
&= e^{F_1 y}[F_9 Sinh(2Ay) + F_{10}Sinh^2(Ay) \\
&\quad + F_{11}Cosh^2(Ay)] + e^{\frac{F_1 y}{2}}[F_{12}Sinh(Ay) \\
&\quad + F_{13}Cosh(Ay)] + K_2 F_3^2
\end{aligned}
\tag{3.113}
$$

$$K_1 = \frac{\eta_{nf}}{\eta_f}, \qquad K_2 = M^2 \frac{\sigma_{nf}}{\sigma_f} + \frac{\eta_{nf}}{\eta_f} \frac{1}{Da}, \qquad F_7 = \frac{F_1 C_1}{2} + AC_2,$$

$$F_8 = \frac{F_1 C_2}{2} + AC_1, \qquad F_9 = K_2 C_1 C_2 + K_1 F_7 F_8, \qquad F_{10} = K_2 C_1^2 + K_1 F_7^2, \tag{3.114}$$

$$F_{11} = K_2 C_2^2 + K_1 F_8^2, \qquad F_{12} = 2K_2 F_3 C_1, \qquad F_{13} = 2K_2 F_3 C_2$$

Solving integrals analytically

$$C_3 = \frac{Ec}{ReA_4}(F_{14} + F_{15} + F_{16} + F_3^2 K_2 y) + E \tag{3.115}$$

$$C_4 = \frac{-Ec}{ReA_4}(F_{18} + F_{19} + F_{20} - \frac{F_3^2 K_2}{F_6} e^{-F_6 y}) + F \tag{3.116}$$

where

$$F_{14} = \frac{e^{F_1 y} F_9(-2A\, Cosh[2A\, y] + F_1 Sinh[2A\, y])}{-4\, A^2 + F_1^2} \tag{3.117}$$

$$F_{15} = \frac{e^{F_1 y} \left(\begin{array}{c} (F_{10} + F_{11})(F_1^2 Cosh[2A\, y] - 2A\, F_1 Sinh[2A\, y]) \\ +(4A^2 - F_1^2)(F_{10} - F_{11}) \end{array} \right)}{-8\, A^2 F1 + 2\, F1^3} \tag{3.118}$$

F_{16}
$$= \frac{2\, e^{\frac{F_1 y}{2}}\left((-2A\, F_{12} + F_1\, F_{13})Cosh[A\, y] + (F_1\, F_{12} - 2A\, F_{13})Sinh[A\, y]\right)}{-4\, A^2 + F_1^2} \qquad (3.119)$$

$$F_{17} = F_1 - F_6 \qquad (3.120)$$

$$F_{18} = \frac{e^{(F_{17})y}F_9(-2A\, Cosh[2A\, y] + (F_{17})Sinh[2A\, y])}{-4\, A^2 + (F_{17})^2} \qquad (3.121)$$

F_{19}
$$= \frac{e^{(F_{17})y}\left(\begin{array}{c}(F_{10} - F_{11})(4A^2 - (F_{17})^2) + (F_{10} + F_{11})\,(F_{17})\,(F_1 Cosh[2A\, y]\\ -F_6 Cosh[2A\, y] - 2A\, Sinh[2A\, y])\end{array}\right)}{2\,(F_{17})(-2A + F_{17})(2A + F_{17})} \qquad (3.122)$$

$$F_{20} = \frac{2\, e^{\frac{1}{2}(F_1 - 2F_6)y}\left(\begin{array}{c}(-2A\, F_{12} + F_{13}(F_1 - 2F_6))Cosh[A\, y]\\ +(F_1 F_{12} - 2\,(AF_{13} + F_{12}F_6))Sinh[A\, y]\end{array}\right)}{(-2\, A + F_1 - 2F_6)(2\, A + F_1 - 2F_6)} \qquad (3.123)$$

The terms E and F in equations (3.115) and (3.116), are integration constants and are resolved by considering the third-type thermal boundary conditions, Eqs. (3.44) and (3.45). These relationships generate a system of equations, Eqs. (3.124) and (3.125), to find the constant values E and F.

$$\frac{k_{nf}}{k_f}\frac{d}{dy}[(C_3 + E) + (C_4 + F)e^{F_6 y}]_{y=0}$$
$$- Bi_1\left([(C_3 + E) + (C_4 + F)e^{F_6 y}]_{y=0} - 1\right) = 0 \qquad (3.124)$$

$$\frac{k_{nf}}{k_f}\frac{d}{dy}[(C_3 + E) + (C_4 + F)e^{F_6 y}]_{y=1}$$
$$+ Bi_2\left([(C_3 + E) + (C_4 + F)e^{F_6 y}]_{y=1}\right) = 0 \qquad (3.125)$$

The *Solve* command of the *Mathematica* software was used to determine the constant values of E and F. The complete solution is not shown here, because the results are too extensive.

3.3.3 Model validation

The validation of the mathematical model was carried out by comparing the current analytical results with the analytical results reported by Ibáñez et al. [22] and the numerical results of López et al. [20] for Al_2O_3/H_2O nanofluid in the limit case when $Da \to \infty$ (absence of porous medium) and when both the radiative effects and the buoyancy force were negligible. An excellent agreement was found, which gives us reliability in the use of the current model. The comparison of results under same conditions is presented in Table 3.1.

Notice that in the absence of porous medium, the current mathematical model exactly coincides with the analytical model reported by Ibáñez et al. [22]. Furthermore, the mathematical model has been validated using the numerical results presented by Ibáñez et al. [27] in presence of porous medium. The effects of a porous medium were considered using a Darcy number $Da = 1$. These results are detailed in Table 3.2.

Table 3.1 *Comparison of present analytical results with previous results [20,22], for the limit case ($Da \to \infty$) when Re=1, Ec=1, P=1, M=0.6, α=0.1, Pr =1, Rd =0, Bi =1, ϕ=0.1.*

y	Velocity			Temperature			Local Entropy		
	Ibáñez et al. [22]	López et al. [20]	Present	Ibáñez et al. [22]	López et al. [20]	Present	Ibáñez et al. [22]	López et al. [20]	Present
0.0	0.031333	0.031333	0.031333	0.790470	0.790477	0.790477	0.082018	0.082020	0.082018
0.1	0.060388	0.060388	0.060388	0.773502	0.773509	0.773509	0.066944	0.066945	0.066944
0.2	0.084642	0.084642	0.084642	0.754483	0.754491	0.754491	0.054097	0.054099	0.054097
0.3	0.103686	0.103686	0.103686	0.733490	0.733499	0.733499	0.044022	0.044024	0.044022
0.4	0.117046	0.117046	0.117046	0.710570	0.710579	0.710579	0.037643	0.037645	0.037643
0.5	0.124179	0.124179	0.124179	0.685725	0.685735	0.685735	0.036411	0.036414	0.036411
0.6	0.124459	0.124458	0.124458	0.658895	0.658905	0.658905	0.042529	0.042532	0.042529
0.7	0.117167	0.117167	0.117167	0.629927	0.629939	0.629939	0.059268	0.059271	0.059268
0.8	0.101483	0.101482	0.101482	0.598543	0.598555	0.598555	0.091457	0.091461	0.091457
0.9	0.076463	0.076462	0.076462	0.564279	0.564293	0.564293	0.146250	0.146255	0.146250
1	0.041032	0.041032	0.041032	0.526421	0.526436	0.526436	0.234386	0.234394	0.234386

Table 3.2 *Comparison of present analytical results with previous results [27], considering a porous medium ($Da = 1$) and the Forchheimer term ($F = 0$), when Re=1, Ec=1, P=1, M=1, α=0.1, Pr =1, Rd =0, Bi =1, ϕ=0.1.*

y	Velocity		Temperature		Local Entropy	
	Ibáñez et al. [27]	Present	Ibáñez et al. [27]	Present	Ibáñez et al. [27]	Present
0.0	0.0273238	0.0273238	0.788109	0.788109	0.0658996	0.0658996
0.1	0.0523923	0.0523923	0.77106	0.77106	0.0551702	0.0551702
0.2	0.0729137	0.0729137	0.752118	0.752118	0.0481525	0.0481525
0.3	0.0887695	0.0887695	0.73129	0.73129	0.0442859	0.0442859
0.4	0.0997472	0.0997472	0.708541	0.708541	0.0433997	0.0433997
0.5	0.105527	0.105527	0.683802	0.683802	0.0458289	0.045829
0.6	0.105664	0.105664	0.656963	0.656963	0.0526245	0.0526246
0.7	0.0995693	0.0995693	0.627864	0.627864	0.0659106	0.0659106
0.8	0.0864824	0.0864825	0.596266	0.596266	0.0894792	0.0894792
0.9	0.0654415	0.0654415	0.561814	0.561814	0.12978	0.12978
1	0.0352445	0.0352445	0.523968	0.523968	0.197596	0.197596

3.4 THERMOPHYSICAL PROPERTY CORRELATIONS

The correlations used to determine the effective properties of Al_2O_3/water nanofluid are shown in Table 3.3. In order to study the effect of uncertainty in the nanofluid thermophysical properties on heat transfer and entropy generation, several empirical and semi-empirical correlations from the literature have been considered. Different authors [42-50] have determined that viscosity and thermal conductivity are the properties with the greatest influence on the behavior of nanofluids. Thus, the present study focuses on the uncertainties of these two properties. Tables 3.4 and 3.5 present the correlations of dynamic viscosity and thermal conductivity used in the current uncertainty study.

Table 3.3 *Correlations of thermo-physical properties of Al_2O_3/water nanofluid.*

Property	Author	Correlation
Density	Pak-Cho [42-45]	$\dfrac{\rho_{nf}}{\rho_f} = (1-\phi) + \phi\dfrac{\rho_s}{\rho_f}$
Heat capacitance	Bourantas [42-45]	$\dfrac{(\rho C_p)_{nf}}{(\rho C_p)_f} = (1-\phi) + \phi\dfrac{(\rho C_p)_s}{(\rho C_p)_f}$
Dynamic viscosity	Brinkman [42-45]	$\dfrac{\eta_{nf}}{\eta_f} = \dfrac{1}{(1-\phi)^{2.5}}$
Thermal conductivity	Maxwell [42-45]	$\dfrac{k_{nf}}{k_f} = \dfrac{k_s + 2k_f + 2\phi(k_s + k_f)}{k_s + 2k_f - \phi(k_s - k_f)}$
Electrical conductivity	Maxwell [41-44]	$\dfrac{\sigma_{nf}}{\sigma_f} = 1 + \dfrac{3\phi\left(\dfrac{\sigma_s}{\sigma_f} - 1\right)}{\left(\dfrac{\sigma_s}{\sigma_f} + 2\right) - \phi\left(\dfrac{\sigma_s}{\sigma_f} - 1\right)}$

Table 3.4 *Semi-empirical and empirical correlations of dynamic viscosity.*

	Model	Correlation	Aplication
Semi-empirical	Brinkman [42-45]	$\dfrac{\eta_{nf}}{\eta_f} = \dfrac{1}{(1-\phi)^{2.5}}$	Spherical nanoparticles
	Lundgren [43]	$\dfrac{\eta_{nf}}{\eta_f} = \dfrac{1}{(1-2.5\phi)}$	Spherical nanoparticles
	Saito [43]	$\dfrac{\eta_{nf}}{\eta_f} = 1 + \left(\dfrac{2.5}{(1-\phi)}\right)\phi$	Spherical nanoparticles
Empirical	Wang/Maiga [43, 45]	$\dfrac{\eta_{nf}}{\eta_f} = 1 + 7.3\phi + 123\phi^2$	Al_2O_3 spherical nanoparticles
	Pak-Cho [43, 46, 50]	$\dfrac{\eta_{nf}}{\eta_f} = 1 + 39.11\phi + 533.9\phi^2$	Al_2O_3 spherical nanoparticles
	Chandrasekar [43, 47]	$\dfrac{\eta_{nf}}{\eta_f} = 1 + 1631\left(\dfrac{\phi}{1-\phi}\right)^{2.8}$	Al_2O_3 spherical nanoparticles

Here the correlation that is obtained from other correlation with the addition of new physical effects has been named semi-empirical or theoretical correlation while the correlation obtained only from experimental measurements has been named empirical or experimental correlation.

The semi-empirical or theoretical correlations can usually be used to determine the properties of different types of nanofluids. However, the empirical or experimental correlations can usually be used for only one type of nanofluid.

Table 3.5 *Semi-empirical and empirical correlations of thermal conductivity*

	Model	Correlation	Aplication
Semi-empirical	Maxwell [42-45]	$$\frac{k_{nf}}{k_f} = \frac{k_s + 2k_f + 2\phi(k_s + k_f)}{k_s + 2k_f - \phi(k_s - k_f)}$$	Spherical nanoparticles
	Bruggeman [42, 45]	$$\frac{k_{nf}}{k_f} = \frac{1}{4}\left[(3\phi - 1)\frac{k_s}{k_f} + (2 - 3\phi)\right] + \frac{k_f}{4}\sqrt{\Delta}$$ $$\Delta = (3\phi - 1)^2 \left(\frac{k_s}{k_f}\right)(\frac{k_s}{k_f})^2 + (2 - 3\phi)^2 + 2(2 + 9\phi - 9\phi^2)\frac{k_s}{k_f}$$	Spherical nanoparticles
	Singh [45, 48]	$$\frac{k_{nf}}{k_f} = 1 + 4\phi$$	Spherical nanoparticles
Empirical	Timofeeva [43,49]	$$\frac{k_{nf}}{k_f} = 1 + 3\phi$$	Al_2O_3 spherical nanoparticles
	Pak-Cho [43, 46, 50]	$$\frac{k_{nf}}{k_f} = 1 + 7.47\phi$$	Al_2O_3 spherical nanoparticles

The Einstein-Barchelor (Ec. 2.38) and Hamilton-Crosser (Ec. 2.30) relationships are used to consider the effect of the nanoparticle shape using the sphericity values a, b and and ψ according to the nanoparticle shape, where $s = 3/\psi$, (see Table 3.6).

Table 3.6 *Correlations that consider the nanoparticle shape for Al_2O_3.*

Nanoparticle shapes	Dynamic viscosity Einstein-Batchelor [42-45] $$\frac{\eta_{nf}}{\eta_f} = (1 + a\phi + b\phi^2)$$		Thermal conductivity Hamilton-Crosser [42-45] $$\frac{k_{nf}}{k_f} = \frac{k_s + (s-1)k_f + (s-1)\phi(k_s + k_f)}{k_s + (s-1)k_f - \phi(k_s - k_f)}$$
Spherical	$a = 2.5$	$b = 6.2$	$\psi = 1$
Blade	$a = 14.6$	$b = 123.3$	$\psi = 0.36$
Brick	$a = 1.90$	$b = 471.4$	$\psi = 0.81$
Platelet	$a = 37.1$	$b = 612.6$	$\psi = 0.52$
Cylinder	$a = 13.5$	$b = 904.4$	$\psi = 0.62$

Figs. 3.2 and 3.3 show the variations of effective viscosity and effective thermal conductivity as a function of the nanoparticle volume fraction ϕ for different shapes of Al_2O_3 nanoparticles, respectively. Fig. 3.2 shows that the highest values of the nanofluid viscosity are provided for the platelet shape followed by cylinder, blade and brick shapes while the spherical shape provides the lowest viscosity values. The previous viscosity sequence corresponds to values of ϕ lower than 0.035 and this sequence changes for values of ϕ greater than 0.035 when the brick shape begins to provide higher viscosity values than the blade shape. In Fig. 3.3, it can be seen that the highest thermal conductivity is obtained for the blade shape followed by the cylinder, platelet, brick and spherical shapes, respectively. This sequence of thermal conductivity values is satisfied for the entire range of explored ϕ values (0.01-0.05). The default value of ϕ used in our calculations is 0.01 (1%).

Figs. 3.4 and 3.5 show the viscosity and thermal conductivity variations as a function of the nanoparticle volume fraction ϕ using different empirical and semi-empirical correlations for the spherical shape of Al_2O_3 nanoparticles in water as a base fluid, respectively. From Fig. 3.4, it is observed that the correlation that provides the highest viscosity values is the Pak-Cho empirical correlation followed by the Wang empirical correlation for the entire domain of explored values of ϕ. On the other hand, the Chandrasekar empirical correlation provides the lowest values of viscosity for small values of ϕ ($\phi<0.025$) while the viscosity values provided by the semi-empirical correlations of Brinkman, Lundgren, Einstein-Batchelor and Saito are the lowest when ϕ is greater than 0.25.

Fig. 3.2 Dynamic viscosity as a function of ϕ for different shapes of Al_2O_3 nanoparticles.
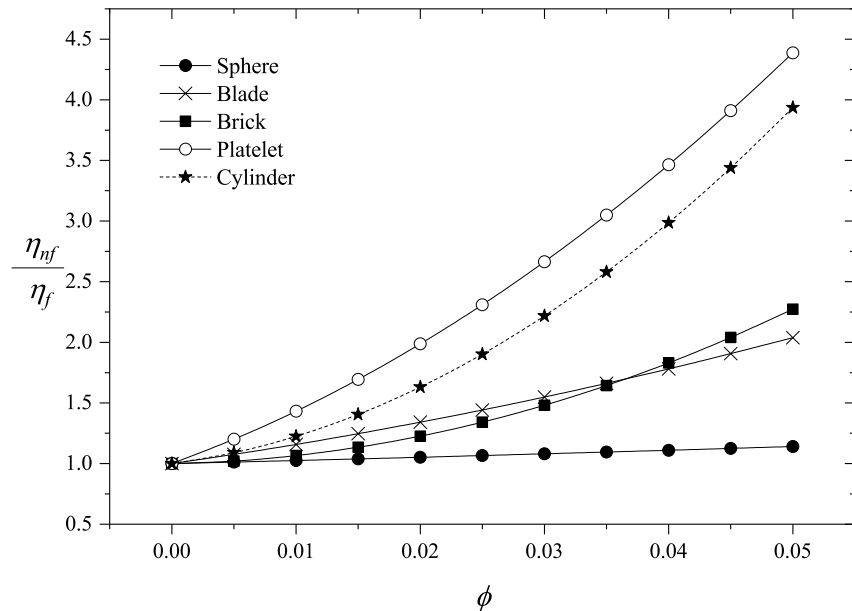
It is noticed that the viscosity values provided by these last four semi-empirical correlations coincide approximately for the entire range of explored values of ϕ. In general, the semi-empirical correlations provide the lowest viscosity values compared to those values provided by the empirical correlations.

Fig. 3.3 *Thermal conductivity as a function of ϕ for different shapes of Al2O3 nanoparticles.*
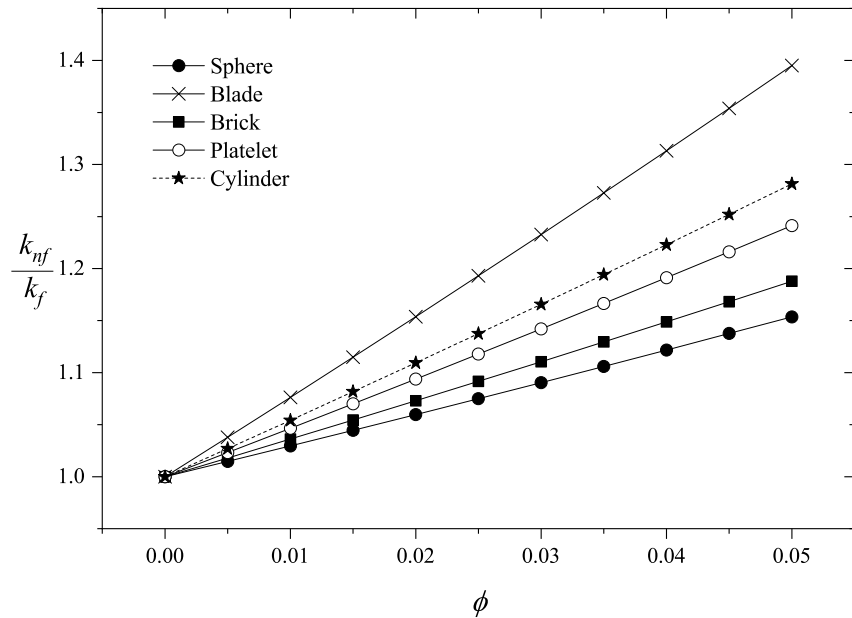
Fig. 3.4 *Dynamic viscosity as a function of ϕ for different correlations (spherical nanoparticles)*
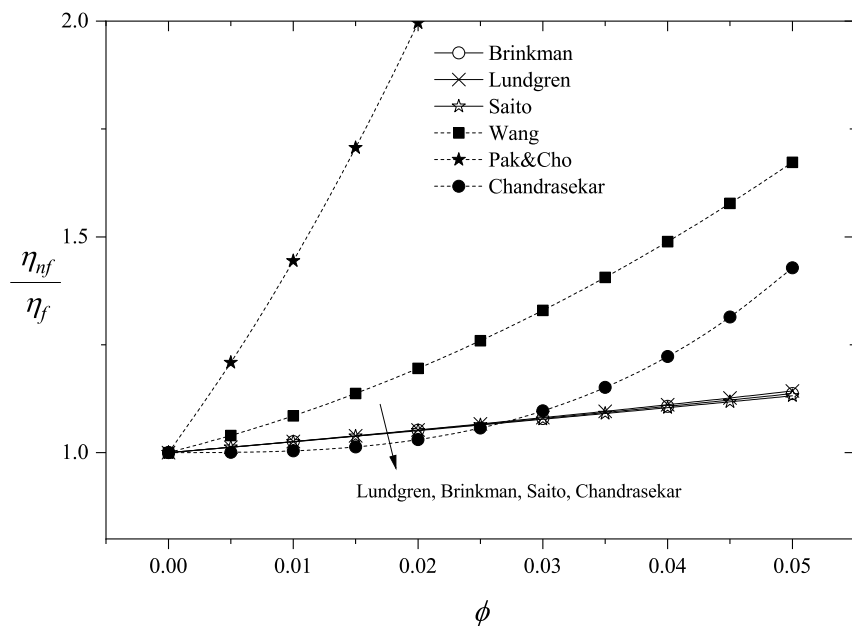
Fig. 3.5 shows that the empirical Pack-Cho correlation predicts the highest conductivity values followed by the semiempirical Sing correlation. The Timofeeva, Maxwell, Bruggeman and Hamilton-Crosser correlations present the lowest values. These lowest values approximately agree except in the case of the Bruggeman correlation that

provides slightly higher values of thermal conductivity when the values of the nanoparticle concentration is greater than 0.03. The above analysis indicates that the largest differences between the estimated values of both dynamic viscosity and thermal conductivity are obtained when the different empirical correlations are used to calculate their values. In addition, the Pack-Cho empirical viscosity correlation and Pack-Cho empirical thermal conductivity correlation provide the highest values of dynamic viscosity and thermal conductivity, respectively.

Fig. 3.5 *Thermal conductivity as a function of ϕ for different correlations (spherical nanoparticles).*
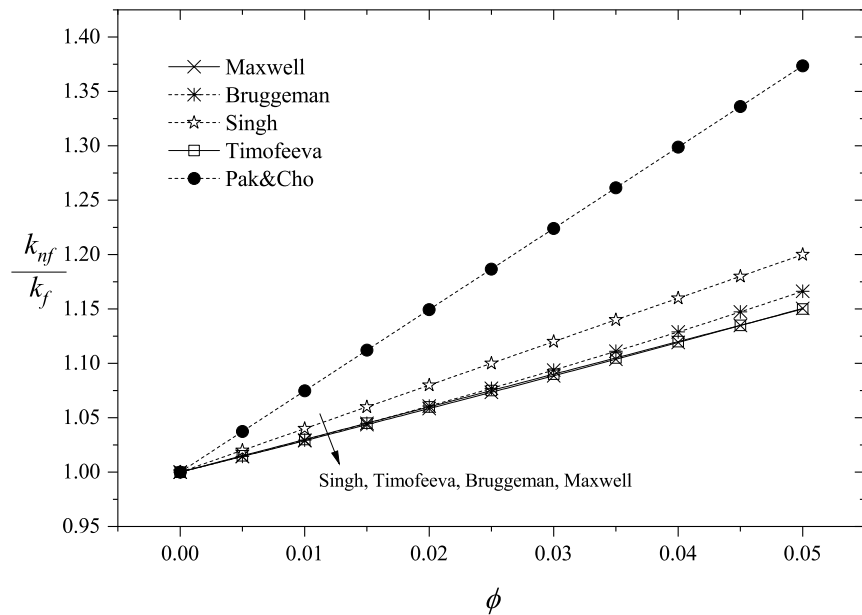
3.5 RESULTS AND DISCUSSION

The effects of both the nanoparticle different shapes and uncertainty in the nanofluid physical properties on the dynamic and thermal behavior of system are analyzed. In particular, the influences on the system optimum operating conditions with minimum entropy generation and maximum heat transfer are investigated.

The section 3.5.1 shows the behavior of Al_2O_3/water nanofluid for different nanoparticle shapes using the correlations of Table 3.6. The impacts of nanoparticle concentration, Darcy number, hydrodynamic slip and Biot number on the velocity, temperature, entropy and Nusselt number are discussed. The investigated value ranges of the parameters are: nanoparticle concentration ϕ (0-0.05), Darcy number Da (1-10), slip parameter α (0-0.1) and Biot number Bi (0-1).

In the sections 3.5.2 to 3.5.4, the effects of different combinations of correlations for the estimation of thermophysical properties of Al$_2$O$_3$/water nanofluid are shown. Fifteen combinations of viscosity and thermal conductivity correlations are considered.

The results are obtained using nine combinations of semiempirical correlations and six combinations of empirical correlations. In this way, the combinations of semiempirical thermal conductivity correlations of Maxwell, Bruggeman and Singh with the semiempirical viscosity correlations of Brinkman, Lundgren and Saito are studied. Moreover, the combinations of the empirical thermal conductivity correlations of Timofeeva and Pak-Cho with the empirical viscosity correlations of Wang, Pak-Cho and Chandraseka are also investigated. At the section 3.5.5, the impacts of solid nanoparticles Al$_2$O$_3$, Cu and TiO$_2$ in water as base fluid on the system optimum operating conditions are reported.

For this chapter the default fixed values $P = 1, \phi = 0.01, M = 1, Bi = 1, Ec = 1, Pr = 1, Rd = 1, Re = 1, Da = 1, \alpha = 0.1$, are considered in the respective figures.

3.5.1 Effects of nanoparticle different shapes

The results considering different shapes of solid nanoparticles for Al$_2$O$_3$/H$_2$O nanofluid are presented in Figs. 3.6-3.18 for five different shapes: spherical, cylindrical, blade, brick, and platelet. In Fig. 3.6, the velocity profiles are presented for two different values of nanoparticle volume fraction. It can be seen that the friction on the microchannel plates causes a decrease in velocity in the regions close to the microchannel plates. It is also shown that the velocity decreases with the increment in the nanoparticle concentration because the amount of nanoparticles within the base fluid increases the viscosity, and consequently, the friction force increases and the flow slows downs. Therefore, the larger the ϕ value, the lower the velocity for all nanoparticle shapes.

When the ϕ value is 0.01, the highest velocity values are reached for spherical nanoparticles followed by brick, blade and cylindrical shapes, respectively, while the lowest velocity values are achieved for platelet shape. This is due to the fact that platelet nanoparticles provide the highest viscosity and hence higher viscous stresses that oppose the movement of nanofluid are presented. A similar sequence is observed when the nanoparticle volume fraction is 5 % ($\phi = 0.05$) with the only difference that the velocity values for the blade shape exceed those values obtained for the brick shape.

Fig. 3.6 *Velocity for different shapes of Al2O3 nanoparticles and two values of φ (0.01,0.05).*
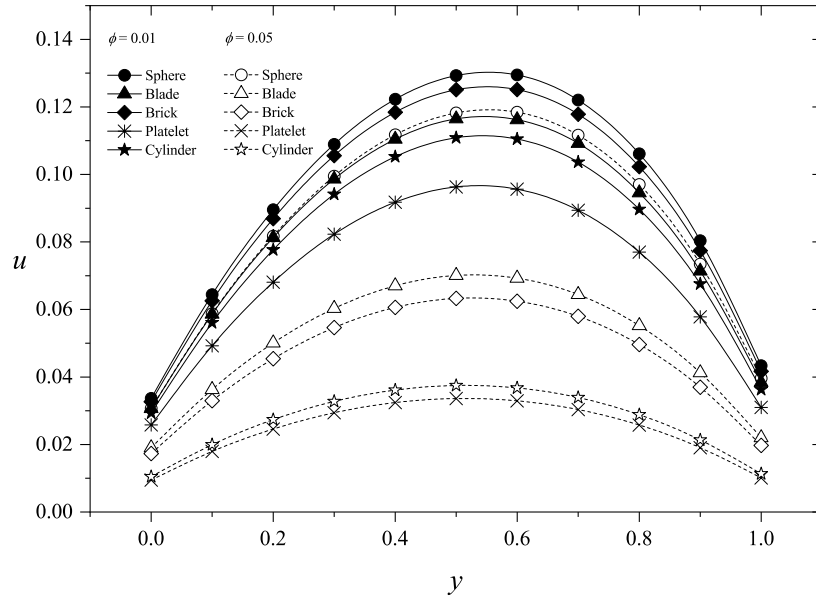
Fig. 3.7 shows the effects of the slip parameter α on the nanofluid velocity profile for different nanoparticle shapes. The increase in the slip parameter causes an increase in velocity due to the decrease in the friction force near the microchannel walls. As α increases, the nanofluid exhibits less adherence to the microchannel plates. When α tends to zero, the non-slip conditions are present, thereby the boundary layer of nanofluid in contact with the microchannel plates has velocity equal to zero. For all nanoparticle shapes, it is observed that the velocity values decrease as the parameter α decreases and vice versa. As in figure 3.6, the highest velocity values are obtained with the spherical shape of nanoparticle and the lowest with the platelet shape for the two explored slip values.

Fig. 3.7 *Velocity for different shapes of Al_2O_3 nanoparticles and two values of α (0.01,1).*
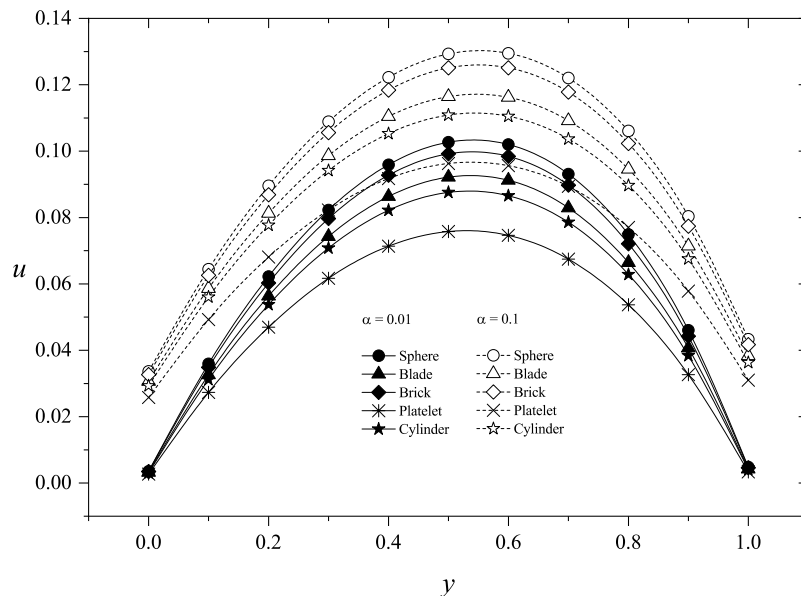
In Fig. 3.8, the influences of Darcy number Da on the nanofluid velocity are shown for different nanoparticle shapes. The existence of porous medium increases the opposition to movement of the nanofluid. From Fig. 3.8, it can be seen that speed increases with increasing Darcy number, this is due to the increase in the porosity of the medium and decrease the friction, increasing the nanofluid motion. The absence of the porous medium is considered when Darcy tends to infinity.

Fig. 3.8 Velocity for different shapes of Al2O3 nanoparticles and two values of Da (1,10). ϕ=0.01
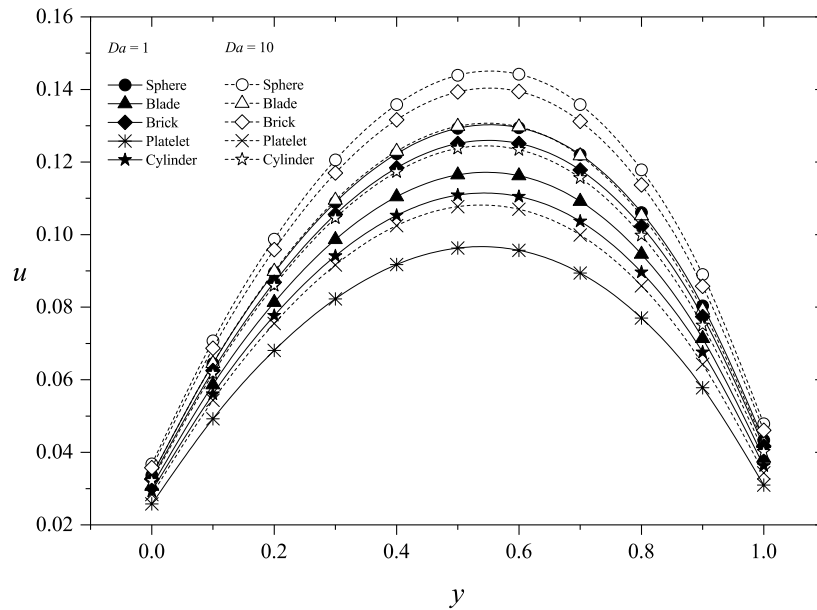
Fig. 3.9 shows that for all nanoparticle shapes the nanofluid temperature in regions near the bottom plate at y = 0 is higher than the temperature in regions near the top plate at y = 1 due to both the convective heating and the injection of hot nanofluid through the bottom hot plate which wars the nanofluid in this region. It is seen that the spherical shape reaches the highest temperature in the bottom plate and the lowest temperature in the top plate while the blade shape has the lowest temperature in the bottom plate and the highest temperature in the top plate. This is in correspondence with the fact that the spherical shape has the lowest thermal conductivity and the highest nanofluid temperature gradient while the blade shape has the highest thermal conductivity and the lowest temperature gradient.

The thermal conductivity of the nanofluid increases when the concentration of nanoparticles increases from 1% to 5% and then there is an increase in heat transport from the hot plate ($y = 0$) to the cold plate ($y = 1$). This causes a reduction in the temperature values near the bottom hot plate for all explored nanoparticle shapes while the opposite occurs near the top cold plate with an increase in the temperature values.

Fig. 3.9
Temperature for different shapes of Al₂O₃ nanoparticles and two values of φ (0.01,0.05).
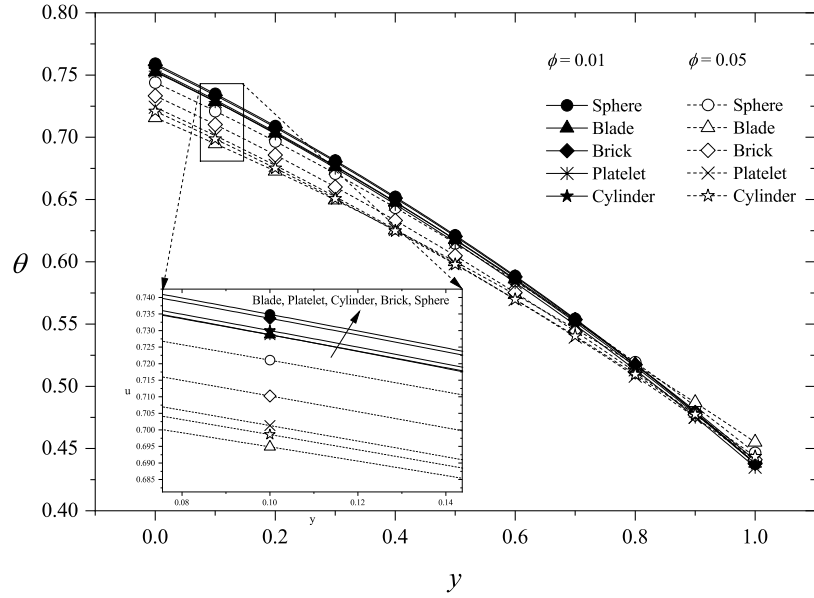
In Fig. 3.10 the behavior of the temperature is shown for different values of Biot number. The Biot number is related to the heat transfer between the nanofluid and the environment through the bottom and top plates of microchannel. If the Biot number increases symmetrically $(Bi_1 = Bi_2)$, the temperature gradient increases with an appreciable decrease of the temperature values in the upper region of microchannel due to the increase in heat transport from the nanofluid to the surrounding environment through the top plate.

Fig. 3.10
Temperature for different shapes of Al₂O₃ nanoparticles and two values of Bi (0.1,1). φ=0.01
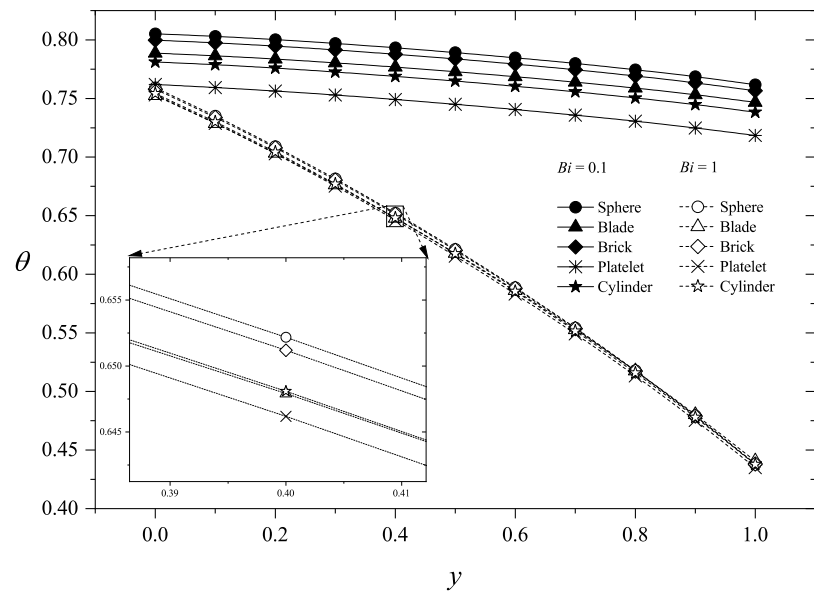
It is also observed that for high values of the Biot number the difference between the temperature values that correspond to each nanoparticle shape tends to disappear in comparison with the results that correspond to lower Biot values. The effects of Darcy number and slip parameter on nanofluid temperature are not significant. For this reason, these behaviors are not presented.

The above velocity and temperature profiles are used to evaluate the heat transfer and calculate the entropy generation considering five different shapes of nanoparticles. In Figure 3.11, the local entropy generation S is presented across the width of microchannel for two values of ϕ. It is observed that there is less entropy production in the lower plate due mainly to the high temperature, which is inversely proportional to entropy. Clearly, the local entropy values for the nanoparticle different shapes depend on the differences in the dynamic viscosity and thermal conductivity that correspond to each nanoparticle shape. The friction of nanofluid in the microchannel plates is greater than in the central zone. Therefore, the irreversibilities due to friction increase in the regions close to the plates while these irreversibilities tend to decrease in the channel center. There is a higher local entropy generation for spherical nanoparticles throughout the entire cross section of microchannel for the two explored values of ϕ. The spherical shape provides greater irreversibility associated to viscous dissipation, Joule heating and Darcy drag due to the high values of both velocity and velocity gradient. On the other hand, the entropy decreases with the nanoparticle concentration due to the increase in the nanofluid dynamic viscosity with the consequent decrease in its velocity and velocity gradient.

Fig. 3.11 Local entropy generation for different shapes of Al$_2$O$_3$ nanoparticles and two values of ϕ (0.01, 0.05).
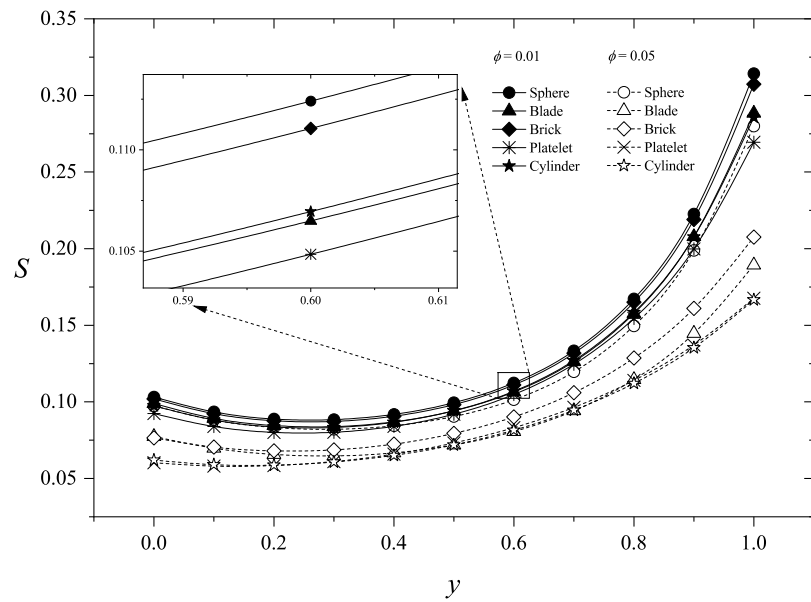
The results of global entropy $< S >$ as a function of the nanoparticle concentration are presented in Fig. 3.12. It is found that when the values of nanoparticle volume fraction increase, the total entropy tends to decrease until it reaches a limit value for all considered nanoparticle shapes. This indicates that optimal values of ϕ are not reached. The platelet shape has the lowest total entropy due to the fact that this shape provides higher viscosity, which results in a lower velocity and velocity gradient (see Figs. 3.6 and 3.7). Therefore, lower values of irreversibilities associated to viscous dissipation, Joule heating and Darcy drag are obtained. The global entropy decreases from 0.133 to 0.088 when the nanofluid concentration increases from 0 to 0.045 for platelet shape. Although the heat transfer contribution by conduction and radiation increases with ϕ, the decrease of viscous dissipation, Joule heating and Darcy drag irreversibilities are dominant and the total entropy decreases.

Fig. 3.12 Global entropy as a function of ϕ for different shapes of Al_2O_3 nanoparticles.
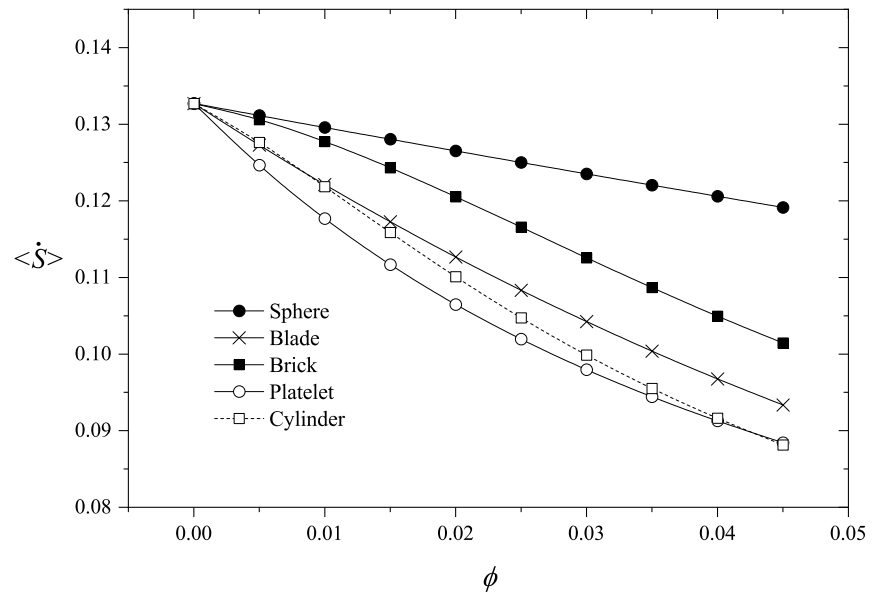
It can be seen from Fig. 3.13 that as the values of the Darcy number increase, the entropy production increases up to a limit value. Here the irreversibility associated with heat flow by conduction and radiation tends to decrease due to the temperature increase, which is inverse to the entropy generation. However, the irreversibility associated to viscous dissipation and Joule heating increases and prevails. The differences obtained between each nanoparticle shape are mainly due to the different viscosity values that correspond to each shape. It is obtained that the shapes with higher viscosity generate lower entropy due to the low nanofluid velocity and velocity gradient.

Fig. 3.13 *Global entropy as a function of Da for different shapes of Al2O3 nanoparticles. φ=0.01*
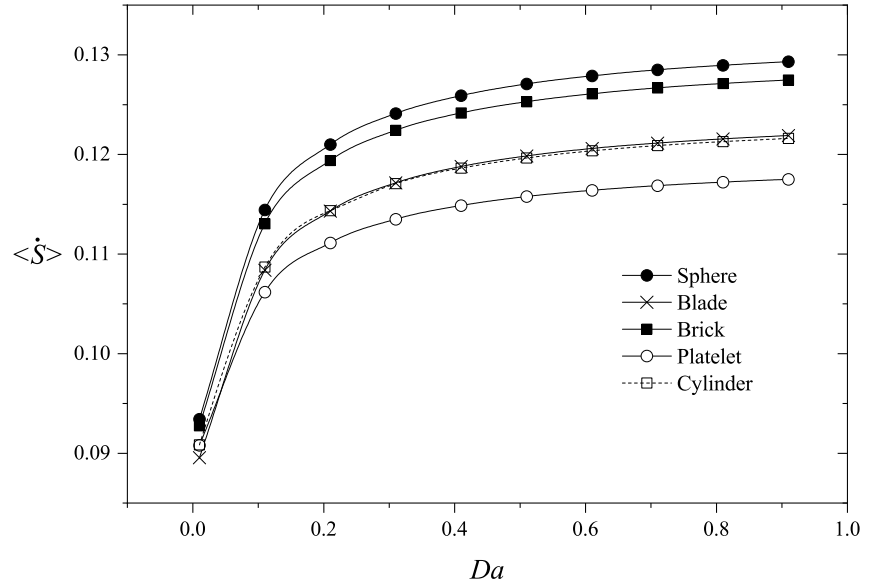
Therefore, when the Darcy number increases from 0 to 0.9, the largest increase of total entropy occurs from 0.093 to 0.129 (38 %) for the spherical shape while the smallest increase of total entropy occurs from 0.091 to 0.117 (28 %) for the platelet shape (see Fig. 3.13). On the other hand, nanoparticle shapes with higher thermal conductivity induce lower average temperature of nanofluid and lower temperature gradient.

Fig. 3.14 *Global entropy as a function of α for different shapes of Al$_2$O$_3$ nanoparticles. φ=0.01, Re=2.*
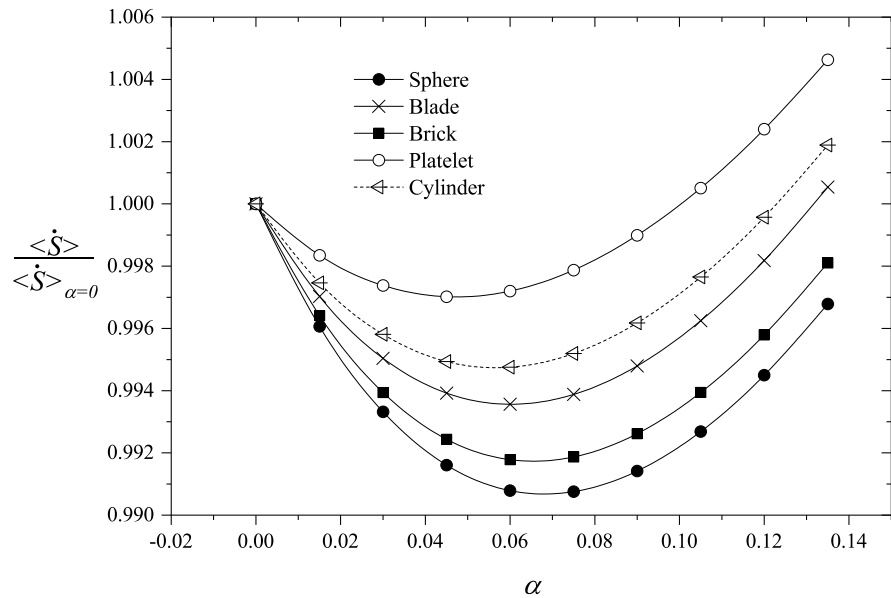
The normalized global entropy production as a function of single α for different nanoparticle shapes is presented in Fig. 3.14. Optimal values of α with minimal entropy generation are reached for all shapes. It can be seen that these optimal values of α shift towards larger values while the corresponding minimum values of normalized global entropy decrease when the nanofluid dynamic viscosity decreases.

Thus, on the one hand, the spherical shape has the lowest normalized entropy followed by the brick, blade, cylinder, and platelet shapes, respectively, and on the other hand, the irreversibility associated with viscous dissipation is higher for the spherical shape. The independent contributions of each irreversibility term show that the greatest contribution is due to the irreversibilities associated with conduction and radiation heat transfer. It is also obtained that irreversibilities due to heat flux $< \dot{S} >_q$, Darcy drag $< \dot{S} >_{Da}$ and Joule heating $< \dot{S} >_J$ increase with α while the irreversibilities due to viscous dissipation $< \dot{S} >_v$ decrease. Irreversibility due to viscous dissipation $< \dot{S} >_v$ tends to decrease and is dominant at lower values of a, due to which the global entropy decreases and then increases.

In Fig. 3.15, the global entropy generation rate normalized by its value at $Bi_1 = 0$ as a function of lower plate Biot number is shown for different nanoparticles shapes. The normalized global entropy reaches a minimum value for a given value of Bi_1 for all explored nanoparticle shapes. As in previous works [25], it is found that the optimal conditions only appear for asymmetric convective heat transfer ($Bi_1 \neq Bi_2$). When Biot numbers are equal, the global entropy always increases and does not present minima.

Fig. 3.15 *Global entropy as a function of Bi_1 for different shapes of Al_2O_3 nanoparticles. $\phi=0.01$, $Bi_2=1$, $Rd=0.1$.*
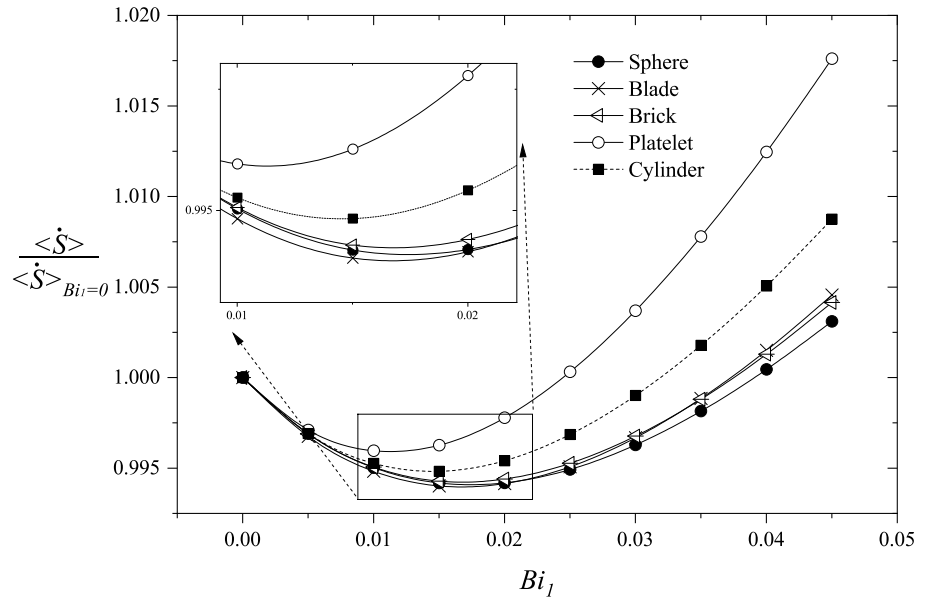
The different entropy contributions as function of Bi_1 indicate that only the irreversibilities due to heat transfer $< \dot{S} >_q$ increases with Bi_1 while the irreversibilities due to viscous dissipation $< \dot{S} >_v$, Darcy drag $< \dot{S} >_{Da}$ and Joule heating $< \dot{S} >_J$ decrease. It is observed that the platelet shape has the highest normalized global entropy values while the spherical shape shows the lowest normalized global entropy values.

Furthermore, the spherical shape presents the highest value of the optimal Biot number followed by the brick, blade, cylindrical and platelet shapes, respectively.

In Figs. 3.16-3.18, the results related to internal heat transfer denoted by the Nusselt number are presented for different nanoparticle shapes. The direction of heat flux is from the bottom hot plate to the top cold plate. The heat transport from the bottom hot plate to the nanofluid decreases when the nanofluid temperature increases. However, the heat transport from the nanofluid to the cold plate increases.

In Fig. 3.16 it can be seen that the heat transport through the hot plate at $y = 0$ increases with the nanoparticle volume fraction for all explored nanoparticle shapes due to the increase of thermal conductivity. The blade shape has the highest heat transport for the entire range of explored ϕ values due to its higher thermal conductivity while the platelet shape has the lowest Nu number for nanoparticle concentration values between 0 % and 4 %. For concentrations greater than 4%, the lowest Nu value corresponds to the brick shape.

Figure 3.17 shows that it is possible to reach maximum heat transfer conditions for all nanoparticle shapes at upper cold plate when the slip parameter is varied. The optimal slip values with maximum heat transfer or maximum Nu number practically do not vary for each nanoparticle shape. The blade shape shows the highest Nu values with a maximum value equal to 5.13 while the platelet shape shows the lowest Nu values with a maximum value equal to 5. On the other hand, Fig. 3.18 shows that the Nusselt number always decreases with the slip parameter at lower hot plate for all nanoparticle shapes. Once more, the blade shape provides the highest values of Nu.

Fig. 3.16 Nusselt number at y=1 as a function of ϕ for different shapes of Al$_2$O$_3$ nanoparticles.
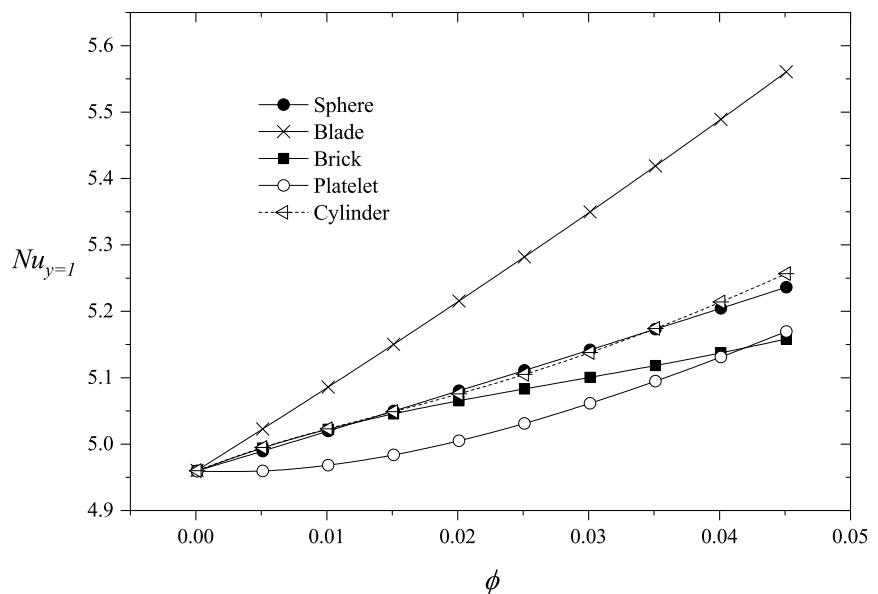
Fig. 3.17 *Nusselt number at y=1 as a function of α for different shapes of Al₂O₃ nanoparticles. φ=0.01, M=0.1, Da=10.*
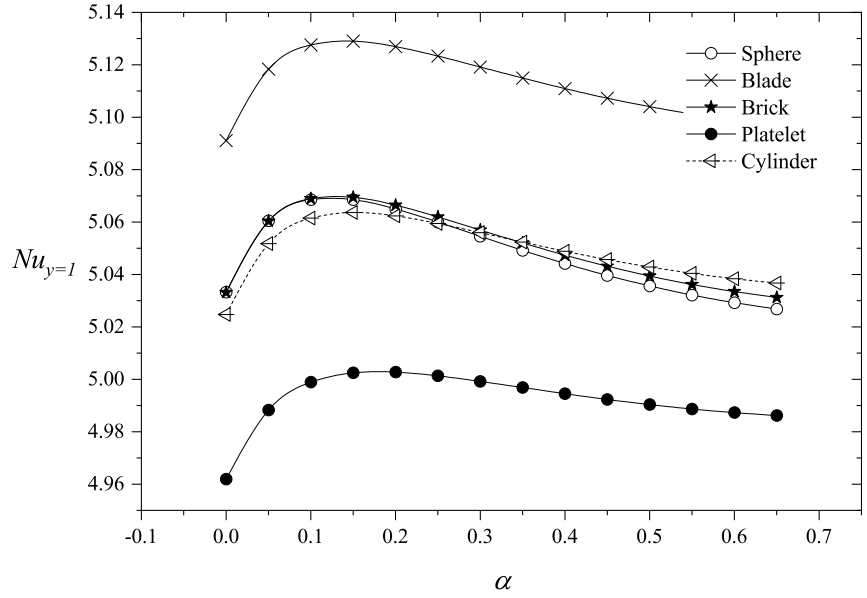
Fig. 3.18 *Nusselt number at y=0 as a function of α for different shapes of Al₂O₃ nanoparticles. φ=0.01, M=0.1, Da=10.*
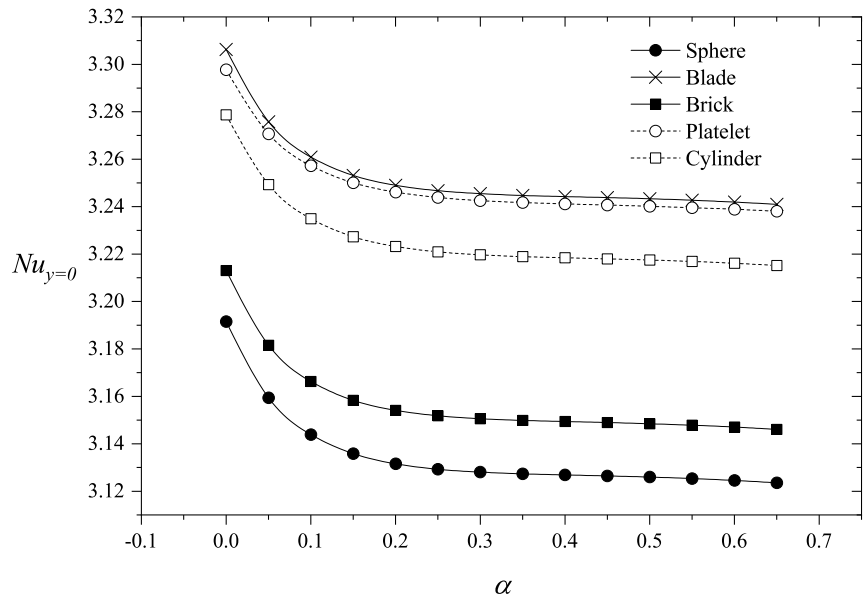
3.5.2 Effects of uncertainty in thermophysical properties on velocity and temperature profiles

Different combinations of dynamic viscosity and thermal conductivity correlations of nanofluid are used for the uncertainty analysis. Table 3.7 contains the combinations from SM1 to SM9 formed with semi-empirical correlations and Table 3.8 contains the combinations from EM1 to EM6 formed with empirical correlations. In Figs. 3.19A and 3.19B, the different velocity profiles are observed for all studied combinations. Models with semi-empirical correlations (Fig. 3.19A) show less variation between them compared to the empirical models (Fig. 3.19B). The models that provide similar viscosity values have velocity profiles superimposed on each other.

As previously stated, the models that predict the lowest viscosity produce the highest velocity in the nanofluid. In this way, the Saito viscosity correlation predicts the highest velocity values for the SM7, SM8 and SM9 semi-empirical combinations while the Chandrasekar viscosity correlation estimates the highest velocity values for the EM5 and EM6 empirical combinations. Note that, in Fig. 3.19B, models with empirical correlations are compared with the most common semi-empirical combination (Ref. SM1). This is applied to all figures with empirical combinations of the present subsection.

Table 3.7 *Combinations of semi-empirical correlations for Al_2O_3.*

Model	Dynamic viscosity	Thermal conductivity
SM1	Brinkman	Maxwell
SM2	Brinkman	Bruggeman
SM3	Brinkman	Singh
SM4	Lundgren	Maxwell
SM5	Lundgren	Bruggeman
SM6	Lundgren	Singh
SM7	Saito	Maxwell
SM8	Saito	Bruggeman
SM9	Saito	Singh

Table 3.8 *Combinations of empirical correlations for Al$_2$O$_3$.*

Model	Dynamic viscosity	Thermal conductivity
EM1	Wang/Maiga	Timofeeva
EM2	Wang/Maiga	Pak-Cho
EM3	Pak-Cho	Timofeeva
EM4	Pak-Cho	Pak-Cho
EM5	Chandrasekar	Timofeeva
EM6	Chandrasekar	Pak-Cho

Figs. 3.20A and 3.20B show the different temperature profiles for each studied combination. The Fig. 3.20A presents the temperature profiles for different models of semiempirical correlations of viscosity and thermal conductivity while the Fig. 3.20B illustrates the temperature profiles for different models of empirical correlations of viscosity and thermal conductivity.

The differences between the predicted temperature values by each model are mainly due to the different correlations of thermal conductivity present in each of them. In this way, the SM1, SM4 and SM7 combinations with the semiempirical Maxwell correlation of thermal conductivity have the highest temperature of nanofluid due to the low thermal conductivity while the SM3, SM6 and SM9 combinations with Singh correlation have the lowest temperature values. From Fig. 3.20A, it can be noticed that there is no significant difference in the temperature values estimated by the different semi-empirical models.

In the case of the empirical models (EM1-EM6) presented in Fig. 3.20B, a lower temperature values are obtained compared to the semi-empirical models due mainly to their high values of the nanofluid viscosity with the consequent decrement in the velocity and velocity gradient. This indicates that the effects of both thermal conductivity and dynamic viscosity on the temperature profiles can be observed for empirical models.

The results reveal that the temperature decreases when the thermal conductivity increases and, on the other hand, it increases when the dynamic viscosity decreases. For the empirical models, unlike the semi-empirical ones, there is a difference between the temperature values estimated by each model.

Fig. 3.19
Nanofluid velocity profiles for different combinations of A) semi-empirical correlations and B) empirical correlations of viscosity and thermal conductivity. $\phi=0.01$.
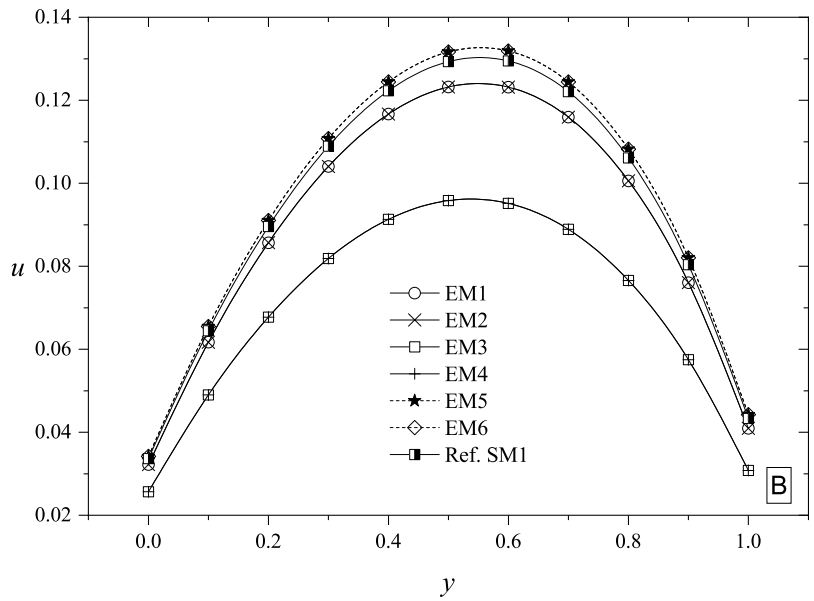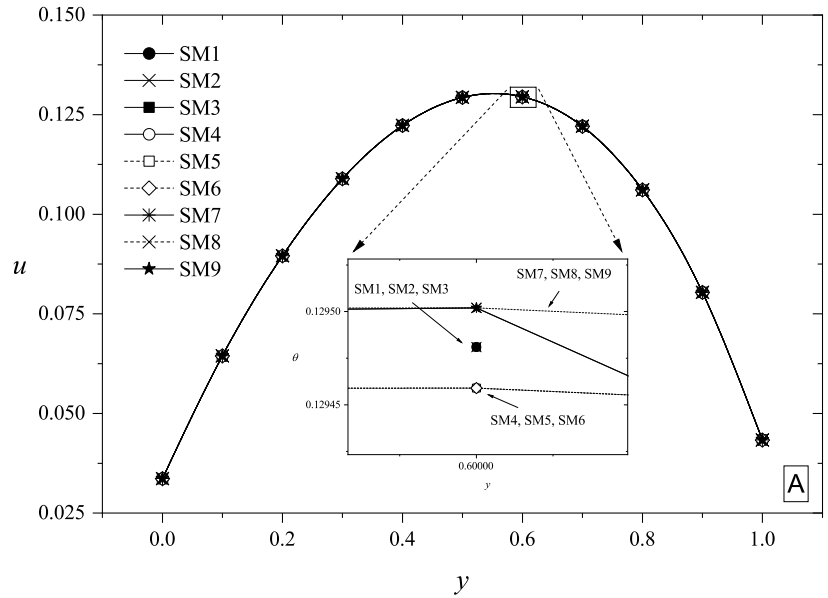
Fig. 3.20
Nanofluid temperature profiles for different combinations of A) semi-empirical correlations and B) empirical correlations of viscosity and thermal conductivity. $\phi=0.01$.
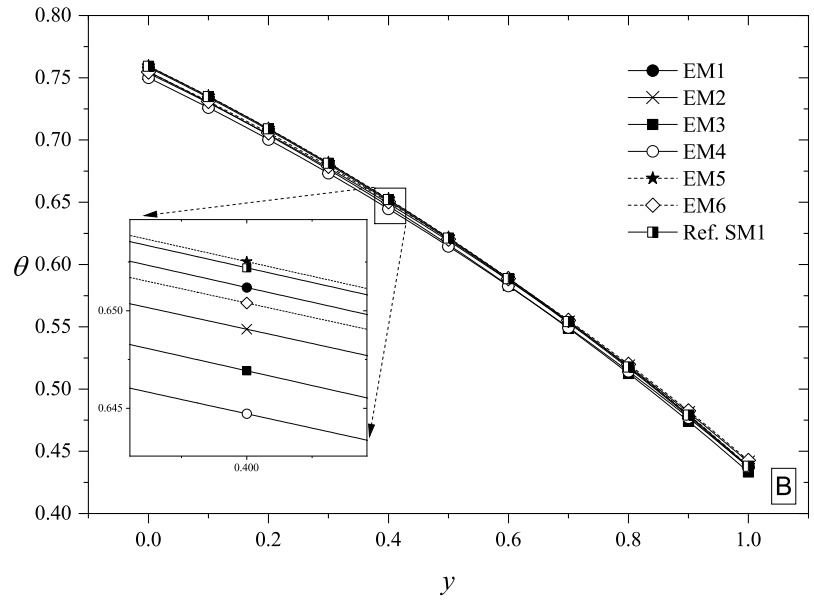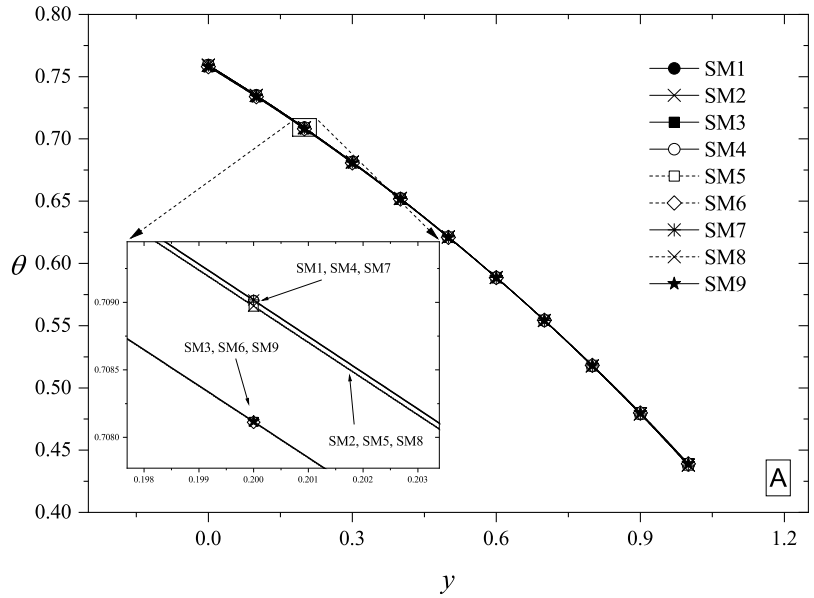
3.5.3 Effects of uncertainty in thermophysical properties on entropy production

The effects of the semi-empirical and empirical models on the global entropy production are presented in Figs. 3.21-3.26. Fig. 3.21 shows the total entropy as a function of nanoparticle volume fraction for the nine combinations of semi-empirical correlations. It is observed that the SM3, SM6 and SM9 models have the lowest values of global entropy due mainly to the Singh thermal conductivity correlation, which predicts higher thermal conductivity values compared to the other models. Therefore, lower temperature gradient is obtained and the entropy production associated to heat flux by conduction and radiation decreases. The global entropy decreases from 0.133 to the smallest value of 0.116 when the nanofluid concentration increases from 0 to 0.045 for SM6 model.

Fig. 3.21 Global entropy as a function of ϕ for combinations with semi-empirical correlations.
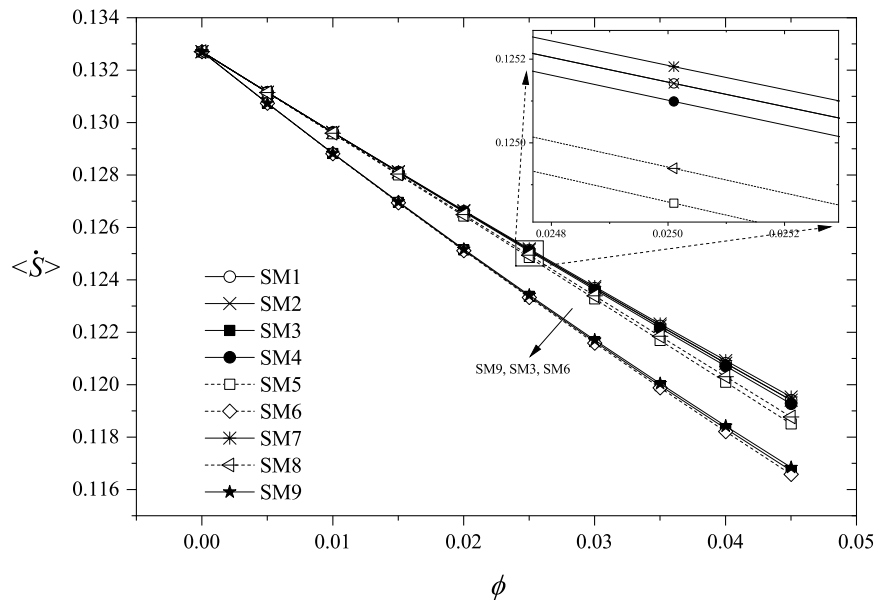
The effects of the models with empirical correlations on the global entropy are presented in Fig. 3.22. There is higher entropy for small values of nanoparticle concentration. The EM5 model presents the largest entropy values. This is caused by the Timofeeva correlation, which provides low values of thermal conductivity for volume fraction values below 5 % and hence the temperature gradient increases with the consequent increment in irreversibilities associated to conduction and radiation heat flux. On the other hand, the smallest entropy values correspond to the EM4 model due to the Pak-Cho viscosity correlation, which predicts a high dynamic viscosity with the consequent decrement of velocity and velocity gradient.

Here the irreversibility contributions associated to friction and Joule heating decrease. When the concentration of nanoparticles is 0.045, the largest decrease in total entropy occurs from 0.115 in the M5 model to 0.082 in the EM4 model, that is, approximately 28 %.

Fig. 3.22 *Global entropy as a function of ϕ for combinations with empirical correlations.*
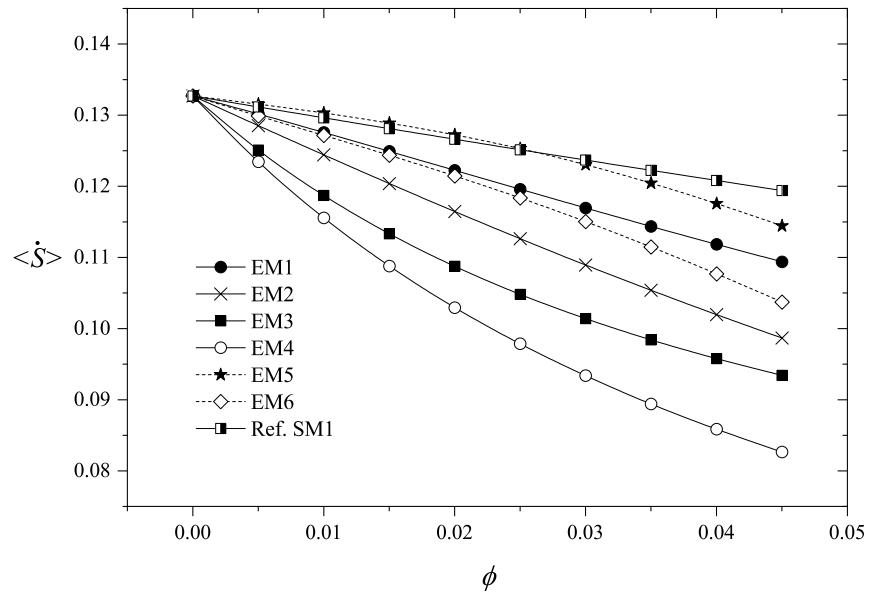
The effects of uncertainty in thermo-physical properties of nanofluid on the system optimal operating conditions with minimal entropy are analyzed in Figs. 3.23-3.26. Figure 3.23 shows the global entropy as a function of hydrodynamic slip for the nine models of semi-empirical correlations of viscosity and thermal conductivity explored. It is observed that the optimal value of slip parameter of 0.07 is approximately the same for all the studied models. The changes in global entropy are mainly due to the different estimations of thermal conductivity while the effect of viscosity correlations is very small because the semiempirical viscosity correlations provide similar viscosity values (see Fig. 3.4). In this way, the Bruggeman and Maxwell thermal conductivity correlations that predict lower values of nanofluid thermal conductivity and higher temperature gradient have higher entropy values while the opposite happens with the Singh thermal conductivity correlation. Thus, SM3, SM6 and SM9 models have the lowest values of global entropy.

Figure 3.24 shows the normalized global entropy as a function of hydrodynamic slip for the six combinations of empirical correlations of viscosity and thermal conductivity. It is found that both the normalized minimum entropy values and the optimal slip values change depending of the used model. These changes are mainly due to the irreversibility associated with viscous dissipation, which is dominant. The Pak-Cho

viscosity correlation in EM3 and EM4 models estimates the highest viscosity (see Fig. 3.4), thus a lower velocity and velocity gradient are obtained (see Fig. 3.19B). This causes that the irreversibilities associated to viscous dissipation, Joule heating and Darcy drag decrease and the smallest non-normalized global entropy values that correspond to the largest normalized global entropy values are obtained. Once more, the EM3 model show the smallest non-normalized global entropy values or largest normalized global entropy values.

Fig. 3.23 *Global entropy as a function of α for combinations with semi-empirical correlations. φ=0.01, Re=2.*
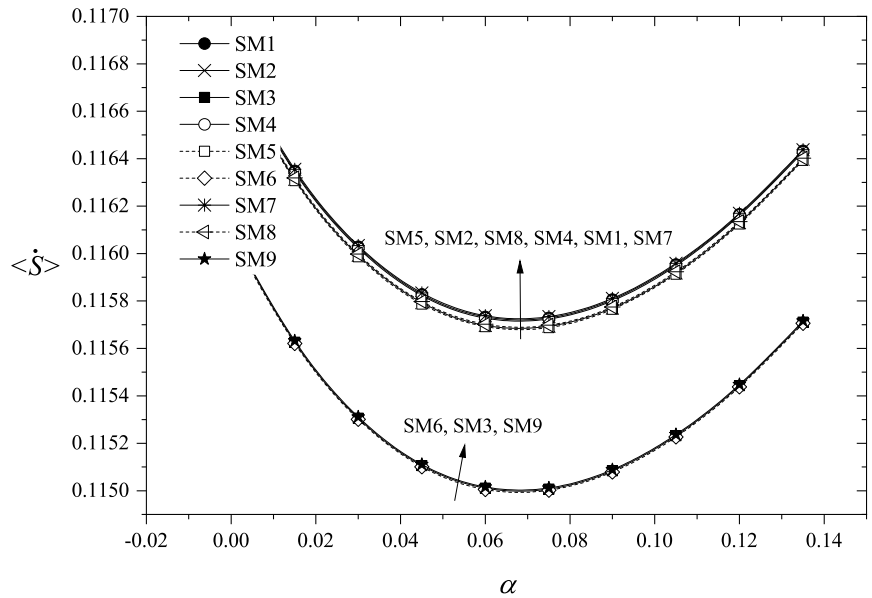
Fig. 3.24 *Global entropy as a function of α for combinations with empirical correlations. φ=0.01, Re=2.*
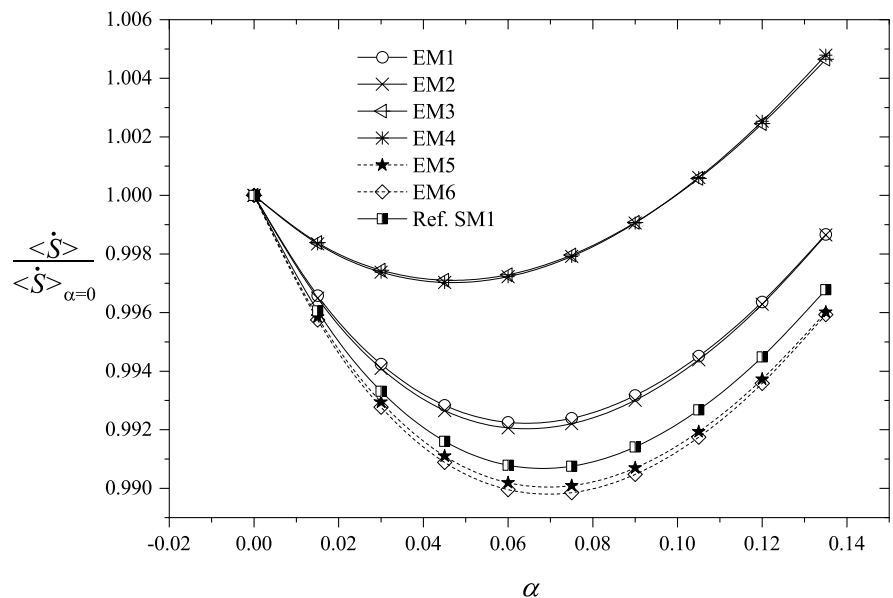
On the other hand, when the same viscosity correlation is used, the models that contain the Timofeeva thermal conductivity correlation provide slightly higher normalized entropy values compared to models that contain Pak-Cho thermal conductivity correlation.

In Figs. 3.25 and 3.26 the global entropy production as a function of lower plate Biot number Bi_1 is illustrated for different combinations of semi-empirical and empirical correlations, respectively. From Fig. 3.25, it is noted that semi-empirical combinations with same thermal conductivity correlation have similar trends. Furthermore, optimum conditions are found for all the models and the results, regardless of the used model, do not vary greatly. In Fig. 3.26, the global entropy is normalized with its value at $Bi_1 = 0$. It is found that the optimal values of Bi_1 change depending on the combination of empirical correlations. When the dynamic viscosity increases, the Bi_1 optimal values move to lower amounts and the corresponding minimum normalized global entropy values increase. It is observed that in the empirical models that have the same thermal viscosity correlation, the highest values of normalized global entropy are obtained for the models that contain the Timofeeva thermal conductivity correlation. Thus, the EM1, EM3 and EM5 models have higher values of normalized global entropy than the models EM2, EM4 and EM6, respectively.

Fig. 3.25 *Global entropy as a function of Bi1 for combinations with semi-empirical correlations.* ϕ=0.01, Bi₂=1, Re=2.

Fig. 3.26 *Global entropy as a function of Bi_1 for combinations with empirical correlations. $\phi=0.01$, $Bi_2=1$, $Re=2$.*
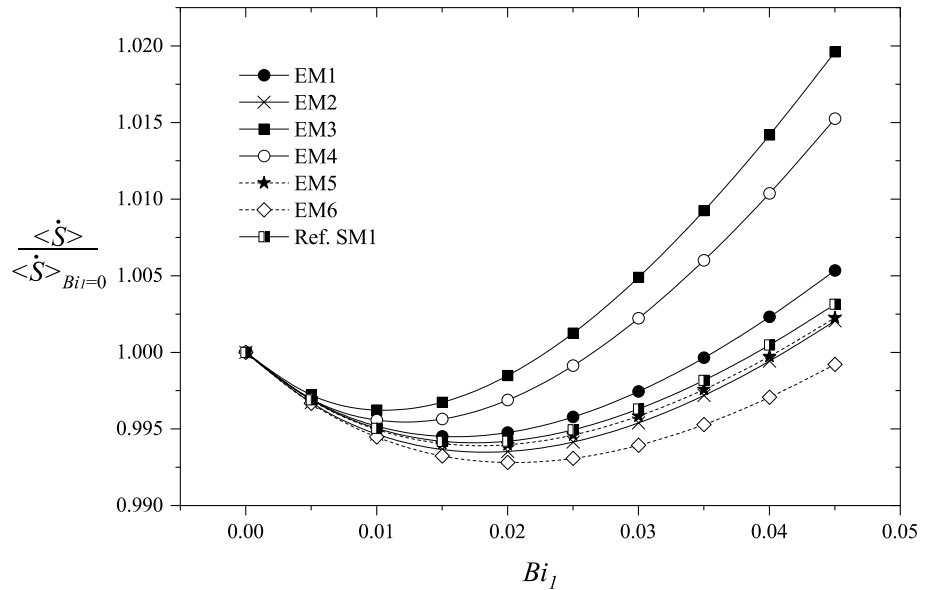
3.5.4 Effects of uncertainty in thermophysical properties on the optimum heat transfer conditions

Figures 3.27 and 3.28 show the Nusselt number as a function of hydrodynamic slip at upper plate for semi-empirical and empirical combinations of dynamic viscosity and thermal conductivity correlations. From Figure 3.27 it can be seen that all the models with semi-empirical correlations present maximum Nusselt values. It is found that the main variations are caused by the thermal conductivity correlations present in the different combinations, that is, the Maxwell, Bruggeman and Singh correlations. The Maxwell thermal conductivity correlation present in the SM1, SM4 and SM7 models predicts the lowest thermal conductivity values. Therefore, this correlation provides the lowest values of Nusselt number while the Singh correlation present in the SM3, SM6 and SM9 models predicts the highest values of thermal conductivity and Nusselt. The optimal slip value with maximum heat transfer is approximately the same for all models. The highest value of the Nusselt maximum values is 5.092 for these theoretical models.

In the case of empirical or experimental models, maximum values of the Nusselt number are also reached for all the explored models. In this case, the EM6 model that contains the Chandrasekar viscosity correlation and the Pak-Cho thermal conductivity correlation provides the highest Nu values with a maximum value of 5.17 while the EM3 model that contains the Pak-Cho viscosity correlation and the Timofeeva thermal conductivity correlation provides the lowest Nu values with a maximum value of 4.96 (see Fig. 3.28).

Fig. 3.27 *Nusselt number as a function of α at y=1 for different semi-empirical combinations. φ=0.01, M =0.1, Da=10.*
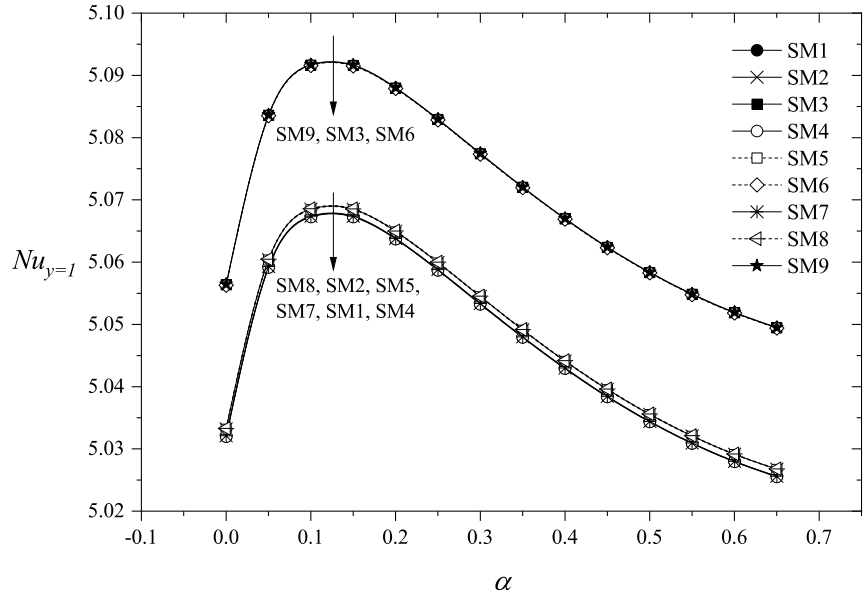
Fig. 3.28 *Nusselt number as a function of α at y=1 for different empirical combinations. φ=0.01, M =0.1, Da=10*
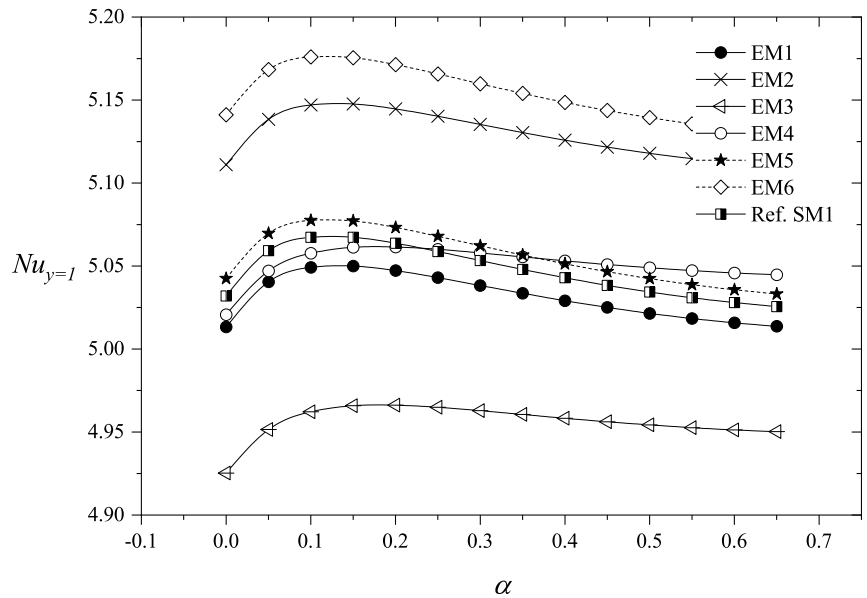
The above is in correspondence with the fact that the Chandrasekar viscosity correlation and the Pak-Cho thermal conductivity correlation in EM6 provide the lowest viscosity and the highest thermal conductivity, respectively. However, the Pak-Cho viscosity correlation and the Timofeeva thermal conductivity correlation in EM3 provide the highest viscosity and the lowest thermal conductivity, respectively. It is also observed that the optimal values of slip parameter are between 0.1 and 0.15 for all the empirical models.

3.5.5 Effects of different types of nanofluids on optimum operating conditions

In this section, the impacts of different types of solid nanoparticles in water as base fluid on optimal operating conditions are reported. For this purpose, the global entropy production as a function of hydrodynamic slip and Biot number is presented for Al_2O_3, Cu and TiO_2 solid nanoparticles.

Table 3.9 shows the thermo-physical properties of water and solid nanoparticles while the velocity, temperature, and local entropy production profiles are presented in Table 3.10 for each nanoparticle when $\phi = 0.01$ (1 %). In Table 3.10, the results reveal that the Al_2O_3/water nanofluid velocity is the greatest because the Al_2O_3 solid nanoparticle has the lowest value of density followed by TiO_2 and Cu, respectively. Furthermore, the temperature of the Cu/H_2O nanofluid is lower near the bottom wall, and higher near the top wall, therefore, the copper nanofluid has a lower temperature gradient. This is because copper has a higher thermal conductivity, therefore the heat transport from $y = 0$ to $y = 1$ is greater.

The entropy depends directly on the velocity, velocity gradient, and temperature gradient, but is inverse to the temperature of the nanofluid. The highest values of local entropy production are reached for TiO_2/water nanofluid due mainly to the increase of temperature gradient that produce an increase in the irreversibilities associated to heat flux by radiation and conduction while the lowest values of local entropy are reached for Cu/water nanofluid due mainly to the decrease of temperature gradient and velocity that produce a decrease in the irreversibilities associated to conduction and radiation heat flux, Joule heating and Darcy drag.

Table 3.9 *Thermophysical properties of water and solid nanoparticles.*

	Al_2O_3	Cu	TiO_2	H_2O
Specific heat [J/kgK]	765	385	686.2	4179
Electrical conductivity [S/m]	1×10^{-12}	59.6×10^6	2.6×10^6	5.5×10^{-6}
Thermal conductivity [W/mK]	40	400	8.9528	0.613
Dynamic viscosity [kg/ms]	--	--	--	8.91×10^{-4}
Density [kg/m³]	3970	8933	4250	997.1

Table 3.10 *Velocity, temperature and local entropy production profiles for different types of conventional nanofluids. Re=1, Da=1, P=1, M=1, α=0.1, Pr =1, Rd =1, Bi =1, φ=0.01.*

	Velocity			Temperature			Local entropy		
y	Al_2O_3	Cu	TiO_2	Al_2O_3	Cu	TiO_2	Al_2O_3	Cu	TiO_2
0.0	0.0336525	0.033262	0.0334996	0.759203	0.75902	0.759583	0.103213	0.101694	0.102705
0.1	0.0644587	0.0637412	0.0641574	0.734946	0.734779	0.735268	0.0935086	0.0926043	0.0931912
0.2	0.0895759	0.0886531	0.0891418	0.709015	0.708872	0.709276	0.0888876	0.0884517	0.0887926
0.3	0.108922	0.107907	0.108379	0.681437	0.681323	0.681633	0.0884775	0.0883745	0.0886086
0.4	0.122287	0.121283	0.121668	0.652208	0.652124	0.652332	0.0919164	0.0920103	0.0922514
0.5	0.129314	0.128411	0.128658	0.621297	0.621243	0.621342	0.0994972	0.0996441	0.0999881
0.6	0.129481	0.128749	0.12883	0.58865	0.588625	0.588605	0.112447	0.112496	0.113019
0.7	0.122064	0.121465	0.12155	0.554177	0.554181	0.554035	0.133419	0.133231	0.133968
0.8	0.106111	0.105608	0.105825	0.517743	0.517777	0.517492	0.167328	0.166833	0.167725
0.9	0.0803895	0.0800262	0.0802942	0.479129	0.479197	0.478763	0.222755	0.222081	0.222863
1.0	0.0433362	0.0431477	0.0433482	0.437989	0.438096	0.4375	0.314339	0.314082	0.314058

In Fig. 3.29, the global entropy is shown as a function of the nanoparticle concentration for the three types of studied nanofluids. It is found that TiO_2/water nanofluid presents the highest entropy values and Cu/water nanofluid the lowest values for the entire range of explored ϕ values. This is in correspondence with the fact that TiO_2 has the lowest thermal conductivity and Cu the highest. As ϕ increases, the difference between the entropy values obtained for each type of nanofluid is greater. Thus, the global entropy for Cu is approximately 1.1 and 1.8 % smaller than the global entropy for Al_2O_3 and TiO_2, respectively, at $\phi = 0.045$.

Fig. 3.29 *Global entropy as a function of φ for different nanofluid types.*
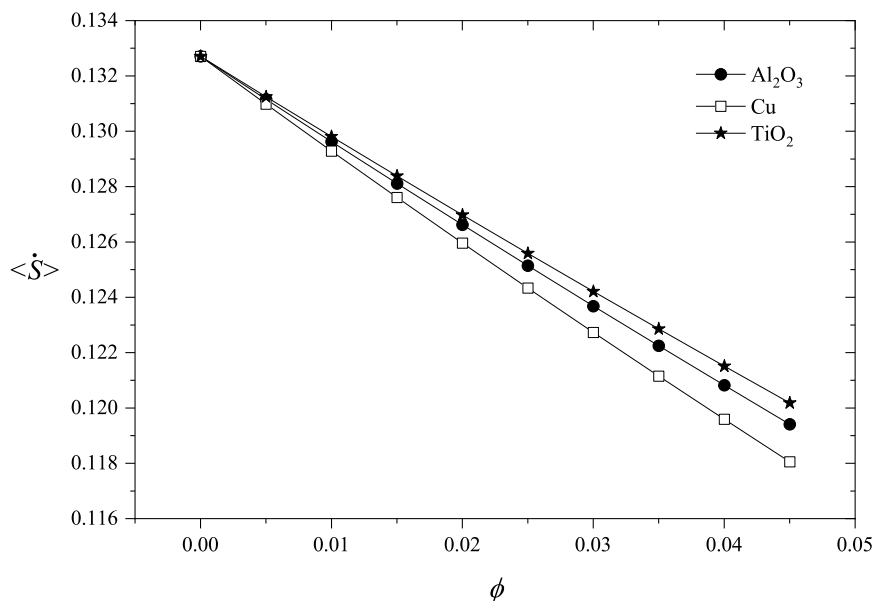
Fig. 3.30 Global
entropy as a
function of α for
different
nanofluid types.
$\phi=0.01$, Re=2.
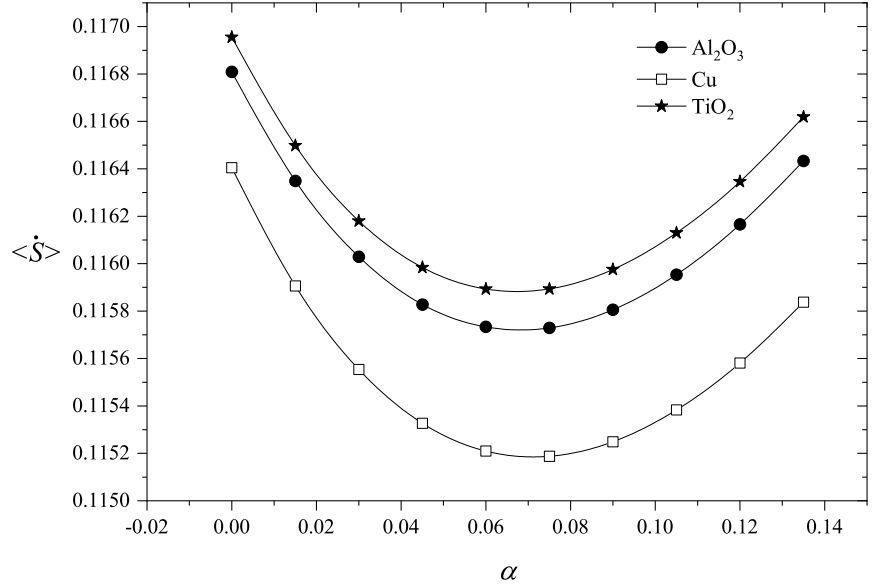
In Figs. 3.30 and 3.31, the impacts of different types of solid nanoparticles in water as base fluid on the optimal operating conditions are shown. Fig. 3.30 reports the global entropy production as a function of slip α for symmetric slip conditions while Fig. 3.31 presents the global entropy production as a function of lower plate Biot number Bi_1 for asymmetric heat transfer. It is seen that, independent of nanofluid type, optimum operating conditions are achieved for all curves of both figures with minimum values of global entropy production for certain values of slip flow and Biot number.

From Fig. 3.30, it can be seen that the optimum value of the slip parameter with minimum entropy slightly varies depending on the solid nanoparticle type. The optimum slip value is approximately 0.06 for Al_2O_3/H_2O nanofluid and moves to higher values of 0.065 and 0.075 for TiO_2/H_2O and Cu/H_2O nanofluids, respectively. This means that the slip value at which the decrease in the irreversibility associated to viscous dissipation ceases to dominate is different for each nanofluid. It is also noticed that the minimum value of global entropy for Cu/H_2O nanofluid equal to 0.1152 is the lowest of the minima while the highest value of the minima equal to 0.1159 is reached for TiO_2/H_2O nanofluid. Also, the minimum value of global entropy achieved for Cu/H_2O was 0.47 and 0.64 % lower than the minimum value of TiO_2/H_2O and Al_2O_3/H_2O, respectively.

In Fig. 3.31, it is observed that the optimum value of Biot number $Bi_{1opt} = 0.015$ is approximately the same for the three types of nanofluids. Here, in similar way to Fig. 3.30, the minimum value of global entropy for Cu/H_2O is the lowest minimum but the minimum value of global entropy for Al_2O_3/H_2O is the highest minimum. The minimum dimensionless global entropy value achieved for Cu/H_2O was 0.6 % lower than the minimum value achieved for Al_2O_3/H_2O.

Fig. 3.32 illustrates the behavior of the Nusselt number for the microchannel upper plate when the slip parameter is varied. It is noticed that there are maximum *Nu* values for all types of explored nanofluids. The highest values of *Nu* are reached for Cu nanoparticles due to its high thermal conductivity that increases the system internal heat transfer with a maximum value of 5.08 which is 0.2 and 0.5 % greater than the maximum *Nu* value achieved for Al₂O₃ and TiO₂, respectively.

Fig. 3.31 Global entropy as a function of Bi_1 for different nanofluid types. $\phi=0.01$, $Bi_2=1$, $Rd=0.1$.
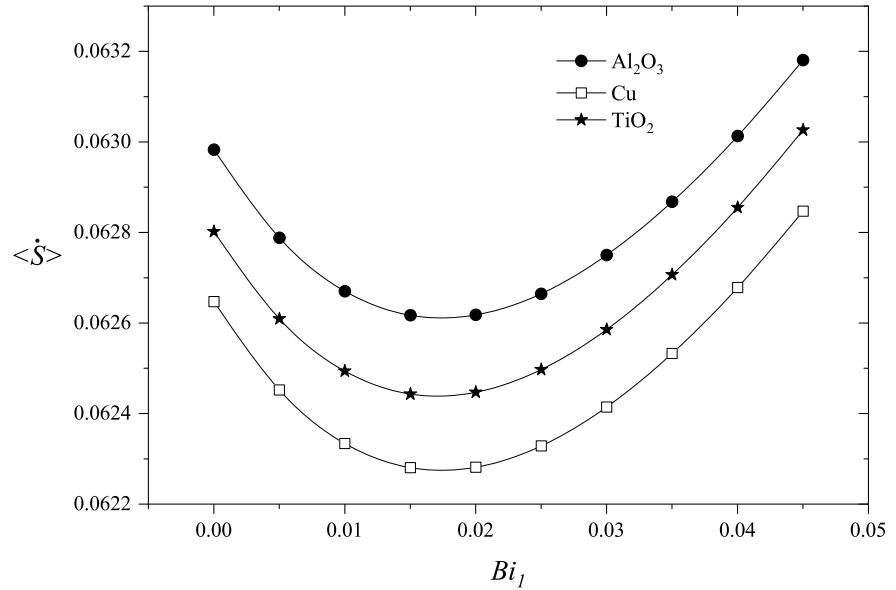
Fig. 3.32 Nusselt number as a function of α at $y=1$ for different nanofluid types. $\phi=0.01$, $M=0.1$, $Da=10$
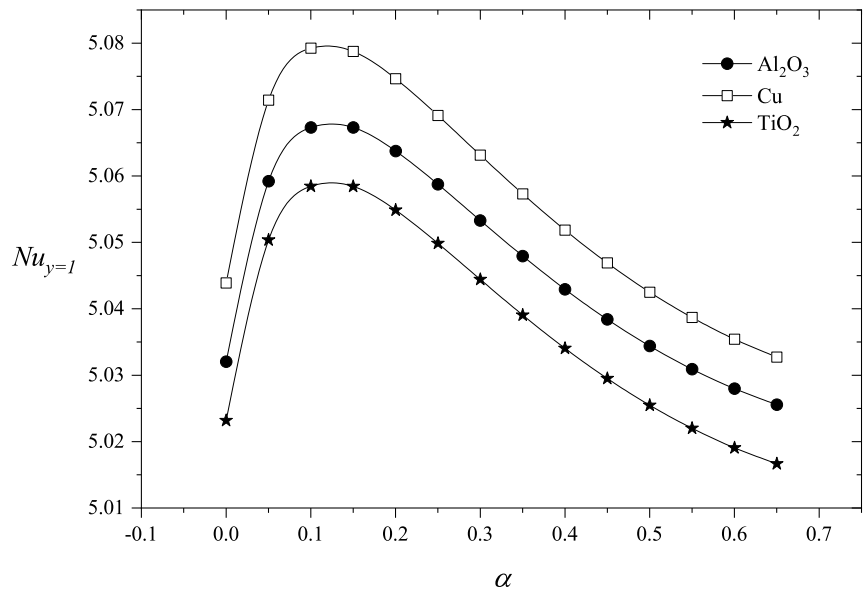
3.6 CONCLUSIONS

The MHD nanofluid flow through a horizontal microchannel of permeable plates filled with a porous medium was modeled considering hydrodynamic slip, suction/injection and thermal radiation. The exact solutions of the velocity and temperature fields were used to determine the entropy production and to evaluate the internal heat transfer in the system. The effects of different shapes of nanoparticles (spherical, blade, brick, platelet, and cylindrical) and uncertainties in nanofluid thermo-physical properties on optimum design conditions with minimum entropy production and maximum heat transport were analyzed. For this purpose, fifteen combinations of experimental and theoretical correlations of dynamic viscosity and thermal conductivity were studied. Furthermore, the effects of three different types of conventional nanofluids on the optimum operating conditions were investigated. It was confirmed that the nanoparticle shape and the uncertainties in the thermophysical properties of nanofluid affect the optimum operating conditions of system with minimum losses of useful energy and maximum heat transport.

The fundamental findings are listed below:

- Optimum values of Biot number with minimum losses of useful energy and optimum values of slip length with minimum losses of useful energy and maximum heat transport were found for symmetric slip conditions and asymmetric heat transfer.
- Optimum conditions were achieved for all studied nanoparticle shapes and all explored combinations of experimental and theoretical correlations of dynamic viscosity and thermal conductivity.
- Optimum values of slip α_{opt} and bottom plate Biot number Bi_{1opt} with minimum total entropy production were achieved. These optimum values varied in the ranges 0.045-0.075 for the slip and 0.01-0.015 for the Biot number, respectively, depending of the nanoparticle shape. The spherical shape provided the highest optimum values of both quantities while the platelet shape provided their lowest optimum values. Also, the optimum values of slip with maximum heat transfer were between 0.1 and 0.15 for all nanoparticle shapes.
- The spherical shape reached the lowest values of both viscosity and thermal conductivity. This is in correspondence with the fact that the spherical shape provided the highest values of velocity, velocity gradient and temperature gradient with the consequent increment of entropy production. Therefore, when the Darcy number increased from 0 to 0.9, the greatest increase of total entropy occurred from 0.093 to 0.129 (38 %) for the spherical shape while the smallest increase of total entropy occurred from 0.091 to 0.117 (28 %) for the platelet shape (see Fig. 3.13).
- The platelet shape showed the greatest increase in dynamic viscosity. Therefore, this shape provided the smallest values of velocity and velocity gradient (see Figs. 3.6-3.7), and was the most effective to achieve the optimum conditions with the lowest

minimum value of entropy production due to the decrease in Darcy drag $< \dot{S} >_{Da}$ and Joule heating $< \dot{S} >_{J}$. By varying ϕ from 0 to 0.05, the dynamic viscosity and thermal conductivity of platelet shape increased by approximately 3.5 and 0.24 times, respectively.

- The enhancement in Nusselt number was more appreciable for the nanoparticle blade shape due to their high values of thermal conductivity compared to the other spherical, platelet, cylindrical and brick shapes (see Fig. 3.3). Thus, the maximum value of heat transfer coefficient was improved 2.6 % for the top plate compared to platelet shape with an increment from 5 to 5.13 (see Fig. 3.17).

- The experimental Pack-Cho dynamic viscosity and Pack-Cho thermal conductivity correlations provided the higher values of both viscosity and thermal conductivity when the spherical shape was considered. These correlations showed an increase in the nanofluid dynamic viscosity and thermal conductivity of 42 % and 7.5 %, respectively, when the nanoparticle concentration increased from 0 to 0.01 (see Figs. 3.4 and 3.5).

- The combinations of experimental viscosity and experimental thermal conductivity correlations produced the greatest variations of the system optimum operating conditions compared to the combinations of theoretical correlations. This is because the estimated values of viscosity and conductivity using the different theoretical correlations differ very little from each other.

- When the slip was varied, the EM6 experimental model provided the highest values of the heat transfer coefficient at top plate with a maximum Nusselt of 5.17 achieved at $\alpha_{opt} = 0.1$ (see Fig. 3.28). This was due mainly to the higher thermal conductivity values provided by the Pak-Cho correlation.

- On the other hand, when ϕ was varied from 0 to 0.045, the EM4 experimental model provided the lowest values of global entropy production (see Fig. 3.22) due to the high thermal conductivity and dynamic viscosity values provided by the Pak-Cho correlations. This implied that low values of velocity and gradients of both velocity and temperature were reached. The global entropy decreased from 0.115 for the EM5 model to 0.082 (28.7 %) for the EM4 model at $\phi = 0.045$.

- Optimum conditions with minimum losses of useful energy and maximum heat transport were achieved for the three types of nanoparticles investigated in water as base fluid. Both the best thermal performance and the lowest minimum value of global entropy were achieved when Cu nanoparticles were used. When the slip was varied, the minimum value of global entropy achieved for Cu was 0.47 and 0.64 % lower than the minimum value of TiO_2 and Al_2O_3, respectively. Also, the maximum value of heat transfer achieved for Cu improved by approximately 0.2 and 0.4 % compared to Al_2O_3 and TiO_2, respectively (see Figs. 3.30 and 3.32).

- Optimum Biot number equal to 0.015 with minimum losses of useful energy remained approximately constant for the three types of studied nanofluids while the optimum slip value was approximately 0.06 for Al_2O_3/H_2O nanofluid and moved to higher values of 0.065 and 0.075 for TiO_2/H_2O and Cu/H_2O nanofluids, respectively.

The present analytical results related to the effects of different correlations on the system optimum operating conditions have not been presented in previous works. Moreover, these analytical solutions of the equations that describe the dynamic and thermal behavior of system can be useful to validate numerical solutions of other more complex models that can be reduced to the present solutions for certain limiting conditions.

In addition, the present optimal working conditions are useful in the design of thermal systems such as heat exchangers and MHD micropumps for applications with nanofluids.

3.7 REFERENCES

[1] Ramezanpour M, Siavashi M, Raeni AQ, Blunt MJ. Pore-scale simulation of nanoparticle transport and deposition in a microchannel using a Lagrangian approach. Journal of Molecular Liquids. 2022; 355: 118948. https://doi.org/10.1016/j.molliq.2022.118948

[2] Soumya DO, Gireesha BJ, Venkatesh P. Tangent-hyperbolic nanoliquid flow in a microchannel, thermal and irreversibility rate analysis. Waves in Random and Complex Media. 2022. https://doi.org/10.1080/17455030.2022.2108157

[3] Izadi A, Siavashi M, Rasam H, Xiong Q. MHD enhanced nanofluid mediated heat transfer in porous metal for CPU cooling. Applied Thermal Engineering. 2020; 168: 114843. https://doi.org/10.1016/j.applthermaleng.2019.114843

[4] Qasemian A, Moradi F, Karamati A, Keshavarz A, Shakeri A. Hydraulic and thermal analysis of automatic transmission fluid in the presence of nano-particles and twisted tape: An experimental and numerical study. Journal of Central South University. 2021. 28: 3404–3417. https://doi.org/10.1007/s11771-021-4864-x

[5] Khoshtarash H, Siavashi M, Ramezanpour M, Blunt MJ. Pore-scale analysis of two-phase nanofluid flow and heat transfer in open-cell metal foams considering Brownian motion. Applied Thermal Engineering. 2023; 221: 119847. https://doi.org/10.1016/j.applthermaleng.2022.119847

[6]   Ghachem K, Kolsi L, Larguech S, Alnemer G. Heat and mass transfer enhancement in triangular pyramid solar still using CNT-water nanofluid. Journal of Central South University. 2021; 28, 3434–3448. https://doi.org/10.1007/s11771-021-4866-8

[7]   Albaqawy G, Mesloub A, Kolsi L. CFD investigation of effect of nanofluid filled Trombe wall on 3D convective heat transfer. Journal of Central South University. 2021; 28, 3569–3579. https://doi.org/10.1007/s11771-021-4876-6

[8]   Aouinet H, Dhahri M, Safaei MR, Sammouda H, Anqi AE. Turbulent boundary layers and hydrodynamic flow analysis of nanofluids over a plate. Journal of Central South University. 2021; 28: 3340–3353. https://doi.org/10.1007/s11771-021-4859-7

[9]   Afshari F, Sözen A, Khanlari A, Tuncer AD. Heat transfer enhancement of finned shell and tube heat exchanger using Fe2O3/water nanofluid. Journal of Central South University. 2021; 28: 3297–3309. https://doi.org/10.1007/s11771-021-4856-x

[10] Jalil E, Molaeimanesh GR. Effects of turbulator shape, inclined magnetic field, and mixed convection nanofluid flow on thermal performance of micro-scale inclined forward-facing step. Journal of Central South University. 2021; 28: 3310–3326. https://doi.org/10.1007/s11771-021-4857-9

[11] Sindhu S, Gireesha BJ. Scrutinization of unsteady non-Newtonian fluid flow considering buoyancy effect and thermal radiation: Tangent hyperbolic model. International Communications in Heat and Mass Transfer. 2022; 135: 106062. https://doi.org/10.1016/j.icheatmasstransfer.2022.106062

[12] Felicita A, Berrehal H, Venkatesh P, Gireesha BJ, Sowmya G. Slip flow of Walter's B liquid through the channel possessing stretched walls by employing optimal homotopy asymptotic method (OHAM). Journal of Molecular Liquids. 2022; 353: 118731. https://doi.org/10.1016/j.molliq.2022.118731

[13] Ho CJ, Chen MW, Li ZW. Numerical simulation of natural convection of nanofluid in a square enclosure: effects due to uncertainties of viscosity and thermal conductivity. *International Journal of Heat and Mass Transfer*. 2008;51: 4506-4516. https://doi.org/10.1016/j.ijheatmasstransfer.2007.12.019

[14] Mansour RB, Galanis N, Nguyen CT. Effect of uncertainties in physical properties on forced convection heat transfer with nanofluids. *Applied Thermal Engineering*. 2007; 27: 240-249. https://doi.org/10.1016/j.applthermaleng.2006.04.011

[15] Arefmanesh A, Mahmoodi M. Effects of uncertainties of viscosity models for Al_2O_3–water nanofluid on mixed convection numerical simulations. *International journal of Thermal sciences.* 2011; 50: 1706-1719. https://doi.org/10.1016/j.ijthermalsci.2011.04.007

[16]   Mahdy A, ElShehabey HM. Uncertainties in physical property effects on viscous flow and heat transfer over a nonlinearly stretching sheet with nanofluids. *International communications in heat and mass transfer.* 2012; 39: 713-719. https://doi.org/10.1016/j.icheatmasstransfer.2012.03.019

[17]   Minea AA. Uncertainties in modeling thermal conductivity of laminar forced convection heat transfer with water alumina nanofluids. *International Journal of Heat and Mass Transfer.* 2014; 68: 78-84. https://doi.org/10.1016/j.ijheatmasstransfer.2013.09.018

[18]   Selvakumar RD, Dhinakaran S. Nanofluid flow and heat transfer around a circular cylinder: a study on effects of uncertainties in effective properties. *Journal of Molecular Liquids.* 2016; 223: 572-588. https://doi.org/10.1016/j.molliq.2016.08.047

[19]   Fazeli H, Pourrajabian A, Nikooei E. Simultaneous Optimization of Geometric and Nanofluids Parameters in a Rectangular Microchannel Heat Sink. *Heat Transfer Engineering.* 2022; 43: 1820-1837, https://doi.org/10.1080/01457632.2021.2016138

[20]   López A, Ibáñez G, Pantoja J, Moreira J, Lastres O. Entropy generation analysis of MHD nanofluid flow in a porous vertical microchannel with nonlinear thermal radiation, slip flow and convective-radiative boundary conditions. *International Journal of Heat and Mass Transfer.* 2017; 107: 982-994. https://doi.org/10.1016/j.ijheatmasstransfer.2016.10.126

[21]   Jamshed W, Mohd Nasir NAA, Qureshi MA, Shahzad F, Banerjee R, Mohamed R. Dynamical irreversible processes analysis of Poiseuille magneto-hybrid nanofluid flow in microchannel: A novel case study. *Waves in Random and Complex Media.* 2021; 1-23. https://doi.org/10.1080/17455030.2021.1985185

[22]   Ibáñez G, López A, Pantoja J, Moreira J. Entropy generation analysis of a nanofluid flow in MHD porous microchannel with hydrodynamic slip and thermal radiation. *International Journal of Heat and Mass Transfer.* 2016; 100: 89-97. https://doi.org/10.1016/j.ijheatmasstransfer.2016.04.089

[23]   Mondal P, Dilip KM, Shit GC, Ibañez G. Heat transfer and entropy generation in a MHD Couette–Poiseuille flow through a microchannel with slip, suction–injection and radiation. *Journal of Thermal Analysis and Calorimetry.* 2022; 147: 4253-4273. https://doi.org/10.1007/s10973-021-10731-4

[24]   Gómez I, Ibáñez G, López A, Lastres O, Reyes J. Entropy generation minimization and nonlinear heat transport in MHD flow of a couple stress nanofluid through an inclined permeable channel with a porous medium, thermal radiation and slip. *Heat Transfer.* 2020; 49: 4878-4906. https://doi.org/10.1002/htj.21858

[25]   Ibáñez G, Cuevas S, De Haro ML. Minimization of entropy generation by asymmetric convective cooling. *International Journal of Heat and Mass Transfer.* 2003; 46: 1321-1328. https://doi.org/10.1016/S0017-9310(02)00420-9

[26] Mahian O, Mahmud S, Zeinali SH. Effect of uncertainties in physical properties on entropy generation between two rotating cylinders with nanofluids. *Journal of Heat Transfer*. 2012; 134: 101704. https://doi.org/10.1115/1.4006662

[27] Ibáñez G, López A, López I, Pantoja J, Moreira J, Lastres O. Optimization of MHD nanofluid flow in a vertical microchannel with a porous medium, nonlinear radiation heat flux, slip flow and convective–radiative boundary conditions. *Journal of Thermal Analysis and* Calorimetry. 2019; 135: 3401-3420. https://doi.org/10.1007/s10973-018-7558-3

[28] Aaiza G, Khan I, Shafie S. Energy transfer in mixed convection MHD flow of nanofluid containing different shapes of nanoparticles in a channel filled with saturated porous medium. *Nanoscale Research Letters*. 2015; 10: 1-14. https://doi.org/10.1186/s11671-015-1144-4

[29] Sheikholeslami M, Sajjadi H, Amiri A. Magnetic force and radiation influences on nanofluid transportation through a permeable media considering Al_2O_3 nanoparticles. *Journal of Thermal Analysis and Calorimetry*. 2019; 136: 2477-2485. https://doi.org/10.1007/s10973-018-7901-8

[30] Benkhedda M, Boufendi T, Tayebi T. Convective heat transfer performance of hybrid nanofluid in a horizontal pipe considering nanoparticles shapes effect. *Journal of Thermal analysis and Calorimetry*. 2020; 140: 411-425. https://doi.org/10.1007/s10973-019-08836-y

[31] Saleem S, Qasim M, Alderremy A, Noreen S. Heat transfer enhancement using different shapes of Cu nanoparticles in the flow of water based nanofluid. *Physica Scripta*. 2020; 95: 055209. https://doi.org/10.1088/1402-4896/ab4ffd

[32] Ghadikolaei SS, Yassari M, Sadeghi H, Hosseinzadeh K, Ganji DD. Investigation on thermophysical properties of TiO_2–Cu/H_2O hybrid nanofluid transport dependent on shape factor in MHD stagnation point flow. *Powder technology*. 2017; 322: 428-438. https://doi.org/10.1016/j.powtec.2017.09.006

[33] Sindhu S, Gireesha BJ, Sowmya G, Makinde OD. Hybrid nanoliquid flow through a microchannel with particle shape factor, slip and convective regime. *International Journal of Numerical Methods for Heat and Fluid Flow*. 2022; 32: 3388-3410. https://doi.org/10.1108/HFF-11-2021-0733

[34] Kumar A, Ray RK. Shape effect of nanoparticles and entropy generation analysis for magnetohydrodynamic flow of (Al_2O_3–Cu/H_2O) hybrid nanomaterial under the influence of Hall current. *Indian J Phys.* 2022; 96: 3817–3830. https://doi.org/10.1007/s12648-022-02300-8.

[35] Ellahi R, Hassan M, Zeeshan A. Shape effects of nanosize particles in Cu–H_2O nanofluid on entropy generation. *International Journal of Heat and Mass Transfer*. 2015; 81: 449-456. https://doi.org/10.1016/j.ijheatmasstransfer.2014.10.041

[36] Zeeshan A, Hassan M, Ellahi R. Shape effect of nanosize particles in unsteady mixed convection flow of nanofluid over disk with entropy generation. *Proceedings of the Institution of Mechanical Engineers, Part E: Journal of Process Mechanical Engineering*. 2017; 231: 871-879. https://doi.org/10.1177/0954408916646139

[37] Seyyedi SM, Dogonchi AS, Ganji DD. Entropy generation in a nanofluid-filled semi-annulus cavity by considering the shape of nanoparticles. *Journal of Thermal Analysis and Calorimetry*. 2019; 138: 1607-1621. https://doi.org/10.1007/s10973-019-08130-x

[38] Cengel YA, Ghajar AJ. Heat and mass transfer. *Penerbit McGraw-Hill Education*. 2015.

[39] Zhang C, Zheng L, Zhang X, Chen G. MHD flow and radiation heat transfer of nanofluids in porous media with variable surface heat flux and chemical reaction. *Applied Mathematical Modelling*. 2015; 39: 165-181. https://doi.org/10.1016/j.apm.2014.05.023

[40] Makinde OD. Second law analysis for variable viscosity hydromagnetic boundary layer flow with thermal radiation and Newtonian heating. *Entropy*. 2011; 13: 1446-1464. https://doi.org/10.3390/e13081446

[41] Bejan A. Entropy generation minimization: the method of thermodynamic optimization of finite-size systems and finite-time processes. CRC press, 2013. https://doi.org/10.1201/9781482239171

[42] Gupta M, Singh V, Kumar R, Said Z. A review on thermophysical properties of nanofluids and heat transfer applications. *Renewable and Sustainable Energy Reviews*. 2017; 74: 638-670. https://doi.org/10.1016/j.rser.2017.02.073

[43] Minea AA. A review on the thermophysical properties of water-based nanofluids and their hybrids. *The Annals of "Dunarea de Jos" University of Galati. Fascicle IX, Metallurgy and Materials Science*. 2016; 39: 35-47. https://www.gup.ugal.ro/ugaljournals/index.php/mms/article/view/1279

[44] Saqib M, Khan I, Shafie S. Recent advancement in thermophysical properties of nanofluids and hybrid nanofluids: an overview. *International Journal of Computacional Analysis*. 2019; 1: 16-25. https://doi.org/10.33959/cuijca.v3i2.27

[45] Mahian O, Kianifar A, Kleinstreuer C, Al-Nimr MA, Pop I, Sahin AZ, Wongwises S. A review of entropy generation in nanofluid flow. *International Journal of Heat and Mass Transfer*. 2013; 65: 514-532. https://doi.org/10.1016/j.ijheatmasstransfer.2013.06.010

[46] Buongiorno J. Convective Transport in Nanofluids. *ASME. J. Heat Transfer*. 2006; 128: 240–250. https://doi.org/10.1115/1.2150834

[47] Chandrasekar M, Suresh S, Chandra A. Experimental investigations and theoretical determination of thermal conductivity and viscosity of Al_2O_3/water nanofluid. *Experimental Thermal and Fluid Science*. 2010; 34: 210-216. https://doi.org/10.1016/j.expthermflusci.2009.10.022

[48] Huminic G, Huminic A. Entropy generation of nanofluid and hybrid nanofluid flow in thermal systems: a review. *Journal of Molecular Liquids*. 2020; 302: 112533. https://doi.org/10.1016/j.molliq.2020.112533

[49] Timofeeva EV, Gavrilov AN, McCloskey JM. Thermal conductivity and particle agglomeration in alumina nanofluids: experiment and theory. *Physical Review E*. 2007; 76: 061203. https://doi.org/10.1103/PhysRevE.76.061203

[50] Pak BC, Cho YI. Hydrodynamic and heat transfer study of dispersed fluids with submicron metallic oxide particles. *Experimental Heat Transfer an International Journal*. 1990; 11: 151-170. https://doi.org/10.1080/08916159808946559

CHAPTER IV

ANALYSIS OF HEAT TRANSFER AND OPTIMIZATION OF A HYBRID NANOFLUID FLOW BASED ON ENTROPY MINIMIZATION CONSIDERING NANOPARTICLES SHAPES

4.1 INTRODUCTION

Recent studies confirm that hybrid nanofluids can be more effective and guarantee greater heat transfer compared to unitary nanofluids (a single type of nanoparticle), this has led researchers to develop mathematical modeling to test the efficiency of the hybrid nanofluids in thermal systems. In various applications where heat exchanger devices need to be designed with maximum efficiency, it is necessary to determine the thermophysical and geometric parameters of system that guarantee maximum use of energy or minimum losses of useful energy. The microchannels or heat exchanger enclosures consider various geometries and characteristics depending on the application [1-6]. For example, some applications of nanofluids in solar energy consider flat plate solar collectors, evacuated tube solar collectors, parabolic trough collectors, concentrating solar collectors, linear fresnel reflectors and parabolic dish reflectors [7,8].

There are several studies focused on the implementation of nanofluids in microchannels [9]. These types of structures are important due to their varied applications in engineering designs. Microchannels play a vital role in cooling electronic equipment used in biomedical, aerospace, automotive, and computing fields due to their small size. The utilization of unitary nanofluids in microchannels was recently reported in [10–16].

In particular, researchers have worked to determine the optimum conditions of thermal systems with nanofluid flows considering the effects of nanoparticle shape and size, as well as the size of microchannel and the values of various physical parameters [17-21]. The evaluation of these thermal systems has been carried out using different optimization techniques and calculation methods. In this way, the application of the second law of thermodynamics can be highlighted, which lately many researchers have applied [11,13, 22-28].

The irreversibility analysis allows evaluating the entropy generation rate, which must be minimized to avoid the loss of useful energy. For example, López et al. [11] studied the MHD flow of an Al_2O_3 nanofluid in a vertical microchannel considering nonlinear thermal radiation. Optimum conditions with minimum entropy generation were found for the hydrodynamic slip. Ibáñez et al. [13] performed the analysis of an MHD nanofluid flow in a vertical microchannel considering a porous medium. Optimum operating conditions with minimum entropy production were found for certain values of nanoparticle concentration. Estrada et al. [28] performed the analysis of unitary nanofluid flow in horizontal microchannel considering a porous medium and nanoparticle shape effects. They found optimum values of Biot number and hydrodynamic slip with minimum entropy generation.

In order to improve the properties of unitary nanofluids, hybrid nanofluids were developed with two or more types of nanoparticles dispersed in the base fluid. Various studies indicated that hybrid nanofluids improved the heat transfer characteristics compared to unitary nanofluids, but they also increased the viscosity. Hence, a greater pumping power was required [29-32].

Other studies revealing the effectiveness of hybrid nanofluids were presented in [33-36]. Moghadassi et al. [33] numerically studied the heat transfer performance for Al_2O_3-Cu/water hybrid nanofluid and Al_2O_3/water unitary nanofluid. A greater heat transfer for the hybrid nanofluid was achieved compared to the conventional one. Similarly, Huang et al. [34] experimentally studied the heat transfer and pressure drop for a hybrid nanofluid of MWCNT-Al_2O_3/water. It was found that the heat transfer improved for the hybrid nanofluid mixture and their pressure drop was smaller than that of the Al_2O_3/water.

Minea et al. [35] performed a numerical evaluation of three unitary nanofluids based on oxides and their hybrids using different viscosity models. It was noted that the thermal conductivity increased by 12% when hybrid nanoparticles were used. Bhattad et al. [36] used hybrid nanofluids to improve the heat transfer of a plate evaporator to cool milk. They used aluminum, copper oxide, silica, titania and copper nanoparticles in different combinations. The Cu-CuO hybrid nanofluid provided the highest performance. Other applications of hybrid nanofluid flows can be found in peristaltic devices [37], in a circular tubes [38], rotating disks [39], vertical microchannels [40], and wavy cylindrical microchannels [41].

In addition to above, there are theoretical studies where the effects of different nanoparticle shapes of hybrid nanofluids are considered. Benkhedda et al. [42] performed a numerical study for two nanofluids, the unitary TiO_2/water nanofluid and the Ag-TiO_2/water hybrid nanofluid for an isothermally heated horizontal tube. In this study, four different types of nanoparticle shapes were considered: spherical, cylindrical, platelet, and blade with different volume fractions. It was found that the friction factor increased as the volume fraction of nanoparticles increased for all types of nanoparticle shapes, while it decreased as the Reynolds number increased. The highest heat transfer rate was obtained for the maximum volume concentration of blade-shaped nanoparticles followed by platelet, cylindrical, and spherical shapes, respectively. They also found that the maximum values of the friction factor were obtained for platelet-shaped nanoparticles.

Ghadikolaei et al. [43] studied the effect of induced magnetic field on the flow of a conventional Cu nanofluid and a TiO_2-Cu hybrid nanofluid in water as a base fluid on a stretchable sheet. The nonlinear equations were solved using the Runge-Kutta Fehlberg method.

The results indicated that the use of the TiO_2-Cu hybrid nanofluid is more effective compared to the unitary Cu nanofluid because the heat transfer was improved. Furthermore, platelet-shaped nanoparticles were found to have higher heat transfer compared to cylindrical and blade shapes.

Another study that considered the effect of the nanoparticle shape and the presence of a porous medium was given by Shah et al. [44]. They performed a numerical simulation of an MHD flow of a water-based aluminum nanofluid using Darcy law and the radiation effect. They found an inverse relationship between the temperature gradient and the Lorentz force and analyzed the cylindrical, cubic, platelet and spherical shapes of nanoparticles. However, the performance of the system was not analyzed considering the second law of thermodynamics. Other studies of hybrid nanofluid flows in presence of porous medium were also carried out in [45-50]. Another important parameter that was included in some recent studies was the internal generation of energy in the nanofluid. This effect was considered through an internal heat source parameter [51-53].

The following studies considered the calculation of entropy production as a measure of system efficiency, as well as various effects for different channel geometries using hybrid nanofluid flows. Huminic [54] performed an entropy generation minimization analysis for the hybrid nanofluids of MWCNT + Fe_3O_4 and ND + Fe_3O_4 in water as a base fluid for a tube. It was found that the hybrid nanofluid reduced the entropy compared to the base fluid. Ahammed et al. [55] investigated the heat transfer and entropy generation of a water-based graphene-alumina hybrid nanofluid for a mini-channel heat exchanger coupled to a thermoelectric cooler. They found lower entropy generation with the hybrid graphene-alumina nanofluids compared to the base fluid, but the unitary graphene nanofluid had higher performance in heat transfer analysis. Khan et al. [56] optimized the flow of a graphene-copper oxide MHD hybrid nanofluid between two rotating parallel plates considering chemical reaction. They found that the magnitude of the Nusselt number increased with Eckert number, magnetic parameter and Prandtl number.

Tayebi et al. [57] modeled the flow of Cu-Al_2O_3-water hybrid nanofluid in a ring between two elliptical cylinders. The impacts of various parameters such as nanoparticle concentration, Rayleigh number and dimensionless internal heat generation on entropy generation were examined. Hayat et al. [58] performed numerical simulation and flow optimization of a cobalt-gold ferrite hybrid nanofluid using water and ethylene glycol as base fluids for a curved surface. He compared the unitary and hybrid nanofluids, and determined that the entropy decreased with the magnetic parameter for the hybrid nanofluid unlike the conventional one. Li et al. [59] studied the flow of a water-based Al_2O_3-Cu hybrid nanofluid over a disk considering effects of viscous dissipation, radiation and nonlinear convection.

Other studies about entropy production in hybrid nanofluids can be found in references [60-63]. Ahmad et al. [60] carried out the study of SWCNT-MWCNT hybrid nanofluid in a branched geometry considering the viscosity as a function of the temperature. Jamshed et al. [61] analyzed the MHD flow of a Poiseuille hybrid nanofluid in a horizontal microchannel. Sindhu et al. [62] conducted the study for a porous vertical microchannel with slip, convective boundary conditions and nonlinear heat flux. Yusuf et al. [63] analyzed the irreversibilities on a 3-D stretching sheet in a porous medium using Darcy Forchheimer model.

The revised literature indicates that although several numerical studies were performed for hybrid nanofluids, the simultaneous effects of mixing ratios of nanoparticles, porous medium, nanoparticle shapes, internal heat generation, nonlinear thermal radiation and presence of a magnetic field were not considered. On the other hand, in the entropy analysis of these previous works, optimum values of geometric parameters and/or physical properties that guarantee lower losses of useful energy were not always found.

The current work aims to obtain configurations that guarantee minimum entropy production and maximum heat transfer in heat transfer systems that involve the use of microchannels and hybrid nanofluid flows. Thus, in this second case study new effects are included, such as mixing ratios of nanoparticles, microchannel inclination, nonlinear thermal radiation, internal heat generation and nonlinear Forchheimer term on the optimum operating conditions of hybrid nanofluid flows.

In this way, the nonlinear differential equations for a MHD hybrid nanofluid are solved numerically using Runge-Kutta method together with shooting technique. First, the velocity and temperature profiles are determined and then the values of entropy, Nusselt number and skin friction coefficient are computed. To the best of our knowledge, there are no reports of optimum mixing ratios of nanoparticles for hybrid nanofluids that guarantee minimum entropy production. In the current study, optimum mixing ratios of nanoparticles were reported for Al_2O_3-Cu and TiO_2-Cu in water as base fluid. The possibility of achieving a minimum in entropy production using appropriate mixing ratios of nanoparticles in the base fluid might be useful to optimize the operating conditions of heat transfer microdevices with hybrid nanofluid flows.

4.2 PROBLEM DESCRIPTION AND GOVERNING EQUATIONS
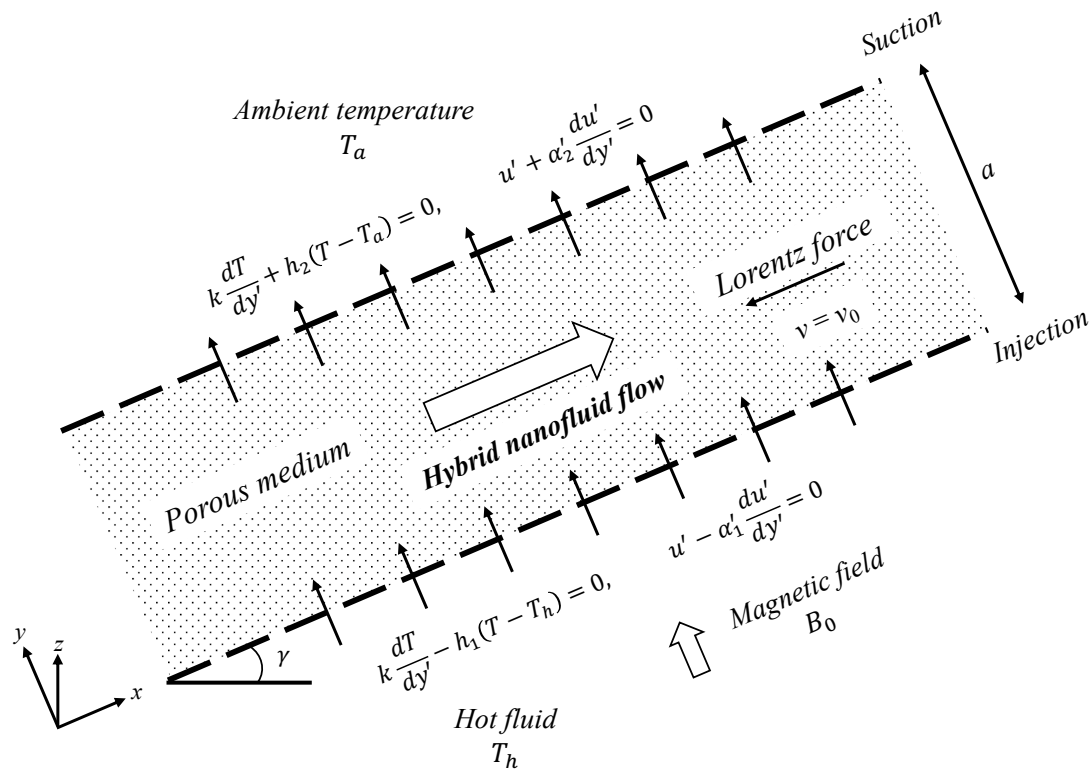
Fig. 4.1 *Geometry of system (Case II).*

A fully developed MHD flow of steady, incompressible and viscous hybrid nanofluid through an inclined microchannel filled with a porous medium and under the effect of an external uniform transverse magnetic field B_o is shown in Figure 1. The microchannel plates are separated by a distance a in presence of a constant pressure gradient $\frac{dP}{dx'}$ applied in the longitudinal direction with the upper plate at $y' = a$ and the lower plate at $y' = 0$. It is also supposed that uniform injection of warm hybrid nanofluid happens across the bottom plate while suction occurs across the upper plate. Moreover, hydrodynamic slip boundary condition at the nanofluid-plate interface is regarded for the solution of the momentum equation while the heat transfer equation is solved considering thermal boundary conditions of the third type, nonlinear thermal radiation, internal energy generation, viscous dissipation and Joule heating. In the flow of hybrid nanofluid subjected to magnetic interactions, an electric current is induced which affects the dynamic and thermal behavior of the hybrid nanofluid due to the apparition of Lorentz force and ohmic heating, respectively. It must be noted that in the present study the nanoparticles and the base fluid move at the same velocity and are in thermal equilibrium, that is, a single-phase nanofluid model is assumed.

4.2.1 Velocity field

The velocity field relative to the movement of the fluid is modeled with the following assumptions:

1. The flow is steady, that is $\frac{\partial}{\partial t} = 0$.
2. The length of the plates in the z axis is much greater than the width of the channel, so the effects on z are neglected.
3. The y component of the velocity is $v = v_0$, which indicates that the flow through the permeable plates is constant.
4. There is a constant pressure gradient p with respect to the x axis.
5. The velocity field is two-dimensional so that the velocity $w = 0$ and $\frac{\partial}{\partial z} = 0$.
6. The fluid is incompressible $\frac{\partial \rho}{\partial t} = 0$.
7. The effect of gravity force and buoyancy force is considered.
8. The effect of the inertial force in the porous medium is considered.
9. An angle of inclination with respect to the horizontal is considered.

From Eq. (2.11) for momentum, the material derivative for the moment at x is developed.

$$\rho \left(\frac{\partial u}{\partial t} + u \frac{\partial u}{\partial x} + v \frac{\partial u}{\partial y} + w \frac{\partial u}{\partial z} \right) = -\frac{\partial p}{\partial x} + \nabla \cdot \tau + \rho g + \mathbf{j} \times \mathbf{B} \tag{4.1}$$

Substituting the viscous stress tensor of the velocity component u (Eq. 3.5) into Eq. (4.1)

$$\rho \left(\frac{\partial u}{\partial t} + u \frac{\partial u}{\partial x} + v \frac{\partial u}{\partial y} + w \frac{\partial u}{\partial z} \right)$$
$$= -\frac{\partial p}{\partial x} + \eta \left(\frac{\partial^2 u}{\partial x^2} + \frac{\partial^2 u}{\partial y^2} + \frac{\partial^2 u}{\partial z^2} \right) + \rho g + \mathbf{j} \times \mathbf{B} \tag{4.2}$$

In Eq. (4.2), terms containing the velocity w, the partial derivatives $\frac{\partial}{\partial z}$ and $\frac{\partial}{\partial t}$, are eliminated, because the flow movement in z is negligible and stationary in all its components. From the continuity equation it is known that $\frac{\partial u}{\partial x} = 0$, additionally $v = v_0$ is considered constant, therefore, Eq. (4.2) is reduced to

$$\rho \left(v_0 \frac{\partial u}{\partial y} \right) = -\frac{\partial p}{\partial x} + \eta \left(\frac{\partial^2 u}{\partial y^2} \right) + \rho g + \mathbf{j} \times \mathbf{B} \tag{4.3}$$

The gravitational force g is decomposed into two components, the component parallel to the microchannel and the component perpendicular to the microchannel. The perpendicular component is neglected, because it does not directly contribute to the movement of the fluid along the microchannel. Then, considering the component parallel to the channel, the force of gravity in the inclined flow direction is

$$F_g = g \sin(\gamma) \tag{4.4}$$

where γ is the angle of inclination of the microchannel with respect to the horizontal, measured in radians. Considering thermal effects, the buoyancy force term is added, which is proportional to the temperature difference $T - T_a$ and the thermal expansion coefficient β. Therefore Eq. (4.3) becomes

$$\rho \left(v_0 \frac{\partial u}{\partial y} \right) = -\frac{\partial p}{\partial x} + \eta \left(\frac{\partial^2 u}{\partial y^2} \right) + g\rho\beta(T - T_a)\sin(\gamma) + \mathbf{j} \times \mathbf{B} \tag{4.5}$$

With Eq. (3.12), the term $\mathbf{j} \times \mathbf{B}$ is substituted, then we have

$$\rho \left(v_0 \frac{\partial u}{\partial y} \right) = -\frac{\partial p}{\partial x} + \eta \left(\frac{\partial^2 u}{\partial y^2} \right) + g\rho\beta(T - T_a)\sin(\gamma) - \sigma B_0^2 u \tag{4.6}$$

With the Darcy equation (Eq. 3.8), the term that considers the effects on the porous medium is added. When the Reynolds number increases and the flow tends to be turbulent, inertia will affect the momentum equation and the Darcy equation is not sufficient to model the effect. Under these studied conditions, the axial pressure drop ∇p_m includes two terms depending on the linear velocity (viscous) and the quadratic velocity (inertia) [64]. This new term is known as the Forchheimer inertial effect, then Eq. (3.8) is

$$-\frac{\partial p_m}{\partial x} = -\frac{\eta}{K}u - \frac{\rho F}{\sqrt{K}}u^2 \tag{4.7}$$

where F is the Forchheimer inertial coefficient. Therefore, adding terms

$$\rho \left(v_0 \frac{\partial u}{\partial y} \right) = -\frac{\partial p}{\partial x} + \eta \left(\frac{\partial^2 u}{\partial y^2} \right) + g\rho\beta(T - T_a)\sin(\gamma) - \sigma B_0^2 u - \frac{\eta}{K}u$$
$$- \frac{\rho F}{\sqrt{K}}u^2 \tag{4.8}$$

Converting to ordinary derivatives, the momentum equation for a MHD flow of a viscous hybrid nanofluid in an inclined microchannel under a uniform transverse magnetic field and considering the Darcy-Forchheimer model is [14]

$$\rho_{hnf} v_0 \frac{du'}{dy'} = -\frac{dp}{dx'} + g(\rho\beta)_{hnf}(T - T_a)\,\sin(\gamma) + \eta_{hnf}\frac{d^2u'}{dy'^2} - \sigma_{nf}B_0^2 u'$$
$$- \frac{\eta_{hnf}}{K}u' - \frac{\rho_{nf}F}{\sqrt{K}}u'^2 \tag{4.9}$$

The term on the left side of Eq. (4.9) is the convective term related to fluid motion. The first term on the right side is the pressure gradient in the longitudinal direction, the second term represents the buoyancy force, the third term is related to the friction force and the fourth term is the Lorentz force. The last two terms represent the Darcy drag and Forchheimer inertial effect in the porous medium, respectively.

Assuming that the surface roughness of each plate is different, the boundary conditions are written as

$$u' - \alpha_1' \frac{du'}{dy'} = 0, \quad \text{en } y' = 0\,' \tag{4.10}$$

$$u' + \alpha_2' \frac{du'}{dy'} = 0, \quad \text{en } y' = a\,' \tag{4.11}$$

where α_1' y α_2' are the slip lengths of the lower and upper plates of microchannel, respectively.

Considering the relations of density $\frac{\rho_{hnf}}{\rho_f}$, dynamic viscosity $\frac{\eta_{hnf}}{\eta_f}$, electrical conductivity $\frac{\sigma_{hnf}}{\sigma_f}$, coefficient of thermal expansion $\frac{(\rho\beta)_{hnf}}{(\rho\beta)_f}$ and introducing the following dimensionless terms of Eq.(4.12)

$$u = \frac{\rho_f a u'}{\eta_f}, \qquad y = \frac{y'}{a}, \qquad \alpha_1 = \frac{\alpha_1'}{a}, \qquad \alpha_2 = \frac{\alpha_2'}{a},$$
$$P = -\frac{a^3 \rho_f}{\eta_f^2}\left(\frac{dp}{dx'}\right), \quad M = B_0 a\sqrt{\sigma_f/\eta_f}, \quad \theta_h = \frac{T_h}{T_a}, \quad \theta = \frac{T - T_a}{T_h - T_a}$$
$$Gr = \frac{ga^3 T_a(\rho\beta)_f}{\rho_f v_f^2} \qquad Re = \frac{v_0 a \rho_f}{\eta_f}, \qquad Da = \frac{k}{a^2} \tag{4.12}$$

Equation (4.9) become

$$\frac{\rho_{hnf}}{\rho_f} Re \frac{du}{dy} = P + \frac{(\rho\beta)_{hnf}}{(\rho\beta)_f} Gr(\theta_h - 1)\theta \sin(\gamma) + \frac{\eta_{hnf}}{\eta_f}\frac{d^2u}{dy^2} - \frac{\sigma_{hnf}}{\sigma_f}M^2u$$
$$- \frac{\eta_{hnf}}{\eta_f}\frac{u}{Da} - \frac{\rho_{hnf}}{\rho_f}\frac{F}{\sqrt{Da}}u^2 \tag{4.13}$$

and the boundary conditions Eqs. (4.10) and (4.11)

$$u - \alpha_1 \frac{du}{dy} = 0, \ \text{ at } \ y = 0 \tag{4.14}$$

$$u + \alpha_2 \frac{du'}{dy'} = 0, \ \text{ at } \ y = 1 \tag{4.15}$$

4.2.2 Temperature field

In this new case study, the effects of heat transfer by nonlinear radiation are considered, as in Lopez et al. [11], Ibañez et al. [13] and Gómez et al. [14], the consideration of these effects increases the precision of the model, but also its resolution complexity. Additionally, various authors have considered the inclusion of a term that represents the generation of internal energy in the nanofluid [52, 53].

From the energy equation (Eq. 3.30), the term related to the radiation heat flux (Eq. 3.32) is added.

$$\rho C_p \left(v_0 \frac{\partial T}{\partial y}\right) = k\left(\frac{\partial^2 T}{\partial y^2}\right) + \eta \left(\frac{\partial u}{\partial y}\right)^2 + \mathbf{j} \cdot (\mathbf{E} + \mathbf{v} \times \mathbf{B}) - \frac{\partial q_r}{\partial y} \tag{4.16}$$

The term that represents the dissipation of energy due to the porous medium can be expressed as an increase in heat due to fluid friction. The energy dissipated by friction is proportional to the square of the fluid velocity. On the other hand, the energy dissipated due to inertial effects or Forchheimer term, is proportional to the cube of the fluid velocity, that is

$$q_m = \frac{\eta}{K}u^2 + \frac{\rho F}{\sqrt{K}}u^3 \tag{4.17}$$

Therefore, the energy equation considering thermal radiation and the effect of a porous medium with the Darcy-Forchheimer model is

$$\rho C_p \left(v_0 \frac{\partial T}{\partial y} \right) = k \left(\frac{\partial^2 T}{\partial y^2} \right) + \eta \left(\frac{\partial u}{\partial y} \right)^2 + \mathbf{j} \cdot (\mathbf{E} + \mathbf{v} \times \mathbf{B}) - \frac{\partial q_r}{\partial y} + \frac{\eta}{K} u^2 \\ + \frac{\rho F}{\sqrt{K}} u^3$$

(4.18)

As in section 3.2.2, the expression $\mathbf{j} \cdot (\mathbf{E} + \mathbf{v} \times \mathbf{B}) = \sigma(u^2 B_0^2)$. Substituting Eq. (3.36) into Eq. (4.18), we have

$$\rho C_p \left(v_0 \frac{\partial T}{\partial y} \right) = k \left(\frac{\partial^2 T}{\partial y^2} \right) + \eta \left(\frac{\partial u}{\partial y} \right)^2 + \sigma(u^2 B_0^2) - \frac{\partial q_r}{\partial y} + \frac{\eta}{K} u^2 + \frac{\rho F}{\sqrt{K}} u^3$$

(4.19)

According to [65], internal heat generation in a medium can be caused by exothermic chemical reactions and this serves as a heat source for the medium. Consideration of the heat source term in the temperature equation can increase the accuracy of predicting the thermal behavior of the fluid. Physically, this thermal represents the internal heat generation q_i of the nanofluid due to exothermic chemical reactions in the solid nanoparticles.

$$q_i = Q_T \, (T - T_a)$$

(4.20)

Where Q_T is the heat source coefficient and $(T - T_a)$ the temperature difference.

From Eq. (4.20), the temperature dependent heat source term is added. Therefore, the energy balance equation is developed considering viscous dissipation, Joule heating, thermal radiation, Darcy-Forchheimer model and internal energy generation.

$$\rho C_p \left(v_0 \frac{\partial T}{\partial y} \right) = k \left(\frac{\partial^2 T}{\partial y^2} \right) + \eta \left(\frac{\partial u}{\partial y} \right)^2 + \sigma(u^2 B_0^2) - \frac{\partial q_r}{\partial y} + \frac{\eta}{K} u^2 + \frac{\rho F}{\sqrt{K}} u^3 \\ + Q_T \, (T - T_a)$$

(4.21)

Transforming Eq. (4.21) to ordinary derivatives, the heat heat transfer equation for a hybrid nanofluid considering an internal heat source becomes [13, 14, 28, 53]

$$(\rho C_p)_{hnf} v_0 \left(\frac{dT}{dy'}\right)$$

$$= k_{hnf} \frac{d^2T}{dy'^2} + \eta_{hnf} \left(\frac{du'}{dy'}\right)^2 + \sigma_{hnf} B_0^2 u'^2 - \frac{dq_r}{dy'} + \frac{\eta_{hnf}}{K} u'^2 \qquad (4.22)$$

$$+ \frac{\rho_{hnf} F}{\sqrt{K}} u'^3 + Q_T \ (T - T_a)$$

The first term on the left side of Eq. (4.22) represents the heat transfer due to convective effects. The first term on the right side corresponds to the conduction heat flux, the second term is related to viscous dissipation, the third term is associated to Joule heating, the fourth term takes into account the heat flux due to nonlinear thermal radiation. The fifth and sixth terms are related to the effects of viscous dissipation in the porous medium and the last term corresponds to the effect of internal heat generation.

The convective boundary conditions of the third type that Eq. (4.22) must satisfy are

$$k_{hnf} \frac{dT}{dy'} - h_1(T - T_h) = 0, \ \ \text{at} \ y' = 0 \qquad (4.23)$$

$$k_{hnf} \frac{dT}{dy'} + h_2(T - T_a) = 0, \ \ \text{at} \ y' = a \qquad (4.24)$$

where T_h is the temperature of the hot fluid, T_a is the ambient temperature, while h_1 y h_2 are the convection heat transfer coefficients for bottom and top plates.

The nonlinear thermal radiation using Rosseland diffusion approximation can be written as [11, 14]

$$q_r = -\frac{4\sigma^*}{3k^*} \frac{dT^4}{dy'} = -\frac{16\sigma^* T^3}{3k^*} \frac{dT}{dy'} \qquad (4.25)$$

where, k^* is the mean Rosseland absorption coefficient and σ^* is the Stefan-Boltzmann constant. Then, developing the nonlinear radiative term

$$-\frac{dq_r}{dy'} = \frac{d}{dy'} \left(\frac{16\sigma^* T^3}{3k^*} \frac{dT}{dy'}\right) \qquad (4.26)$$

$$-\frac{dq_r}{dy'} = \frac{16\sigma^*}{3k^*} \left(3T^2 \left(\frac{dT}{dy'}\right)^2 + T^3 \frac{d^2T}{dy'^2}\right) \qquad (4.27)$$

Considering the relations of density $\frac{\rho_{hnf}}{\rho_f}$, dynamic viscosity $\frac{\eta_{hnf}}{\eta_f}$, heat capacity $\frac{(\rho C_p)_{hnf}}{(\rho C_p)_f}$, thermal conductivity $\frac{k_{hnf}}{k_f}$, electrical conductivity $\frac{\sigma_{hnf}}{\sigma_f}$, coefficient of thermal expansion $\frac{(\rho\beta)_{hnf}}{(\rho\beta)_f}$ and introducing the following dimensionless terms of Eq.(4.22).

$$u = \frac{\rho_f a u'}{\eta_f}, \qquad y = \frac{y'}{a}, \qquad \alpha_1 = \frac{\alpha_1'}{a}, \qquad \alpha_2 = \frac{\alpha_2'}{a}, \qquad \theta = \frac{T-T_a}{T_h-T_a},$$

$$\theta_h = \frac{T_h}{T_a}, \qquad Bi_1 = ah_1/k_f, \quad Bi_2 = ah_2/k_f, \quad P = -\frac{a^3\rho_f}{\eta_f^2}\left(\frac{dp}{dx'}\right), \qquad Re = \frac{v_0 a\rho_f}{\eta_f},$$

$$Gr = \frac{ga^3 T_a(\rho\beta)_f}{\rho_f v_f^2}, \qquad Da = \frac{k}{a^2}, \qquad Pe = RePr, \quad Ec = \frac{v_0^2}{(C_p)_f}(T_h - T_a), \quad Pr = \frac{\eta_f(C_p)_f}{k_f},$$

$$M = B_0 a\sqrt{\sigma_f/\eta_f}, \qquad Br = EcPr = \frac{\eta_f^3}{a^2\rho_f^2 k_f T_a}, \qquad H = \frac{Q_T a^2}{k_f}.$$

(4.28)

Equation (4.22) become

$$Pe\frac{(\rho C_p)_{hnf}}{(\rho C_p)_f}\left(\frac{d\theta}{dy}\right)$$
$$= \left(\frac{k_{hnf}}{k_f} + Rd\big((\theta_h - 1)\theta + 1\big)^3\right)\frac{d^2\theta}{dy^2}$$
$$+ 3\,Rd\,(\theta_h - 1)\big((\theta_h - 1)\theta + 1\big)^2\left(\frac{d\theta}{dy}\right)^2 \qquad (4.29)$$
$$+ \frac{Br}{(\theta_h - 1)}\left[\frac{\eta_{hnf}}{\eta_f}\left(\frac{du}{dy}\right)^2 + \frac{\sigma_{hnf}}{\sigma_f}M^2 u^2 + \frac{\eta_{hnf}}{\eta_f}\frac{u^2}{Da}\right.$$
$$\left. + \frac{\rho_{hnf}}{\rho_f}\frac{F}{\sqrt{Da}}u^3\right] + H\theta$$

and the boundary conditions Eqs. (4.23) and (4.24)

$$\frac{k_{hnf}}{k_f}\frac{d\theta}{dy} - Bi_1(\theta - 1) = 0, \text{ at } y = 0 \qquad (4.30)$$

$$\frac{k_{hnf}}{k_f}\frac{d\theta}{dy} + Bi_2(\theta) = 0, \text{ at } y = 1 \qquad (4.31)$$

where θ_h is dimensionless temperature and the radiation parameter is equivalent to $Rd = \frac{16\sigma^* T_a^3}{3k^* k_f}$.

4.2.3 Entropy generation

From Eq. (3.49), where the local entropy is shown as the sum of irreversibilities present in the system, we have

$$S = \frac{k}{T^2}\left(\frac{\partial T}{\partial y}\right)^2 + \frac{\eta}{T}\left(\frac{\partial u}{\partial y}\right)^2 + \frac{\sigma}{T}(u^2 B_0^2) + S_r + S_{Da} + S_F \tag{4.32}$$

The radiation irreversibility S_r is incorporated into Eq. (4.32) as in Eq. (3.51)

$$S = \frac{k}{T^2}\left(\frac{\partial T}{\partial y}\right)^2 + \frac{1}{T^2}\left(\frac{16\sigma^* T^3}{3k^*}\right)\left(\frac{\partial T}{\partial y}\right)^2 + \frac{\eta}{T}\left(\frac{\partial u}{\partial y}\right)^2 + \frac{\sigma}{T}(u^2 B_0^2) \tag{4.33}$$

The Eq. (2.25) states that the entropy flux $\mathbf{J}_s$ is equal to the heat flux $\mathbf{J}_q$ divided by the temperature, therefore the irreversibility due to friction S_{Da} in the porous medium and inertial effects by Forchheimer S_F is added considering Eq. (4.17)

$$\begin{aligned} S = {} & \frac{k}{T^2}\left(\frac{\partial T}{\partial y}\right)^2 + \frac{1}{T^2}\left(\frac{16\sigma^* T^3}{3k^*}\right)\left(\frac{\partial T}{\partial y}\right)^2 + \frac{\eta}{T}\left(\frac{\partial u}{\partial y}\right)^2 + \frac{\sigma}{T}(u^2 B_0^2) + \frac{1}{T}\frac{\eta}{K}u^2 \\ & + \frac{1}{T}\frac{\rho F}{\sqrt{K}}u^3 \end{aligned} \tag{4.34}$$

Transforming terms into ordinary derivatives, the local entropy generation [13, 14] for a hybrid nanofluid considering the irreversibility due to nonlinear radiative heat flow and the irreversibility due to Forchheimer drag is

$$\begin{aligned} S' = {} & \frac{1}{T^2}\left(k_{hnf} + \frac{16\sigma^* T^3}{3k^*}\right)\left(\frac{\partial T}{\partial y'}\right)^2 \\ & + \frac{1}{T}\left[\eta_{hnf}\left[\left(\frac{du'}{dy'}\right)^2 + \frac{u'^2}{K}\right] + \sigma_{hnf} B_0^2 u'^2 + \frac{\rho_{hnf} F}{\sqrt{K}}u'^3\right] \end{aligned} \tag{4.35}$$

In dimensionless form, equation (4.32) is given by

$$\begin{aligned} S = {} & \frac{(\theta_h - 1)^2}{[(\theta_h - 1)\theta + 1]^2}\left(\frac{k_{hnf}}{k_f} + Rd[(\theta_h - 1)\theta + 1]^3\right)\left(\frac{\partial \theta}{\partial y}\right)^2 \\ & + \frac{Br}{(\theta_h - 1)\theta + 1}\left[\frac{\eta_{hnf}}{\eta_f}\left[\left(\frac{du}{dy}\right)^2 + \frac{u^2}{Da}\right] + \frac{\sigma_{hnf}}{\sigma_f}M^2 u^2 \right. \\ & \left. + \frac{\rho_{hnf}}{\rho_f}\frac{F}{\sqrt{Da}}u^3\right] \end{aligned} \tag{4.36}$$

In Eq. (4.36), S is normalized by k_f/a^2. The first two terms on the right side corresponds to the irreversibilities due to heat flux by conduction and radiation S_q, the third term is the irreversibility associated to viscous dissipation S_v, the fourth term represents the irreversibility due to the viscous shear stress in the porous medium solid-nanofluid interface S_{Da} (Darcy friction), the fifth term is the irreversibility associated to Joule heating S_J and the sixth term represents the irreversibility due to Forchheimer drag S_F. Therefore, the different contributions can be represented as

$$S_q = \frac{(\theta_h - 1)^2}{[(\theta_h - 1)\theta + 1]^2} \left(\frac{k_{hnf}}{k_f} + Rd[(\theta_h - 1)\theta + 1]^3 \right) \left(\frac{\partial \theta}{\partial y} \right)^2 \tag{4.37}$$

$$S_v = \frac{Br}{(\theta_h - 1)\theta + 1} \left(\frac{\eta_{hnf}}{\eta_f} \right) \left(\frac{du}{dy} \right)^2 \tag{4.38}$$

$$S_{Da} = \frac{Br}{(\theta_h - 1)\theta + 1} \left(\frac{\eta_{hnf}}{\eta_f} \right) \frac{u^2}{Da} \tag{4.39}$$

$$S_J = \frac{Br}{(\theta_h - 1)\theta + 1} \left(\frac{\sigma_{hnf}}{\sigma_f} M^2 u^2 \right) \tag{4.40}$$

$$S_F = \frac{Br}{(\theta_h - 1)\theta + 1} \left(\frac{\rho_{hnf}}{\rho_f} \frac{F}{\sqrt{Da}} u^3 \right) \tag{4.41}$$

4.2.4 Heat transfer

The internal heat transfer denoted by the Nusselt number considering nonlinear thermal radiation, comes from Eq. (3.56) $Nu = \frac{h \cdot a}{k_f}$. The heat transfer coefficient h with a nonlinear radiative term is

$$h = \frac{q}{\Delta T} = \frac{\left(-k - \frac{16\sigma^* T^3}{3k^*} \right) \left(\frac{\partial T}{\partial y} \right)}{T - T_b} \tag{4.42}$$

Substituting Eq. (4.42) into (3.56), the Nusselt number becomes

$$Nu = \frac{a \left(-k - \frac{16\sigma^* T^3}{3k^*} \right)}{k_f (T - T_b)} \left(\frac{\partial T}{\partial y} \right) \tag{4.43}$$

For the bottom plate $y = 0$, the internal heat transfer [13, 14] considering the nonlinear thermal radiation for a hybrid nanofluid can be expressed

$$Nu_{y'=0} = -\frac{a\left(k_{hnf} + \frac{16\sigma^* T^3}{3k^*}\right)}{k_f(T_{(y'=0)} - T_b)}\left(\frac{\partial T}{\partial y'}\right)_{y'=0}$$

(4.44)

where T_b is the global temperature which is the average temperature of the nanofluid in the cross section of microchannel, $T_b = \frac{\int_0^a u'T \, dy'}{\int_0^a u'dy'}$. $T_{(y'=0)}$ is the hybrid nanofluid temperature at $y = 0$.

In dimensionless term Eq. (4.44) is given by

$$Nu_{y=0} = -\frac{\left(\frac{k_{hnf}}{k_f} + Rd[(\theta_h - 1)\theta + 1]^3\right)}{\theta_{y=0} - \frac{\int_0^1 u\theta \, dy}{\int_0^1 u \, dy}}\left(\frac{d\theta}{dy}\right)_{y=0}$$

(4.45)

To calculate the Nusselt number on the upper wall, θ and $\frac{d\theta}{dy}$ are evaluated at $y = 1$.

4.2.5 Skin friction coefficient

The skin friction coefficient represents a form of drag that acts as a resistance to the nanofluid motion in contact with the microchannel walls. When the skin friction coefficient increases, the energy expenditure necessary to reach a certain flow value also increases. Therefore, the motion of a nanofluid flowing through a given duct is improved when this resistance is reduced. C_f is defined as the skin friction coefficient and τ_w is the shear stress in the microchannel wall [66, 67].

$$C_f = \frac{a^2 \tau_w}{\rho_f v_f^2}$$

(4.46)

$$\tau_w = \eta_{hnf}\left(\frac{\partial u'}{\partial y'}\right)_{y'=a}$$

(4.47)

Where v_f is the kinematic viscosity of the base fluid.

Introducing into Eq. (4.46) the corresponding dimensionless terms of Eq. (4.12) and knowing that $\nu_f = \eta_f/\rho_f$, the dimensionless skin friction coefficient becomes

$$C_f = \frac{\eta_{hnf}}{\eta_f}\left(\frac{du}{dy}\right)_{y=0} \tag{4.48}$$

where $\left(\frac{du}{dy}\right)_{y=0}$ is the nanofluid velocity gradient evaluated at $y = 0$. To determine C_f at the top plate, the velocity gradient $\frac{du}{dy}$ is evaluated at $y = 1$.

4.3 SOLUTION OF EQUATIONS

The momentum and energy equations Eqs. (4.13) and (4.29) are coupled nonlinear equations. These equations must be solved by numerical methods. Considering the boundary conditions of Eqs. (4.14), (4.15), (4.30) and (4.31), the Runge-Kutta numerical method with the shooting technique was used. The differential equations with boundary conditions were converted to an initial value problem.

4.3.1 Numerical solution

In the method used, a variable change needs to be made. The system for first order differential equations was defined by

$$\frac{du}{dy} = p \tag{4.49}$$

$$\frac{d\theta}{dy} = q \tag{4.50}$$

Solving for $\frac{dp}{dy}$ and $\frac{dq}{dy}$, Eqs. (4.13) and (4.29) become

$$\frac{dp}{dy} = \frac{\eta_f}{\eta_{hnf}}\left(-P + Re\frac{\rho_{hnf}}{\rho_f}p - \frac{(\rho\beta)_{hnf}}{(\rho\beta)_f}Gr(\theta_h - 1)\theta\sin(\gamma) + \frac{\sigma_{hnf}}{\sigma_f}M^2u\right.$$
$$\left. + \frac{\eta_{hnf}}{\eta_f}\frac{u}{Da} + \frac{\rho_{hnf}}{\rho_f}\frac{F}{\sqrt{Da}}u^2\right) \tag{4.51}$$

$$\frac{dq}{dy} = \left(\frac{1}{\frac{k_{hnf}}{k_f} + Rd\left((\theta_h - 1)\theta + 1\right)^3} \right) \left(Pe \frac{(\rho C_p)_{hnf}}{(\rho C_p)_f} q \right.$$

$$- 3\, Rd\, (\theta_h - 1)\left((\theta_h - 1)\theta + 1\right)^2 q^2$$

$$- \frac{Br}{(\theta_h - 1)} \left[\frac{\eta_{hnf}}{\eta_f} p^2 + M^2 \frac{\sigma_{hnf}}{\sigma_f} u^2 + \frac{\eta_{hnf}}{\eta_f} \frac{u^2}{Da} \right.$$

$$\left. \left. + \frac{\rho_{hnf}}{\rho_f} \frac{F}{\sqrt{Da}} u^3 \right] - H\theta \right) \tag{4.52}$$

Initial conditions are defined to perform the shooting technique

$$u(0) = \varepsilon \tag{4.53}$$

$$p(0) = \frac{\varepsilon}{\alpha_1} \tag{4.54}$$

$$\theta(0) = \delta \tag{4.55}$$

$$q(0) = \frac{k_f}{k_{nf}} \left(Bi_1(\delta - 1) \right) \tag{4.56}$$

where ε and δ are initial values and are proposed by an iterative solution method. This method is performed until the following conditions at the upper boundary $y = 1$ are satisfied

$$q(1) = -\frac{k_f}{k_{nf}} Bi_2\, \theta(1) \tag{4.57}$$

$$p(1) = -\frac{u(1)}{\alpha_2} \tag{4.58}$$

The solution algorithm developed is based on the Bolzano method (method normally used to calculate roots of nonlinear equations). Bolzano's theorem establishes that a continuous function takes values with opposite signs, that is $f(a) \cdot f(b) < 0$, where in the interval (a, b) there exists at least one point c where $f(c) = 0$.

This is done considering that the conditions Eqs. (4.57) and (4.58) are equations with real roots, that is

$$q(1) + \frac{k_f}{k_{nf}} Bi_2\, \theta(1) = 0 \qquad\qquad (4.59)$$

$$p(1) + \frac{u(1)}{\alpha_2} = 0 \qquad\qquad (4.60)$$

When the equalities of equations (4.59) and (4.60) are satisfied with a precision of six significant digits, the last used values of ε and δ are taken.

The Mathematica *NDSolve* command is used to solve numerically the coupled nonlinear differential equations in each iteration. Fig. 4.2 presents the flow chart of the program to find the values of ε and δ. Here the variables V and T are equivalent to ε and δ respectively.
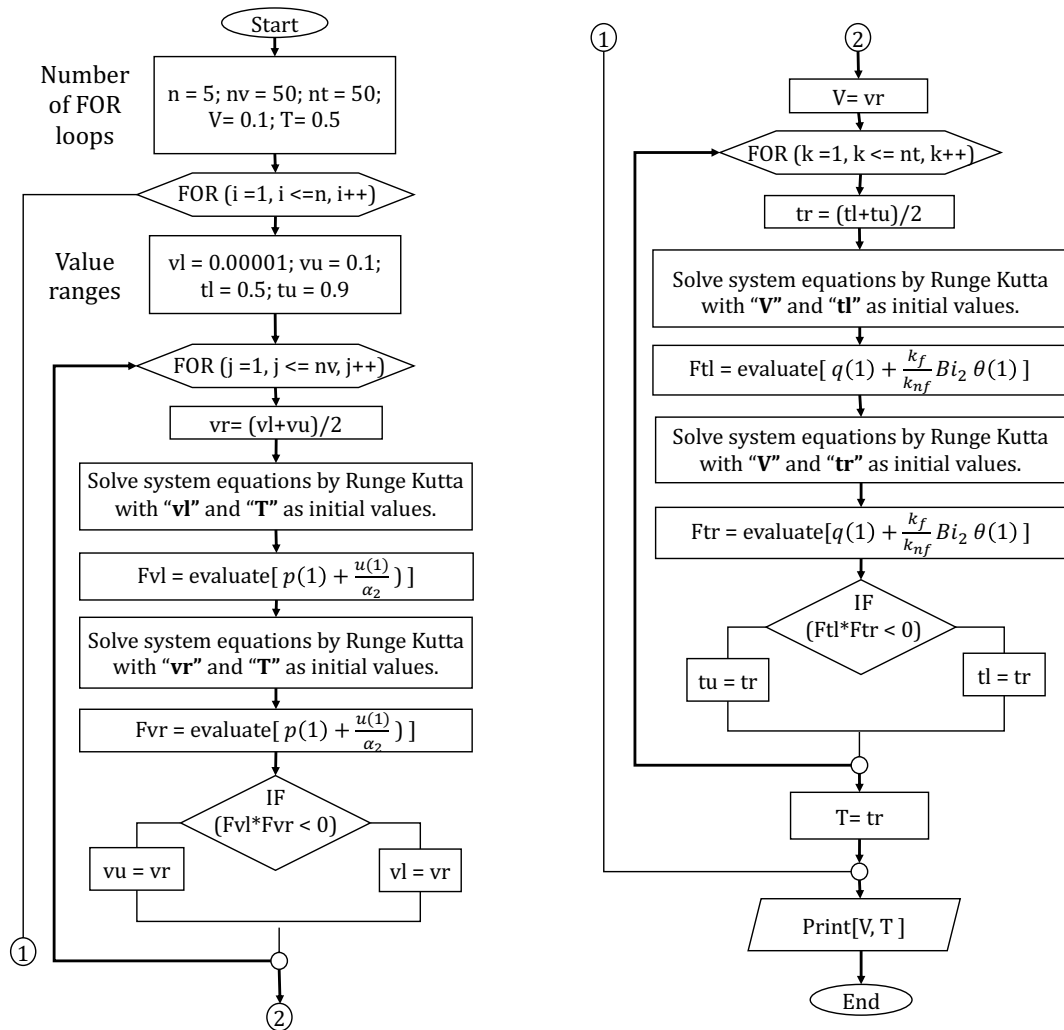

Fig. 4.2 *Flowchart of algorithm.*

114

4.3.2 Model validation

The validation of the current numerical results was carried out by comparing the numerical predictions with the analytical results obtained by Estrada et al. [28]. For this purpose, the limiting case of absence of buoyancy force, Forchheimer drag and internal heat source for unitary Al_2O_3/water nanofluid with nanoparticle concentration of $\phi = 0.01$ was considered. The validation results are presented in Table 4.1. Excellent agreement is observed, which guarantees the accuracy and reliability of the method and numerical predictions.

Table 4.1 Comparison of present numerical results with previous analytical results [28] for $Rd = Gr = F = H = 0$, $\theta_h = 2$, $Re = 1$, $Ec = 1$, $P = 1$, $M = 1$, $\alpha = 0.1$, $Pr = 1$, $Bi = 1$, $\phi_1 = 0.01$ y $\phi_2 = 0$.

y	Velocity		Temperature		Local entropy	
	Analytical [28]	*Numerical*	*Analytical [28]*	*Numerical*	*Analytical [28]*	*Numerical*
0.0	0.0336525	0.0336525	0.840677	0.840677	0.0716096	0.0716096
0.1	0.0644587	0.0644587	0.823877	0.823877	0.0586957	0.0586957
0.2	0.0895759	0.0895759	0.804454	0.804454	0.0506842	0.0506842
0.3	0.108922	0.108922	0.782364	0.782364	0.0466779	0.0466779
0.4	0.122287	0.122287	0.757497	0.757497	0.0463181	0.0463181
0.5	0.129314	0.129314	0.729676	0.729676	0.0499177	0.0499177
0.6	0.129481	0.129481	0.698662	0.698662	0.0587347	0.0587347
0.7	0.122064	0.122064	0.664127	0.664127	0.0754707	0.0754707
0.8	0.106111	0.106111	0.625623	0.625623	0.105152	0.105152
0.9	0.0803895	0.0803895	0.582507	0.582507	0.156692	0.156692
1	0.0433362	0.0433362	0.533832	0.533832	0.245741	0.245741

4.4 THERMOPHYSICAL PROPERTIES OF NANOFLUID

The correlations that define the thermophysical properties of hybrid nanofluids (Table 4.2) are taken from literature [68]. Volume fractions of two types of nanoparticles ϕ_1 and ϕ_2 are considered and the total volume fraction is taken to be $\phi = \phi_1 + \phi_2$.

The effects of five different shapes of nanoparticles (spherical, blade, brick, platelet and cylindrical) on the flow of hybrid nanofluid are explored using the dynamic viscosity correlation of Einstein-Batchelor and the thermal conductivity correlation of Hamilton–Crosser as in [42], where a and b are sphericity coefficients, and $s = 3/\psi$ denotes a contact surface. Table 4.3 shows the values of a, b and ψ for each nanoparticle shape.

Table 4.2 *Correlations of thermo-physical properties of hybrid nanofluid [64].*

Property	Author	Correlation
Density	Pak-Cho [68]	$\dfrac{\rho_{hnf}}{\rho_f} = \left((1-\phi)\rho_f + \phi_1\rho_{s1} + \phi_2\rho_{s2}\right)/\rho_f$
Dynamic viscosity	Brinkman [68]	$\dfrac{\eta_{hnf}}{\eta_f} = \dfrac{1}{\left(1-(\phi_1+\phi_2)\right)^{2.5}}$
Heat capacitance	Bourantas [68]	$\dfrac{(\rho C_p)_{hnf}}{(\rho C_p)_f} = \left((1-\phi)(\rho C_p)_f + \phi_1(\rho C_p)_{s1} + \phi_2(\rho C_p)_{s2}\right)/(\rho C_p)_f$
Thermal conductivity	Maxwell [68]	$\dfrac{k_{hnf}}{k_f} = \dfrac{\left(\dfrac{\phi_1 k_{s1} + \phi_2 k_{s2}}{\phi}\right) + 2k_f + 2(\phi_1 k_{s1} + \phi_2 k_{s2}) - 2\phi k_f}{\left(\dfrac{\phi_1 k_{s1} + \phi_2 k_{s2}}{\phi}\right) + 2k_f - (\phi_1 k_{s1} + \phi_2 k_{s2}) + \phi k_f}$
Electrical conductivity	Maxwell [68]	$\dfrac{\sigma_{hnf}}{\sigma_f} = 1 + \dfrac{3\phi(\phi_1\sigma_{s1} + \phi_2\sigma_{s2} - \phi\sigma_f)}{(\phi_1\sigma_{s1} + \phi_2\sigma_{s2} + 2\phi\sigma_f) - \phi(\phi_1\sigma_{s1} + \phi_2\sigma_{s2} - \phi\sigma_f)}$
Thermal expansion coefficient	Bourantas [68]	$\dfrac{(\rho\beta)_{hnf}}{(\rho\beta)_f} = \left((1-\phi)(\rho\beta)_f + \phi_1(\rho\beta)_{s1} + \phi_2(\rho\beta)_{s2}\right)/(\rho\beta)_f$

Table 4.3 *Hybrid correlations that consider the nanoparticle shape [68- 71].*

Property	Autor	Correlation				
Dynamic viscosity	Einstein-Batchelor	$\dfrac{\eta_{hnf}}{\eta_f} = (1 + a(\phi_1+\phi_2) + b(\phi_1+\phi_2)^2)$				
Thermal conductivity	Hamilton–Crosser	$\dfrac{k_{hnf}}{k_f} = \dfrac{(s-1)k_f + \left(\dfrac{\phi_1 k_{s1} + \phi_2 k_{s2}}{\phi}\right) + (s-1)\phi\left(\left(\dfrac{\phi_1 k_{s1} + \phi_2 k_{s2}}{\phi}\right) + k_f\right)}{(s-1)k_f + \left(\dfrac{\phi_1 k_{s1} + \phi_2 k_{s2}}{\phi}\right) - \phi\left(\left(\dfrac{\phi_1 k_{s1} + \phi_2 k_{s2}}{\phi}\right) - k_f\right)}$				
		Spherical	*Blade*	*Brick*	*Platelet*	*Cylindrical*
a		2.55	14.6	1.9	37.1	13.5
b		6.2	123.3	471.4	612.6	904.4
ψ		1	0.36	0.81	0.52	0.62

In Figs. 4.3 – 4.7 the values of viscosity and thermal conductivity as a function of the volume fraction of nanoparticles ϕ are presented using different shapes of nanoparticles and different types of hybrid nanofluids.

In Fig. 4.3 it is observed that the dynamic viscosity increases with increasing the volume fraction of nanoparticles for all hybrid nanofluids. This trend was approximately linear, it is also observed that the viscosity is the same for all the nanofluids studied, this happens because the Brinkman dynamic viscosity model only depends on ϕ.

Fig. 4.4 shows the thermal conductivity as a function of ϕ for different hybrid nanofluids. The thermal conductivity tends to increase with increasing ϕ for all nanofluids. As mentioned in section 2.5.2, this happens due to Brownian movement and the interaction of the nanolayers with the base fluid that increases heat transfer. The highest thermal conductivity occurs with the Al_2O_3+Cu and TiO_2+Cu nanofluids, due to the thermal properties of copper.

Fig. 4.3 *Dynamic viscosity as a function of ϕ for different types of hybrid nanofluids.*
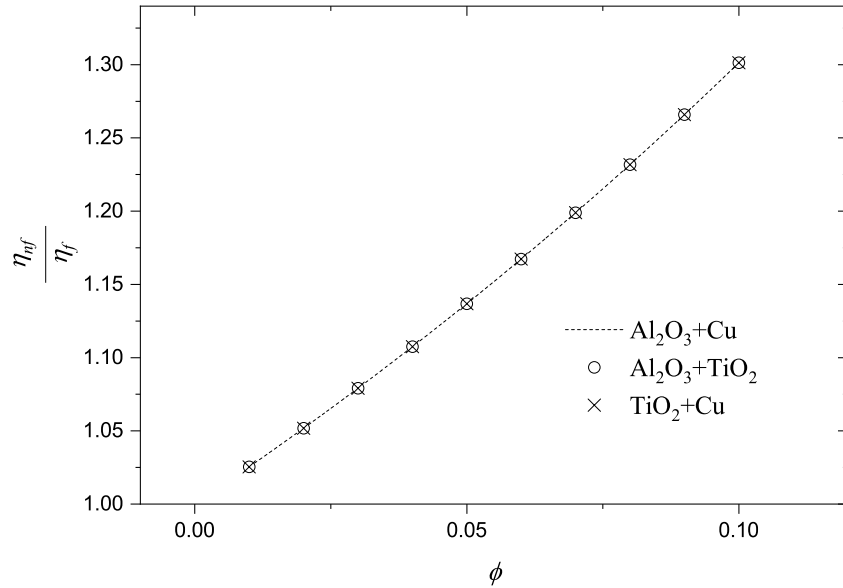
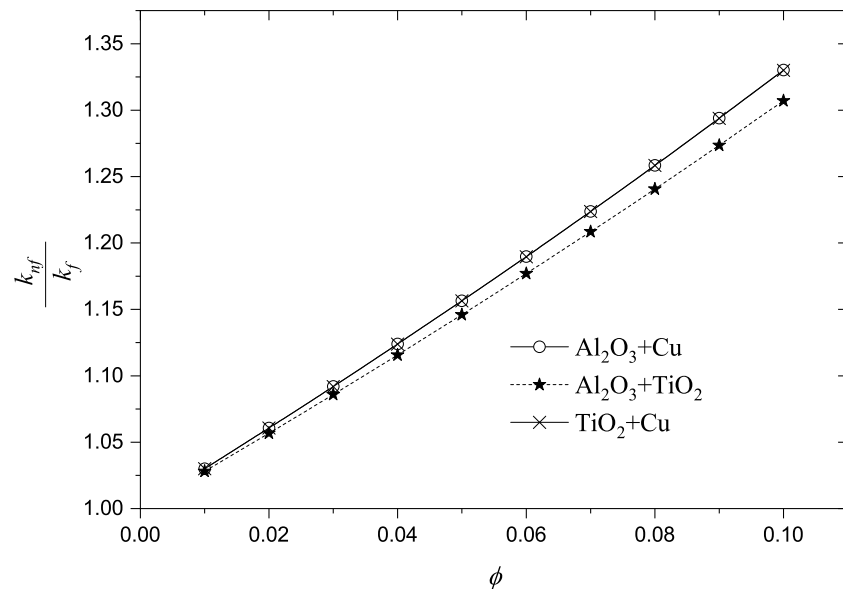**Fig. 4.4** *Thermal conductivity as a function of ϕ for different types of hybrid nanofluids.*

Fig. 4.5 shows the dynamic viscosity as a function of ϕ for different nanoparticle shapes of the Al$_2$O$_3$+Cu hybrid nanofluid. Note that for $0 \leq \phi \leq 0.07$ the highest viscosity is presented using the platelet shape and for $\phi > 0.07$ the cylindrical shape has greater viscosity. It has been found that this behavior is related to the elongation of the nanoparticles, the greater the elongation of the nanoparticles, the greater the friction and the greater the viscosity. The lowest viscosity occurs with the spherical shape, the result of less friction between the nanoparticles.

Fig. 4.5 *Dynamic viscosity as a function of ϕ considering different nanoparticles shapes for Al$_2$O$_3$+Cu nanofluid.*

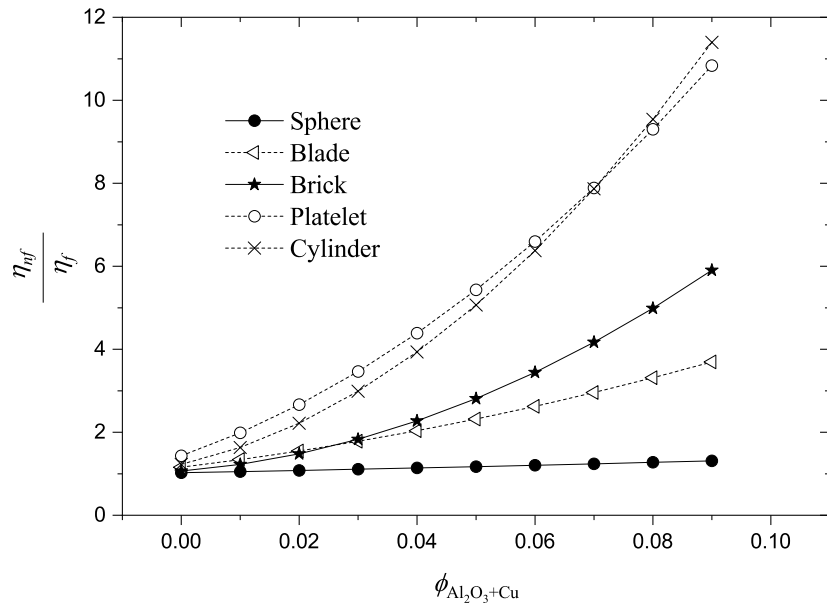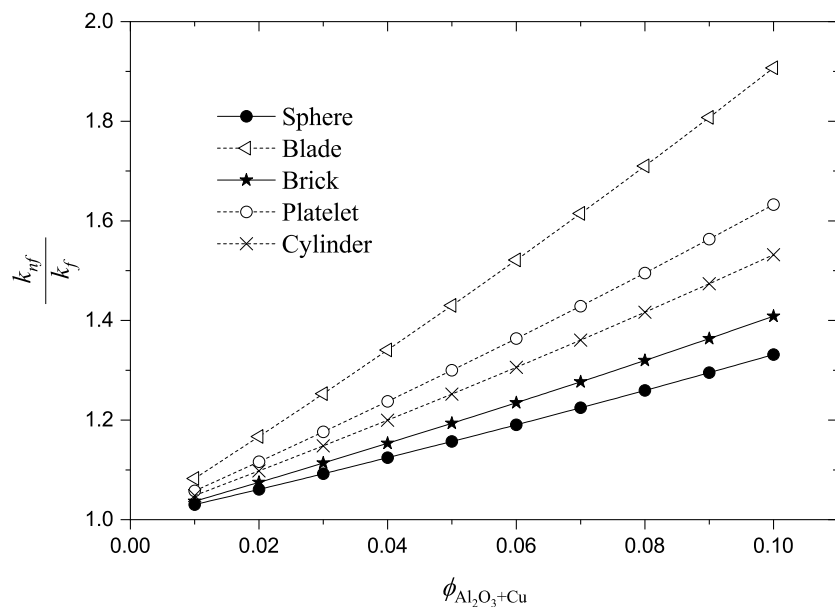**Fig. 4.6** *Thermal conductivity as a function of ϕ considering different nanoparticles shapes for Al$_2$O$_3$+Cu nanofluid.*

118

Fig. 4.6 shows the thermal conductivity as a function of ϕ using different shapes of nanoparticle for the Al₂O₃+Cu hybrid nanofluid. The highest values of thermal conductivity are obtained with the blade shape and the lowest viscosity is found with the spherical shape, this trend is inversely related to the sphericity coefficient ψ (see Table 4.3). With lower values of ψ the thermal conductivity is greater.

Fig. 4.7 Thermal conductivity as a function of ϕ_1 and ϕ_2 for different types of hybrid nanofluids, with $\phi = \phi_1 + \phi_2 = 0.1$
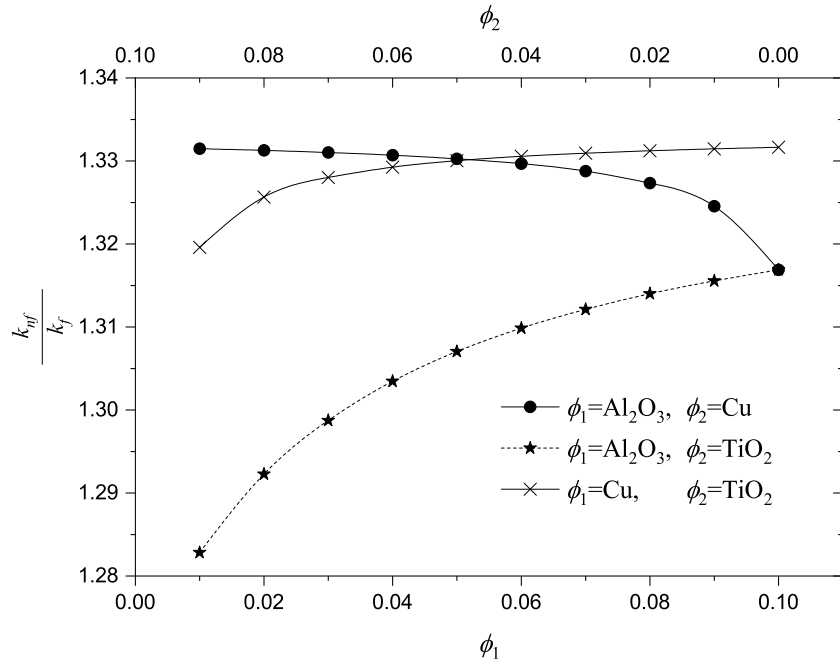

Fig. 4.7 presents the results obtained using different volume fractions ϕ_1 and ϕ_2 for thermal conductivity, with a total volume fraction $\phi = 0.1$. It is observed that for the Al₂O₃+Cu nanofluid, the thermal conductivity decreases as the percentage of Al₂O₃ nanoparticles increases and Cu decreases. On the other hand, in the Al₂O₃+TiO₂ nanofluid, the thermal conductivity increases as the percentage of Al₂O₃ nanoparticles increases and TiO₂ decreases. For Cu+TiO₂, the thermal conductivity increases due to the increase in the percentage of Cu nanoparticles and a decrease in TiO₂.

Although not shown here, the dynamic viscosity does not vary when using different types of nanoparticles, because the prediction models only take into account the effect of volume fraction of nanoparticles.

4.5 RESULTS AND DISCUSSION

With the aim to investigate the impacts of different parameters on heat transfer, entropy generation and skin friction in the system, the effects of ten relevant parameters are presented and discussed in detail. These parameters and their range of investigated values are: nanoparticle volume fraction ϕ (0-0.12), Darcy number Da (1-11), Forchheimer parameter F (1-10), hydrodynamic slip α (0.01-0.1), Biot number Bi (0.8-1), nonlinear radiation parameter Rd (1-1.2), Hartmann number M (1-2), Grashof number Gr (1-2), internal heat source H (1-2) and microchannel inclination angle γ ($\pi/6, \pi/4, \pi/2$).

In the first subsection (Fig. 4.8-4.16), the velocity and temperature profiles are shown for water-based Al$_2$O$_3$-Cu nanoparticles, while in the second (Figs. 4.17-4.23), the effects of relevant parameters on the entropy generation are shown. Optimum operating conditions with minimum entropy generation are achieved. In particular, optimum concentrations of nanoparticles are obtained for Al$_2$O$_3$-Cu/water hybrid nanofluid.

The heat transfer results are presented in the third subsection (Figs. 4.24-4.27). The Nusselt number Nu is calculated for the lower and upper plates. Optimum operating conditions with maximum heat transfer are observed for the studied hybrid nanofluid. The fourth subsection (Figs. 4.28-4.29) presents the analysis of the effects of various parameters on the skin friction coefficient C_f for the upper and lower plates of microchannel, while in the fifth subsection (Figs. 4.30-4.36), the effects of different nanoparticle shapes on the velocity, temperature, entropy, heat transfer and skin friction coefficient for the Al$_2$O$_3$-Cu/water nanofluid are analyzed.

Finally, the effects of different combinations of nanoparticles on optimum conditions for hybrid nanofluids of Al$_2$O$_3$-Cu, Cu-TiO$_2$ and TiO$_2$-Al$_2$O$_3$ are presented in Figs. 4.37-4.41. New optimum proportions of nanoparticle concentrations for Cu-TiO$_2$ /water hybrid nanofluid are achieved.

For this chapter the default fixed values, $\phi_1 = 0.05, \phi_2 = 0.05, Re = 1, Da = 1, P = 1, M = 1, \alpha = 0.1, \gamma = \pi/4, Ec = 1, Bi = 1, Rd = 1, Gr = 1, Pr = 1, F = 1, H = 1, \theta_h = 2$, are considered in the respective figures.

4.5.1 Effects of parameters on velocity and temperature profiles

In Figs. 4.8-4.16, the effects of ϕ, Da, F, Re, Gr, γ, M, α y H on the hybrid nanofluid velocity profiles and the effects of ϕ, Rd, Bi, Pr, Gr, γ y H on the hybrid nanofluid temperature profiles are investigated. In Fig. 4.8, the impacts of different concentration ratios of nanoparticles ϕ_{Al2O3}/ϕ_{Cu} are shown. These concentration ratio values are taken so that the total concentration $\phi = \phi_{Al2O3} + \phi_{Cu}$ is 0.1. It is observed that higher velocity values are achieved for Al₂O₃ nanoparticles compared to Cu nanoparticles because Al₂O₃ has a lower density than Cu. This property becomes relevant since the total concentration value $\phi = 0.1$ is the same for all cases and hence the viscosity is also the same. The hybrid nanofluid with the combination $\phi_{Al2O3} = 0.05$ and $\phi_{Cu} = 0.05$ presents the lowest velocity at the upper region of the microchannel with a decrease in velocity of approximately 3.5% at $y = 0.5$.

Fig. 4.8
Nanofluid velocity profiles for different mixing ratios of nanoparticles $\phi_{Al_2O_3}/\phi_{Cu}$.
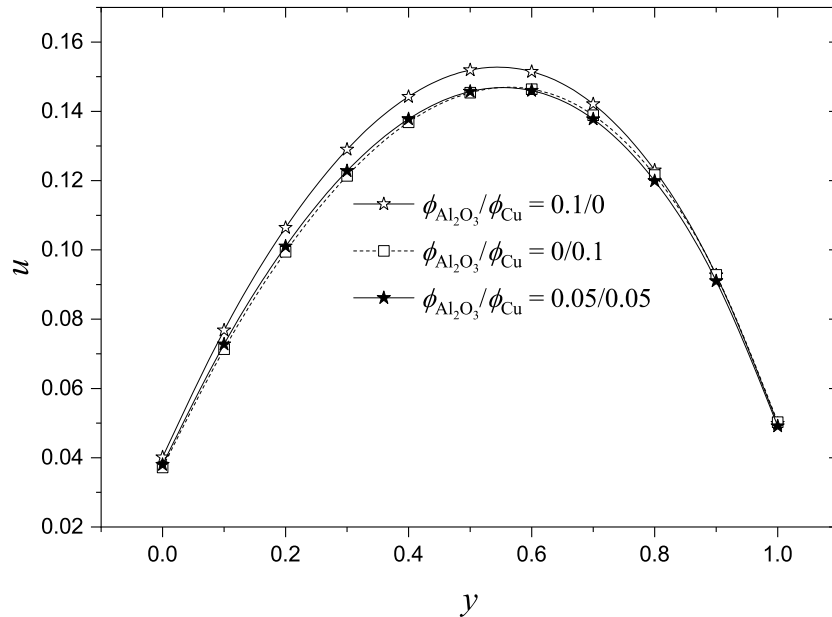
In Fig. 4.9, the temperature profiles are observed for different concentrations of each type of nanoparticle. The concentrations $\phi_{Al2O3} = 0.1$ and $\phi_{Cu} = 0$ (absence of Cu nanoparticles) slightly increases the temperature on the bottom plate due to a lower thermal conductivity of Al₂O₃ compared to that of Cu. The opposite happens for the concentrations $\phi_{Al2O3} = 0$ and $\phi_{Cu} = 0.1$ (absence of Al₂O₃ nanoparticles) with a higher temperature in the microchannel region close to the top plate due to the higher thermal conductivity of Cu compared to that of Al₂O₃. This fact causes a greater heat flow from the hot bottom plate to the cold top plate of microchannel. The lowest temperature values at the microchannel bottom region ($y = 0 - 0.5$) occur for the hybrid nanofluid when $\phi_{Al2O3} = 0.05$ and $\phi_{Cu} = 0.05$ compared to the other two proportions of nanoparticles.

Fig. 4.9

Nanofluid temperature profiles for different mixing ratios of nanoparticles $\phi_{Al_2O_3}/\phi_{Cu}$.
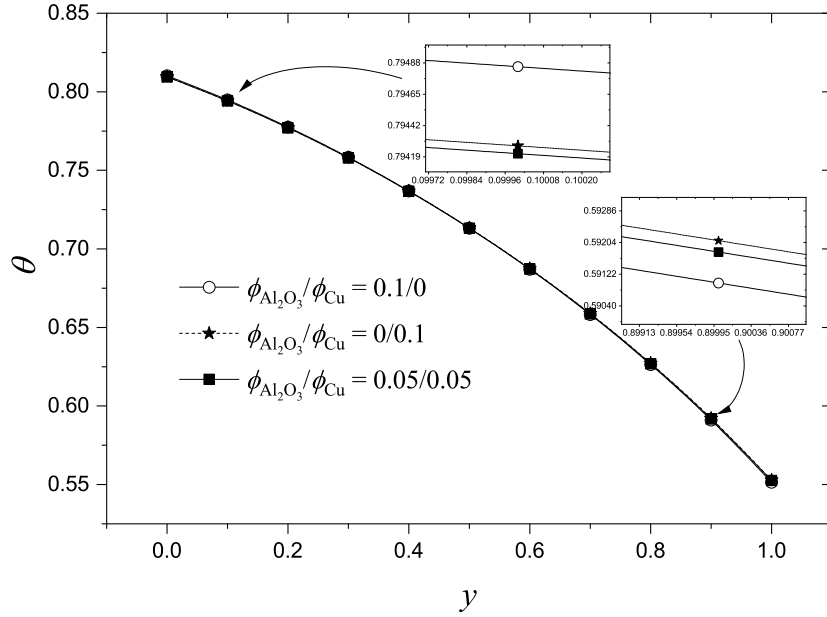

Fig. 4.10

Nanofluid velocity profiles for different values of Da and F. $\phi_{Al_2O_3} = 0.05$, $\phi_{Cu} = 0.05$.
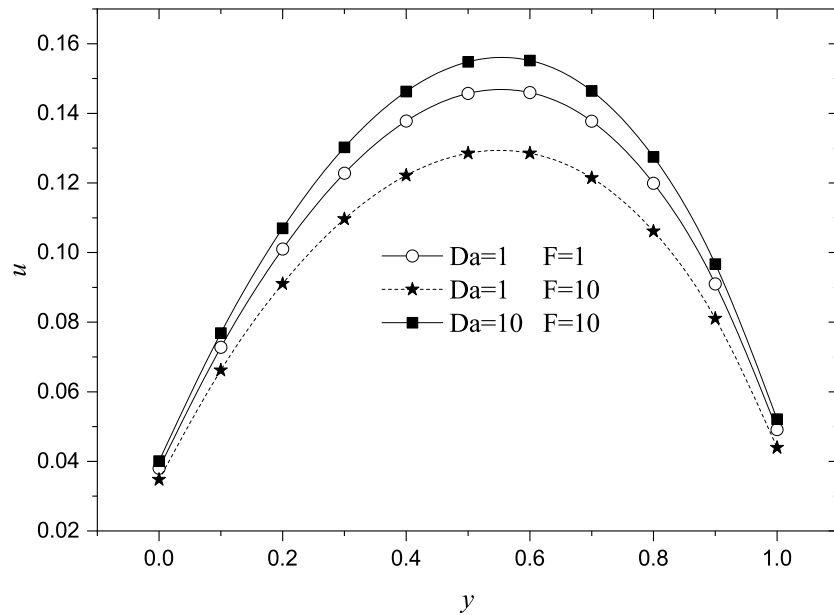

Fig. 4.10 shows the hybrid nanofluid velocity for different values of Da and F. When F or the inertial effect in the porous medium increases, the velocity decreases because the drag of the porous medium increases. Thus, the flow resistance increases and the hybrid nanofluid velocity decreases. When F increases from 1 to 10, the velocity decreases from 0.1457 to 0.1285 in the microchannel center ($y = 0.5$). On the other hand, the velocity increases 20% in the microchannel center when Da increases from 1 to 10 due to the increment of the medium permeability.

When Da increases from 1 to 10, the temperature of the nanofluid increases slightly due to the increment in the viscous heating caused by the increment in the velocity. The opposite occurs as F increases and therefore the temperature decreases slightly. These temperature variations are very small and for this reason they are not shown.

Fig. 4.11 shows the effect of the radiation parameter Rd and the Biot number for symmetric conditions ($Bi_1 = Bi_2$) on the temperature profile. For Rd variations from 0.5 to 1, the temperature decreases throughout the microchannel by approximately 9%, this occurs due to the increment in heat transfer from the nanofluid to the environment. On the other hand, increasing Bi from 1 to 2 increases the temperature gradient. Thus, the temperature increases from 0.81 to 0.85 on the hot bottom plate and decreases from 0.55 to 0.45 on the cold top plate. This is due to the increment of heat flow from the hot medium to the hybrid nanofluid through the bottom plate and the increment of heat flow from the nanofluid to the environment through the cold top plate of microchannel.

Fig. 4.11
Nanofluid temperature profiles for different values of Rd and Bi.
$\phi_{Al_2O_3} = 0.05,$
$\phi_{Cu} = 0.05.$
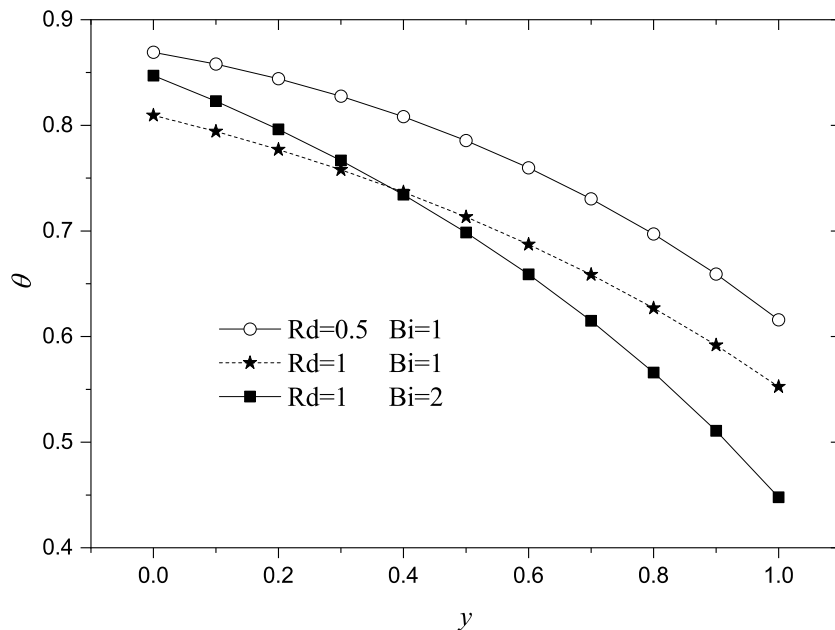
Although not shown here, increasing Rd from 0.5 to 1 decreases the velocity in the microchannel center from 0.15 to 0.145, equivalent to a decrement of 3%. This fact is due to the increase in the viscosity of the hybrid nanofluid caused by the decrement in temperature. On the other hand, increasing Bi from 1 to 2 decreases the velocity by approximately 2% near the upper plate due to the decrement in temperature for this microchannel region.

Fig. 4.12 shows the effect of Grashof number Gr and microchannel inclination angle γ on the velocity profile. It is observed that increasing Gr from 1 to 2 increases the velocity in the microchannel center from 0.16 to 0.23 (41%) due to the buoyancy force increment. On the other hand, an inclination angle of $\pi/2$, which represents a vertical microchannel, generates a greater buoyancy force. An increase in velocity of 13% was found for a vertical microchannel ($\pi/2$) compared to an inclined microchannel at 45º ($\pi/4$).

In Fig. 4.13, the temperature profiles are shown for Gr and γ. The temperature increases with the increment in Gr from 1 to 2 and γ from $\pi/4$ to $\pi/2$ due to the increment in heat by viscous dissipation caused by the increment in the hybrid nanofluid velocity gradient.

Fig. 4.12
Nanofluid velocity profiles for different values of Gr and γ. $\phi_{Al_2O_3} = 0.05$, $\phi_{Cu} = 0.05$.
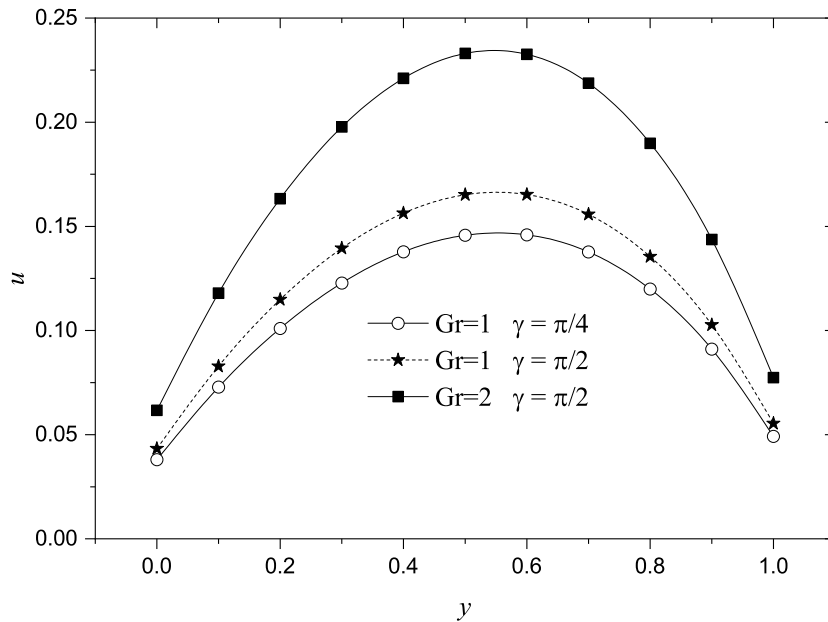
The effects of the internal heat source H and the Reynolds number Re on the velocity profiles are shown in Fig. 4.14. Increasing the internal heat source parameter H increases the velocity in the microchannel center by approximately 4 %. This behavior occurs due to the increment in temperature with the consequent decrement in the viscosity of hybrid nanofluid. Increasing Re tilts the velocity profile to the right and the velocity decreases near the hot bottom plate (y=0.3) by approximately 11% due to the increment in injection. However, the velocity of the hybrid nanofluid increases near the cold top plate (y=0.9) by 7% due to the increment in suction.

*Fig. **4.13***
Nanofluid
temperature
profiles for
different values
of Gr and γ.
$\phi_{Al_2O_3} = 0.05$,
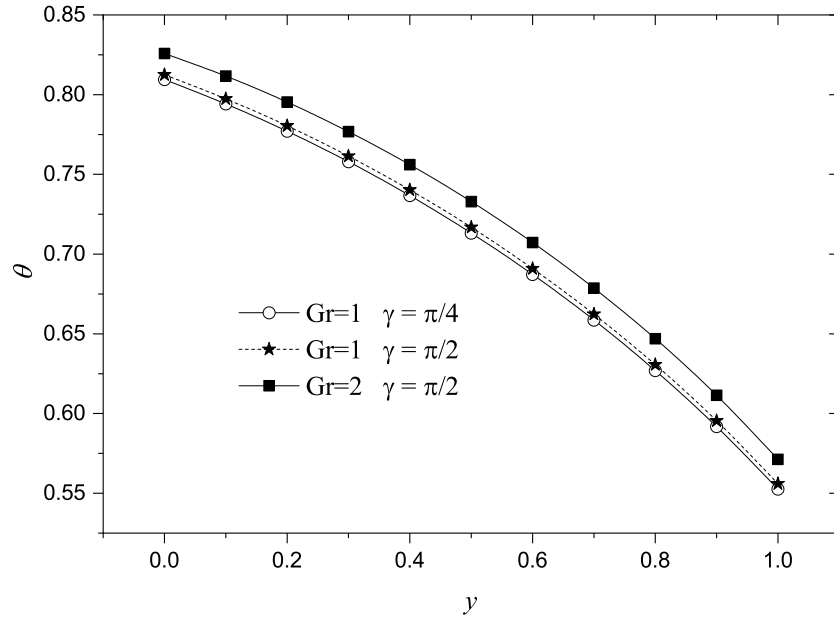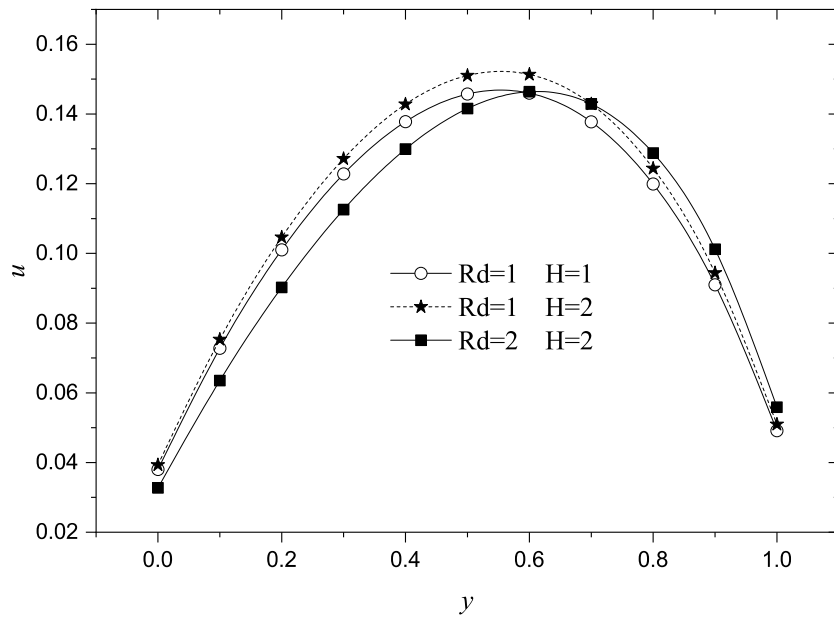$\phi_{Cu} = 0.05$.

Fig. 4.14
Nanofluid
velocity profiles
for different
values of Re and
H. $\phi_{Al_2O_3} = 0.05$,
$\phi_{Cu} = 0.05$.

On the other hand, it was obtained that with the increment of *Re* the temperature increases by approximately 4% throughout the microchannel due to the injection of hot fluid into the microchannel through the bottom plate.

Fig. 4.15 shows the temperature profiles for different values of H and Pr. When H increases from 1 to 2, the temperature increases up to 12%. It is evident that the internal heat generation produces a higher temperature in the hybrid nanofluid. On the other hand, increasing Pr from 1 to 2 increases the temperature by approximately 4.5%. This indicates that the heat diffusion rate is lower than the momentum diffusion rate. Although not shown here, increasing Pr from 1 to 2 increases the nanofluid velocity in the microchannel center by 2% due to the increment in the temperature with the consequent decrement in the hybrid nanofluid viscosity.
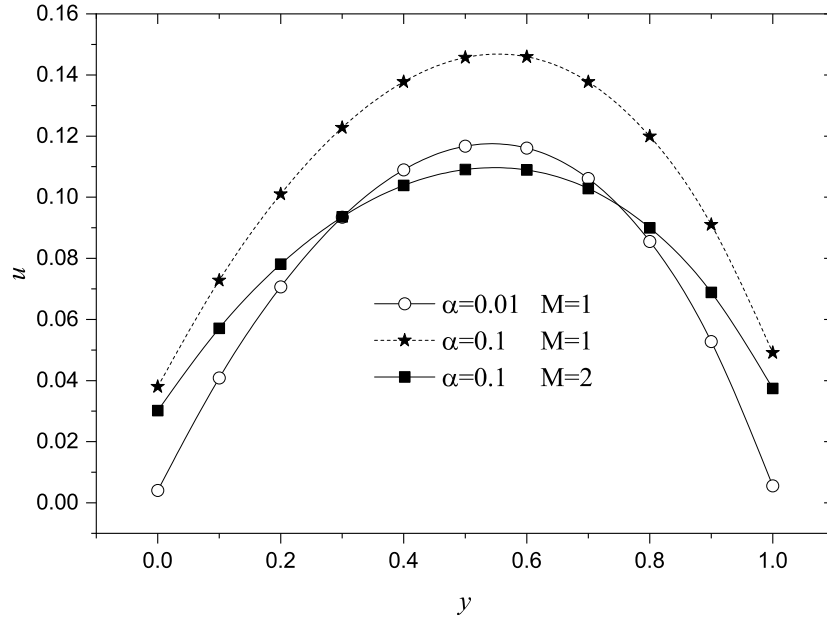
Fig. 4.15
Nanofluid
temperature
profiles for
different values
of Pr and H.
$\phi_{Al_2O_3} = 0.05,$
$\phi_{Cu} = 0.05.$
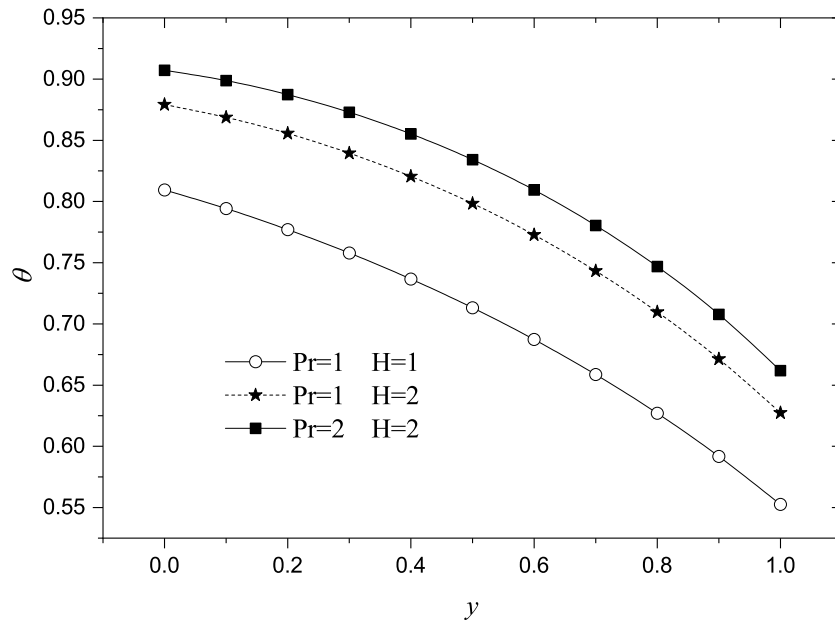
In Fig. 4.16, the effects of slip α and Hartmann number M on the hybrid nanofluid velocity are observed. It is found that increasing the parameter α increases the velocity values throughout the profile due to the reduction of friction on the walls. On the other hand, the velocity profile flattens and decreases by approximately 25% at the center of the channel with the increment of M from 1 to 2 due to the effect of the Lorentz force that opposes the motion of hybrid nanofluid.

A very small increase in temperature was found when α increases from 0.01 to 0.1. This effect occurs due to the increase in the nanofluid velocity which causes an increment in the viscous dissipation associated to the friction with the porous medium and in the Joule heating. Increasing M, the temperature slightly decreases throughout the profile because both the velocity and the velocity gradient decrease. Therefore, the viscous dissipation associated with both porous medium friction and wall friction decreases.

Fig. 4.16

Nanofluid velocity profiles for different values of α and M. $\phi_{Al_2O_3} = 0.05$, $\phi_{Cu} = 0.05$.


4.5.2 Effects of parameters on entropy generation

In this section, the effects of different parameters on entropy are analyzed. The local entropy S for different values of ϕ_1 and ϕ_2 is shown in Fig. 4.17. It is observed that S values are smaller in the bottom region of microchannel due to the higher temperature in this region which has an inverse behavior to entropy. There is also a small increment of entropy in the bottom and top plates of microchannel due to the irreversibility associated to friction between the microchannel plates and the hybrid nanofluid. For concentrations of $\phi_{Al_2O_3} = 0.1$ and $\phi_{Cu} = 0$ which corresponds to absence of Cu nanoparticles, higher local entropy values are obtained near the plates, approximately 11% at $y = 0$ and 0.1% at $y = 1$ compared to the other two concentrations explored.

This fact occurs due to the increment in irreversibility associated to viscous dissipation S_v in the microchannel plates for the Al₂O₃/water nanofluid. For the inverse case of absence of Al₂O₃ nanoparticles ($\phi_{Al_2O_3} = 0$ and $\phi_{Cu} = 0.1$), the entropy is greater at the center of the microchannel ($y = 0.5$) with an increase of approximately 2% because the irreversibility associated to heat transfer S_q is greater than the irreversibility S_v in this microchannel region. The high thermal conductivity of Cu causes a decrement in the nanofluid temperature and hence the entropy increases. Furthermore, it is observed that approximately from $y = 0.6$ to $y = 1$, the lowest entropy values are obtained for concentrations of $\phi_{Al_2O_3} = 0.05$ and $\phi_{Cu} = 0.05$.

Fig. 4.17 Local entropy for different nanoparticle mixing ratios $\phi_{Al_2O_3}/\phi_{Cu}$ with total $\phi = 0.1$.
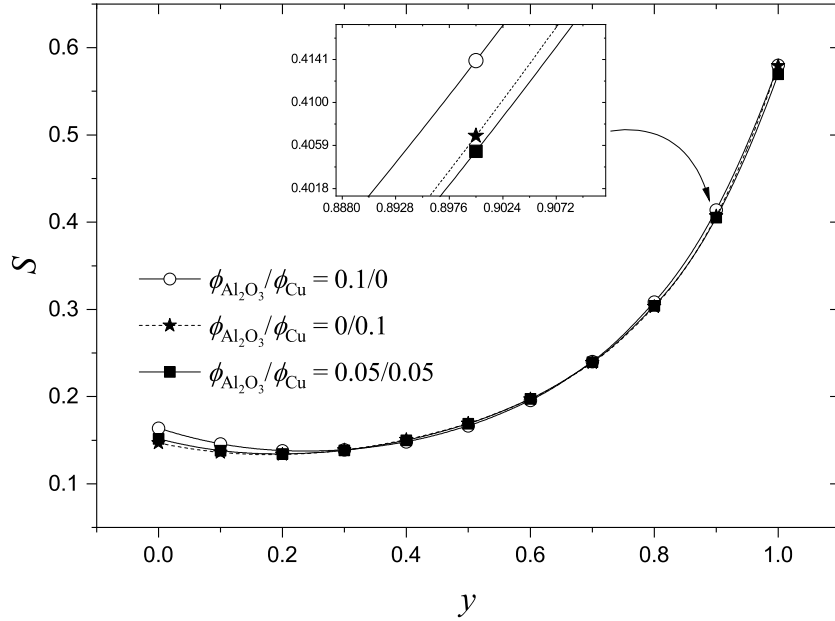

In Figs. 4.18 – 4.23, the effects of different physical parameters on the global entropy $< \dot{S} >$ are analyzed. In Fig. 4.18, it is observed that $< \dot{S} >$ decreases with the increment in ϕ from 0 to 0.1 due to the decrement in irreversibility associated with the viscous dissipation S_v, which is dominant. When Gr increases from 1 to 1.5, the global entropy increases by approximately 10.8% for all values of ϕ. On the other hand, increasing the channel inclination from 45° ($\pi/4$) to 90° ($\pi/2$) increases the global entropy in the microchannel by approximately 14.5%. This happens mainly due to the increase in velocity and irreversibility associated to viscous dissipation.

Fig. 4.18 Global entropy as function of ϕ for different values of γ and Gr.
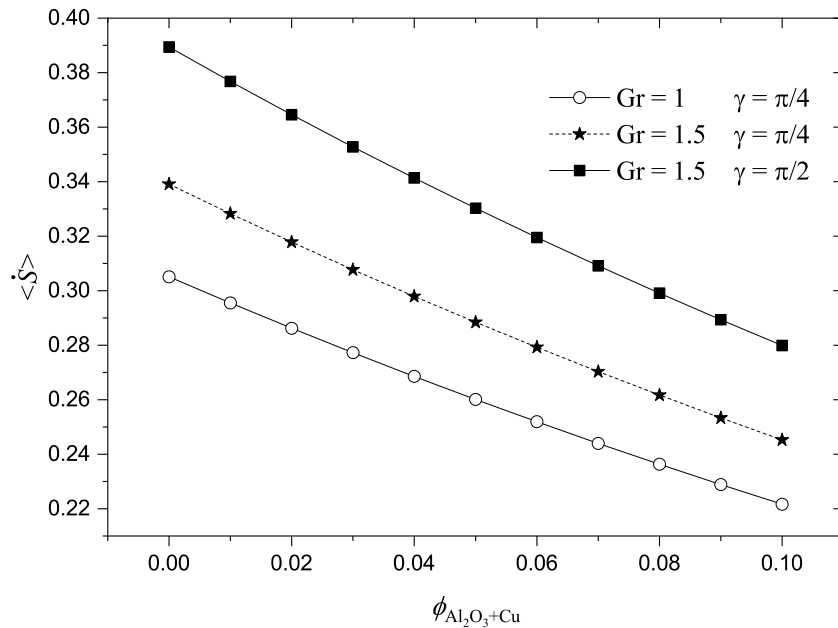
In Fig. 4.19, $< \dot{S} >$ is reported as a function of various mixing ratios of nanoparticles $\phi_{Al_2O_3}/\phi_{Cu}$ for different values of Gr and H. The total nanoparticle concentration $\phi = \phi_{Al_2O_3} + \phi_{Cu}$ remains constant with a value of 0.1 for all different mixing ratios of nanoparticles. Thus, when the Cu concentration in the mixture increases, the Al₂O₃ concentration decreases, and vice versa. Optimum ratios of the hybrid nanofluid nanoparticles with minimum entropy are found for all cases. In this way, an optimum ratio of $\phi_{Al_2O_3}/\phi_{Cu} = 0.07/0.03$ with minimum global entropy are obtained for $Gr = 1.2$. It is observed that as Gr increases, the optimum value of mixing ratio moves to higher values, therefore the optimum concentration of Al₂O₃ increases while that of Cu decreases in the mixture. On the other hand, the increase in H does not modify the optimum nanoparticle mixing ratio with minimum entropy. From Fig. 4.19, it is also observed that the global entropy always increases when both Gr and H.

Fig. 4.19 *Global entropy as function of different nanoparticle mixing ratios $\phi_{Al_2O_3}/\phi_{Cu}$ with total $\phi = 0.1$ for different values of Gr and H.*
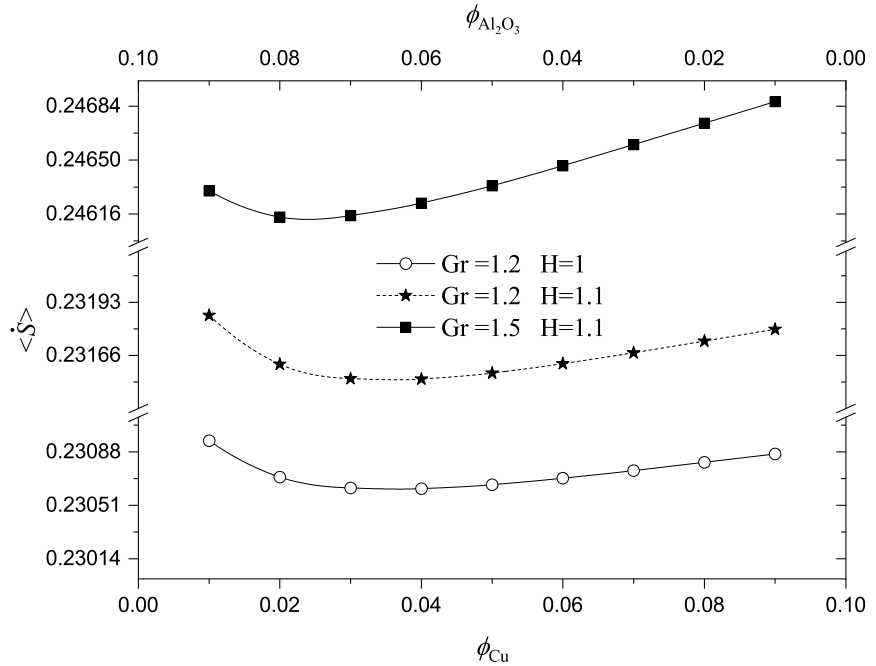

The thermal conductivity, density and thermal expansion coefficient of Cu are higher than those of Al₂O₃, therefore the effective density of the hybrid nanofluid increases for higher concentration of Cu in the mixture and lower values of velocity and velocity gradient are reached. This fact decreases the irreversibilities associated with viscous dissipation due to friction in both the porous medium and the microchannel plates. For this reason, when the Cu concentration increases from 0 to 0.1 and the Al₂O₃ concentration decreases from 0.1 to 0, initially the entropy decreases until it reaches a minimum value. Once the minimum value is reached, the entropy starts to increase with the increment in the Cu concentration (decrement in the Al₂O₃ concentration).

This increment is due to both the decrement in temperature caused by the high thermal conductivity of Cu and the increment in the velocity of the nanofluid caused by the high thermal expansion coefficient of Cu, which produces an increment in the buoyancy force. It is also found that these optimum conditions only are achieved for inclined and vertical microchannels where the effect of buoyancy force exists.

Optimum mixing ratios of $\phi_{Al_2O_3}/\phi_{Cu}$ are also found for total concentration of 5%. Fig. 4.20 presents optimum ratios with minimum entropy production for different values of Gr. The $\phi_{Al_2O_3}/\phi_{Cu}$ optimum ratios are: 0.025/0.025 for $Gr = 1.1$, 0.03/0.02 for $Gr = 1.2$ and 0.036/0.014 for $Gr = 1.5$. From Fig. 4.20, it can be noted that the optimum conditions move to higher ratios, that is, lower Cu concentration and higher Al₂O₃ concentration when Gr increases due to the increment in the buoyant force.

Fig. 4.20 Global entropy as function of different nanoparticle mixing ratios $\phi_{Al_2O_3}/\phi_{Cu}$ with total $\phi = 0.05$ for different values of Gr.
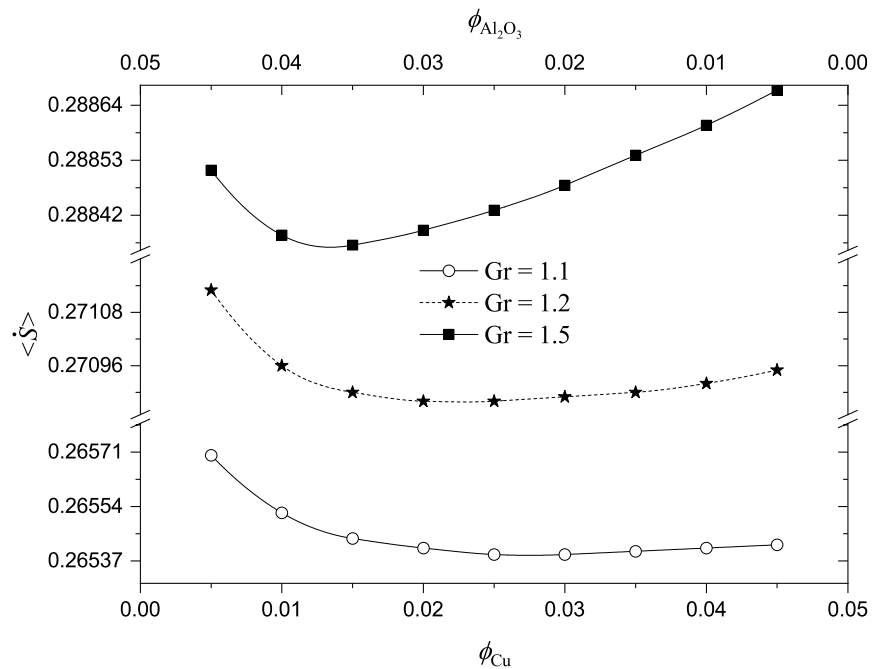
Optimum values of hydrodynamic slip with minimum total entropy generation are presented in Fig. 4.21. It is observed that the entropy decreases with the increment in the Hartmann number M from 1 to 1.2. This effect is due to the decrement in the velocity and velocity gradient which reduces the irreversibility associated to friction in the porous medium and the microchannel plates. The inverse occurs for the increment in the inclination angle from π/6 to π/40 and therefore the entropy increases. The minimum entropy is reached in all cases for slip values between α=0.06 and α=0.07. It is important to mention that for low values of Reynolds number ($Re < 2$), the optimum conditions disappear.

Fig. 4.21 *Global entropy as function of α for different values of M and γ. $Re = 2$, $\phi_{Al_2O_3} = 0.05$, $\phi_{Cu} = 0.05$.*
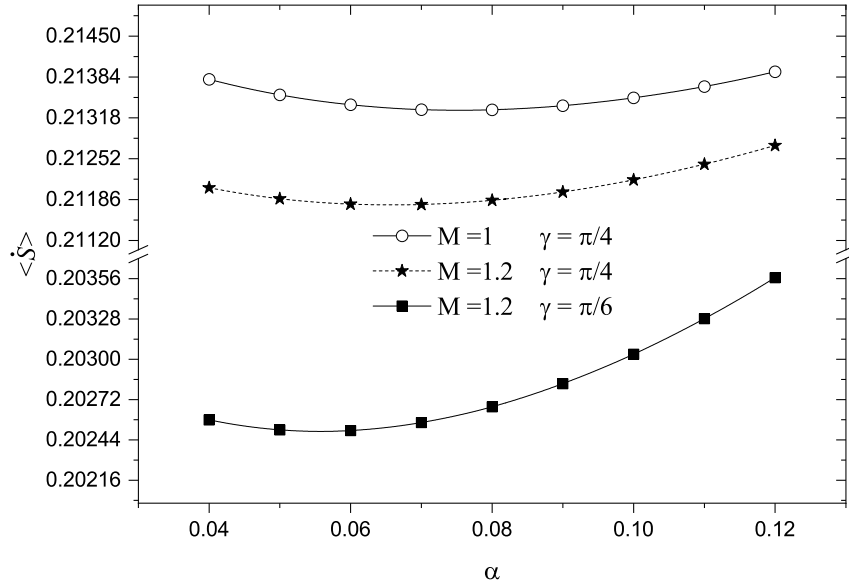

Entropy global $<\dot{S}>$ as function of H is presented in Fig. 4.22. It is observed that the entropy always increases with H because a lower viscosity and a higher velocity that increases the irreversibilities S_{Da}, S_J, and S_F are reached. When Da increases from 1 to 2, the global entropy increases by approximately 1.1%. Once more, this effect occurs due to the increment in the hybrid nanofluid velocity when the permeability of the porous medium increases. On the other hand, when the Forchheimer parameter F increases, the entropy decreases due to the increment of the inertial effect in the porous medium that decreases the velocity. When F increases from 1 to 2, the entropy decreases by approximately 0.3%.

Fig. 4.22 *Global entropy as function of H for different values of Da and F. $\phi_{Al_2O_3} = 0.05$, $\phi_{Cu} = 0.05$.*
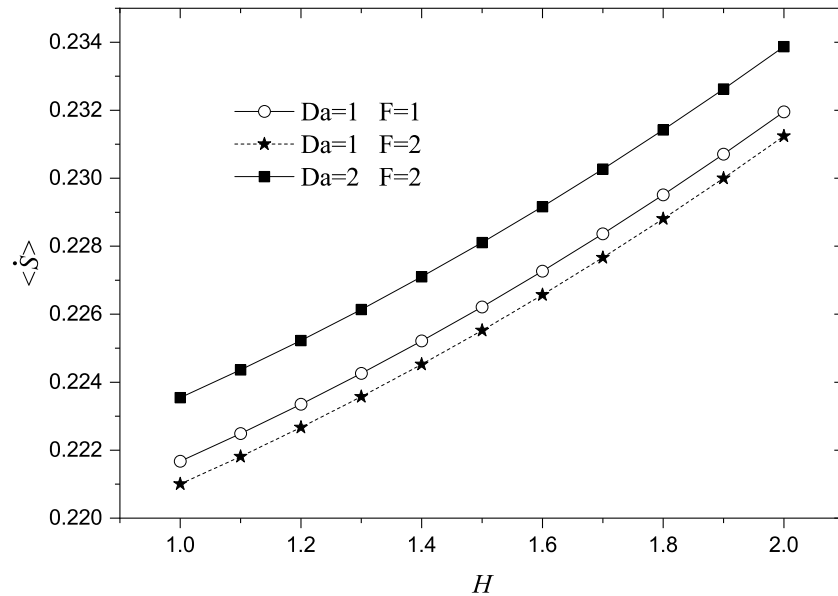
The effects of Rd and Bi on the global entropy are shown in Fig. 4.23. It is observed that when Rd increases from 1 to 1.2, the global entropy increases approximately 9.5%. This fact is caused by the decrement in the hybrid nanofluid temperature. Also, with the increase of Bi from 0.8 to 1, the global entropy increases approximately 23% due to the increment in the temperature gradient caused by the increment in the convective heat transfer through the microchannel plates.

Fig. 4.23 *Global entropy as function of ϕ for different values of Rd and Bi.*
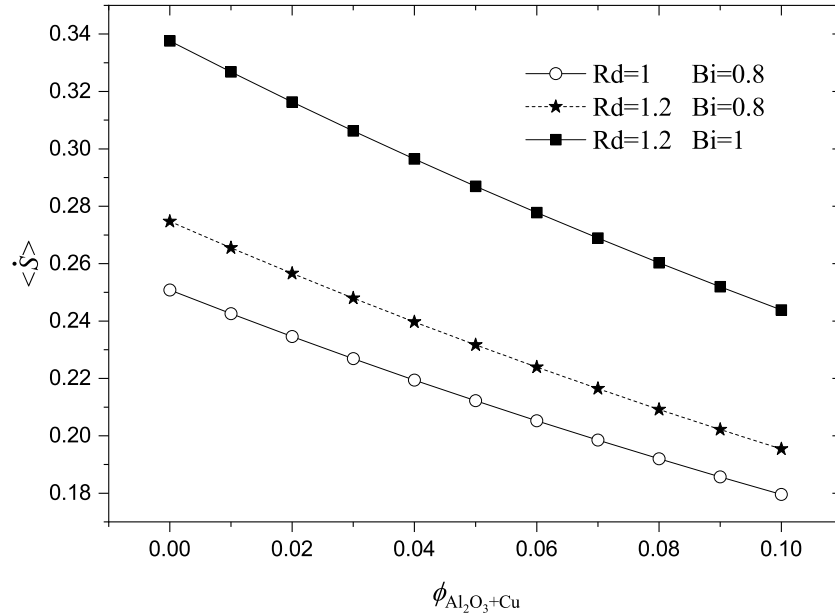
4.5.3 Effects of parameters on heat transfer

The Nusselt number is analyzed for the lower and upper plates of microchannel considering different values of ϕ, Rd, α, Gr, γ, H, M, Da and F (Figs. 4.24-4.27). The effect of the total volume fraction ϕ on heat transfer is observed in Fig. 4.24. When ϕ increases, the heat transfer in the nanofluid increases due mainly to the improvement in the nanofluid thermal conductivity. Increasing M from 1 to 2 increases the heat transfer near the hot bottom plate $y = 0$ due to the increment in the temperature gradient across the bottom plate. Furthermore, when the inclination angle of the microchannel γ increases, $Nu_{y=0}$ decreases due to the reduction in the temperature gradient near the bottom plate. On the other hand, Fig. 4.25 shows that the effects of M and γ on the upper plate $Nu_{y=1}$ are inverse. This happens due to the fact that the temperature gradient in this region of the microchannel decreases with M and increases with γ.

Fig. 4.24 Nusselt number at hot bottom plate as function of φ for different values of M and γ.
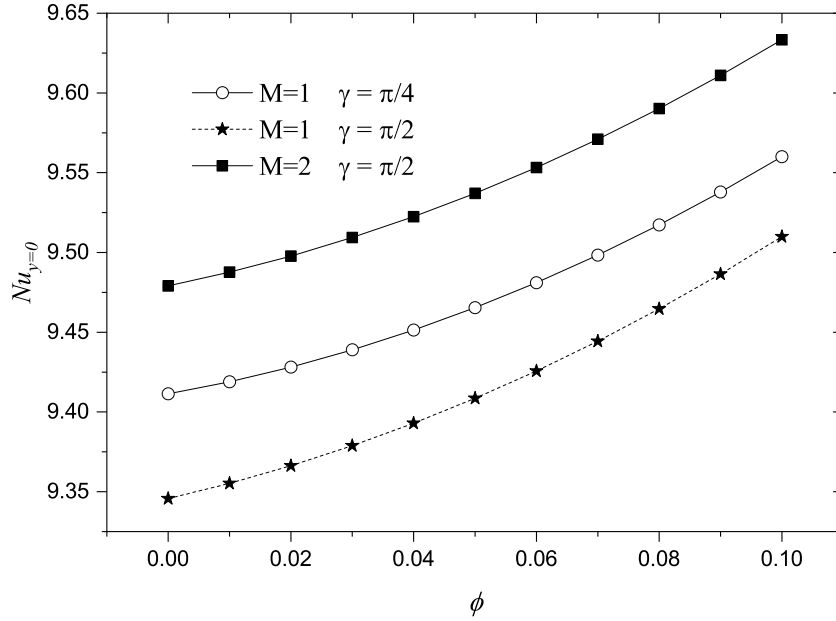
Fig. 4.25 Nusselt number at cold top plate as function of φ for different values of M and γ.
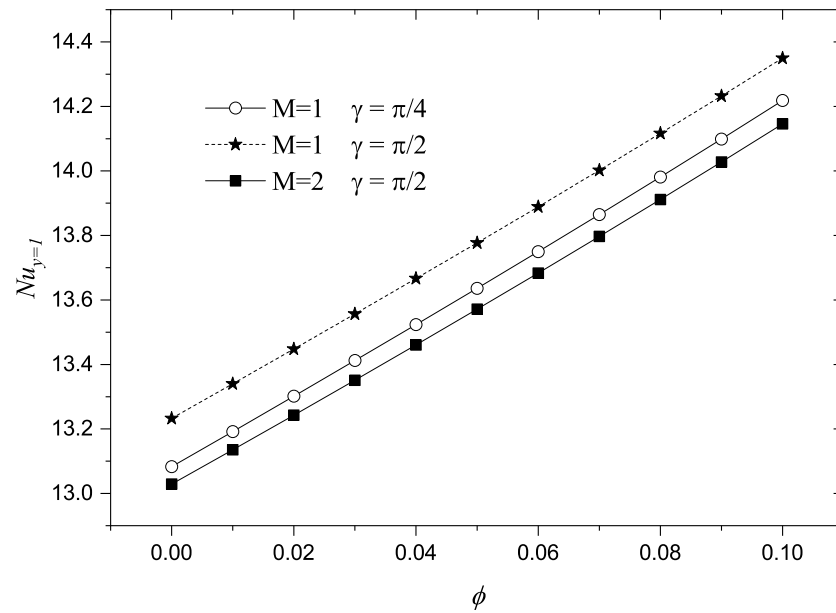
The increment or decrement in the global temperature T_b of the nanofluid causes different effects on the Nusselt number for both microchannel plates. When T_b increases, the $Nu_{y=1}$ increases and the $Nu_{y=0}$ decreases. This fact is because $|\theta_{y=1} - T_b|$ decreases for the top plate and $|\theta_{y=0} - T_b|$ increases for the bottom plate. Fig. 4.26 shows the results of $Nu_{y=0}$ as a function of Gr. When Gr increases, the Nu number increases by reaching a maximum value and then decreases.

This initial increment in the heat transfer with Gr occurs due to the increment in the global temperature T_b that causes a lower temperature difference with the hot bottom plate. After reaching the maximum value, the Nu begins to decrease due to the decrease in the temperature gradient evaluated in $y = 0$ which becomes predominant. Note that optimum conditions with maximum heat transfer are found at approximately $Gr = 0.6$ for all cases. Increasing the radiation parameter Rd from 1 to 1.1 increases the heat transfer from 10.56 to 11.43 (8.2%). On the other hand, when H increases from 0.1 to 0.2, Nu decreases from 11.43 to 11.35 due to to the decrease in the nanofluid temperature gradient near the bottom plate.

Fig. 4.26 Nusselt number at hot bottom plate as function of Gr for different values of Rd and H.
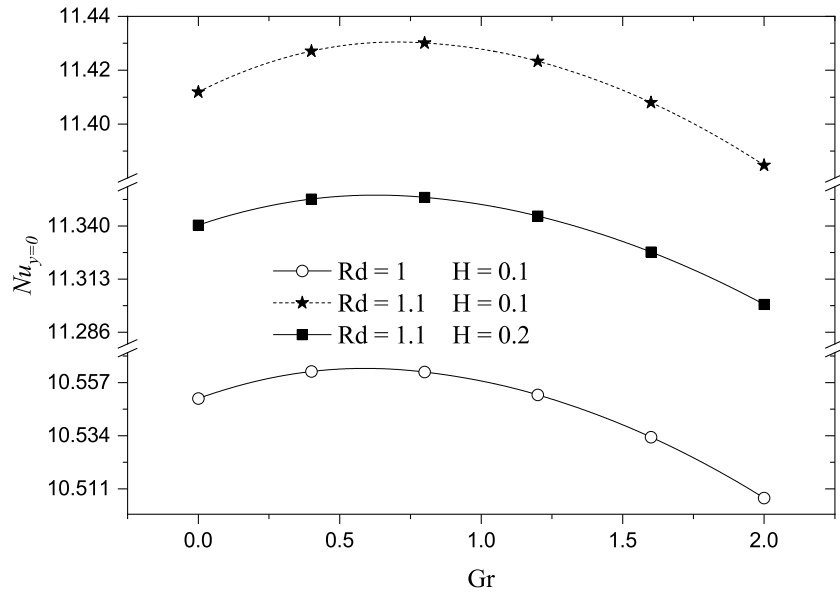
In Fig. 4.27, the Nusselt number for the cold top plate is presented, it is observed that a maximum heat transfer is reached at approximately $\alpha = 0.09$ and then Nu decreases. This happens because the increment in the temperature gradient is dominant for low values of α, while the increment in the temperature difference between T_b and the temperature of the top plate dominates for higher values of α. Optimum conditions with maximum heat transfer are achieved for all curves. Increasing Da from 10 to 11 causes a slight increase in the maximum value of heat transfer of 0.02% due to the increase in the temperature gradient. On the other hand, increasing F from 1 to 2 decreases the maximum value of heat transfer by 0.06% due to a decrease in the temperature gradient in the top plate. These maximum heat transfer values are achieved using an inclination angle of $\gamma \leq \pi/6$ for low velocity values and $M = 0.1$. Thus, for higher values of inclination and velocity, the optimum conditions disappear because the increase in the temperature difference between T_b and the temperature of the top plate dominates for the entire range of explored α values, hence de Nu always increases.

Fig. 4.27 *Nusselt*
number at cold
top plate as
function of α for
different values
of Da and F.
$Rd = 0.1, H = 0,$
$M = 0.1, \gamma = \pi/$
$6, \phi_{Al_2O_3} = 0.05,$
$\phi_{Cu} = 0.05.$
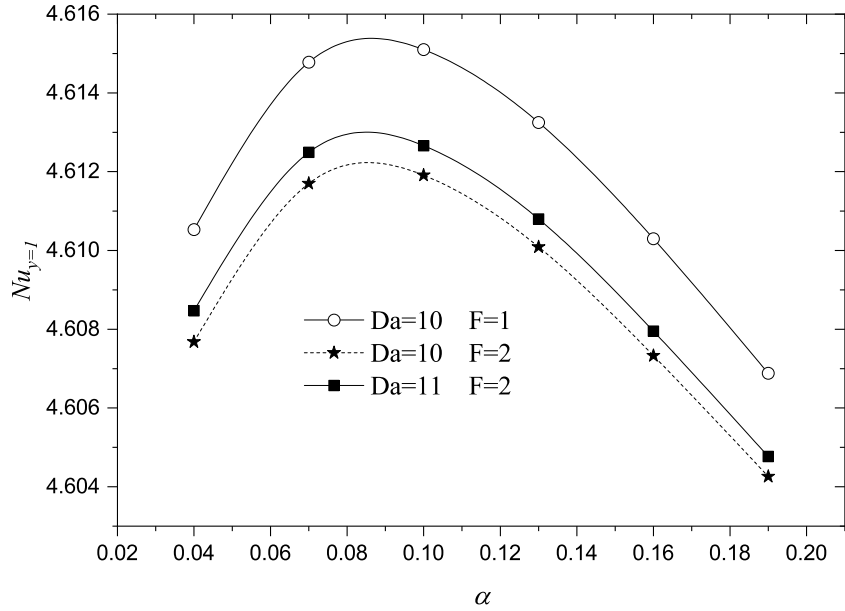
4.5.4 Effects of parameters on skin friction

In Figs. 4.28-4.29, the effects of ϕ, M, Rd, Da y H on the skin friction coefficient C_f are presented. The skin friction coefficient is calculated from the viscosity correlation and velocity gradient of the hybrid nanofluid. In Fig. 4.28 it is observed that C_f at $y = 0$ decreases with the increment in ϕ because the reduction in the nanofluid velocity gradient prevails over the viscosity increment. This decrement of C_f is 5.3% when ϕ varies from 0 to 0.1. Also, it is observed that the skin friction coefficient C_f decreases with both M and Rd due to the reduction in the velocity gradient.

The values of the skin friction coefficient at $y = 1$ are shown in Fig. 4.29, it is observed that there are maximum values of C_f approximately at $\phi = 0.04$. These maximum values move towards larger values of ϕ when H increases. For small values of ϕ, the skin friction coefficient increases with ϕ due to the increment in the effective dynamic viscosity and reaches a maximum after which the skin friction coefficient begins to decrease because the decrement in the velocity gradient with ϕ becomes dominant. When H and Da increase, C_f increases due to the increment in the velocity gradient that occurs for both cases.

Fig. 4.28 Skin friction coefficient at bottom plate as function of ϕ for different values of M and Rd.
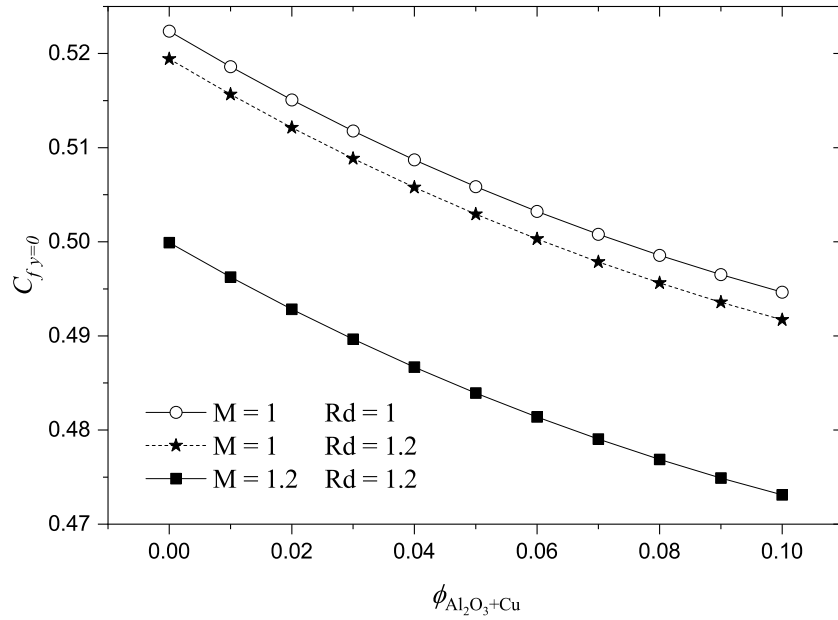
Fig. 4.29 Skin friction coefficient at top plate as function of ϕ for different values of H and Da.
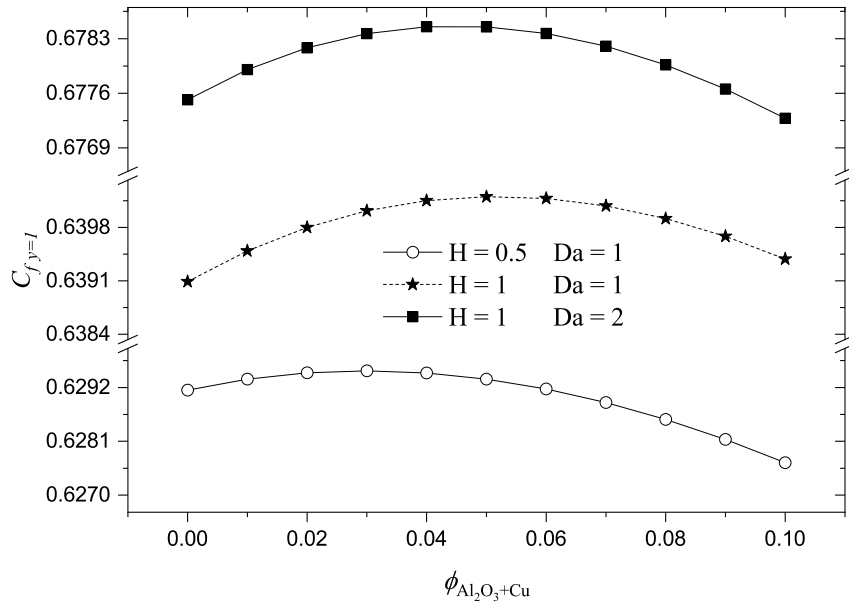
4.5.5 Effects of solid nanoparticle shapes

In Figs. 4.30-4.36, the impacts of different nanoparticle shapes on the dynamic and thermal behavior of Al_2O_3-Cu/H_2O hybrid nanofluid, as well as on the system optimum operating conditions, are presented. The effects of spherical, blade, brick, platelet and cylindrical shapes of nanoparticles are examined. In Fig. 4.30, the velocity profiles are presented. It is observed that the spherical shape provides the highest velocity values followed by blade, brick, platelet and cylindrical shapes, respectively.

These differences are mainly due to the different viscosity values provided for each shape. For $\phi = 0.1$, the spherical shape has the lowest viscosity, while the cylinder shape has the highest viscosity. This fact is related to the sphericity factor, so that in Eq. (19) at higher values of a and b, the viscosity increases. The increment in the velocity at the microchannel center is 86% for the spherical shape compared to the cylindrical one.

Fig. 4.30
Nanofluid velocity profiles for different nanoparticle shapes. $\phi_{Al_2O_3} = 0.05$, $\phi_{Cu} = 0.05$.
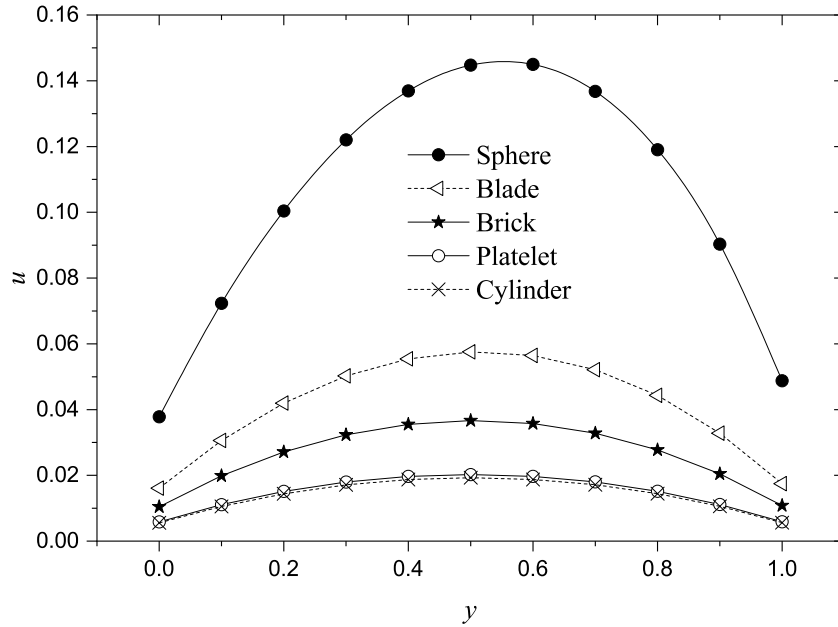
Fig. 4.31 shows the temperature profiles for each shape of Al₂O₃-Cu hybrid nanoparticles, these temperature values mainly depend on the thermal conductivity provided by each nanoparticle shape. It is observed that near the bottom plate higher temperature values of 0.81 are achieved for spherical nanoparticles while lower temperature values of 0.78 are reached for blade nanoparticles. This is because the blade shape has a higher thermal conductivity and hence the temperature is lower in that microchannel region. This is also related to the contact surface of each nanoparticle shape. Thus, the blade shape has the largest contact surface in the Hamilton-Crosser model Eq. (21) and this improves heat transfer. Near the top plate, higher temperature values are reached for the blade shape (0.5837) and lower temperature values are reached for the brick and spherical shapes (0.5494). This indicates that higher temperature gradients are achieved for the brick and spherical shapes while the lowest temperature gradient is provided by the blade shape.

Fig. 4.31
Nanofluid temperature profiles for different nanoparticle shapes. $\phi_{Al_2O_3} =$ 0.05, $\phi_{Cu} =$ 0.05.
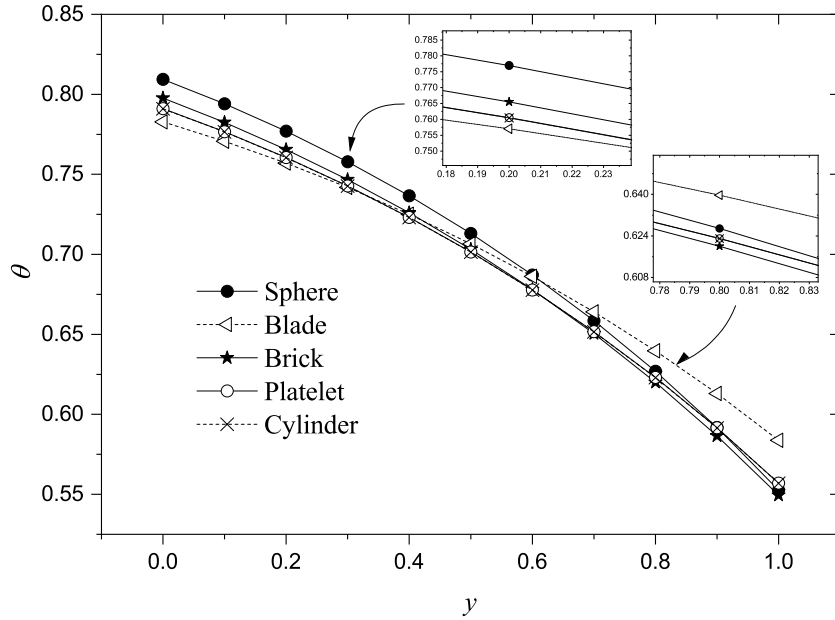
Fig. 4.32 *Local entropy for different nanoparticle shapes. $\phi_{Al_2O_3} =$ 0.05, $\phi_{Cu} =$ 0.05.*
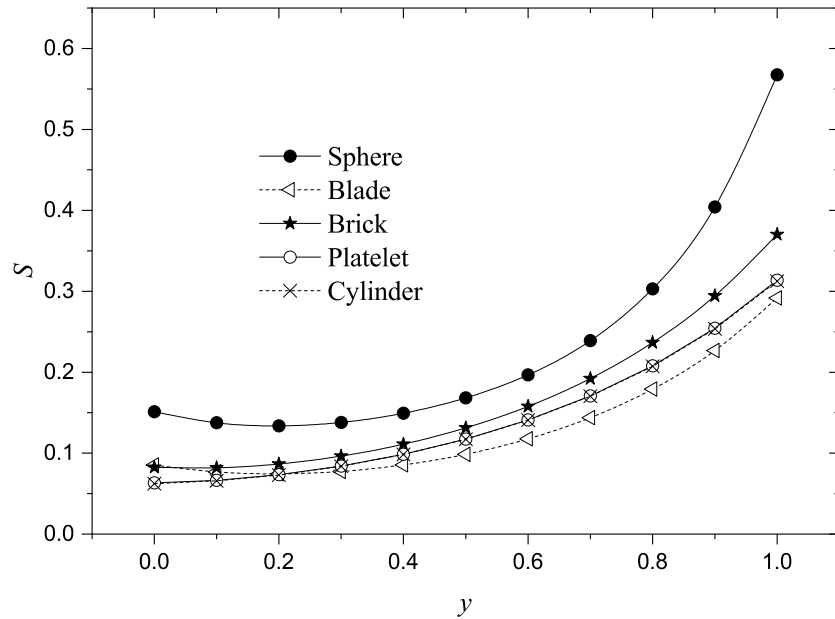
In Fig. 4.32, the local entropy S is presented. It is observed that the highest entropy values are achieved for the spherical shape while the lowest entropy values are provided by the blade-shaped nanoparticles. A reduction of 41% of entropy in the center of the microchannel ($y = 0.5$) can be achieved with the blade shape compared to the spherical shape. This is directly related to the irreversibility due to heat transfer which dominates. Thus, the lowest entropy values occur for the nanoparticle shapes that provide a lower temperature gradient in the hybrid nanofluid, which depends on the thermal conductivity.

138

In Figs. 4.33 and 4.34, the global entropy for different nanoparticle shapes is shown. It is found that the global entropy $<\dot{S}>$ always decreases with ϕ. This is due to the increment in the hybrid nanofluid viscosity with ϕ, which decreases both the velocity and the velocity gradient. Therefore, the irreversibilities S_v, S_{Da}, S_J, and S_F decrease. In Fig. 4.33, it is shown that for ϕ values between 0.01 and 0.08 the platelet shape presents the lowest entropy while for ϕ values greater than 0.08 the blade shape provides the lowest entropy values. It is also found that the spherical shape always produces the greatest production of entropy.

Fig. 4.33 *Global entropy as function of ϕ for different nanoparticle shapes.*
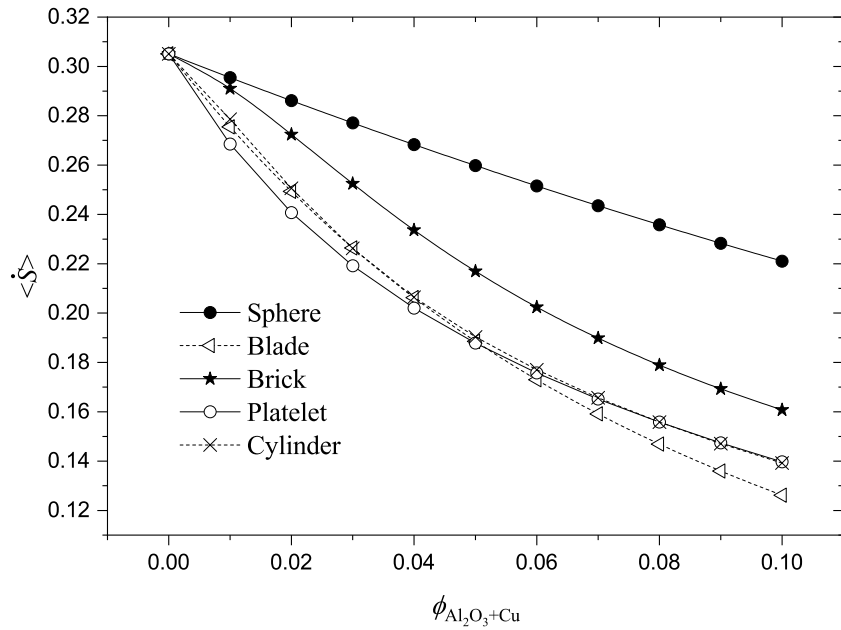
The optimum mixing ratios of nanoparticles for different shapes are presented in Fig. 4.34. It is observed that optimum proportions are found for all shapes of nanoparticles. The highest value of optimum mixing ratio is reached at approximately $\phi_{Al_2O_3}/\phi_{Cu} = 0.075/0.025$ for the spherical shape. This optimum value moves towards lower values of $\phi_{Al_2O_3}$ and higher values of ϕ_{Cu} when the thermal conductivity increases. Thus, the lowest mixing ratio $\phi_{Al_2O_3}/\phi_{Cu} = 0.03/0.07$ is achieved for the blade shape.

The heat transfer for the bottom plate $Nu_{y=0}$ as a function of Gr is shown in Fig. 4.35. It is observed that the highest heat transfer is achieved for the blade shape followed by cylindrical, platelet, brick and spherical shapes, respectively. For all nanoparticle shapes, optimum Gr values are achieved with maximum heat transfer. These optimum values of Gr number are 0.5, 1, 2, 3 and 2.7 for the spherical, blade, brick, platelet and cylindrical shapes, respectively. There is an increase in the Nusselt number of approximately 9.5% for the blade shape compared to the spherical shape.

Fig. 4.34
Normalized global entropy as function of different nanoparticle mixing ratios $\phi_{Al_2O_3}/\phi_{Cu}$ with total $\phi = 0.1$ for different nanoparticle shapes.
$\gamma = \pi/2.$
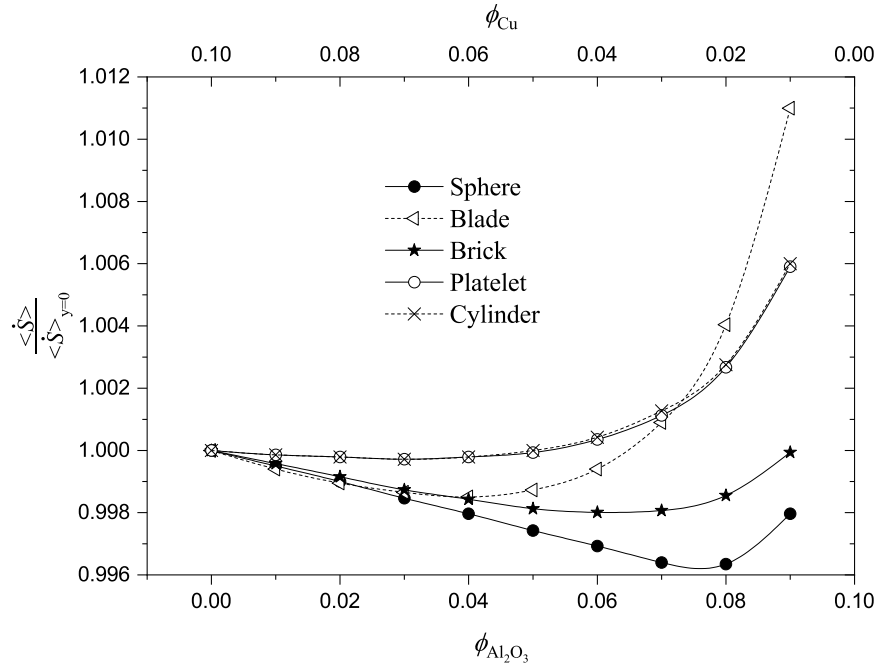
Fig. 4.35 Nusselt number at bottom plate as function of Gr for different nanoparticle shapes. $H = 0.1$, $\phi_{Al_2O_3} = 0.05$, $\phi_{Cu} = 0.05$.
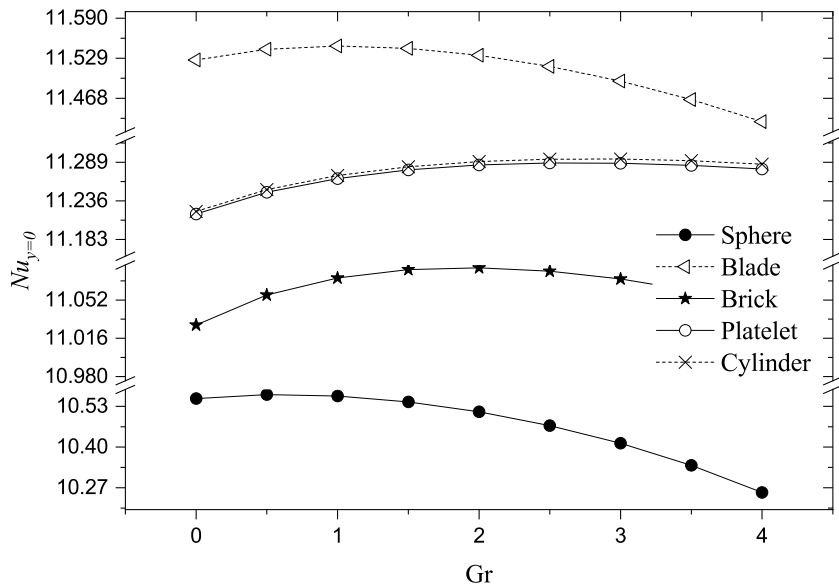
Fig. 4.36 shows the skin friction coefficient C_f as a function of ϕ for each nanoparticle shape. There are maximum values of the skin friction coefficient for all shapes. These maxima occur at low values of ϕ (0.02 and 0.03) for the nanoparticle shapes with higher viscosity (cylindrical and platelet) and these maxima move towards higher values of ϕ (0.05 and 0.06) for the shapes with lower viscosity (brick, blade and spherical).

The highest value of skin friction coefficient of 0.647 occurs for the blade shape at $\phi = 0.05$ and the lowest value of 0.638 is provided by the cylindrical shape. An increment of approximately 0.8% is found for the maximum value of the skin friction when the blade shape is compared to spherical shape.

Fig. 4.36 *Skin friction coefficient at cold top plate as function of φ for different nanoparticle shapes.*
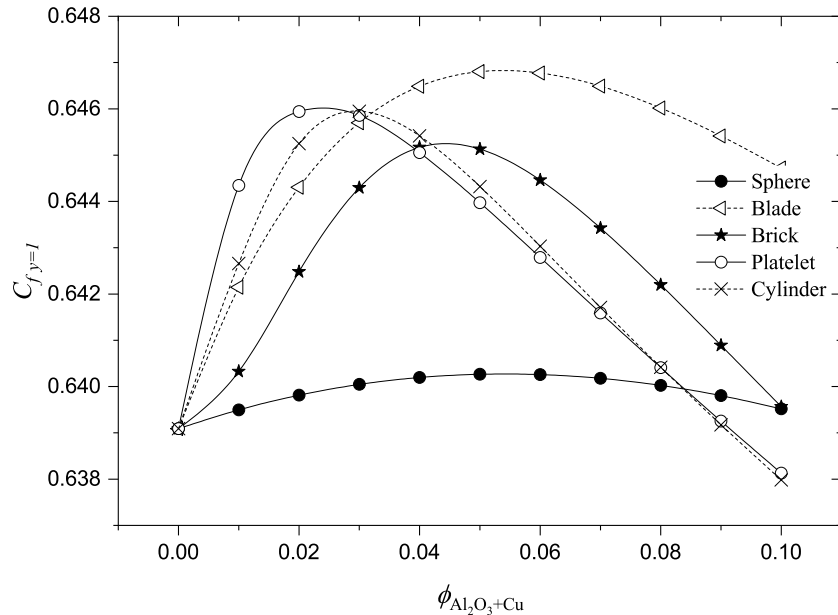
4.5.6 Effects of different types of hybrid nanofluids

In this subsection, the effects of different types of hybrid nanofluids on entropy and heat transfer are examined (Figs. 4.37-4.41). The hybrid nanofluids of Al_2O_3-Cu, TiO_2-Al_2O_3 and TiO_2-Cu in water as base fluid are compared with each other and the impacts of the parameters ϕ, Gr, Da and F are analyzed. In Table 4.4, the thermophysical properties of water and solid nanoparticles of Al_2O_3, Cu and TiO_2 are shown.

In Fig. 4.37 the global entropy S is presented for concentrations of $\phi_1 = \phi_2 = 0.05$. It is observed that the highest entropy values are reached for the mixture of TiO_2-Al_2O_3 nanoparticles while the lowest values occur for Al_2O_3-Cu and TiO_2-Cu. This fact is due to the presence of Cu nanoparticles in the last two combinations which provides greater density and thermal conductivity to the nanofluid. This causes a decrement in both the velocity and the irreversibility associated to friction. The entropy decreases approximately 1.2% for Al_2O_3-Cu and TiO_2-Cu nanoparticles compared to TiO_2-Al_2O_3 mixture at $\phi = 0.1$.

Table 4.4 *Thermophysical properties of water and solid nanoparticles [14, 28]*

	Al_2O_3	Cu	TiO_2	H_2O
Specific heat [J/kgK]	765	385	686.2	4179
Electrical conductivity [S/m]	1×10^{-12}	59.6×10^6	2.6×10^6	5.5×10^{-6}
Thermal conductivity [W/mK]	40	400	8.9528	0.613
Dynamic viscosity [kg/ms]	--	--	--	8.91×10^{-4}
Density [kg/m³]	3970	8933	4250	997.1
Thermal expansion coefficient [1/K]	0.85×10^{-5}	1.67×10^{-5}	0.9×10^{-5}	21×10^{-5}

*Fig. **4.37** Global entropy as function of ϕ for different nanofluids.*
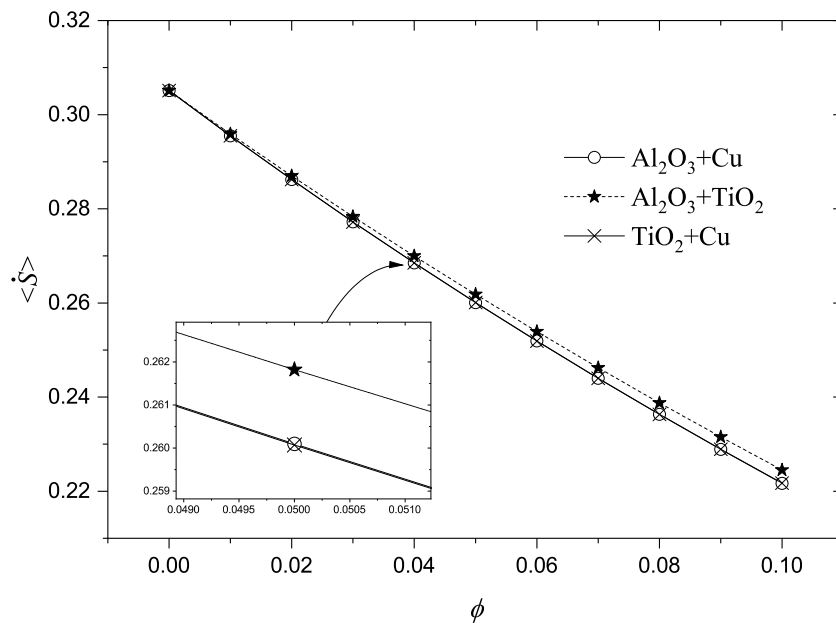
The heat transfer for the hot bottom plate $Nu_{y=0}$ as a function of Gr for the three types of nanofluids studied is illustrated in Fig. 4.38. It is observed that $Nu_{y=0}$ presents maximum values for all types of hybrid nanofluids at $Gr = 0.6$ approximately. The highest heat transfer values are achieved for the Al₂O₃-TiO₂/H₂O hybrid nanofluid with an improvement of 0.5% compared to the other two types of hybrid nanofluids. This fact happens because the global temperature of hybrid nanofluid T_b increases due the low thermal conductivity of the Al₂O₃-TiO₂ mixture compared to Cu-TiO₂ y Al₂O₃-Cu. Therefore, $\left|\theta_{y=0} - T_b\right|$ decreases for the Al₂O₃-TiO₂ mixture and consequently the Nusselt number increases. The reverse behavior occurs for Cu-containing hybrid nanofluids.

Fig. 4.38 *Nusselt number at hot bottom plate as function of Gr for different nanofluids.*
$H = 0.1$,
$\phi_{Al_2O_3} = 0.05$,
$\phi_{Cu} = 0.05$.
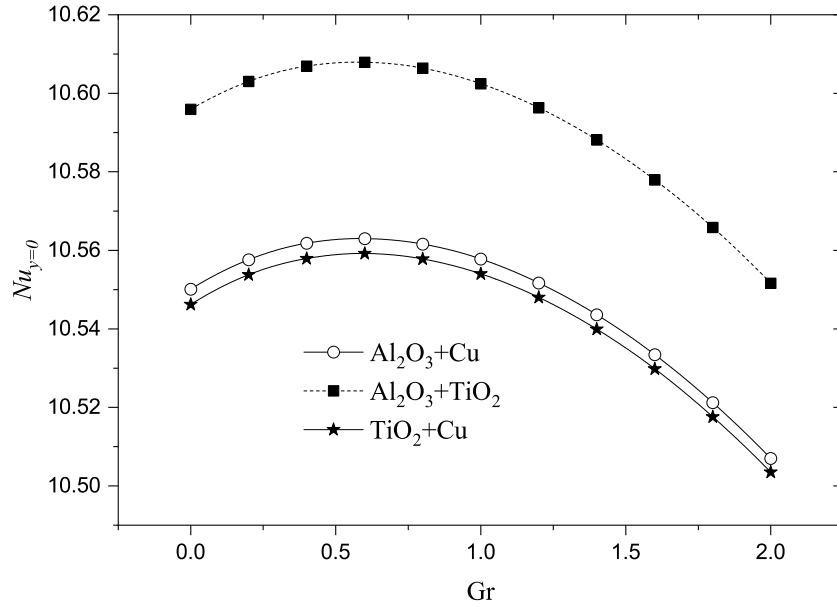
Fig. 4.39 shows the skin friction coefficient as a function of ϕ for the different types of nanofluids. The highest values of C_f are found for Al₂O₃-TiO₂ while the lowest values were reached for Cu-TiO₂ and Al₂O₃-Cu. This is because these last two mixtures have greater density and thermal conductivity. Due to this, the nanofluid velocity gradient decreases and this decrement predominates over the increment in the dynamic viscosity in such a way that the skin friction decreases. The C_f decreases by approximately 2% for both Cu-TiO₂ and Al₂O₃-Cu compared to Al₂O₃-TiO₂ at $\phi = 0.1$.

Fig. 4.39 *Skin friction coefficient at bottom plate as function of ϕ for different nanofluids.*
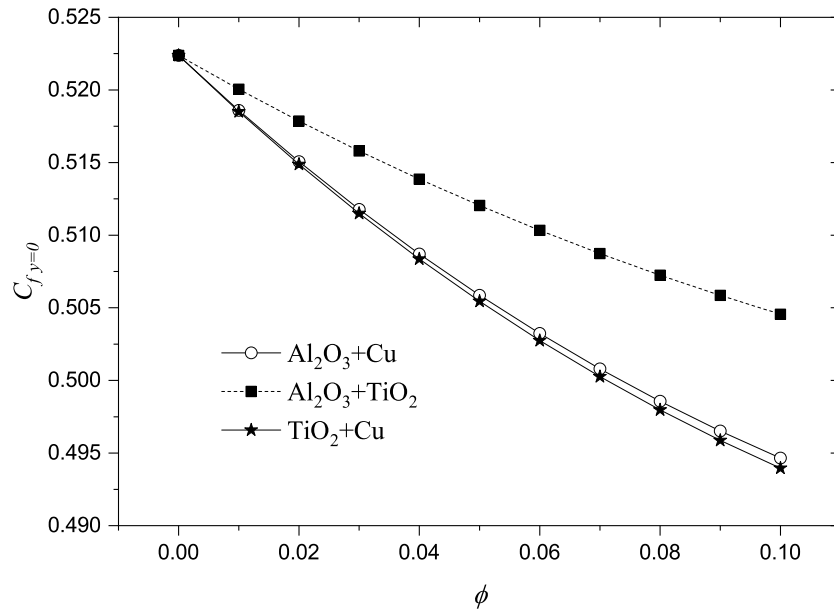
In Fig. 4.40, the global entropy $< \dot{S} >$ as a function of different mixing ratios for the water-based TiO$_2$-Al$_2$O$_3$ hybrid nanofluid is presented for total volume fraction $\phi = \phi_{Al2O3} + \phi_{Cu}$ of 0.1. The global entropy decreases with the increment in the concentration of Al$_2$O$_3$ nanoparticles and the decrement of the concentration of TiO$_2$. This decrease in $< \dot{S} >$ occurs due to the decrease in irreversibility associated to viscous dissipation caused by the low thermal expansion coefficient of Al$_2$O$_3$ compared to TiO$_2$. The entropy decreases by approximately 2% when the ratio $\phi_{Al_2O_3}/\phi_{TiO_2} = 0.01/0.09$ changes to $\phi_{Al_2O_3}/\phi_{TiO_2} = 0.09/0.01$.

Fig. 4.40 Global entropy as function of different nanoparticle mixing ratios $\phi_{Al_2O_3}/\phi_{TiO_2}$ with total $\phi = 0.1$ for different values of Gr and H.
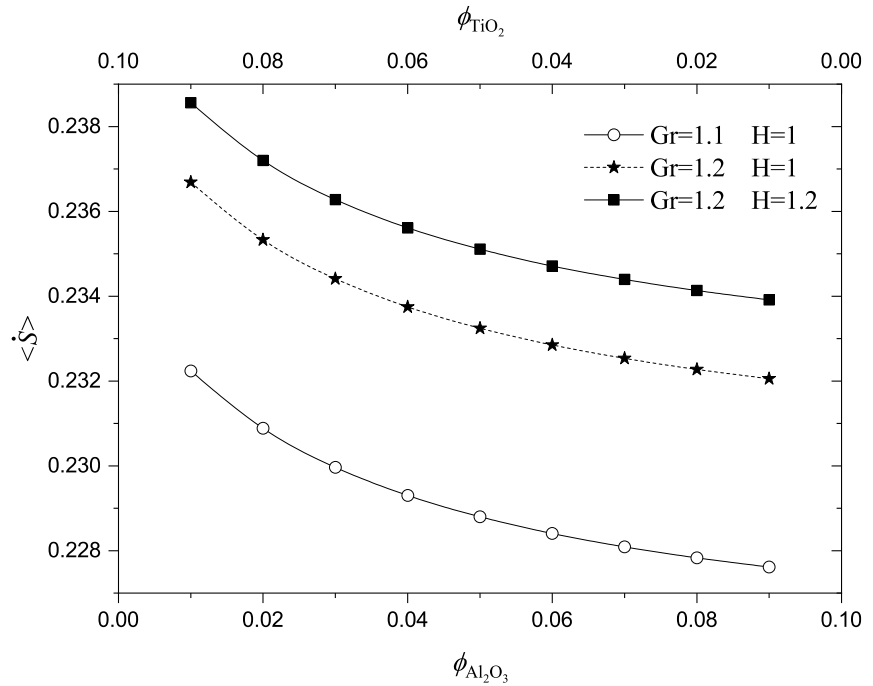
Fig. 4.41 presents the global entropy as a function of different mixing ratios of Cu-TiO$_2$ hybrid nanofluid for total $\phi = \phi_{Cu} + \phi_{TiO_2} = 0.1$. Optimum mixing ratios with minimum entropy generation are observed for all curves. The entropy reaches a minimum of 0.2452 for $Da = 1$ and $F = 1$ equivalent to an improvement of 0.32% compared to the minimum 0.2463 achieved for $Da = 1.2$ and $F = 1$. The optimum conditions are approximately achieved for a mixing ratio with $\phi_{Cu} = 0.03$ and $\phi_{TiO_2} = 0.07$ in all cases.

When the concentration of Cu increases and that of TiO$_2$ decreases in the mixture, the entropy decreases due to the increment in the effective density of the nanofluid. This produces a decrease in velocity and velocity gradient with a consequent decrease in irreversibilities associated with viscous dissipation, which predominates until the entropy reaches a minimum value for a given value of the nanoparticle mixing ratio.

Later, the global entropy increases because the effect produced by the increase in Cu concentration begins to predominate. This increase in the concentration of Cu in the mixture produces a decrease in the temperature of the nanofluid due to its high thermal conductivity with the consequent increase in entropy.

Fig. 4.41 Global entropy as function of different nanoparticle mixing ratios ϕ_{Cu}/ϕ_{TiO_2} with total $\phi = 0.1$ for different values of Da and F. Gr = 1.5.

4.6 CONCLUSIONS
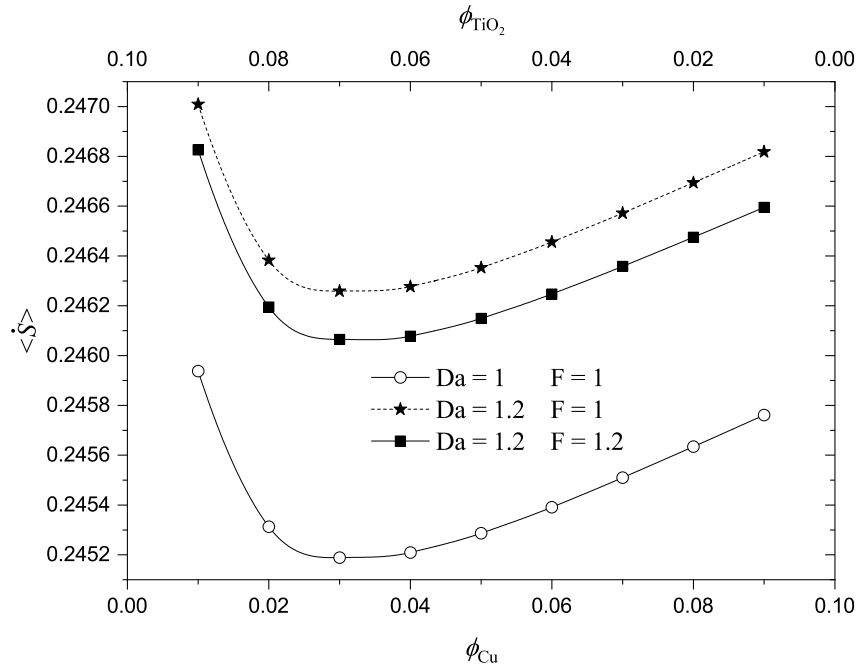
The MHD flow of a hybrid nanofluid through an inclined microchannel with permeable walls and filled with a porous medium was studied for different mixing ratios of nanoparticles considering nonlinear thermal radiation and internal heat generation. The governing equations of momentum and energy were solved numerically using the Runge-Kutta method together with the Shooting Technique. The effects of different mixing ratios of nanoparticles and different shapes of nanoparticles (spherical, blade, brick, platelet and cylindrical) on heat transfer and entropy production for the Al_2O_3-Cu/H_2O hybrid nanofluid were investigated. Also, the impacts of different types of hybrid nanofluids (Al_2O_3-Cu/H_2O, TiO_2-Cu/H_2O and Al_2O_3-TiO_2/H_2O) on the optimum operating conditions were explored. The main contributions and findings are summarized below:

- Optimum values of hydrodynamic slip α between 0.06 and 0.07 with minimum global entropy $< \dot{S} >$ were found for all explored conditions with $Re \geq 2$.

- The increment in both Grashof number Gr and inclination angle γ increased $<\dot{S}>$ due to the increment in the velocity and velocity gradient caused by the buoyancy forces which resulted in a favorable pressure gradient. Therefore, the irreversibilities associated to friction and Joule dissipation also increased. When Gr increased from 1 to 1.5, the $<\dot{S}>$ value increased by approximately 10.8% for all values of the total concentration of nanoparticles ϕ, while the increment in γ from 45º ($\pi/4$) to 90º ($\pi/2$) increased the $<\dot{S}>$ value by approximately 14.5%.

- Increasing the internal heat generation H, $<\dot{S}>$ was increased due to the increment in the coolant temperature, which increased both the velocity and velocity gradient. Therefore, once again the irreversibilities associated to friction and Joule heating increased.

- Optimum values of nanoparticle mixing ratio $\phi_{Al_2O_3}/\phi_{Cu}$ in the base fluid with minimum $<\dot{S}>$ were achieved for Al_2O_3-Cu/H_2O hybrid nanofluid, which implies a lower loss of useful energy in the system. These optimum values of $\phi_{Al_2O_3}/\phi_{Cu}$ were obtained for both 0.05 and 0.1 values of the total volume fraction of nanoparticles ϕ in the mixture. These optimum conditions have not been reported in previous works.

- For ϕ=0.1, the optimum values of $\phi_{Al_2O_3}/\phi_{Cu}$ with minimum $<\dot{S}>$ were 0.08/0.02 and 0.07/0.03 depending on the values of Gr and H explored, while for ϕ=0.05, the optimum values of $\phi_{Al_2O_3}/\phi_{Cu}$ were 0.025/0.025, 0.03/0.02 and 0.036/0.014 for Gr 1.1, 1.2 and 1.5, respectively. It was also noticed that the optimum value of $\phi_{Al_2O_3}/\phi_{Cu}$ moved to higher values with Gr due to the increment in the buoyancy force, while it remained approximately constant when H was varied.

- Maximum value of $Nu_{y=0}$ (Nusselt number at hot bottom plate) was found at $Gr = 0.6$, while maximum value of $Nu_{y=1}$ (Nusselt number at cold top plate) was found at $\alpha = 0.09$.

- Increasing the radiation parameter Rd from 1 to 1.1, the maximum value of $Nu_{y=0}$ at $Gr = 0.6$ increased from 10.56 to 11.43 (8.2%), while when H increased from 0.1 to 0.2, it decreased from 11.43 to 11.35 due to the decrement in the nanofluid temperature gradient near the bottom plate.

- When H and Da increased, C_f increased due to the increment in the velocity gradient. This means that a higher energy supply (greater pumping power) will be required to achieve the desired flow and heat transfer.

- The highest values of $<\dot{S}>$ were reached for the spherical shape because this nanoparticle shape provided the greatest values of velocity, velocity gradient and temperature gradient. For values of total ϕ less than 0.05, the platelet shape presented the lowest values of $<\dot{S}>$, while for values of total ϕ greater than 0.05 it was the blade shape. Thus, $<\dot{S}>$ decreased from 0.22 to 0.125 (43 %) for the platelet shape compared to the spherical one at $\phi = 0.1$.

- Optimum values of $\phi_{Al_2O_3}/\phi_{Cu}$ with minimum $< \dot{S} >$ were found for all nanoparticle shapes. These optimum values were 0.075/0.025, 0.06/0.04, 0.04/0.06 and 0.03/0.07 for the spherical, brick, blade, cylindrical and platelet shapes, respectively.
- Optimum Gr values with maximum heat transfer were found for all studied nanoparticle shapes at hot bottom plate. The highest values of $Nu_{y=0}$ were achieved for the blade shape due to its high thermal conductivity, while the lowest values of $Nu_{y=0}$ occurred for the spherical shape. Therefore, the heat transfer was enhancement by approximately 9.3% for the blade shape compared to the spherical.
- Undesired maximum values of C_f were found for all explored shapes. These maximum values of C_f were reached at ϕ values between 0.02 and 0.03 for cylindrical and platelet shapes, and between 0.05-0.06 for the brick, blade, and spherical shapes. The highest value of C_f=0.647 was provided for the blade shape at $\phi = 0.05$, while its smallest value was provided by the spherical shape for $\phi \leq 0.082$ and by the cylindrical shape for $0.082 < \phi < 0.1$.
- Finally, in addition to Al_2O_3-Cu nanoparticles, TiO_2-Cu and Al_2O_3-TiO_2 hybrid nanoparticles in water as base fluid were also examined. The smallest values of $< \dot{S} >$ were achieved for Al_2O_3-Cu/H_2O and TiO_2-Cu/H_2O compared to Al_2O_3-TiO_2/H_2O. Moreover, the TiO_2-Cu/H_2O hybrid nanofluid provided an optimum nanoparticle mixing ratio of $\phi_{TiO_2}/\phi_{Cu} = 0.07/0.03$ with minimum $< \dot{S} >$.
- The highest values of heat transfer for the hot bottom wall were provided by the Al_2O_3-TiO_2/H_2O nanofluid with an enhancement of 0.5% compared to the other two hybrid nanofluids examined, and the lowest values of the friction coefficient were found for the TiO_2-Cu/H_2O and Al_2O_3-Cu/H_2O nanofluids with a decrement of 2% compared to Al_2O_3-TiO_2/H_2O at $\phi = 0.1$.

A good engineering design of heat transfer systems with hybrid nanofluid flows through microchannels such as CPUs and MHD micropumps aims to minimize useful energy losses. Hence, the possibility of achieving a minimum in entropy production using appropriate mixing ratios of nanoparticles in the base fluid for hybrid nanofluids, which is the main result of present study, might be useful to optimize the operating conditions of these heat transfer devices.

4.7 REFERENCES

[1]   Izadi M, Sheremet MA, Mehryan SAM. Natural convection of a hybrid nanofluid affected by an inclined periodic magnetic field within a porous medium. *Chinese Journal of Physics*. 2020; *65*, 447-458. https://doi.org/10.1016/j.cjph.2020.03.006

[2]   Ghachem K, Kolsi L, Larguech S, Alnemer G. Heat and mass transfer enhancement in triangular pyramid solar still using CNT-water nanofluid. *Journal of Central South University*. 2021; 28, 3434–3448. https://doi.org/10.1007/s11771-021-4866-8

[3]   Afshari F, Sözen A, Khanlari A, Tuncer AD. Heat transfer enhancement of finned shell and tube heat exchanger using Fe2O3/water nanofluid. *Journal of Central South University*. 2021; 28: 3297–3309. https://doi.org/10.1007/s11771-021-4856-x

[4]   Sindhu S, Gireesha BJ. Scrutinization of unsteady non-Newtonian fluid flow considering buoyancy effect and thermal radiation: Tangent hyperbolic model. *International Communications in Heat and Mass Transfer*. 2022; 135: 106062. https://doi.org/10.1016/j.icheatmasstransfer.2022.106062

[5]   Felicita A, Berrehal H, Venkatesh P, Gireesha BJ, Sowmya G. Slip flow of Walter's B liquid through the channel possessing stretched walls by employing optimum homotopy asymptotic method (OHAM). *Journal of Molecular Liquids*. 2022; 353: 118731. https://doi.org/10.1016/j.molliq.2022.118731

[6]   Mondal P, Dilip KM, Shit GC, Ibáñez G. Heat transfer and entropy generation in a MHD Couette–Poiseuille flow through a microchannel with slip, suction–injection and radiation. *Journal of Thermal Analysis and Calorimetry*. 2022; 147: 4253-4273. https://doi.org/10.1007/s10973-021-10731-4

[7]   Xiong Q, Altnji S, Tayebi T, Izadi M, Hajjar A, Sundén B, Li LK. A comprehensive review on the application of hybrid nanofluids in solar energy collectors. *Sustainable Energy Technologies and Assessments*. 2021; *47*: 101341. https://doi.org/10.1016/j.seta.2021.101341

[8]   Wole-Osho I, Okonkwo EC, Abbasoglu S, Kavaz D. Nanofluids in solar thermal collectors: review and limitations. *International Journal of Thermophysics*. 2020; *41*: 1-74. https://doi.org/10.1007/s10765-020-02737-1.

[9]   Kumar K, Kumar R, Bharj RS. Entropy generation analysis due to heat transfer and nanofluid flow through microchannels: a review. *International Journal of Exergy*. 2020; *31*(1): 49-86. https://doi.org/10.1504/IJEX.2020.104728.

[10] Ibáñez G, López A, Pantoja J, Moreira J. Entropy generation analysis of a nanofluid flow in MHD porous microchannel with hydrodynamic slip and thermal radiation. *International Journal of Heat and Mass Transfer*. 2016; 100: 89-97. https://doi.org/10.1016/j.ijheatmasstransfer.2016.04.089

[11] López A, Ibáñez G, Pantoja J, Moreira J, Lastres O. Entropy generation analysis of MHD nanofluid flow in a porous vertical microchannel with nonlinear thermal radiation, slip flow and convective-radiative boundary conditions. *International Journal of Heat and Mass Transfer*. 2017; 107: 982-994. https://doi.org/10.1016/j.ijheatmasstransfer.2016.10.126

[12] Chamkha AJ, Molana M, Rahnama A, Ghadami F. On the nanofluids applications in microchannels: a comprehensive review. *Powder Technology*. 2018; *332*: 287-322. https://doi.org/10.1016/j.powtec.2018.03.044.

[13] Ibáñez G, López A, López I, Pantoja J, Moreira J, Lastres O. Optimization of MHD nanofluid flow in a vertical microchannel with a porous medium, nonlinear radiation heat flux, slip flow and convective–radiative boundary conditions. *Journal of Thermal Analysis and* Calorimetry. 2019; 135: 3401-3420. https://doi.org/10.1007/s10973-018-7558-3

[14] Gómez I, Ibáñez G, López A, Lastres O, Reyes J. Entropy generation minimization and nonlinear heat transport in MHD flow of a couple stress nanofluid through an inclined permeable channel with a porous medium, thermal radiation and slip. *Heat Transfer*. 2020; 49: 4878-4906. https://doi.org/10.1002/htj.21858

[15] Ramezanpour M, Siavashi M, Raeni AQ, Blunt MJ. Pore-scale simulation of nanoparticle transport and deposition in a microchannel using a Lagrangian approach. Journal of Molecular Liquids. 2022; 355: 118948. https://doi.org/10.1016/j.molliq.2022.118948

[16] Soumya DO, Gireesha BJ, Venkatesh P. Tangent-hyperbolic nanoliquid flow in a microchannel, thermal and irreversibility rate analysis. Waves in Random and Complex Media. 2022. https://doi.org/10.1080/17455030.2022.2108157

[17] Ellahi R, Hassan M, Zeeshan A. Shape effects of nanosize particles in Cu–H2O nanofluid on entropy generation. *International Journal of Heat and Mass Transfer*. 2015; *81*: 449-456. https://doi.org/10.1016/j.ijheatmasstransfer.2014.10.041.

[18] Zeeshan A, Hassan M, Ellahi R, Nawaz M. Shape effect of nanosize particles in unsteady mixed convection flow of nanofluid over disk with entropy generation. *Proceedings of the Institution of Mechanical Engineers, Part E: Journal of Process Mechanical Engineering*. 2017; *231*(4): 871-879. https://doi.org/10.1177/0954408916646139.

[19] Shashikumar NS, Gireesha BJ, Mahanthesh B, Prasannakumara BC, Chamkha AJ. Entropy generation analysis of magneto-nanoliquids embedded with aluminium and titanium alloy nanoparticles in microchannel with partial slips and convective conditions. *International Journal of Numerical Methods for Heat & Fluid Flow*. 2019; *29*(10): 3638-3658. https://doi.org/10.1108/HFF-06-2018-0301.

[20] Bhattad A, Sarkar J. Effects of nanoparticle shape and size on the thermohydraulic performance of plate evaporator using hybrid nanofluids. *Journal of Thermal Analysis and Calorimetry*. 2021; *143*(1): 767-779. https://doi.org/10.1007/s10973-019-09146-z.

[21] Ahmadi AA, Arabbeiki M, Ali HM, Goodarzi M, Safaei MR. Configuration and optimization of a minichannel using water–alumina nanofluid by non-dominated sorting genetic algorithm and response surface method. *Nanomaterials*. 2020; *10*(5): 901. https://doi.org/10.3390/nano10050901.

[22] Makinde OD. Second law analysis for variable viscosity hydromagnetic boundary layer flow with thermal radiation and Newtonian heating. *Entropy*. 2011; *13*(8): 1446-1464. https://doi.org/10.3390/e13081446.

[23] Bejan A. Entropy generation minimization: the method of thermodynamic optimization of finite-size systems and finite-time processes. *CRC press*. 2013. https://doi.org/10.1201/9781482239171

[24] Mahian O, Kianifar A, Kleinstreuer C, Al-Nimr MA, Pop I, Sahin AZ, Wongwises S. A review of entropy generation in nanofluid flow. *International Journal of Heat and Mass Transfer*. 2013; 65: 514-532. https://doi.org/10.1016/j.ijheatmasstransfer.2013.06.010

[25] Al-Zamily AMJ. Analysis of natural convection and entropy generation in a cavity filled with multi-layers of porous medium and nanofluid with a heat generation. *International Journal of Heat and Mass Transfer*. 2017; *106*: 1218-1231. https://doi.org/10.1016/j.ijheatmasstransfer.2016.10.102.

[26] Huminic G, Huminic A. Entropy generation of nanofluid and hybrid nanofluid flow in thermal systems: a review. *Journal of Molecular Liquids*. 2020; *302*: 112533. https://doi.org/10.1016/j.molliq.2020.112533.

[27] Kumar A, Ray RK. Shape effect of nanoparticles and entropy generation analysis for magnetohydrodynamic flow of (Al_2O_3–Cu/H_2O) hybrid nanomaterial under the influence of Hall current. *Indian J Phys.* 2022; 96: 3817–3830. https://doi.org/10.1007/s12648-022-02300-8.

[28] Estrada R, Ibáñez G, López A, Lastres O, Pantoja J, Reyes J. Analytical analysis of impacts of nanoparticle shapes and uncertainty in thermophysical properties on optimum operating conditions of MHD nanofluid flow in a microchannel filled with porous medium. *Journal of Thermal Analysis and Calorimetry*. 2024; *149*(1): 265-298. https://doi.org/10.1007/s10973-023-12678-0.

[29] Leong KY, Ahmad KK, Ong HC, Ghazali MJ, Baharum A. Synthesis and thermal conductivity characteristic of hybrid nanofluids–a review. *Renewable and Sustainable Energy Reviews*. 2017; *75*: 868-878. https://doi.org/10.1016/j.rser.2016.11.068.

[30] Hayat T, Nadeem S. Heat transfer enhancement with Ag–CuO/water hybrid nanofluid. *Results in physics*. 2017; *7*: 2317-2324. https://doi.org/10.1016/j.rinp.2017.06.034.

[31] Babu JR, Kumar KK, Rao SS. State-of-art review on hybrid nanofluids. *Renewable and Sustainable Energy Reviews*. 2017; *77*: 551-565. https://doi.org/10.1016/j.rser.2017.04.040.

[32] Esfe MH, Alirezaie A, Rejvani M. An applicable study on the thermal conductivity of SWCNT-MgO hybrid nanofluid and price-performance analysis for energy management. *Applied Thermal Engineering*. 2017; *111*: 1202-1210. https://doi.org/10.1016/j.applthermaleng.2016.09.091.

[33] Moghadassi A, Ghomi E, Parvizian F. A numerical study of water based Al2O3 and Al2O3–Cu hybrid nanofluid effect on forced convective heat transfer. *International Journal of Thermal Sciences*. 2015; *92*, 50-57. https://doi.org/10.1016/j.ijthermalsci.2015.01.025.

[34] Huang D, Wu Z, Sunden B. Effects of hybrid nanofluid mixture in plate heat exchangers. *Experimental Thermal and Fluid Science*. 2016; *72*: 190-196. https://doi.org/10.1016/j.expthermflusci.2015.11.009.

[35] Minea AA. Hybrid nanofluids based on Al2O3, TiO2 and SiO2: numerical evaluation of different approaches. *International Journal of Heat and Mass Transfer*. 2017; *104*: 852-860. https://doi.org/10.1016/j.ijheatmasstransfer.2016.09.012.

[36] Bhattad A, Sarkar J. Effects of nanoparticle shape and size on the thermohydraulic performance of plate evaporator using hybrid nanofluids. *Journal of Thermal Analysis and Calorimetry*. 2021; *143*(1): 767-779. https://doi.org/10.1007/s10973-019-09146-z.

[37] Zahid UM, Akbar Y, Abbasi FM. Entropy generation analysis for peristaltically driven flow of hybrid nanofluid. *Chinese Journal of Physics*. 2020; *67*: 330-348. https://doi.org/10.1016/j.cjph.2020.07.009.

[38] Zhang S, Lu L, Wen T, Dong C. Turbulent heat transfer and flow analysis of hybrid Al2O3-CuO/water nanofluid: An experiment and CFD simulation study. *Applied Thermal Engineering*. 2021; *188*: 116589. https://doi.org/10.1016/j.applthermaleng.2021.116589.

[39] Gupta G, Rana P. Comparative study on Rosseland's heat flux on three-dimensional MHD stagnation-point multiple slip flow of ternary hybrid nanofluid over a stretchable rotating disk. *Mathematics*. 2022; *10*(18): 3342. https://doi.org/10.3390/math10183342.

[40] Xu H, Sun Q. Generalized hybrid nanofluid model with the application of fully developed mixed convection flow in a vertical microchannel. *Communications in Theoretical Physics*. 2019; *71*(8): 903. https://doi.org/10.1088/0253-6102/71/8/903.

[41] Khosravi R, Rabiei S, Khaki M, Safaei MR, Goodarzi M. Entropy generation of graphene–platinum hybrid nanofluid flow through a wavy cylindrical microchannel solar receiver by using neural networks. *Journal of Thermal Analysis and Calorimetry*. 2021; *145*: 1949-1967. https://doi.org/10.1007/s10973-021-10828-w

[42] Benkhedda M, Boufendi T, Tayebi T, Chamkha AJ. Convective heat transfer performance of hybrid nanofluid in a horizontal pipe considering nanoparticles shapes effect. *Journal of Thermal analysis and Calorimetry*. 2020; *140*: 411-425. https://doi.org/10.1007/s10973-019-08836-y.

[43] Ghadikolaei SS, Yassari M, Sadeghi H, Hosseinzadeh K, Ganji DD. Investigation on thermophysical properties of Tio2–Cu/H2O hybrid nanofluid transport dependent on shape factor in MHD stagnation point flow. *Powder technology*. 2017; *322*: 428-438. https://doi.org/10.1016/j.powtec.2017.09.006.

[44] Shah Z, Babazadeh H, Kumam P, Shafee A, Thounthong P. Numerical simulation of magnetohydrodynamic nanofluids under the influence of shape factor and thermal transport in a porous media using CVFEM. *Frontiers in Physics*. 2019; *7*: 164. https://doi.org/10.3389/fphy.2019.00164.

[45] Manohar GR, Venkatesh P, Gireesha BJ, Ramesh GK. Numerical treatment for Casson liquid flow in a microchannel due to porous medium: A hybrid nanoparticles aspects. *Proceedings of the Institution of Mechanical Engineers, Part C: Journal of Mechanical Engineering Science*. 2022; *236*(2): 1293-1303. https://doi.org/10.1177/09544062211008933.

[46] Manjunatha S, Puneeth V, Anandika R, Gireesha BJ. Analysis of multilayer convective flow of a hybrid nanofluid in porous medium sandwiched between the layers of nanofluid. *Heat Transfer*. 2021; *50*(8): 8598-8616. https://doi.org/10.1002/htj.22292.

[47] Hussain S, Mehmood K, Sagheer M, Farooq A. Entropy generation analysis of mixed convective flow in an inclined channel with cavity with Al2O3-water nanofluid in porous medium. *International Communications in Heat and Mass Transfer*. 2017; *89*: 198-210. https://doi.org/10.1016/j.icheatmasstransfer.2017.10.009.

[48] Shashikumar NS, Thriveni K, Madhu M, Mahanthesh B, Gireesha BJ, Kishan N. Entropy generation analysis of radiative Williamson fluid flow in an inclined microchannel with multiple slip and convective heating boundary effects. *Proceedings of the Institution of Mechanical Engineers, Part E: Journal of Process Mechanical Engineering*. 2021; 09544089211049863. https://doi.org/10.1177/095440892110498.

[49] Manohar GR, Venkatesh P, Gireesha BJ, Ramesh GK. Numerical treatment for Casson liquid flow in a microchannel due to porous medium: A hybrid nanoparticles aspects. *Proceedings of the Institution of Mechanical Engineers, Part C: Journal of Mechanical Engineering Science*. 2022; *236*(2): 1293-1303. https://doi.org/10.1177/09544062211008933.

[50] You X. Nanoparticle sphericity investigation of Cu-Al2O3-H2O hybrid nanofluid flows between inclined channels filled with a porous medium. *Nanomaterials*. 2022; *12*(15): 2552. https://doi.org/10.3390/nano12152552.

[51] Al-Zamily AMJ. Analysis of natural convection and entropy generation in a cavity filled with multi-layers of porous medium and nanofluid with a heat generation. *International Journal of Heat and Mass Transfer*. 2017; *106*: 1218-1231. https://doi.org/10.1016/j.ijheatmasstransfer.2016.10.102.

[52] Rana P, Bhargava R, Bég OA, Kadir A. Finite element analysis of viscoelastic nanofluid flow with energy dissipation and internal heat source/sink effects. *International Journal of Applied and Computational Mathematics*. 2017; *3*: 1421-1447. https://doi.org/10.1007/s40819-016-0184-5.

[53] Gireesha BJ, Sindhu S. Entropy generation analysis of nanoliquid flow through microchannel considering heat source and different shapes of nanoparticle. *International Journal of Numerical Methods for Heat & Fluid Flow*. 2020; *30*(3): 1457-1477. https://doi.org/10.1108/HFF-06-2019-0472.

[54] Huminic G, Huminic A. The heat transfer performances and entropy generation analysis of hybrid nanofluids in a flattened tube. *International Journal of Heat and Mass Transfer*. 2018; *119*: 813-827. https://doi.org/10.1016/j.ijheatmasstransfer.2017.11.155.

[55] Ahammed N, Asirvatham LG, Wongwises S. Entropy generation analysis of graphene–alumina hybrid nanofluid in multiport minichannel heat exchanger coupled with thermoelectric cooler. *International Journal of Heat and Mass Transfer*. 2016; *103*: 1084-1097. https://doi.org/10.1016/j.ijheatmasstransfer.2016.07.070

[56] Khan MI, Hafeez MU, Hayat T, Khan MI, Alsaedi A. Magneto rotating flow of hybrid nanofluid with entropy generation. *Computer methods and programs in biomedicine*. 2020; *183*: 105093. https://doi.org/10.1016/j.cmpb.2019.105093.

[57] Tayebi T, Öztop HF, Chamkha AJ. Natural convection and entropy production in hybrid nanofluid filled-annular elliptical cavity with internal heat generation or absorption. *Thermal Science and Engineering Progress*. 2020; *19*: 100605. https://doi.org/10.1016/j.tsep.2020.100605.

[58] Hayat AU, Ullah I, Khan H, Weera W, Galal AM. Numerical Simulation of Entropy Optimization in Radiative Hybrid Nanofluid Flow in a Variable Features Darcy–Forchheimer Curved Surface. *Symmetry*. 2022; *14*(10): 2057. https://doi.org/10.3390/sym14102057.

[59] Li YX, Khan MI, Gowda RP, Ali A, Farooq S, Chu YM, Khan SU. Dynamics of aluminum oxide and copper hybrid nanofluid in nonlinear mixed Marangoni convective flow with entropy generation: Applications to renewable energy. *Chinese Journal of Physics.* 2021; *73*: 275-287. https://doi.org/10.1016/j.cjph.2021.06.004.

[60] Ahmad S, Nadeem S, Ullah N. Entropy generation and temperature-dependent viscosity in the study of SWCNT–MWCNT hybrid nanofluid. *Applied Nanoscience.* 2020; *10*: 5107-5119. https://doi.org/10.1007/s13204-020-01306-0.

[61] Jamshed W, Mohd Nasir NAA, Qureshi MA, Shahzad F, Banerjee R, Eid MR, Ahmad S. Dynamical irreversible processes analysis of Poiseuille magneto-hybrid nanofluid flow in microchannel: A novel case study. *Waves in Random and Complex Media.* 2021; 1-23. https://doi.org/10.1080/17455030.2021.1985185.

[62] Sindhu S, Gireesha BJ. Entropy generation analysis of hybrid nanofluid in a microchannel with slip flow, convective boundary and nonlinear heat flux. *International Journal of Numerical Methods for Heat & Fluid Flow*. 2021; *31*(1): 53-74. https://doi.org/10.1108/HFF-02-2020-0096.

[63] Yusuf TA, Mabood F, Khan WA, Gbadeyan JA. Irreversibility analysis of Cu-TiO$_2$-H$_2$O hybrid-nanofluid impinging on a 3-D stretching sheet in a porous medium with nonlinear radiation: Darcy-Forchhiemer's model. *Alexandria Engineering Journal*. 2020; *59*(6): 5247-5261. https://doi.org/10.1016/j.aej.2020.09.053.

[64] Nojoomizadeh M, D'Orazio A, Karimipour A, Afrand M, Goodarzi M. Investigation of permeability effect on slip velocity and temperature jump boundary conditions for FMWNT/Water nanofluid flow and heat transfer inside a microchannel filled by a porous media. *Physica E: Low-dimensional Systems and Nanostructures.* 2018; 97: 226-238. https://doi.org/10.1016/j.physe.2017.11.008

[65] Cengel YA, Ghajar AJ. Heat and mass transfer. *Penerbit McGraw-Hill Education*. 2015.

[66] Rahimi-Gorji M, Pourmehran O, Gorji-Bandpy M, Ganji DD. Unsteady squeezing nanofluid simulation and investigation of its effect on important heat transfer parameters in presence of magnetic field. *Journal of the Taiwan Institute of Chemical Engineers.* 2016; *67*: 467-475. https://doi.org/10.1016/j.jtice.2016.08.001.

[67] Monaledi RL, Makinde OD. Entropy generation analysis in a microchannel Poiseuille flows of nanofluid with nanoparticles injection and variable properties. *Journal of Thermal Analysis and Calorimetry*. 2021; *143*: 1855-1865. https://doi.org/10.1007/s10973-020-09919-x.

[68] Saqib M, Khan I, Shafie S, Qushairi A. Recent advancement in thermophysical properties of nanofluids and hybrid nanofluids: an overview. *City Univ. Int. J. Comput. Anal.* 2019; *3*(2): 16-25. https://researchgate.net.

[69] Gupta M, Singh V, Kumar R, Said Z. A review on thermophysical properties of nanofluids and heat transfer applications. *Renewable and Sustainable Energy Reviews.* 2017; 74: 638-670. https://doi.org/10.1016/j.rser.2017.02.073

[70] Minea AA. A review on the thermophysical properties of water-based nanofluids and their hybrids. *The Annals of "Dunarea de Jos" University of Galati. Fascicle IX, Metallurgy and Materials Science.* 2016; 39: 35-47. https://www.gup.ugal.ro/ugaljournals/index.php/mms/article/view/1279.

[71] Mahian O, Kianifar A, Kleinstreuer C, Al-Nimr MA, Pop I, Sahin AZ, Wongwises S. A review of entropy generation in nanofluid flow. *International Journal of Heat and Mass Transfer.* 2013; 65: 514-532. https://doi.org/10.1016/j.ijheatmasstransfer.2013.06.010

CHAPTER V

CONCLUDING REMARKS AND RECOMMENDATIONS

5.1 CONCLUSIONS

In this thesis work, two problems were studied focused on the optimization of the MHD flow of nanofluids in microchannels formed by parallel permeable plates, various dynamic and thermal effects that increased the precision of the model were considered. The main novelties for the first case study (horizontal microchannel with unitary nanofluid) are the presentation of analytical solutions to the momentum and energy equations, and the determination of optimal design parameters with minimum entropy generation and maximum heat transfer. The solutions can be used to calibrate similar models. The use of different models for estimating thermophysical properties (dynamic viscosity and thermal conductivity) from several authors was analyzed. It was found that empirical (experimental) correlations differ greatly from semi-empirical (theoretical) ones and the optimal values found change when using different correlations. Furthermore, in the analysis of the effect of nanoparticle shapes, optimal configurations were found for all shapes with minimum entropy and maximum heat transfer.

In the second case study (inclined microchannel with hybrid nanofluid) numerical solutions were presented, the Runge-Kutta with shooting technique method was used, the calculation of the initial values was carried out automatically creating a solution algorithm based on the method from Bolzano. The main novelties of this study were to find optimal volume fraction proportions for the hybrid nanofluids of $Al_2O_3+Cu+H_2O$ and TiO_2+Cu+H_2O, with minimal entropy generation, in addition to optimal proportions for different nanoparticle shapes.

These findings have not been presented in previous studies, therefore, the existence of optimal volume fraction proportions for hybrid nanofluids that guarantee minimal energy loss allows us to move towards the design of more efficient thermal systems.

The importance of these theoretical studies lies in the fact that they are the basis for conducting experimental research with unitary and hybrid nanofluids, obtaining optimal proportions for nanofluids, broadens the possibilities of finding better working fluids by combining base fluids and different types of solid nanoparticles. The results of this research can be used in the design of thermal systems, where microchannels are used and allows defining the best options focused on the optimization of heat transfer devices.

5.2 SUGGESTIONS FOR FUTURE WORK

Research on nanofluids has grown recently. The trends suggest that there are still needs in the study of thermophysical properties, mainly in dynamic viscosity and thermal conductivity. It has been proven that the development of new prediction models for these properties is pertinent, since there are discrepancies in the results. It is also important to determine new experimental models for different shapes of nanoparticles, because current correlations do not consider certain aspects of the nanoparticle morphology. There are studies where differences with theoretical models are reported. Strictly speaking, current correlations cannot accurately predict the specific property, because external factors such as temperature, which directly affect viscosity, thermal conductivity, density, electrical conductivity, etc., are not taken into account.

Because the study of hybrid nanofluids is relatively new, there are still many needs for the modeling of these fluids. Most correlations for hybrid thermophysical properties are generated theoretically, from unitary correlations, assuming that the total volume fraction can be divided into two types of nanoparticle, therefore the results present the same trend as a unitary nanofluid, not however, experimental studies could show different results. Then, the need arises to develop new empirical correlations that corroborate or refute these results.

Some suggestions for future research are listed below:

a) It is necessary to study the performance of different types of nanoparticles, such as silver, gold and copper oxide, and the use of different base fluids such as ethylene glycol replacing water, on the developed models.
b) It is recommended to compare the use of different correlations of thermophysical properties for hybrid nanofluids on the optimal values found.
c) It is recommended to consider convective-radiative thermal boundary conditions applied to hybrid nanofluids, this to increase model reliability.
d) It is important to carry out studies considering non-steady and turbulent flows in microchannels.
e) The impacts of chemical reaction could also be included in the current model.
f) It is recommended to perform the analysis using ternary hybrid nanofluids for different proportions of their nanoparticle concentrations in order to explore the effects on optimal design conditions.

NOMENCLATURE

a	characteristic length [m] (distance between plates)
Bi	Biot number
B_o	magnetic field [T]
Br	Brinkman number
C_p	specific heat [J·kg^{-1}·K^{-1}]
C_f	skin friction coefficient
Da	Darcy number
Ec	Eckert number
F	Forchheimer drag coefficient
$F/\sqrt{K}$	inertial coefficient [1·m^{-1}]
Gr	Grashof number
g	gravitational acceleration (m·s^{-2})
h	convective heat transfer coefficient [W·m^{-2}K^{-1}]
H	heat source parameter
M	Hartmann number
k	thermal conductivity [W·m^{-1}·K^{-1}]
K	porous medium permeability [m^2]
k^*	mean Rosseland absorption coefficient [1·m^{-1}]
Nu	Nusselt number
p	pressure [N·m^{-2}]
P	dimensionless pressure gradient
Pe	Peclet number
Pr	Prandtl number
Q_T	heat source coefficient [W·m^{-3}·K^{-1}]
q	heat flux per unit area [W·m^{-2}]
Rd	radiation parameter
Re	Reynolds number
S	local entropy generation [W·m^{-3}·K^{-1}]
$<\dot{S}>$	global entropy generation
T	temperature [K]
u	velocity [m·s^{-1}]
x	axial coordinate [m]
y	transverse coordinate [m]

GREEK SYMBOLS

v_0 uniform suction/injection velocity [m·s^{-1}]

v_f kinematic viscosity [m^{-2}·s]

α slip length [m]

β thermal expansion coefficient (K^{-1})

γ inclination angle (rad)

η dynamic viscosity [kg·m^{-1}·s^{-1}]

θ dimensionless temperature

θ_h dimensionless temperature parameter

ρ density [kg·m^{-3}]

σ electrical conductivity [S·m-1]

σ^* Stefan-Boltzmann constant [W·m^{-2}·K^{-4}]

τ viscous stress tensor

τ_w wall shear stress [N·m^{-2}]

ϕ total nanoparticle concentration

ϕ_1 nanoparticle concentration 1

ϕ_2 nanoparticle concentration 2

ψ sphericity factor

SUBSCRIPTS

1   bottom plate

2   top plate

f base fluid

nf unitary nanofluid

hnf hybrid nanofluid

s solid nanoparticle